Development of Binary Semiconductor Elongated Nanopatterns by Energetic Ion irradiation / Photon illumination for Optoelectronics/Photonics Applications

A thesis submitted in partial fulfillment of the requirements for the degree of Doctor of Philosophy

Mr Upamanyu Das
Reg. No. 024 of 2009
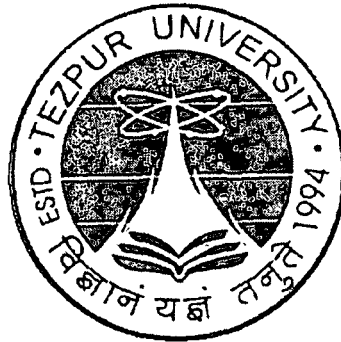
**Department of Physics
School of Science & Technology
Tezpur University
Napaam, Tezpur- 784028
Assam, India**

July 2010

Abstract

Now-a-days, the impact of nanoscience and nanotechnology has spread out all over the globe. This technology involves precise utilization of nanoscaled materials. These nanostructured materials (NSM)[1] are quantum confined condensed matter system. These NSMs are the ultra-fine material structures having an average crystallite size of the order of a few to several nanometers (10^{-9}m). Typically, it represents an intermediate state of matter in the transition region between bulk solid and molecular structure[2, 3, 4].

Amongst massive number of list of materials available in today's world, researchers have effectively fabricated mainly metallic (Au, Ag, Pt etc.), semiconductor (Ge, Si, ZnS, CdS, CdTe, ZnSe, ZnO etc.) and oxide (TiO_2, Ga_2O_3, Al_2O_3, MgO etc.) systems.

There has been considerable research interest in semiconductor nanoscale systems with special emphasis on II-VI semiconductor types. These semiconductor NSMs have unique characteristics in the sense that materials with similar chemical composition but different dimension behave differently. The properties of NSMs gradually change from bulk behavior to molecular behavior with decreasing particle si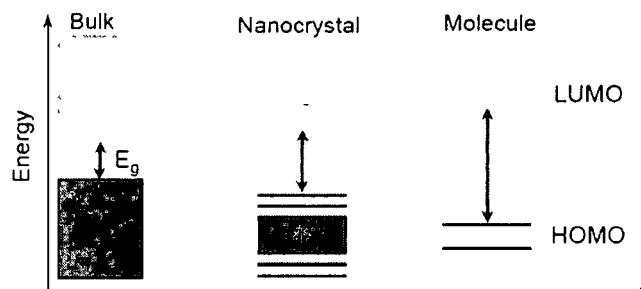ze[5,6]. The quantum size effect (QSE) that dominates in low dimensional structures with large surface-to-volume ratio results in the band gap enhancement along with the evolution of discrete energy levels. Owing to size and shape dependent tunable physical properties exhibited by semiconductor nanostructures they are considered as vital components in the next generation technology[7, 8].

It is known that, II-VI semiconductor nanoparticles (spherically symmetric nanostructures) have potential applications, for instance, in photocatalysis[9],

Figure 1 · *Evolution of energy band/states in bulk, nanoscale and molecular systems*

photovoltaics[10, 11] and optoelectronics[12] devices etc. In contrast, elongated II-VI semiconductor nanostructures[13] (nanowires, nanorods, nanostrips etc.) have several additional advantages such as tunable upconversion[14], polarized light emission[15] and high-gain lasing action[16] etc. Both spherical and elongated forms can be promising candidates for next generation displays[17], lasers[18], bio-markers[19] etc., due to their high luminescence quantum efficiency[20], spectral tunability, color purity, high optical gain with lower threshold[21] and high environmental stability[22]. Amongst the II-VI binary semiconductors, Zinc Sulfide (ZnS) and Zinc Oxide (ZnO) nanostructures have received a great deal of attention in past years[23, 24].

This thesis will focus on the synthesis and optoelectronic characterizations of ZnS and ZnO based nanostructured systems. The irradiation and transition metal impurity doping aspects will also be highlighted. To be specific, transition from spherical to elongated structure along with aspect ratio dependent optoelectronic properties will be reported.

We have planned our work that involves synthesis, characterization and application of semiconductor nanostructures with due emphasis on elongated systems. The nanostructures are prepared in organic hosts by suitable chemical/physico-chemical methods. We also stress upon growth of 1-dimensional elongated nanopatterns through solution growth and solid state routes. The various types of characterization tools used include X-ray diffractometer (XRD), scanning electron microscopy (SEM), transmission electron microscopy (TEM), UV-VIS optical absorption spectroscopy (OAS), atomic force microscopy (AFM), magnetic force microscopy (MFM) and photoluminescence spectroscopy (PL) etc. We also encounter to understand growth mechanism that facilitates in transforming nanoparticles to elongated nanopatterns.

For modification of nanostructures, they are irradiated with energetic ion beams of different ion species while fluence was varied in the range $10^{10} - 10^{13}$ ions/cm^2. Irradiation lead structural and optoelectronic properties have been compared and analyzed. Chemically synthesized, ion irradiated and photon induced elongated nanostructures have also been elaborated.

In order to grow size selective nanostructures, we have chosen two nontoxic media. First one is a water soluble polyvinyl alcohol (PVOH) polymer and the other one is a cationic surfactant called cetyl-trimethylammonium bromide (CTAB). In the first

case, the long chains of the PVOH media, which generally exist in serpent structures (coil and cage like) help in growing and encapsulating nanostructures In contrast, CTAB was used to facilitate controlled nanostructure ordering Instances of surfactant guided formation of elongated nanostructures (nanorods) have been noticed[25]

A typical TEM image of ZnS and ZnO nanoparticles grown in PVOH dielectric matrix is shown in figure 2 and figure 3 The XRD pattern (not shown) has revealed that ZnS has a cubic zinc blende structure whereas ZnO crystallizes into hexagonal wurtzite structure The surfactant (CTAB) assisted growth and evolution from spherically symmetric nanoparticle to asymmetric elongated nanostructures for ZnO and ZnS systems are shown in Figure 4 and 5 As CTAB facilitates controlled growth through micellear formation, ZnS and ZnO nanorods can be produced accordingly
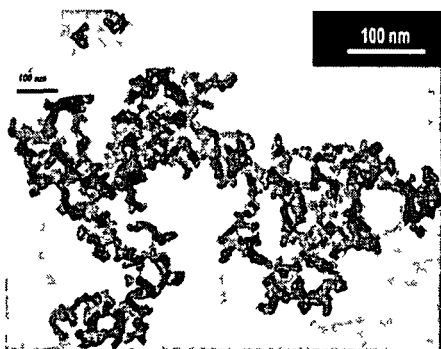

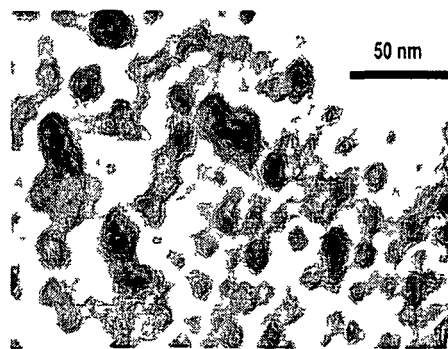*Figure 2: : TEM micrograph of ZnS nanoparticles in PVOH matrix*

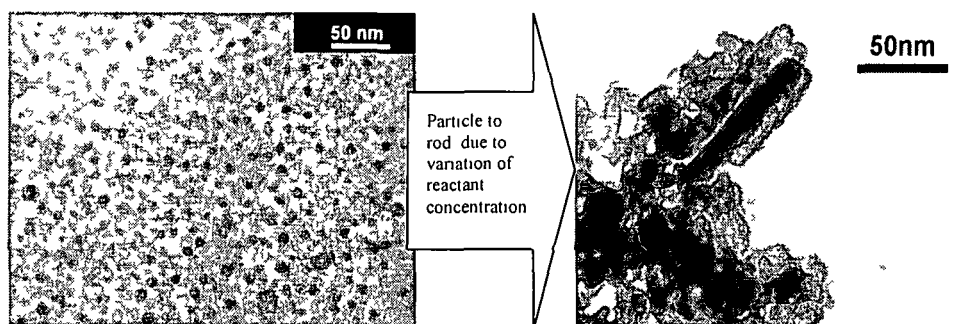*Figure 3 : TEM micrograph of ZnO nanoparticles in PVOH matrix*

Particle to rod due to variation of reactant concentration

Figure 4A: TEM microgrpah of ZnS nanoparticles in CTAB

Figure 4B : TEM microgrpah of ZnS nanorods in CTAB

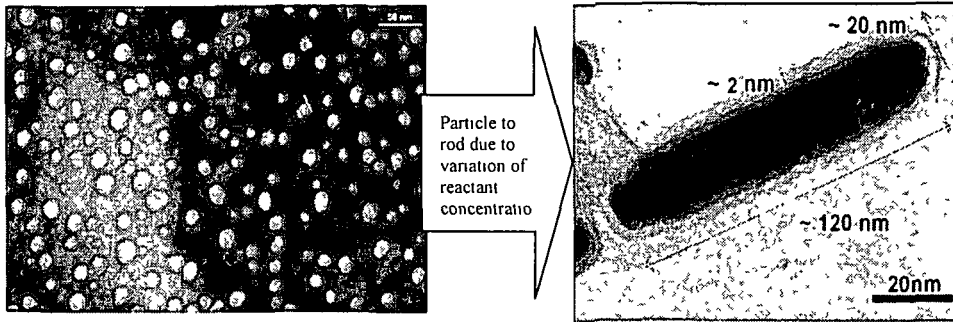Particle to rod due to variation of reactant concentratio

Figure 5A : TEM microgrpah of ZnO
nanoparticles in CTAB

Figure 5B : TEM microgrpah of ZnO
nanorod in CTAB

With an aim to explore optoelectronic properties, we have modified morphological and structural aspects of the synthesized nanosystems.   For modification, we used three technologically viable approaches:

    (a) through fabrication process

    (b) through energetic ion irradiation

    (c) through photon illumination

By controlling concentration of reactants and growth temperature, one can control aspect ratio of the nanostructures. On the other hand, through energetic ion bombardment (with the electronic energy loss greater than the nuclear energy loss calculated form SRIM[26]) one can allow nanoparticles to grow along the ion path giving rise to elongated nanostructures[27]. The formation of elongated ZnO nanostructures by 80 MeV N^{+6} ion irradiation has been confirmed. In the thesis, we shall discuss and compare nanostructure modification due to 150 MeV Titanium (Ti^{+11}), 100 MeV Silver (Ag^{+6}) and 80 MeV Nitrogen(N^{+6}) ion impact. Also, modification of nanostructures through photon illumination shall be considered.

The light emission properties of undoped and doped nanostructured systems have been investigated. In-depth analysis on the fluence dependent tunability in the photoluminescence spectrum will be discussed. The band-edge, defect related (zinc vacancy, sulfur vacancy, oxygen vacancy etc.) and impurity related emission characteristics will be presented in a quantitative and qualitative manner.

Typical photoluminescence spectra of unirradiated and 80 MeV N^{+6} irradiated ZnO nanostructures are shown in figure 6. The band-edge emission peak is clearly located at ~□375nm whereas the defect related (surface trap) emission is characterized by a broad band, peaking at ~490nm. The dominance of defect emission over band-edge emission is typical in nanostructured systems[28]. With increase in ion
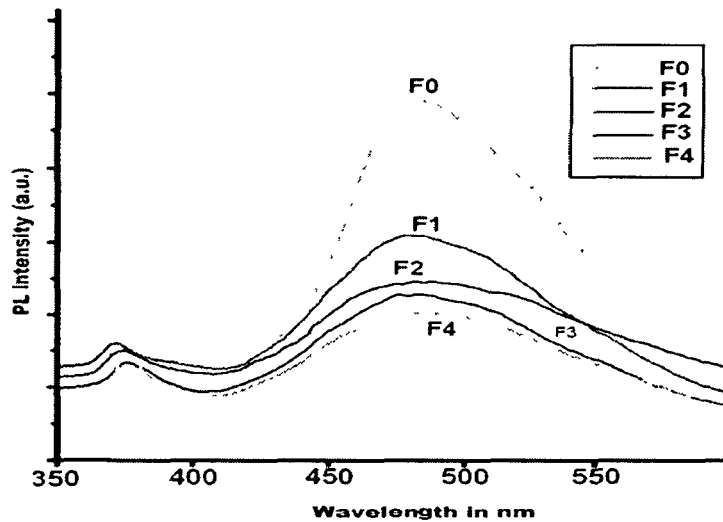

Figure 6 : Photoluminescence spectrum of ZnO nanopartilces – F0 unirradiated and irradiated at fluences 1.25X10^{10} ion/cm^2(F1), 5 0X10^{10} ion/cm^2 (F2), 2.0X10^{11} ion/cm^2, 8X10^{11} ion/cm^2(F4)

fluence, the

defect emission drops at a faster rate compared to its band-edge counterpart (figure 6). It is important to quote here that the asymmetrically broadened defect emission peak becomes more symmetric with increase in ion fluence cases.

Similarly, the PL response of Mn doped ZnS nanostructures are shown in figure 7. An intense luminescence peak (orange yellow emission) was observed at ~□580nm, which is ascribed to the impurity activated states[29]. This peak is so intense that it could suppress the sulfur vacancy related emission peak observable at ~425nm[30]. With increased Mn-doping concentration, the relative intensity due to Mn^{+2} and S^{-2} emission increases. Furthermore, for ZnS:Mn, ZnS:Cr, ZnS:Co, ZnS:Cu nanosystems, quantitative and qualitative analysis on photoluminescence aspects will be discussed in great detail.

The thesis will comprise of six chapters and each chapter will be arranged in sub-sections. The introductory chapter (i.e., chapter 1) will include motivation, historical background and challenges with regard to various kinds of semiconductor nanostructures. In chapter 2, we shall discuss on materials and
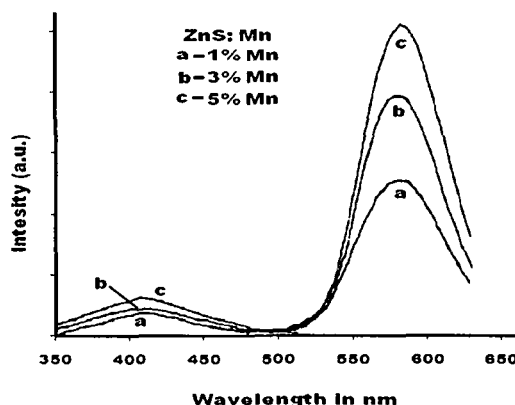

Figure7 : PL spectra of ZnS:Mn nanostructures

methodologies. A detailed synthesis protocol and characterization of binary semiconductor nanostructures will be presented in chapter 3. Chapter 4 will deal with the organization of nanostructures using ion irradiation and photon illumination. The luminescence and optoelectronic properties alongwith possible applications will be highlighted in chapter 5. The irradiation led tunability in the luminescence[31, 32] properties can be employed for various optoelectronic and photonic devices, particularly in sensors and display devices which work on a selective range of the electromagnetic spectrum. Lastly, conclusive remarks and future directions will be discussed in chapter 6.

References:

[1] R. Birringer and H. Fleiter in "Enclopedia of Material Science and Engineering "(R.W.Cahn,ed.) Suppl. Vol. 1. p. 339. Pergamon Press, Oxford, U.K. 1988

[2] Henglein A, Topics in current chemistry, 143 (1998) 113

[3] Brus L E, Appl. Phys. A 53 (1991) 465

[4] Wang Y and Herron N, J. Phys. Chem. 95 (1991) 525

[5] Henglein A, Topics in current chemistry, 143 (1998) 113

[6] Brus L E, Appl. Phys. A 53 (1991) 465

[7] J. Nanda, K. S. Shipway, I. Willner, J. Chem. Soc. Perkin Trans, 2 (1999) 1925

[8] C B Murray, D J Norris and M F Bawendi, J. Am. Chem. Soc. 115, (1993) 8706

[9] Q. Wan , T. H. Wang, J. C. Zhao Appl. Phys. Lett. 87, (2005) 083105

[10] P. Ravirajan, A. M. Peiró, M.K. Nazeeruddin, M. Graetzel, D. D. C. Bradley, J.R. Durrant, J. Nelson, J. Phys. Chem. B, 110 (2006), 7635

[11] W.V. Huynth, J.J. Dittmer, A.P. Alivisatos, Science 295 (2002) 2425.

[12] F Henneberger et al 1991 Semicond. Sci. Technol. 6 A41-A50

[13] Wei Lu et al 2006 J. Phys. D: Appl. Phys. 39 R387-R406

[14] J Ouyang, J A. Ripmeester, X Wu, D Kingston, K Yu, A G. Joly, Wei Chen, J. Phys. Chem. C, 111 (2007), 16261

[15] J.Hu, L.Li, W.Yang, L.Manna, L.Wang, A.P.Alivisatos, Science 292 (2001) 2060

[16] M. Kazes, D.Y. Lewis, Y. Ebenstein, T. Mokari, U. Banin, Adv. Mater. 14 (2002) 317.

[17] D. Banerjee, S. H. Jo, Z. F. Ren, Advanced Materials 16(2004) 2028

[18] R. Hauschild, H. Lange1, H. Priller, C. Klingshirn1, R. Kling, A. Waag, H. J. Fan, M. Zacharias, H. Kalt, phys. stat. sol.(b) 243 (2006) 853

[19] W J Parak, T Pellegrino, C Plank, Nanotechnology 16 (2005) R9

[20] X. Liu, X. Ni1, J. Wang, X. Yu, Nanotechnology 19 (2008) 485602

[21] C Zhang, F Zhang, T Xia, N Kumar, J Hahm, J Liu, Z LWang, J Xu Opt.Exp.17(2009) 7893

[22] P. K. Nayak, J. Jang, C. Lee, Y. Hong, Appl. Phys. Lett. 95, (2009)193503

[23] X. Fang; Y Bando, U. K. Gautam, T Zhai; H Zeng; X Xu; M Liao; D Golberg, Critical Reviews in Solid State and Materials Sciences, 34(2009) 190

[24] C. Klingshirn , physica status solidi (b) 244 (2007) 3019

[25] R. Chakraborty, U. Das, D. Mohanta , A. Choudhury, Ind. J Phy, 83(2009) 479

[26] srim.org

[27] D. Mohanta, G.A. Ahmed, A.Choudhury, F.Singh , D.K. Avasthi, G. Boyer , G.A. Stanciu, EPJ: Appl. Phys. 35 (2006) 29

[28] A Cavallini, L Polenta, M Rossi, T Richter, M Marso, R Meijers, R Calarco, H Luth, Nano Letters, 6(2006)1548

[29] R.N. Bhargava, D. Gallagher, Phys. Rev. Lett. 72 (1994) 416

[30] D. Denzler, M. Olschewski, and K. Sattlera, J Appl. Phys. 84 (1998) 2841

[31] U Das, D.Mohanta, A.Choudhury, F. Singh, D.K. Avasthi, Ind. J. Phys.,81 (2007) 155

[32] U. Das, D. Mohanta, A.Choudhury, F.Singh, D.K Avasthi, Ind. J.Phys, 82(2008)163

DECLARATION

I hereby declare that the thesis entitled "Development of Binary Semiconductor Elongated Nanopatterns by Energetic Ion irradiation / Photon illumination for Optoelectronics/Photonics Applications" being submitted to the Department of Physics, Tezpur University, Napaam, Tezpur, Assam (India) in fulfillment of the requirements for the award of the degree of Doctor of Philosophy, has previously not formed the basis for the award of any degree, diploma, associateship, fellowship or any other similar title or recognition.

25 july 2010

(Upamanyu Das)

ACKNOWLEDGEMENTS

Department of Physics :: Tezpur University
Napaam, Tezpur, Assam-784 028 (India)

Dr. Dambarudhar Mohanta
Assistant Professor

Phone: 03712-267007-9 Extn-5558
Fax: (+91) 3712-267005,6
E-mail- best@tezu.ernet.in

Date ....

CERTIFICATE

This is to certify that the thesis entitled "**Development of Binary Semiconductor Elongated Nanopatterns by Energetic Ion irradiation / Photon illumination for Optoelectronics/Photonics Applications**" being submitted by **Mr Upamanyu Das** to the Department of Physics, Tezpur University, Tezpur, Assam (India) in fulfillment of the requirements for the award of the degree of Doctor of Philosophy, is a record of original bonafide research work carried out by him. He has worked under my guidance and supervision and has fulfilled the requirements for the submission of this thesis. The results contained in the thesis to the best of my knowledge have not been submitted in part or full to any other university or institute for award of any degree or diploma.

(D. Mohanta)

PREFACE

After the great success of microelectronics in the last century, the nanoscale materials emerged as the building blocks of the next generation of electronic, optoelectronic and chemical sensing devices The development and deployment of these materials play a role in terms of speed and compatibility while achieving the goals nanotechnology

This thesis is the description of a number of development methods of ZnS and ZnO nanostructures alongwith their optoelectronic properties An emphasis was made on developing spherically symmetric nanoparticles to elongated nanostructures (nanorods) by various means The irradiation and metal impurity doping aspects are being highlighted To be specific, transition from spherical to elongated structures alongwith aspect ratio dependent optoelectronic properties are also discussed

The thesis is comprised of six major chapters where each chapter will be arranged in some sub-sections The introductory chapter (i e , Chapter-1) will includes motivation, historical background and challenges with regard to various kinds of semiconductor nanostructures In Chapter-2, materials and methodologies used to carry out various experimental works are discussed The techniques used for modification and characterizations of the nanostructure are elaborated in this Chapter A detailed synthesis protocol and characterization of binary semiconductor nanostructures (ZnS, ZnO) are presented in Chapter 3 Chapter 4 deals with the works on the development of elongated nanopatterns due to ion irradiation and photon illumination The luminescence responses applicable to optoelectronics/photonics, of the developed nanostructured are highlighted in chapter 5 The irradiation led modification and tunability in the optoelectronics/photonics properties material are discussed in the Chapter Lastly, conclusive remarks and future directions will be discussed in chapter 6

Upamanyu Das

Upamanyu Das

Abbreviations

AFM	Atomic force microscopy
CCD	Charged Coupled Devices
CL	Cathedoluminesnce
CNT	Carbon Nanotube
CVD	Chemical Vapour Deposition
DMS	Diluted Magnetic Semiconductor
DNA	Deoxyribonucleic acid
EBOM	Effective Band Order Model
EDS	Energy dispersive spectroscopy
EMA	Effective Mass Approximation
FTIR	Fourier Transform Infra Red
FWHM	Full width half maxima
HRTEM	High resolution transmission electron Microscopy
HOMO	Highest Occupied Molecular Orbital
IR	Infra Red
IP-EMA	Infine potential Effective Mass Approximation
JCPDS	Joint Committee on Powder Diffraction Standards
LCAO	Linear Combination of Atomic Orbital
LCAO-MO	Linear Combination of Atomic Orbital-Molecular Orbital
LUMO	Lowest Unoccupied Molecular Orbital
LED	Light Emitting Diode
MFM	Magnetic force microscopy
MO	Molecular Orbital
MWNT	Multi wall nanotube
NC	Nanocrystal
NSM	Nanostructure Material
QD	Quatnum Dot
rpm	round par minute
SEM	Scanning Electron Microscopy
STM	Surface Tunneling microscopy
SWNT	Single wall nanotube
SPM	Surface probe microscopy
TB	Tight Binding
TEM	Transmission Electron Microscopy
UV	ultra violet
XRD	X-ray diffraction

List of Figures

Chapter 2

Chapter 3

Chapter 5

List of Tables

CONTENTS

DECLARATION

CERTIFICATE

ACKNOWLEDGEMENT

PREFACE

Abbreviations

List of Figures

List of Tables

Chapter 3:
Fabrication of II-VI semiconductor nanostructures

Chapter 4

Organization and modification of binary semiconductor nanostructures

Chapter 5 :

Luminescence Characteristics for optoelectronic /photonics applications

Chapter 6 :

Conclusion and future directions

PUBLICATIONS

ADDENDA

Chapter 1

Introduction

Now-a-days, the impact of nanoscience and nanotechnology is spread out all over the globe. This technology involves precise utilization of nanostructured material (NSM) [1]. These NSMs are the ultra-fine material structures having an average phase or grain size on the order of a few nanometers (10^{-9}m). Each nanoparticle in NSMs can be considered as a "nano crystallite" of a typical size of the order of few nanometers, consisting of 100's to 1,000,000's of atoms. It is a state of matter in the transition region between bulk solid and molecular structure [2-5]. The importance of NSMs is being realized owing to its unique size-dependent characteristics in the sense that materials with similar chemical composition but different dimension behave differently. With size reduction, its physical properties gradually shift form bulk behavior towards molecular behavior.

Although NSMs are considered as an invention in the area of modern science, they actually have a long history. NSMs were used by artisans as far back as the 9th century in Mesopotamia for generating a glittering effect on the surface of pots. Egyptians also knew to use the healing powers of gold nanoparticles against wounds and physical ailments. The use of colloidal particles of gold and different materials was known and used by the Romans toward the middle age (for e.g. staining of glass). In modern times, it was the great alchemist Paracelsus who first prepared gold colloid solution (16th century). He called his purple solution of gold *Aurum Potable* (Latin: potable gold) and believed it cured all manner of physical, mental, and spiritual ailments. But serious study on gold colloids did not start until the mid-19th century by Faraday, who prepared the first pure colloidal gold which he called 'activated gold' [6]. He used phosphorus to reduce a solution of gold chloride for the development his colloidal gold. These colloidal solutions were the first, which gives us an idea about size effects. Faraday was the first started to study the size dependence of the physical properties of a material. He also used gold, but proceeded in the other direction to study the size effect: he started with very small pieces of gold (nanocrystalline gold) in

solution and, by pressing them together, made bigger pieces of gold. His amazement at what he observed is clear from the March 11, 1856 entry in his diary [6].

". and then put on the gold above the convex surface of a rock crystal plano convex lens and pressed it by hand steadily, rocking it a little. This pressure converted the violet or dark tint of the place [of contact] to a beautiful green - far more beautiful than any I have seen in a gold leaf beaten - the effect was perfect."

Faraday was one of the greatest scientists of the 19th century. So, it is not at all surprising that his diary continues with, what we now know to be, a rather accurate explanation of this phenomenon:

"Has the pressure converted the layer of atoms into a continuous layer by expansion and welding, and is that all the difference? I rather think it is. . . . So it appears that these different layers are all gold, and owe their different appearances not to composition but to physical differences."

Faraday discovered that the color (or to be more precise: the electronic structure) of a metal can become size dependent below a certain critical size. What this critical size was, and why it was different for the different metals that he investigated, was something that Faraday could not understand fully. In the early twentieth century, work on the glasses containing Cadmium Sulphide (CdS) showed that there was a red-shift in the absorption threshold with the growth of CdS particle size [7]. So far, it is the first experiment that proved that this size dependence of material properties also applied to semiconductors. It was found that both the absorption and the emission of CdS shifted towards shorter wavelengths for smaller crystallite sizes. Again, a qualitative explanation was sought in terms of the reduced size of the CdS crystal and shifting of absorption peaks.

During the first half of 20th century it was revealed that a material can become strongly dependent on the size of the material below a certain threshold size. But no adequate explanation of the size effects was at that time. It was the seventies, the impetus progress in the development of analytical skills and the fabrication of low-

dimensional semiconductor structures made it possible to understand physical basis of such effects in quantitative qualitative ways.

In the late 1960's researchers reported differences between the absorption spectra of colloidal semiconductor particles and the spectra of the corresponding macro-crystalline materials in 1967, Berry reported that the absorption onset of suspensions of crystals of AgBr [8] and AgI [9] was shifted to shorter wavelengths as compared to the macro-crystalline material, and made the following statement:

"The observed shift of the absorption curve to shorter wavelengths should not be regarded as suggesting a mechanism in which the band gap is widened, but as either a decreased number of absorbing atoms or a decreased efficiency of the phonon-assisted electronic transitions."

In 1968, Stasenko presented experiments on the thin films of CdS [10], motivated by the prediction from Sandomirskii (1963) that for very thin semiconductor films the band gap is inversely proportional to the square of the film thickness [10]. The results were in good agreement with the theoretically predicted shift of the bandgap and he reported: *"Such a forbidden-energy gap increase is connected with quantum effects"*

It was realized in the early 1980's that these quantum effects are not only responsible for the different properties of the nanostructured materials as compared to the macro crystalline material, but also for some the peculiar behavior of particles. Some 15 years after the firm statement by Berry, it was shown that the mechanism that he ruled out (widening of the band gap) is in fact responsible for his observations. In the last two decade researcher successfully explain most of the properties in low dimensional systems.

Among the massive number of materials available in the today's world, people able to develop and analysis large variety of materials at nanoscale regime as -

- Metals: gold [Au], silver [Ag], palladium, platinum, cobalt.
- Semiconductors: Elemental (Si, Ge), II-VI (ZnS, CdS, CdTe, ZnSe),III-V(GaAs, GaN, InP, GaAs), IV-VI(PbS, PbTe, PbTe) systems
- Oxides: ZnO , TiO_2,Ga_2O_3, Al_2O_3,MgO etc.

All of these materials show extensively new verities of properties, which make them as candidate for today's technology base world. Metal nanoparticles (Ag, Au etc) exhibit plasmon absorbance bands in the visible spectral region that are controlled by the size of the particles [11]. Numerous studies reported on the labeling for bioassays and staining of biological tissues using those metal nanoparticles as means to analyze and visualize biological processes [12-18]. Among the Oxides materials, the well-known nanocrystalline film of titanium dioxide was shown to be utilized for dye-sensitized solar cells [19, 20]. Now a day, effort is being put worldwide to develop and assemble quality semiconductor nanostructures for variable application in industries. This thesis is focused on II-VI binary semiconductor nanostructures and their relevance to optoelectronics.

1.1 Semiconductor Nanostructure Materials

A typical semiconductor has an electrical conductivity between that of a conductor and an insulator (10^3 ohm^{-1}cm^{-1} to 10^{-8} ohm^{-1}cm^{-1}) There are four major types of semiconductor materials as listed below -

Elemental semiconductors: The elemental semiconductor materials comprise of elements from group IV of the periodic table. The materials crystallized into posses narrow indirect band gaps. Silicon (Si) and Germanium (Ge) are typical of such kind.

Binary compounds semiconductor: These kinds of semiconductors are compounds of two different group elements.

The choices are -

   Column III with column V (III-V's): $A_{III}B_V$

   Example :GaAs, GaN, InP etc

   Column II with column VI (II-VI's): $A_{II}B_{VI}$

   Example : ZnS, CdS, ZnO etc

   Column IV with Column VI (IV-VI's): $A_{IV}B_{VI}$

   Example : PbS, PbSe, PbTe etc

The energy band gap of II-VI systems are found wider while for the IV-VI system it is found narrower.

	III	IV	V	VI
	B 5	C 6	N 7	O 8
II	Al 13	Si 14	P 15	S 16
Zn 30	Ga 31	Ge 32	As 33	Se 34
Cd 48	In 49	Sn 50	Sb 51	Te 52
Hg 80	Tl 81	Pb 82	Bi 83	Po 84

Figure 1.1: Part of a periodic table

Ternary alloy semiconductor: These are alloys of two binary compound semiconductors. Ternary alloys have two elements from one column and one from another. Depending on the substation sites (cationic/anionic) can have two options:

$$A_{III(x)}B_{III(1-x)}C_V = [A_{III}C_V]_{(x)} + [B_{III}C_V]_{(1-x)}$$

$$A_{III}B_{V(y)}C_{V(1-y)} = [A_{III}B_V]_{(y)} + [A_{III}C_V]_{(1-y)}$$

Some of the commonly used ternary semiconductor alloys are Aluminium gallium arsenide ($Al_xGa_{1-x}As$), Indium gallium arsenide (In_xGa_{1-x} As), Aluminium indium antimonide ($Al_xIn_{1-x}Sb$), Gallium arsenide nitride ($Ga_xAs_{1-x}N$), Aluminium gallium phosphide ($Al_xGa_{1-x}P$), Indium gallium nitride ($In_xGa_{1-x}N$), Indium arsenide antimonide ($In_xAs_1.Sb$)

Quaternary alloys semiconductor: Quaternaries alloys are consisting of 4 elements. It may be mixer of four binary semiconductor or three binary semiconductors. Some such semiconductors are: Aluminium gallium indium phosphide (AlGaInP); Aluminium gallium arsenide phosphide (AlGaAsP); Indium gallium arsenide phosphide (InGaAsP); Aluminium indium arsenide phosphide (AlInAsP); Aluminium gallium arsenide nitride (AlGaAsN); Indium gallium arsenide nitride (InGaAsN); Indium aluminium arsenide nitride (InAlAsN).

Although nanostructured materials are objects made out of metallic, semiconductor or insulating materials, in the last two decades, there has been much research on nanoparticles made out of semiconductor system, especially on II-VI semiconductor types, e.g. CdSe, CdTe, CdS, ZnS, etc. Any of these semiconductor material containing grain size or clusters below 100 nm or layer, filament of that dimension is considered as semiconductor nanostructure. It is a state of matter in the transition region between bulk solid and molecular structure. The NSMs materials have unique characteristics in the sense that materials with similar chemical composition but different dimension behave differently. The properties gradually change from bulk behavior to molecular behavior with decreasing particle size. It is due to the quantum mechanical phenomenon which dominates in low dimension al structures which results and are associated with:

- Enhancement in band gap and evolution of discrete energy levels

- Extremely high surface to volume ratio (>>1) compared to bulk which is about 10% for 100 Å particles and 90% for 10 Å particles.

- Enhancement in excitonic binding energy with respect to bulk as a result of which the exciton absorption can be visible at the room temperature

- Enhancement in the oscillator strength with respect to bulk
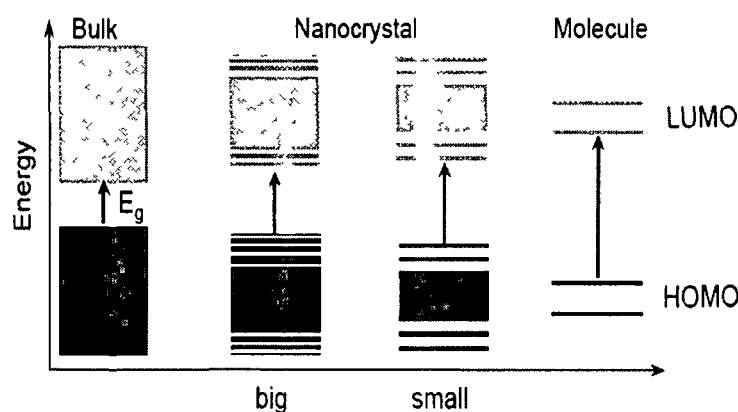
Figure 1.2 : Evolution of energy gap (E_g) in bulk, nanocrystal and molecule

Since in a NSM, most of the atoms are displayed on the surface than the core, surface reactivity increases at large. It has been reported that their optical, electronic, magneto-optical and catalytic properties can be uniquely vary with size [21-23]. It is expected that the size dependent properties of the nanocrystals is just enormous. To name a few are microelectronics, electro-optics, nonlinear optics, catalysis, photography, electrochemistry and many more.

The specific properties of NSMs materials can have two different possible origins. First, *Size effects*, which result from the spatial confinement of carrier motion in a low-dimensional system. An example is the confinement of electron wavefunctions inside a region whose size is smaller than the electron mean free path. This class of effects may give birth to completely new properties. Second one is the *surface effects*, which are a consequence of the significant volume fraction of matter located near surfaces, interfaces, or domain walls.

1.2 Quantum effect in Semiconductor Nanostructure

From Faraday (1856) to Berry (1967) all observed change of properties in ultra-small particles and Stasenko (1968) has shown that this can be explained considering quantum mechanics in to account. Upto eighties, it was thought that this quantum confinement effect is the only phenomenon responsible for change of properties at nanoscale. Higher surface to volume ratio, discretization of energy levels and enhancement in surface energy etc. decides the physical properties of the Nanostructured Materials at large.

1.2.1 Quantum effects in Semiconductor Nanostructures:

In the early eighties, quantum confinement effect on small particles in suspension was first reported in the early 1980s by Ekimov[25] , Efros [26] and Papavassiliou [27]. Later, Brus et al. [28,29] laid out the proper framework for understanding such effects from the view point of molecular quantum physics.

This quantum confinement is observed in semiconductor crystals with sizes of few nanometer due finite size of the crystal, which limits the motion of electrons, holes, and excitons (a quasi-particle a electron-hole pair interacting each other via coulomb potential) cab be resticted along one or more direction .

The excitons correspond to a hydrogen like bound state of an electron-hole pair and characterized by an exciton Bohr radius defined as [30] -

$$a_B = \frac{4\pi\varepsilon_o\varepsilon_r\hbar^2}{e^2}\left(\frac{1}{m^*_e} + \frac{1}{m^*_h}\right)$$

(1.1)

With ε_r relative dielectric constant (high frequency), m^*_e effective mass of electron, m^*_h effective mass of hole . This exciton Bohr radius (a_B) is considerably larger the respective value for a hydrogen atom (~0.53Å). For most of the semiconductors it is ~ 1- 10 nm.

The excitonic Bohr radius is a useful parameter in quantifying the quantum confinement effect in NSMs. We can say "Quantum confinement effects" arise when the size of a nanocrystal is comparable to the length parameters i.e., the deBroglie wavelength λ and exciton Bohr radius a_B of the carriers (electrons, holes, excitons).

When the radius of a particle approaches the exctonic Bohr radius a_B the movement of carriers (excitons, electrons, holes) is confined and coulomb interaction is increased, thereby increasing excitonic binding energy. This leads to drastic changes in the electronic structure of NSMs. The changes include shift of the energy levels to higher energy, the development of discrete feature of the spectra and the development of strong oscillator strength between selective transitions.

The first explanation for the quantum confinement effect in nanocrystals was *Effective Mass Approximation* (EMA) given by Efros and Efros [26]. This approach, based on the 'particle in a box model' and the effective masses of the electron (m^*_e) and the hole (m^*_h), with parabolic bands.

EMA is based on the following assumptions- (1) The crystal structure of the Quantum dot (nanoparticle) is same as that of the bulk material (2) The QD is assumed to be spherical in shape with a radius R (3)The potential barrier at the surface of the QD is infinite

The real space stationary Schrödinger equation for an electron in a bulk crystalline solid with a spatially periodic potential is

$$\left[\frac{-\hbar^2}{2m^*} \nabla^2 + V(r) \right] \Psi_k(r) = E_k \Psi_k(r) \tag{1.2}$$

Where the first term represents the kinetic energy operator for the electron and $V(r)$ is the periodic potential energy experienced by the electron. The potential V may include the ionic potential with respect to lattice translations such that

$$V(r) = V(r+T) \tag{1.3}$$

Where, T is lattice translational vector.

The Bloch theorem indicates that an eigenfunction of the Schrodinger equation for a periodic potential is the product of a plane wave $e^{ik \cdot r}$ times a function $U_k(r)$ which has the same periodicity as periodic potential $V(r)$. Thus we get

$$\Psi_k(r) = e^{ik \cdot r} U_k(r) \tag{1.4}$$

$$\text{with } U_k(r) = U_k(r+T) \tag{1.5}$$

Assuming a parabolic band, the eigenvalues of Equation (1.2) for the eigenfunctions $\psi_{v,k}(r)$ can be given by

$$E(k) = \frac{\hbar^2 k^2}{2m^*} \quad (1.6)$$

with m^* being the effective mass of electron or hole.

An excited state of a nanocrystal can be considered quantum mechanically as electron-hole-pair states inside a spherical potential. In the envelope function approximation, the eigenstate is composed of an envelope function $\psi(r)$ and a periodic part U_k of Bloch function $\psi_k(r)$ -

$$i.e, \quad \Psi_k(r) = U_k(r)\Psi(r) \quad (1.7)$$

For non-interacting electron-hole pairs, the envelop function consists of independent contributions from electrons and holes and can be written as

$$\psi(r_e, r_h) = \phi_e(r_e) \ \phi_h(r_h) \quad (1.8)$$

The periodic part is assumed to be the same in the barrier (well) , so -

$$U_k(r)_{barrier} = U_k(r)_{well} = U_k(r) \quad (1.9)$$

The Hamiltonian operator for the envelope function in single parabolic potential approximation and without coulomb interaction is given by -

$$H = -\frac{\hbar^2}{2m_e}\nabla_e^2 - \frac{\hbar^2}{2m_h}\nabla_h^2 + V_e(r_e) + V_h(r_h) \quad (1.10)$$

Such that the confining potential $V(r)$ becomes

$$V_i(r_i) = 0 \quad for \quad r_i < R \quad (i = e, h)$$
$$V_i(r_i) = \infty \quad for \quad r_i > R \quad (i = e, h) \quad (1.11)$$

The normalized wave function ϕ_i for electron and hole can be obtained by solving the Schrodinger equation using the wave function Eq.(1.8) and Hamiltonian eq. (1.10) with boundary conditions eq. (1.12) [Davydov 1987]. This results in

$$\phi_{nlm}^i(r) = Y_{lm}\sqrt{\frac{2}{R^3}} \frac{J_l\left(\chi_{nl}\frac{r}{R}\right)}{J_{l+1}(\chi_{nl})} \quad (1.12)$$

with $-l \leq m \leq -l$ and $l = 0, 2, 3.....$;

J_l are Bessel functions and Y_{lm} are spherical harmonics

The energy eigenvalues can be derived by applying the boundary condition that the wavefunction has to vanish at the QD matrix interface, i.e.

$$J_l(\chi_{nl}\frac{r}{R})|_{R=r}=0 \tag{1.13}$$

This gives the eigenvalues -

$$E^e_{nl} = \frac{\hbar^2}{2m_e}\frac{\chi^2_{nl}}{R^2} \qquad \text{(for electron)} \tag{1.14a}$$

$$E^h_{nl} = \frac{\hbar^2}{2m_h}\frac{\chi^2_{nl}}{R^2} \qquad \text{(for hole)} \tag{1.14b}$$

Where χ_{nl} is the nth zero of the spherical Bessel function of order l; m_e, m_h are the effective masses of electron and hole respectively ; R is the radius of the nanocrystal.

Thus, labeling the quantum number l=0,1,2...., the first roots are

$$\chi_{1s}=3.1416; \quad \chi_{1p}= 4.493; \quad \chi_{1d}= 2\pi =6.2822; \quad \chi_{2s}= 7.725 \text{ etc}$$

The lowest quantized energy state with $n=1$ and $l=0$ is given by

$$E^e_{10} = \frac{\hbar^2}{2m_e}\frac{\pi^2}{R^2} \qquad \text{(for electron)} \tag{1.15a}$$

$$E^h_{10} = \frac{\hbar^2}{2m_h}\frac{\pi^2}{R^2} \qquad \text{(for hole)} \tag{1.15b}$$

Using these results we can calculate the energy levels of electron and hole using the values of χ_{nl} in Table 1.2 [Appendix 1]

So the enhancement in band gap due to quantum confinement

$$\Delta E = \frac{\hbar^2\pi^2}{2R^2}\left(\frac{1}{m_e}+\frac{1}{m_h}\right) \tag{1.16}$$

It theory also implies that the energy discretization scales with the square of the inverse radius(R).
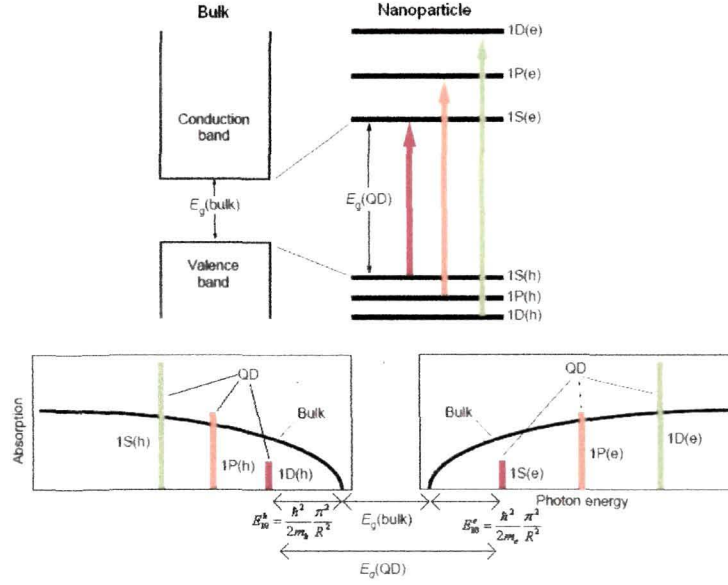
Figure 1.3 : Different energy levels of spherically symmetric semiconductor nanostructure (quantum dot) according to EMA compared to bulk material

The quantum mechanical picture of a particle in a spherical potential as given above deals with the envelope function. The Bloch part assumed to be a simple direct bandgap semiconductor with parabolic and isotropic bands. In reality, the Bloch part, for example, for semiconductor materials with indirect band gap and for anisotropic crystal structures (e.g. zinc-blende, wurtzite, perovskite etc) needs modification for a better understanding of the optical behavior of QDs.

Though EMA described by addressed quite well about the quantum confinement effect, however Efros and Efros has excluded the columbic interaction between hole and electrons present in the Quantum Dot. Brus et al (1983) have considered Coulomb interaction between the localized carriers which has modified the single-particle picture to a great extent. The modified Hamiltonian with the Coulomb interaction between the electron and hole inside the QD can be expressed as

$$H = -\frac{\hbar^2}{2m_e}\nabla_e^2 - \frac{\hbar^2}{2m_h}\nabla_h^2 - \frac{e^2}{\varepsilon_2|r_e - r_h|} + V_e(r_e) + V_h(r_h) \qquad (1.17)$$

Where, ε_2 is the dielectric constant of the QD. $|r_e - r_h|$ is the difference in the coordinates defining the columbic interaction between the electron and hole.

Using perturbation approach Brus [28, 29] developed the expression for the lowest excited state energy as -

$$E_{gn} = E_{gb} + \left(\frac{\hbar^2 \pi^2}{2R^2}\right)\left[\frac{1}{m_e^*} + \frac{1}{m_h^*}\right] - 1.8\frac{e^2}{\varepsilon_2 R} \qquad (1.18)$$

Using variational calculations Kayanuma give the expression for the lowest excited state energy as [31],

$$E_{gn} = E_{gb} + \left(\frac{\hbar^2 \pi^2}{2R^2}\right)\left[\frac{1}{m_e^*} + \frac{1}{m_h^*}\right] - 1.786\frac{e^2}{\varepsilon_2 R} - 0.248E_{RY}^* \qquad (1.19)$$

Where $E_{RY}^* = \frac{e^4}{2\varepsilon\hbar^2}\left(\frac{1}{m_e^*} + \frac{1}{m_h^*}\right)^{-1}$, bulk exciton binding energy

Later on Kayanuma identified two limiting cases depending upon the ratio of the radius of the quantum dot to the Bohr exciton radius, a_B of the bulk solid [32]. For $R/a_B \gg 1$, the exciton can be pictured as a particle moving inside the quantum dot with only little increment in confinement energy. This is the weak confinement regime. In the strong confinement regime $R/a_B \ll 1$ and independent particle confinement effects comes to the forefront. It was pointed out that in this regime, the electron and the hole should be viewed as individual particles in their respective single particle ground states with negligible spatial correlation between them owing to the increased kinetic energy term. Kayanuma[31] further found that the strong confinements are observable upto $R \cong 2a_B$. In this regime $R \sim 2a_B$, EMA is valid to a great extent in the where the effective mass approximation is relatively more valid, though quantitatively EMA fails to account for the observed changes.

The equation (1.19) gives a good fit of the experimentally observed relation between E and R for the case of weak confinement regime. But, it is unable to observed phenomena explain the strong confinement regime where the EMA with infinite barriers breaks down. Thus, for larger sizes of the nanocrystallites, the infinite potential effective mass approximation (IP-EMA) gives a good description of the band gap variation with size. However, it grossly overestimates the change, ΔE_g, in the bandgap for smaller nanocrystals. In the infinite potential EMA (IP-EMA) model, it was essentially neglects any possibility extending of the wavefunction beyond the surface

of the nanocrystals as a consequence of the assumption of a rigid wall (infinite potential). This model ignores the tunneling possibility of the electrons and the holes of the surface atom to outside the nanocrystal.

To overcome the shortcomings of the IP-EMA, Kayanuma and Momiji [33] used the finite potential to account for the experimental data for small CdS crystallites. The confining potentials V_e, for the electron and V_h, for the hole, satisfy the relation E_g + V_e + V_h = E_{1g}, where E_{1g} is the band gap energy of the surrounding material. The resulting problem was solved by variational principle in the Hylleraas coordinate system.In addition to spherical clusters, Kayanuma and Momiji also treated cylindrical shaped microcrystallites in EMA model . Lo and Sollie (1991), Tran Thoai etal (1990) and Hu et al (1990) used variational calculation in finite potential well to improve further the EMA model.

Although the finite potential effective mass of the electron describes quite well using a single conduction band, the top level of the valence band in these semiconductor systems is degenerate and the description of the hole effective mass requires more number of bands. In this context, the multi-band effective mass approximation (MBEM) theory [34] represents a substantial improvement over the single band, infinite potential EMA model. For CdSe nanocrystals, the size dependence up to 10 excited statesin the absorption spectra are successfully described by the uncoupled multi-band EMA [34,35] . This includes the valence band degeneracy, but does not couple the valence and conduction bands. Banin et al [36] have used the multi-band EMA including the valence and the conduction band coupling. They use an eight band Luttinger-Kohn Hamiltonian to calculate the quantum size levels in InAs. Such improvements over the over simplified IP-EMA model was found to satisfactory.

The other approach which is widely used to explain the band structure of nanostructures is *Linear combination of atomic orbital theory- molecular orbital theory (LCAO).* This is based on a bottom up approach where the combination of atomic orbital and molecular orbital (LCAO-MO) is considered. In this method, nanoparticles are considered as large molecules and the overall wave function in a nanoparticle can be constructed form the wave function of individual atomic orbital. It

provides a more detailed basis for predicating the evolution of the electronic structure of clusters, from atoms and/or molecules to nanoparticles to bulk materials.
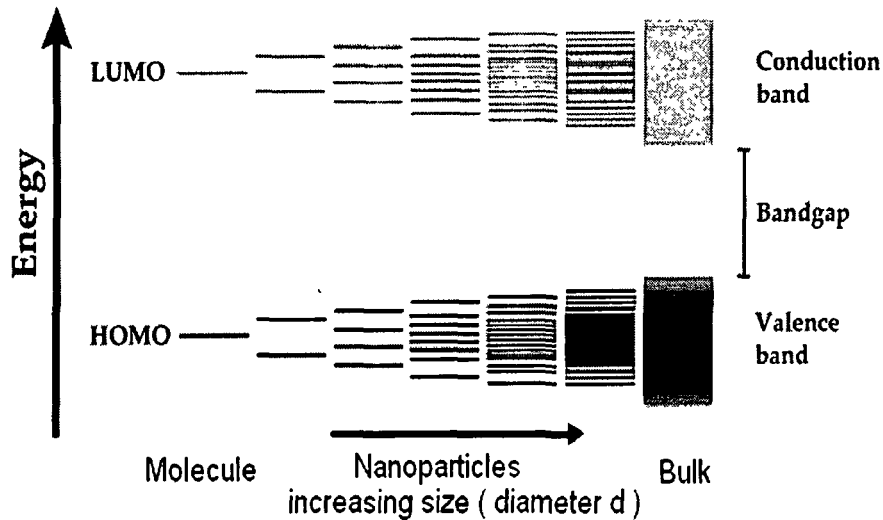
Figure 1.4 : Evolution of the energy level-distribution according to LCAO- MO : *when going from a two-atom molecule (left) to a bulk semiconductor, with a small cluster and a quantum dot as intermediate cases. The more atoms (atomic orbitals) a system has, the more energy levels arise with a decreasing energy difference between the levels, and between the HOMO and LUMO level (i.e a decreasing bandgap). The figure illustrates that a quantum dot can be viewed as a very large molecule, but also as a small semiconductor crystal*

The simplest case is that of a molecule consisting of only two atoms, where two atomic orbitals combine to make a bonding and an anti-bonding molecular orbital (MO). When only the low-energy (bonding) MO is filled with electrons, it is called the Highest Occupied Molecular Orbital (HOMO). In that case, the high-energy (anti-bonding) level is empty and referred to as the Lowest Unoccupied Molecular Orbital (LUMO). As the number of atoms increase, the discrete energy band structure changes form large energy steps to small energy steps that are to a continuous energy band. The energy difference between the top of the HOMO and bottom of the LUMO (equals to the band gap E_g) gets decreased, and the bands split into discrete energy

levels of reduced mixing of atomic orbitals for a small number of atoms. Therefore, the small size of the nanoparticles results in quantized electronic band structures intermediate between the atomic/molecular and bulk crystalline molecular orbitals. When the molecule becomes larger, more energy levels arise, and the energy spacing between the HOMO and LUMO becomes smaller.

In this model, a nanoparticle (quantum dot) can be regarded as a very large molecule or cluster consisting of a few hundred or thousand atomic valence orbitals, forming as many MOs. Still, there exist discrete energy levels at the edges of the "bands", and the spacing between the HOMO and LUMO levels (i.e. the bandgap) becomes smaller when the it increases in size. This explains both quantum confinement effects from a molecular point-of-view. Finally, when the semiconductor becomes even larger, the energy-spacing between the MO levels becomes so small that the different energy levels cannot be distinguished experimentally and it is considered as a band of continuous energy levels in a bulk semiconductor.

This LCAO-MO approach provides the tight-binding model (Slater and Koster [37]) which is an efficient scheme to calculate the electronic structure of periodic solids. As this method is computationally much less demanding compared to other methods such as the plane-wave methods, it has been extensively employed to calculate electronic structures of various metals, semiconductors, clusters and a number of complex systems such as alloys and doped systems.

The tight-binding electronic parameters, namely the orbital energies and the hopping strengths, were determined by fitting the ab initio band dispersions to the band dispersion obtained form the tight-binding Hamiltonian, given by

$$H = \sum_{il_1\sigma} \varepsilon l_1 a_{il_1\sigma}^+ a_{il_1\sigma} + \sum_{ij} \sum_{l_1,l_2,\sigma} \left(t_{ij}^{l_1l_2} a_{il_1\sigma}^+ a_{il_1\sigma} + h.c \right) \qquad (1.20)$$

where, the electron with spin σ is able to hop from orbital labeled l_1 with onsite energies equal to εl_1 in the ith unit cell to those labeled l_2 in the jth unit cell with a hopping strength $t_{ij}^{l_1l_2}$, with the summations l_1 and l_2 running over all the orbitals considered on the atoms in a unit cell, and i and j over all the unit cells in the solid. To calculate the eigen value spectra of nanocrystals, we need to know the ε's for the various orbitals and the t's for the interactions. These are evaluated by performing a

TB-fit with a prudent choice of the basis orbitals and the interactions, to the band structure of the bulk solid obtained from first principle calculations such as pseudo-potential methods.

Lippens and Lannoo [38] was the first to use 'Tight Binding Method' to calculate the variation band gap with size for Cds and ZnS nanocrystals. They use sp^3s^* orbital basis with only the nearest neighbor interactions as suggested by the work of Vogl et al.[39] for bulk semiconductor materials. The calculations were carried out for clusters ranging in size from 17 atoms (3 shells) to 2563 atoms (15 shells). They took the valence band to be parabolic but non-parabolicity is considered for the conduction band. Wang and Herron (1996) successfully calculate the energy levels of the CdS clusters (~20Å) using tight binding model considering non-parabolic valence and conduction band. Sarma et al studied in details of band gap enhancement of the semiconductor quantum dot based on TB model and gives the expression for band gap enhancement as [40-42].

$$\Delta E_g = \frac{1}{aD^2 + bD + c}$$ (1.21)

Where, D is the diameter of quantum dot. The a, b and c parameters are dependent on the system [Appendix 2].
They have developed a method for estimating the diameters and diameter-distribution from the UV spectra [42].

Einevol (1989) used both EMA and TB model and gives a new model known as Effective bond order model (EBOM). In the method he used effective mass model (k.p) for the conduction band and tight-binding methods for the valence bands to determine the energy states in low dimensional structures. Later, Ramakrishna and Friesner [43] used the Empirical pseudo-potential method to calculate the band structure of CdS and GaP nanocrystals upto 30Å radius in the zinc-blende phase. The calculated variation agrees quite well with the experimental data points. Lin-Wang Wang, Alex Zunger and coworkers [44-49] also employed the semi-empirical pseudopotential method in semiconductor nanostructures. They calculate the electronic structure of Si [44], CdSe [46] and InP [47] quantum dots.

Quantitative theoretical approaches have been employed during the two decades to improve the model to determine the exact electronic structures of semiconductor nanoparticles, by using different perturbations and boundary condition in the Hamiltonian. Sercel and Vahala (1990) have introduced non-parabolic bands in the k.p perturbation theory and calculated quantum-dot band structure of GaAs(AlGaAs) and InAs(GaSb) systems.
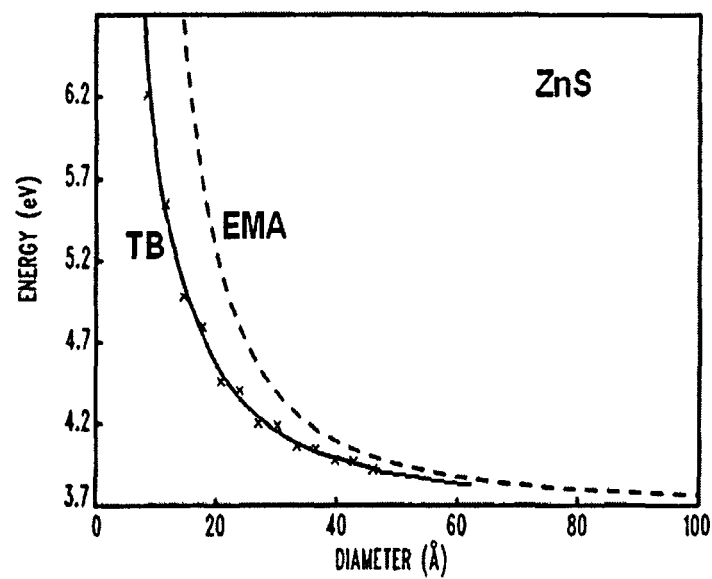
Figure 1.5 : Variation of band gap (E_g) vs. diameter using TB model and EMA

Each of the above models has its own advantage and limitation. In fact, the EMA and EBOM overestimate confinement energies, but the TB model to gives an underestimated picture. It is also recognize that the methods breaks down for the smallest nanoparticles (<1nm), because of possible surface and interface along with structural changes.

1.2.2 Oscillator strength

It is defined as the strong radiative transition that occurs between two energy levels. The enhancement of oscillator strength in nanoparticles (QD) results due to quantum confinement effects. Wang and Herron [3] also treated the dependence of

oscillator strengths on crystallite size on the basis of quantum confinement of carriers and spatial overlap of electron and hole wavefunction. Both exciton binding energies and oscillator strengths can increase in nanoparticles. The expression given for the oscillator strength of exciton is

$$f = f_{exciton} = \frac{2m_e{}^*}{\hbar^2} \Delta E |M|^2 |U|^2 \qquad (1.22)$$

Where, ΔE – transition energy , *M* – Transition
dipole moment $|U|^2$ – the probability of finding electron and
hole one the same site (overlap integral)

In the weak confinement regime $(R\!>\!>\!a_B)$, there is only a small overlap between electron and hole wave functions. In this case $|U|^2$ is independent of size and the macroscopic transition dipole moment determines the oscillator strength f. Therefore, in this regime f_{nano} increases linearly with increasing nanoparticle volume (V). This is nothing but the effect of "giant" oscillator strength for bound excitons which has been discussed by Kayanuma [32], Hanamura [50,51], Takagahara[52,53] and many others. Again, in the strong confinement regime, $(R\!<\!a_B)$ due to high probability of finding an electron and a hole (e.g. at a particular unit cell), there is an increased overlap of electron and hole wavefunctions. So, $|U|^2$ increases with decreasing cluster volume. As a result, f_{nano} is now only weakly dependent on cluster size [29]. However, the oscillator strength f_{nano}/V now increased with decreasing cluster size and scales roughly as $(a/R_b)^3$. The exciton absorption band should therefore become stronger as R increases, and so excitonic type features in the absorption spectra become visible even at room temperature (Bryant88). So, the Exciton oscillator strength (f_{ex}) increases with decreasing size and it determines the absorbance and emission properties of the nanoparticle whereas total oscillator strength f_{nano} weakly depends on size. The oscillator strength per unit volume $f_{nano}/V \sim (a_b/R)^3$ and it determines the magnitude of the absorption coefficient. For nanoparticle dispersed in matrix, the appropriate coefficient is determined by dividing the absorption coefficient of the sample with the volume fraction of the cluster.

1.3 Different Types of Nanostructure Materials:

Depending upon the nature of quantum confinement, different kinds of low dimensional structures have been observed. When the confinement is precisely along one direction, the structure is 2 dimensional structures known as quantum well. If confinement is along two directions it is a 1D nanostructure, quantum wire. Again, if confinement occurs in all the three directions, one obtains a quasi zero dimensional quantum dots. For quantum dot or a semiconductor nanoparticle is of the size of bulk Bohr-exciton radius, where carriers are supposed to be confined along the three directions. All of them are categorized as NSM and show drastically different physical properties depending on material type, size, shape, degree of crystallinity, orientation etc. and make them useful as potential candidates for a wide variety of applications.

(A)

Bulk material

No confinement

$L_{X,Y,Z} > L_0$

No nanostructures
(3D)

(B)

Quantum Wells /Thin film

One-dimensional
confinement

$L_{X,Y} > L_0 > L_Z$

**Two-dimensional
nanostructures
(2D)**

(C)

nanowire/nanorod

Two-dimensional
confinement

$L_X > L_0 > L_{Y,Z}$

One-dimensional
nanostructures
(1D)

(D)

Quantum Dots/ nanoparticles

Three-dimensional
confinement

$L_0 > L_{X,Y,Z}$

Zero-dimensional
nanostructures
(0D)
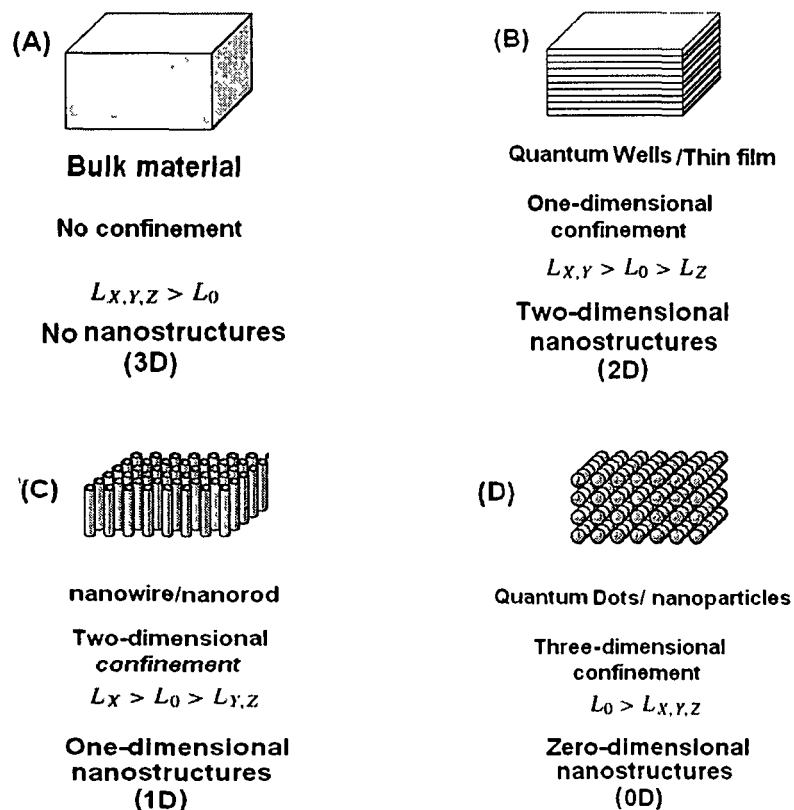
Figure 1.6 : Bulk vs. low dimensional structures and their confinements   (A) 3D Bulk (B) 2D nanostructures (C) 1D nanostructures (D) Quasi 0D nanostructures

1.3.1 Symmetric and asymmetric nanostructures

Among the NSMs the most common type is spherically symmetric nanostructures also known as nanosphere or nanoparticle Nanospheres can be developed in the form of assemblies of a few nm dimensions only These are quasi zero dimensional nanostructure where the movement of the carriers are confined in all three direction
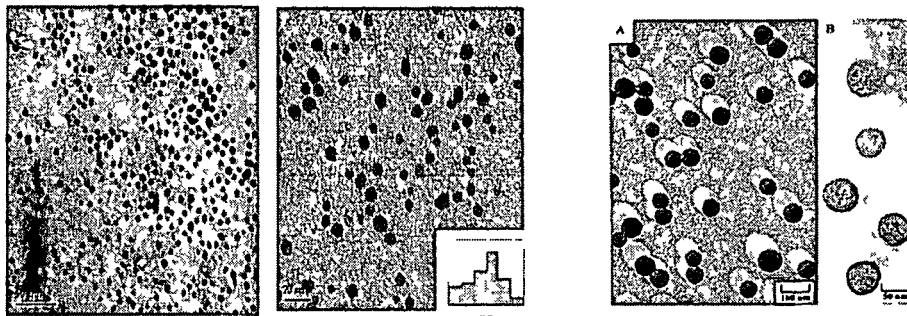
Figure 1.7 : Spherically symmetric Au nanoparticles   **Figure 1.8 :** CdS nanoparticles

The other type of nanostructures is one dimensional nanostructures (e g nanorod, nanotube, nanobelt, nanofiber etc) Such asymmetric kinds of nanostructures are generated in the form of periodic, higher archival assembly In these one dimensional nanostructures the movement of the carriers is restricted in two directions
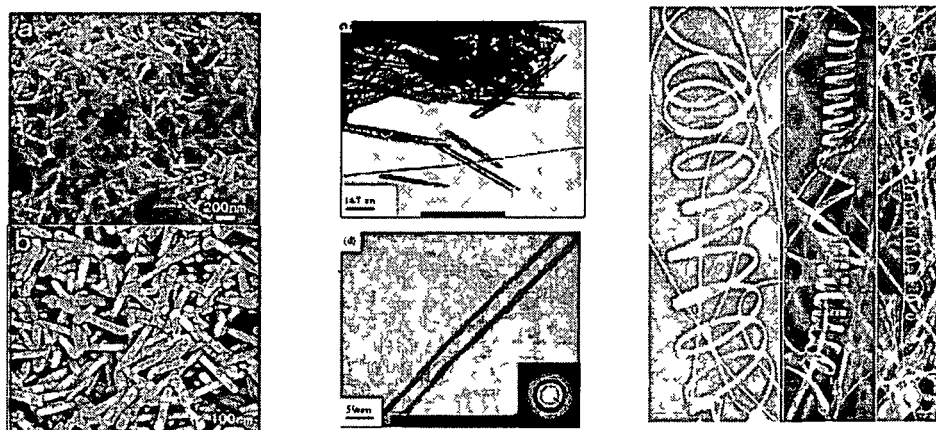
Figure 1.9 : ZnS nanorods   **Figure 1.10 :** ZnS nanotubes   **Figure 1.11 :** ZnO nanobelts

Over the years, various workers have developed different kinds of decorative nanostructures by adopting both chemical and physical approach. Mark Well and and coworkers have grown different kinds of asymmetric silicon carbide nanostructures. They have used vapour-liquid-solid process to produced nanoflowers, nanotrees and
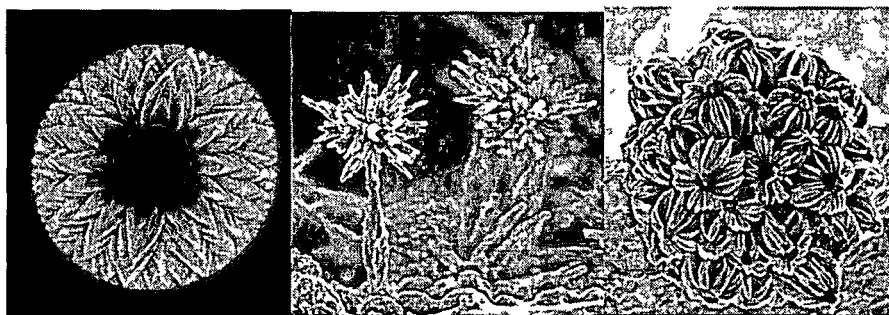
Figure 1.12: Nanoflower, nanotrees and nanobouquents of SiC

nanobouquets of the given material (Figure 1.12). They have also explored the use of these materials as water-repellent coatings and as a base for of solar cell [59]. Researchers form Institute of Microelectronics and Nanyang Technological University, Singapore have to show that the flower shaped photo-anode (Figure 1.13a) can improve the energy conversion efficiency of dye-sensitized solar cells (DSSCs) by 90% compared to conventional anodes made of rod-shaped structures [60]. Prashant Kr Singh group form IIT, Roorkee able to develop ZnO nanoflower [Figure 1.13b] by ultrasonication method [62]. Wurtzite ZnO nanobridges and aligned nanonails have been synthesized by thermal vapor transport and condensation method [63] by J. Y.

Figure 1.13: ZnO nanoflower through (a) ultrasonication (b) hydrothermal method
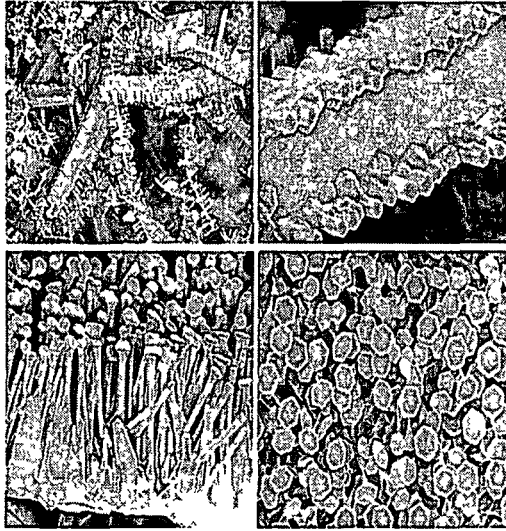
Figure 1.14 : ZnO nanobridges and aligned nanonails
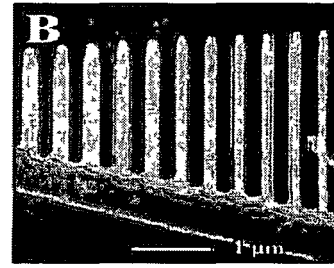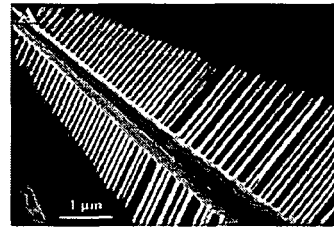
Figure 1.15 : ZnO nanocomb

Lao et al (Figure 1.15). H. Yan etal (2003) produced ZnO nanocomb and show its applicability as ultraviolet laser array [64].

Zhong Wang research group [58] has successfully developed single-crystal seamless nanorings made of piezoelectric zinc oxide [Figure 1.17]. They have made the nanorings by a solid-vapour technique. Silica nanosprings (figure 1.18) were synthesized by D. Zhang and coworkers using a simple, low temperature, chemical vapor deposition method via a vapor–liquid–solid mechanism [65]. These nanosprings (Figure 1.18) show excellent uniformity and heliciy in high and repeatable yields.
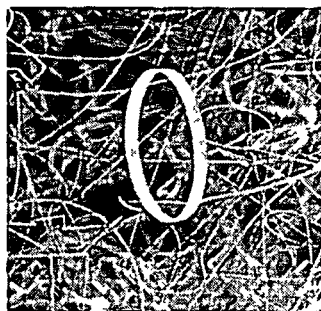
Figure 1.16 : ZnO nanorings
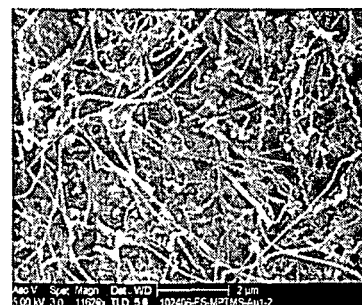
Figure 1.17 : Slica nanosprings
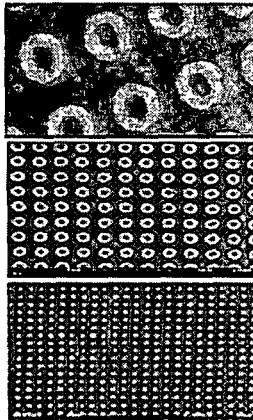
Figure 1.18 : Ag nanorings   Figure 1.19 : Au nanorings   Figure 1.20 : Co nanorings
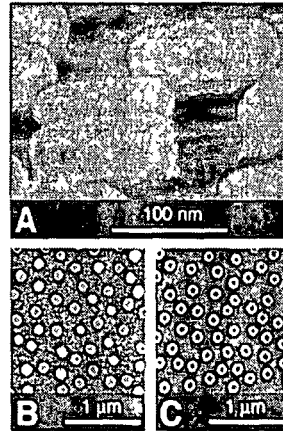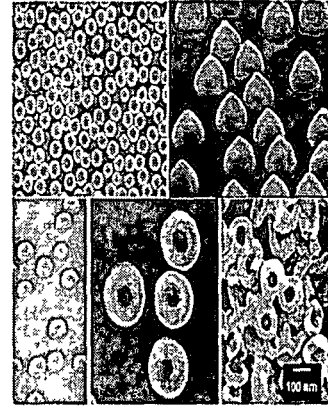
F. Q. Julie Stern of Center for Nanoscale Systems, Harvard University have successfully develop silver nanorings (Figure 1 19) [66]. Again, gold nanorings and nanodisks prepared by colloidal lithography by J. Aizpurua et al [67]. They found that ring like gold nanoparticles exhibit tunable plasmon resonance behavior. Zhu et al have to developed magnetic nanorings (Figure 1.21) using Electron beam lithography (EBL) and showed its applicability in memory devices. [68].

1.3.2 Elongated Nanostructures

The quasi zero dimensional nanostructures are generally spherical in shape and symmetric in nature. Although they have potential for wide range of applications, recent interest on asymmetric nanostructures has revealed that, as compared to spherical nanostructures, the elongated nanostructures (such as nanowires, nanorods or nanostrips) have several additional advantages. An intensifying research on the elongated structures has been put forward in the recent past. In particular, their novel electrical and mechanical properties are the topics of current interest. Further , the 1D nanostructure can be categorized as per definite morphology. These include whiskers, nanowires, nanorods, fibers, nanotubes, nanocables, nanotubules etc. Whiskers and
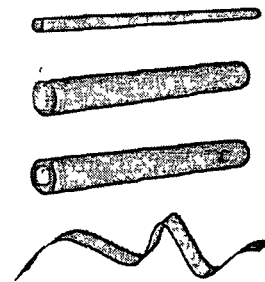
Figure 1.21 : Schematic of elongated nanowire, nanorod, nanotube, and nanobelt

23

nanorods are essentially shorter versions of fibers and nanowires. The One-dimensional structures with diameters ranging from several nm to several hundred nm have been referred to as whiskers and fibers in early literature, whereas nanowires and nanorods are more recent and refer to 1D nanostructures whose width does not exceed 100 nm.

Nanotubes

A regular hollow cylinder of several nm dia can be termed as nanotubes. The side surfaces of the nanotube in this sense may be well-faceted. Many materials have been used to produce such structures. Research on one-dimensional hollow nanostructures took-off with the publication in 1991 of Iijima's seminal paper outlining the discovery of carbon nanotubes(CNT), "Helical Microtubules of Graphitic Carbon." [69] More recently, carbon nanotubes have been reported of being grown up to lengths of several centimeters [70] with the internal dia a few nanometer only. The cross-sections of carbon nanotubes are only a few nanometers thick.

CNT are made up of a hexagonal network of carbon atoms forming a crystalline graphite sheet. This sheet is 'rolled up' to form a tubular structure. If the tube consists of only a single carbon sheet that meets end on end, then the CNT is referred to as a single wall nanotube (SWNT). However, if the nanotube consist is of multiple sheets rolled up coaxially or, if the nanotube is rolled up somewhat spirally, then the CNT is referred to as a multi-wall nanotube (MWNT).

The other important characteristic of the nanotube is the chirality, or the rolled direction of the nanotube. The chirality has a large impact on the physical properties. [71] There are three distinct types of nanotubes based on their chirality: *chiral*, *armchair*, and *zig-zag*. The difference between the three is understandable in the idea of a chiral vector and angle. The chiral vector and angle is illustrated in Figure (1.23) on a two-dimensional hexagonal lattice. The chiral vector is determined as $C_h = n a_1 + m a_2$, where a_1 and a_2 are unit vectors and n and m are integers. The chiral angle, θ, is measured relative to a_1. If $0^0 < \theta < 30^0$

it is known as chiral carbon nanotube. When $\theta=30°$ and n=m it is called 'armchair carbon nanotube' . Again if $\theta=0°$ and either 'm' or 'n' is equal to zero the tube will be "Zig-zag carbon nanotube".
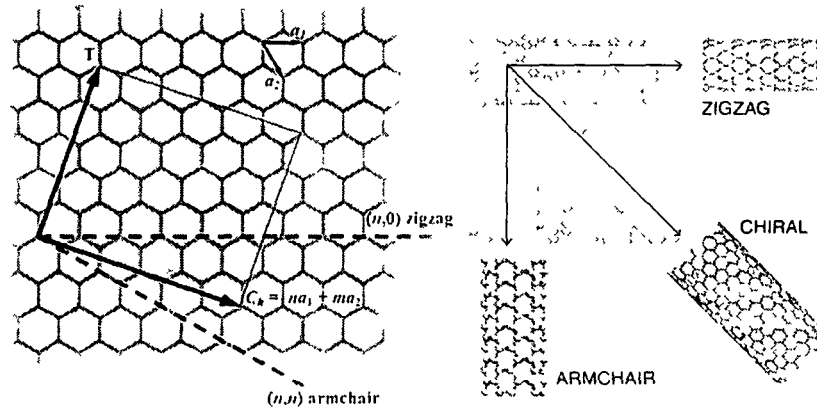
Figure 1.22: Typical Carbon nanotube (CNT) : Zigzag, Chiral and Armchair CNT

Figure (1.23) depicts a three-dimensional view of different kinds of CNT. Armchair nanotubes, have an electronic conduction that closely resemble with metal. Theoretically it is found that these armchair nanotubes can have an electrical current density more than 1000 times stronger than bulk metals like silver and copper . Alternatively, zig-zag CNTs tend to have the same electronic properties as a semiconductor, where electrons must overcome a bandgap in order to enter the conduction band [72,73].

One interesting phenomenon associated with the metallic-conducting nanotubes is ballistic conduction. Ballistic conduction allows electrons to flow through the nanotube without collisions [74]. Therefore, it shows quantized electronic transport without energy dissipation. The lack of energy dissipation means that it generates no heat when conducting electrons. The electronic components that have quantized and generate no heat has vast demand as far as packaging and assembling are concerned. CNT also have novel physical properties . Nanotubes have been shown to have a Young's modulus and tensile strength values in far excess than those for diamonds. In fact, in terms

of tensile strength and elastic modulus, CNTs are one of the strongest materials ever known to mankind.

Researcher has also developed nanotubes of materials which also show some interesting properties then the other form. Chung-Liang Cheng etal (2007) have developed Zn and Sn nanotube array through electrochemical deposition in nanoporous anodic alumina membranes.[75]. Yuji Shinkai and co-workers of Osaka University have reported on the development of TiO_2 nanotube layers were fabricated by electrochemical anodization of Ti foils. They found that the fabricated nanotubes can display high photovoltaic efficiency. Silver and gold nanotubes were also efficiciently developed by others workers [76]. Nanotubes of wide band gap semiconductors can also be fabricated by different methods [77,78].

Nanowires and Nanorods

In recent years the research interest has been shifted from 1D nanostructure nanotubes to other on. The progression shifted from the one-dimensional nanostructure nanotubes to other one-dimensional nanostructures, nanowires and nanorods. The term "nanowire" is widely used to represent long 1D one-dimensional nanostructures that have a specific axial direction with their side surfaces are less well-defined.[79,80]. Typically, nanowires have a radius that is negligible in comparison to their length. There are two distinct types of nanowires. There are ultrafine wires or linear arrays of dots, formed by self-assembly. Related to nanowires are "nanorods." A nanorod is typically much shorter in length than a nanowires. Nanorods show more side facets than nanowires tend to. What differ nanowire and nanorod from nanotubes is the internal geometry of their cross-section. Nanotubes are hollow and have a cross-section resembling the perimeter of a circle. Nanowires and nanorods have solid cores. Their cross-section resembles a filled-in circle or hexagon. In general, nanorods are a short nanowires, and are therefore considered as a subgroup of this nanostructure kind.

Nanowires have been synthesized out of a wide variety of materials, including titanium oxide [81] , indium oxide [82], indium-tin oxide [83],

aluminum [84], and tungsten oxide [85]. Over several decades, Silicon is being considered as a work horse for many technological applications. Owing to its future prospects, research in nanowires was dominated by silicon nanowires. The main synthesis technique that has been used is physical vapor deposition (PVD). PVD is a process of transferring growth species from a source to specified substrates under desirable environment. Several methods have been adopted in order to vaporize in a precise manner. In the case of silicon nanowires, the source material used is generally high purity silicon or silicon dioxide [86,87].

The electronic structure is one of the major benefits of silicon nanowires over CNT. Whereas nanotubes are either metallic or semiconducting depending on the chirality, silicon nanowires are always semiconducting [88]. This characteristic makes silicon nanowires immediately useful, bypassing the hurdle that carbon nanotubes faced over the years to separate out various phases.

Other nanowires materials have been produced via a wide array of synthesis routes. Single crystal nanowires of group II-VI and III-V semiconducting materials have been synthesized, without a passivating layer. Apart from semiconductors, nanowires made from metallic systems have been reported. Beyond PVD and CVD, synthesis methods such as laser ablation and solution-based synthesis, both of which allow complex chemistries beyond binary compounds, have been used to form several types of nanowires.

Nanobelts

One of the most interesting and distinguishing features of nanowires is their very large length with respect to their width, making the sides essentially non-faceted. One of the more distinguishing features of nanorods is that their sides are faceted, but their length is comparable with their width. There is a type of one-dimensional nanostructure that combines the length of nanowires with the faceted structure of nanorods. This structure is the nanobelt. Nanobelts, often referred to as nanoribbons, have two of their dimensions confined to the nanoscale, with the third dimension being relatively very long.

However, unlike nanowires, they exhibit faceted side surfaces, so that their cross section is rectangular. Pan et al. first reported transparent semiconducting oxides synthesized in a belt-like manner in 2001. The reported materials used to synthesize these "nanobelts" were ZnO, CdO, In_2O_3, Ga_2O_3, and SnO_2 [89]. These materials are all transitional metal oxides ranging over three different elemental groups (II-VI, III-VI, and IV-VI) and at least five types of crystallographic structures. Since this first report, nanobelts have also been synthesized in non-oxide semiconductors such as ZnS [90,91], CdS [92], CdSe [93,94] and ZnSe [95]. Nanobelts have several unique properties that make them amenable to study and for use in technology. In general nanobelts can be synthesized as single crystals that are relatively long (about one-two mm). They have a rectangular cross-section that is generally uniform through the length of the belt [96]. The width of the nanobelts can range from as much as one hundred nanometers to as little as six nanometers. They typically have a thickness to width ratio of about one-to-ten. The aspect ratio has also been measured and ranges from about five-to-one to ten-to-one (width to thickness ratio). Though stacking faults may be present, the nanobelts are also essentially dislocation and defect-free. So even if a stacking fault is present, it typically does not terminate within the nanobelt structure and provide a location for scattering processes to occur. Because of the extremely high surface area to volume ratio, the presence of a dislocation is not energetically feasible. Nanobelts also have well-defined crystallographic planes. This means that not only is the fastest growth direction well-defined, but also the top and bottom (along the width) planes and the side (along the thickness) planes are well-defined crystallographic planes and are synthesized along well-defined directions. This allows for tuning of properties and of catalytic surfaces and can have a profound effect on the structure and properties of the synthesized material. It is important to note some of the ways in which nanomaterials differ from their bulk counterparts. One example in nanobelts has to do with their extreme flexibility. Many nanobelts are made of ceramic materials, notorious for their rigidity. However, at the nanoscale nanobelts are very

flexible, enduring great strain without breaking. This strain is also fairly reversible; because of the lack of presence of dislocations the nanobelts should be extremely resistant to fatigue and failure.

In some properties, nanobelts are not all too different from some of their more heavily researched cousins in one-dimensional nanomaterials, nanowires and nanotubes. All three can be synthesized to varying lengths. All three have been shown at varying thicknesses (or diameters). Nanowires and nanobelts can controllably be synthesized along a single crystallographic growth direction. Reliably, nanowires and nanobelts can be synthesized with a precise electronic band structure. However, the differences between the nanostructures are significant. Notably, nanowires often contain defects and dislocations. Mechanically, the presence of these contributes to the fatigue of the material as a whole. Electronically, the presence of defects and dislocations in a material can decrease electron transport due to the increase in possible scattering sites. This decreases both the speed of response and the sensitivity of devices made with the nanowires. This also decreases their usefulness in lasing applications. Nanobelts have shown to have significant use in such applications, even exhibiting a degree of tunability over certain wavelength.

Quantum Confinement in elongated nanostructures :

Studies aimed at understanding the evolution of electronic structure from three-dimensionally confined quantum dots to one-dimensionally confined quantum wells have recently received a fillip following the synthesis of nanocrystals in different shapes. The ability to easily synthesize quantum wires with genuine confinement in two dimensions is particularly significant. It is clear that 2D confined nanorods have properties different from 3D confined spherical nanocrystals as they have different kind of electronic structures.

For the electronic structure of spherical semiconductor nanoparticle (quantum dot) , the EMA in a spherical potential is considered. For nanorod, EMA is applied in a

cylindrical potential. In case of cylindrical potential the energy relative to bulk band gap as a function of nanowire diameter and lengths is [97]

$$\Delta E = \frac{\hbar^2}{2\mu}\left(\left(\frac{\alpha_{01}}{R}\right)^2 + \left(\frac{\pi}{L}\right)^2\right) - \left\langle \Psi(x_e)\Psi(x_h)\left|\frac{e^2}{\varepsilon|x_e - x_h|}\right|\Psi(x_e)\Psi(x_h)\right\rangle \qquad (1.22)$$

where, μ is the reduced effective exciton mass ; ε is the dielectric constant.

Here the fist term is due to quantum confinement effect and second is due to coulomb interaction between the carriers.

Lieber et al used this model to compare the optical properties of Indium Phosphide nanowires of different diameters (10, 15, 20 and 50 nm) . The model provides excellent fits to experimental data [98]. KK Nanda et al used finite-depth square-well model and give some idea about the band gap of nanoparticles and nanorods [99]. All these results and some previous works on heterostructures [100,101] yield the following relationship for the variation of the band gap when the degree of quantum confinement changes from 1D to 3D.

$$\Delta E_g = \frac{\xi\, h^2}{8D^2}\left(\frac{1}{m_h^*} + \frac{1}{m_e^*}\right) \qquad (1.23)$$

Where, D is the diameter, m_e^* and m_h^* the electron and hole effective masses. The value of ξ =1.0 for one dimensionally confined wells, 1.17 for two-dimensionally confined rods and 2.0 for three-dimensionally confined dots. In other words, the band gap increases with decreasing diameter is much more gradual as the degree of confinement increases from one to three dimensions. Despite the degree of approximation used in arriving at the relationship above, high level theoretical calculations using ab initio or less sophisticated methods yield similar results [102,103]. Recently, Lin-Wang Wang et al compare the result this expression with their results obtained for local density approximation and find identical results [104]. Read et al used first principle approximation for electronic structure of one dimensional system and modified the result from EMA for nanorod eq(1.23) by defining

$$\text{D} = d = \frac{a_0 (2M)^{\frac{1}{2}}}{4} \qquad\qquad (1.24)$$

Where, M is the number of atoms per unit cell
and a_0 is the lattice constant.

Kuskovsky give a better explanation on the band structure of nanorod in the strong quantum confinement regime. He also applied the EMA in the infinite cylindrical well as by previous workers but the consider the exciton binding energy enhanced due to one-dimensional confinement has strong significant in the band structure of the nanorods . According to his report the the energy shift [105] -

$$\Delta E = \frac{\hbar^2}{2r^2}\left(\frac{1}{m_e^*} + \frac{1}{m_h^*}\right) x_{ns}^2 - E_B^{1D}(r) \qquad\qquad (1.25)$$

Where, x_{ns} is the sth zero of the Bessel function,
$E_B^{1D}(r)$ is the binding energy of the 1D exciton, which
depends on the geometry of the nanorods.

Now days, TB model and k.p are popular among the researcher to determine the electronic structure of nanorods. Lassen et al applied k.p approximation on InP nanorods while Yorikawa et al done TB calculation for Si nanorods.

1.4 II-VI Semiconductor Nanostructures

The modified physical properties of the nanoscale semiconductor materials have enormous potential for next generation devices. Till now, A large class of semiconductor nanostructures have been produced that includes elemental (Si andGe), materials has been prepared in nanocrystals form, including covalent Si and Ge, I-VII compounds (CuCl, CuBr, AgBr) II-VI compounds (CdSe, CdS, ZnSe, CdTe, PbS and their alloys), III-V semiconductor compounds (GaAs, GaP, InP), and IV-VI compounds etc.

In the nanoscale, II-VI semiconductor show many interesting properties compare to its bulk counter part. The II-VI semiconductors are generally wide and direct band gap materials. Each of them II-VI semiconductors demonstrate some

unique properties, making them useful for desired applications. It was found that Bulk CdS absorbs in the yellow-green region of the visible spectrum and so used as a window material in solar cells. Its band gap can be tuned upto UV region, up to UV region by reducing its size down to 40Å [106]. Similarly ZnS which absorbs light is important from the point of view of electroluminescent display devices. in the UV region can be used as a efficient host to incorporate various ions and hence important for electroluminescent display devices. The band gap of ZnS in the nanometer regime allows us to achieve large quantum efficiency of emission response. Also it can be used as a higher band gap material for passivating other semiconductor quantum dots, thereby increasing their quantum yields to as large as 80%. Materials such as PbSe have a band gap that lies in the infrared region and is used in telecommunication devices. Thus PbSe nanocrystals that emit in the IR region and are useful for telecommunications and IR detectors, with tunable wavelength, thereby increasing the amount the data transfer. Cadmium Selenide (CdSe) has a bulk band gap 1.74eV which lies in the visible spectrum close to IR region. Thus, a decrease in size of CdSe nanocrystals would push the band gap towards the visible region and one can cover the entire range of the visible spectrum by changing the size of the nanocrystals [107]. The quantum efficiencies of these CdSe nanocrystals are very large compared to the bulk material.

The impurity doping (transition metal and rare earth metal) of II-VI semiconductor material made them more applicable in practical world. These impurities influence the nanostructures by introducing impurity centers that can interact with the quantum confines electron-hole pairs. Due to interaction of impurity centers with the quantum-confined electron-hole pair, they do not effect the absorption spectrum but strongly modify the luminescence properties such as high luminescence quantum efficiency, short radiative lifetime , size independent emission color tunability , low-voltage cathodoluminescence , multicolor electroluminescence , etc. These materials are also considered to be the luminophors as far as future technology is concerned. Again, for TM doped semiconductor as the impurities may be paramagnetic, they would can introduce a localized spin into the host nanocrystal and results a new class of diluted magnetic nanostructure (DMS) which is

semiconducting as well as semi magnetic. Such diluted magnetic nanostructures allow us to study of spin–carrier or spin–spin interactions in the strongly quantum-confined regime and open up opportunity to be used as vital components in the new area of Spintronics. A great deal of attention has been paid to doping bulk semiconductors with magnetic ions such as Mn^{2+} that impart unusual Zeeman effect, Faraday rotation, magnetic polaron effects etc. Magnetic doped semiconductor form a unique class of materials, known diluted magnetic semiconductors (DMSs) which have potential in Spintronics applications. Advances in vacuum-technology have allowed preparation of many new nanoscale DMSs that have exhibit novel magnetic, magneto-optical, and magneto- electronic properties. DMS thin films have recently been prepared by vacuum-deposition methods that show large magneto optical effects and the promise of high T_c ferromagnetism. It has been a debate over the recent years with regard to possibility of Mn^{-2} incorporation into the host nanocrystals lattice or on to the nanocrystal surface. To date, solution synthesis of free-standing and high-quality DMS nanostructure has been limited to II-VI chalcogenides (CdS, CdSe, ZnS, and ZnSe).

Although, most of the efforts that have tried to address the doping include Mn doped semiconductor nanocrystal systems, several works were dedicated to rare earth doped and co-doped systems.

Again, in the elongated form semiconductor nanostructures (1D semiconductor nanostructures) show some specific advantages over its spherical form. CdS nanowires have functioned as Fabry-Perot optical cavities and these nanowires have been used as electrically driven lasers [108]. Also, CdSe nanorods can have up to 100% polarized luminescence and could be used as nano-emitters or high resolution detectors of polarized light [109].

Thus, the II-VI Luminescent semiconductor nanocrystals both doped and undoped form are considered to be the materials for the next generation displays, bio-labels lasers etc, due to their high luminescence quantum efficiency, spectral tunability, color purity, high optical gain with lower threshold and high chemical stability. Semiconductor nanocrystals (NC). Among the binary semiconductor nanocrystals , ZnS and ZnO have received extensive more attention in recent years.

This thesis will focus on two particular II-VI semiconductors, as they have offered the most potential for nanostructure in luminescent applications. First one is the Zinc Sulfide (ZnS) and second one is the Zinc Oxide (ZnO). We focused on the excellent photonics/optoelectronic properties of the two materials in the nanoscale.

1.4.1 Zinc Sulfide (ZnS) nanostructures

Zinc Sulfide (ZnS) is a direct wide band gap semiconductor with and energy gap 3.6eV at 300K. Typically, it is encountered in the stable cubic (zinc blende) form. The hexagonal form of ZnS is also known both as a synthetic material and as the mineral wurtzite. The phase transition from the cubic form to the wurtzite form occurs at around 1020^{0}[113].
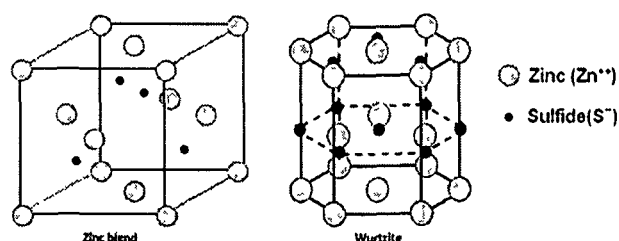
Figure 1.23: Cubic (Zinc blende) and hexagonal (Wurtzite) structure of ZnS

ZnS is considered as a good phosphor candidate since its inception. (Theodore Sidot in 1866). Both in pure and impurity activated form, ZnS is attractive for phosphor and thin-film electroluminescence device applications.

Researchers have argued that it is more useful in the nanoscale regime owing to large surface to volume that leads to enhancement in luminescence properties. Again doping with transition metal and rare earth impurities can be employed selectively to enhance and tune the luminescence properties of the ZnS nanostructures. Doped ZnS nanocrystals have attracted more attention since 1994 form the work of Bhargava et al [114] that reported Mn^{2+} doped ZnS nano semiconductor which are shown to yield both high quantum luminescence efficiency and the lifetime shortening. The results suggested that doped semiconductor nanocrystals form a new class of luminescent materials, which have a wide range of application in devices, light emitting diodes (LED) sensors and lasers [115-118]. A vast

amount of literature from different groups of the globe on the reported on the optical properties of various doped nanocrystals and demonstrated their potential application as luminescent materials. Numerous works are dedicated to various transition metal ions(Cu^{2+}, Mn^{2+}, Pb^{2+}, Ni^{2+}, Cd^{2+}, Co^{2+},) and rare-earth (Eu^{3+}, Sm^{3+}, Tb^{3+}, Er^{3+}) ion as doped systems. These semiconductors have been systematically studied, especially $ZnS:Mn^{2+}$ nanoparticles which have shown to exhibit orange yellow emissions. More recently, many researchers have also paid attention to the co-doped ZnS nanoparticles, considering $Ni^{2+}-Mn^{2+}$, $Pb^{2+}-Cu^{2+}$, $Cu^+ -Cu^{2+}$, $Co^{2+}-Cu^{2+}$, Cu–Al, $Mn^{2+}-$Eu^{3+} , $Cu^{2+}-In^{3+}$, $Cu^{2+}-RE^{3+}$ (Ce^{3+}, Er^{3+}, Tb^{3+}, Nd^{3+}, Y^{3+}),as doping element.

Investigations have already demonstrated optoelectronic properties of these nanostructures. For instance, ZnS:Mn nanocrystalline films have potential application in thin-film electroluminescence (TFEL) device. Adachi et al has prepared ZnS:Mn TFEL device [119] and their results shows the existence of reddish-orange broad band emission centered at 626 nm. Dinsmore et al. [120] prepared the ZnS:Mn copped with ZnO nanoparticle with high cathodoluminescence (CL) intensity. They achieved the maximum luminescence of ~2.8 cd/m^2 under low-driving voltage. It is well-known, that the bulk ZnS:Cu is a good cathode ray tube (CRT) phosphor generally employed for oscilloscopes. The ZnS:Cu nanosctructrues widely studied for possible application in light emitting diode (LED) [121]. Huang et al. fabricated the single layer LED using ZnS:Cu nanocrystals/polymer composite having the low turn on voltage with blue electroluminescence at room temperature [122]. Yang et al. have show high-photovoltaic efficiency of ZnS:Cu [123]. Kushida and Kurita et al.[124-125] discovered a new kind of optical data storage with doped ZnS nanostructure. Recently, Chen et al. discovered the upconversion luminescence of ZnS:Mn, ZnS:Eu, which would fine application as displays and biological probes [126]. Different co-doped systems also show profound luminescence enhancement due to doping. All of this will make significant means in both application and basic science research.

The elongated one dimensional nanostructures ZnS both doped and undoped form have also able to its applicability. For example elongated ZnS have been synthesized in the form of nanowires, nanobelts, nanocombs and most recently, Recently, ZnS nanobelts have been doped with manganese without changing their

crystallography properties [127]. Furthermore, single ZnS nanobelts have been shown to facilitate optically pumped lasing [128].

One-dimensional (1D) nanostructures also show its attractive applicability in electronics and optoelectronic devices [129,130]. In the last decade, various from of elongated ZnS nanostrctures are reported such as wires [131-134], rods [135-138], tubes [139], nanosaws [140, 141], Nanobelts [142] and nanohelices [143] through a wide range of techniques.

Theodore Sidot in 1866 developed the most stable bulk ZnS for the first time by heating zinc-oxide in a stream of hydrogen sulphide. This is one of the most common methods to produce ZnS. The same method is also successfully used in the development of ZnS nanostructures in spherical and elongated form. However, the soft chemical method is explored more for the preparation of ZnS nanostructures in the last two decade due to some specific advantages. There are many approaches of soft chemical methods including chemical precipitation method, microemulsion technique, colloidal chemical method, chemical synthesis method, organic methods, sol–gel method, and ions implantation method, etc. The reasons of adopting these soft chemical methods is ascribed that the impurity more easily substitute the host metal ions position in the lattice of nanocrystal in solution, however, different opinions about whether the impurity ions on the position of the host metal ions in the lattice were presented [144].

Among all of the soft chemical approaches, chemical precipitation method is the most popular technique that is used because of its cheap raw materials, easy handling and large-scale production [145]. Many impurity doped ZnS nanoparticles were also prepared by this method by many people. The processing parameters of raw materials, reaction temperature, solution pH, titration rate, ever stirring rate have effects on properties of final precipitates, such as particle size, particle size distribution, particle shape even stoichiometry. Starting materials can be either oxides or salts; precipitation temperature can be in the range of 0–80^0 C; pH from 2 to 10.3; titration rate about 0.5–0.8 ml/s; fast stirring is good for distribution of particles. Where as Bol and Meijerink. adopt metallic acetate salts and Na_2S in aqueous solution (pH = 10.3) with continuous agitation at room temperature. The conditions of Yang

prepared co-doped ZnS nanoparticles different from Meijerink et al. is that the precipitating anion use TAA and pH equal 2 at 80^0C. The microemulsion technique includes W/O microemulsion (reversed micelles) and O/W microemulsion.

The other preparation technique for ZnS nanoparticles used usually is reversed micelles, which are thermodynamically stable mixtures of four components: surfactant, co-surfactant, organic solvent and water. AOT, SDS (sodium dodecyl sulfate), CTAB (cetyltrimethyl ammonium bromide) are the usual surfactants. Precipitation is one procedure to form nanoparticles by reversed micelles. In this method two reversed micelles containing the anionic and cationic surfactants are mixed. Because every reaction takes place in a nanometer-sized water pool, water-insoluble nanoparticles are formed. It is usually applied in the synthesizing of metal sulfides for example, $ZnS:Cu^{2+}$, $ZnS:Mn^{2+}$, $ZnS:Eu^{3+}$ prepared by Xu et al. [146] and core-shell $ZnS:Mn^{2+}/ZnS$ nanoparticles prepared by Cao et al [147].

The colloidal chemical method is also an important method to produce ZnS nanoparticles. The solvent could be water [148] or alcohol [149], the precipitation anions are usually H_2S and the prepared ZnS colloid is quite transparent. Other methods have also been widely used to synthesize doped ZnS nanoparticles.

All of these methods discussed can also be used to produce elongated ZnS nanostructures (nanorod, nanowire, nanobelt etc) by controlling the stoichiometry, external parameter and the environmental condition. Wang el al has fabricated ZnS nanorods by annealing precursor ZnS nanoparticles, which were prepared by one-step, solid-state reaction of $ZnCl_2$ and Na_2S through grinding by hand at ambient temperature [150]. Zinc sulfide nanorods of wurtzite structure have also been grown using a simple sol-gel method via ultrasonication, in the presence of a capping agent (Mercaptoethanol) [151]. Xi et al have decomposed a sheet-like Zones in a mixed solution of oleic acid/alcohol/hexadecylamine under mild solvothermal conditions to produce ZnS nanorods [152]. These as-prepared nanorods are an average of 25 nm in diameter and 300 nm in length. The template method is also used to produce ZnS nanorods where various kinds of template is used such as porous alumina template, liquid crystal templates [153]. Some physical methods are also successfully used to produce elongated ZnS nanostructures. Veluman used simple physical vapor

deposition technique to develop ZnS nanorod [154]. In the process he maintained uniform vapor stream at a rate of evaporation (~ 2.5Å per second). Evaporation of ZnS nanopowders can also used to produce ZnS nanostructures [155] in elongated form and of different morphology by controlling the reaction temperature and catalyst in the evaporation process.

A new approach popular approach of develop elongated ZnS nanorod is nanostructure in which chemically developed ZnS nanoparticles are made elongated using some physical method by an external effect. Kulkarni et al have done the microwave-irradiation-assisted growth of ZnS nanorod [156]. They have successfully able to grow Zones nanorod of 50-100 nm of diameter and more than 1 µm in length.

1.4.2 Zinc Oxide (ZnO) nanostructures

Among, the II-VI binary semiconductors nanostructures, ZnO have received extensively more attention in recent years. Zinc Oxide (ZnO) is also a direct wide band gap semiconductor and observed in three forms hexagonal wurtzite, cubic zincblende, and the rarely observed cubic rocksalt. The wurtzite structure is most stable in ambient conditions and thus most common in nature. The wurtzite ZnO in its bulk form has a direct band gap of 3.37 eV at room temperature (300^0K) with a relatively large exciton binding energy (60meV). Due to its wide band-gap pure ZnO is colorless and clear. Due to specific electrical, optical and acoustic properties of ZnO it has potential applicability for optoelectronic devices such as LEDs, laser diodes and detectors in the UV wavelength range. Beside the optoelectronic potential of ZnO, its piezoelectric property, its biocompatibility and bio-safe nature [157,158,159] make ZnO as an alternate for next generation semiconductor technology. The ferromagnetic properties of ZnO have potential for Spintronics devices [160,161,162]. In addition, ZnO possesses a number of intrinsic and extrinsic radiative defect levels which emit light in a wide range within the visible region [163]. This is why the room temperature photoluminescence spectrum of ZnO is characterized by the two main peaks, the sharp UV peak centered on 380 nm and another broad deep band emission that lies literally between 400 nm and up to close to 600 nm. The latter is due to deep centers which are caused by intrinsic and/or extrinsic defects. Due to these radiative defects different wavelength emissions from ZnO have been observed. Within the deep broad

band emission, ZnO exhibited violet, blue, green, yellow and orange–red color emissions [164,165], i.e. it covers the whole visible region. A recent investigation on the origin of the visible deep centre mission(s) has suggested that the emission color depends strongly on the growth conditions and the growth method used [166]. This property of multi-color emission adds another potential application for ZnO, namely white light emitting diodes (LEDs), on top of the fact that ZnO has a relatively high exciton binding energy (60 meV), which implies that excitonic laser action can be observed from ZnO even at temperatures at or above room temperature. All these excellent properties together with new findings, e.g. mainly control over synthesizing ZnO nanostructures, have led to substantial interest from researchers world wide.

Although, ZnO nanoparticle show its applicability, recent investigation revels that elongated ZnO nanostructures has some significant advantages over the spherical types [167]. N. E. Hsu et al have demonstrated the polarized emission features of the ZnO nanorods with surface defect states [168]. Wendy et al. has shown that semiconductor nanorods can be employed to fabricate readily processed and efficient hybrid solar cells. By controlling nanorod lengths, one can precisely control the electron transport and e-h recombination characteristics. Tuning the band gap by altering the nanorod radius enables one to optimize the overlap between the absorption spectrum and the solar emission spectrum with improved photo-voltaic efficiency [169]. In addition, lasing with lower gain threshold [170] and suppressed non-irradiative Auger-recombination [171] are other important advantages of 1D nanostructure.

Today, high quality LEDs on p-type crystalline as well as arbitrary (amorphous) substrates and n-ZnO nanorods are recently demonstrated [172,173]. The possibility of integrating n-ZnO nanorods with other p-type substrates has led to an increase in the global interest due to the potential of developing high brightness white light emitting diodes.

The doped counter part of the ZnO nanostructures have also show their importance due to their additional advantages such as short luminescence life-time, size independent emission color tunability, low-voltage cathodoluminescence and alternate-current electroluminescence. A ZnO nanostructured system can be made

highly conductive by doping, making it a promising candidate as interconnects in future generations of nanometer-scale electronics [174], as emitters in field emission arrays [175], or as constituents of magnetic storage devices [176]. They are attractive building blocks of nanoelectronics [177] and nanophotonics [178]. Again, ZnO was reported to experience p-type conductivity can be induced in natural that can be induced in natural hexagonal hexagonal crystal structure of ZnO nanowire and was ascribed due to the presence of oxygen vacancies. The combined magnetic and transport properties as well as high Curie temperature, have made doped ZnO a technologically viable candidate for Spintronics applications [179,180].

Regardless of the fact that research work on ZnO in the thin film form started during the 1930s [181], the interest faded away during the 1980s. The main reason was the fact that it is difficult to dope the material with both n and p-type polarities, and particularly p type. The possibility to dope with n- and p-type polarities is a prerequisite for optoelectronic applications. Many efforts to grow ZnO thin films on other p-type substrates have been a focus for some time as a route to overcome the p-type doped ZnO difficulty. Nevertheless, the lattice mismatch between different substrates and ZnO hinders the possibility of defect free growth of ZnO thin film heterostructures. Even very close lattice structure materials like 4H p-SiC and p-GaN used as substrates have not achieved acceptable device quality for the overgrown n-ZnO films. Limited success using ZnO thin films on p-type semiconductor substrates has been reported for LEDs and lasers; some recent reports can be found in [182,183].

The early growth of bulk ZnO crystals can be achieved using different techniques. The simplest, oldest, and still widely used today is the gas (vapor) transport technique [184,185]. It is even used today for the growth of different ZnO nanostructures [186]. Xiang Yang Kong and Zhong Lin Wang developed ZnO Nanohelixes, Nanosprings, and Nanorings using vapour phase synthesis by just controlling different parameters in the process [187]. A simplified gas transport technique method to achieve nanowires, nanoribbons and nanorods was reported by Yao et al. [188], in which ZnO powder was mixed with graphite and heated to 1100 °C. After cooling down, nanostructures were found to form on the wall of the furnace.

Besides nanowires, nanobelts and nanorods, other complex ZnO nanostructures such as nanotubes [189-191] nano-tetrapods [192-195] also developed using this process.

In general, ZnO has a strong tendency for self-organized growth. This important property has led to global interest to grow ZnO nanostructures with dimensions of diameters from several nanometres up to a few hundred nanometers and lengths up to a few millimetres. Besides the ease of growing ZnO even in the nanostructure form, the advantage for LEDs would be the integration of n-ZnO nanorods on other p-type substrates due to the fact that nanorods of ZnO have no need for a lattice matched substrate for the overgrowth [196], in contrast to thin films. It was recently demonstrated that ZnO nanorods can even be grown on the tip of an amorphous quartz pipette tip a few micrometres in diameter [197]. The stress/strain at the interface between the p-type substrate and the ZnO nanorods can be easily released through the large surface area of the latter (ZnO nanorods). For utilizing ZnO nanostructures it is also a great advantage to have the possibility of using different methods for the growth. Therefore, the quality of the nanostructures achieved by different methods will be of interest to compare regarding the advantages and disadvantages of each method.

Another, common method for the growth of ZnO is the metal–organic chemical vapor deposition (MOCVD). A great advantage of this method is the relatively low requirements concerning the vacuum system because the typical reactor pressure is several hundred millibars, compared to molecular beam epitaxy systems (MBE), where ultrahigh vacuum is required. Many groups which are growing ZnO with MOCVD employ additional catalysts such as Au using the vapour–liquid–solid mechanism (VLS) for the formation of nanostructures [198,199]. In this system no catalyst is required, resulting in higher purity of the ZnO because there will be no impurities resulting from any catalyst. The density and diameter can be well controlled only by choosing the appropriate growth parameters. The whole MOCVD system is quite complex and the epitaxial runs are relatively expensive [200].

Electrodeposition is another approach to develop ZnO nanostructures. In electrodeposition, a voltage has to be provided, leading to a redox reaction at the electrodes. A great advantage of this method is that the growth is possible on selected

areas of the pre-structured substrate; additionally, the pre-structured areas can be used as a contact region to the nanorods [201]. Pulsed laser deposition (PLD) is a relatively young, but very flexible and widely used, growth technique for high quality oxide thin films and also nanostructures.

Nevertheless, the chemical growth technique is the cheapest and popular method for the development of all kinds of ZnO nanostructures. In this process, the typical growth temperatures are below 100 °C, allowing the fabrication even on substrates such as plastic, which is not allowed to be exposed to higher temperatures Recently, cutting edge achievements in growth of ZnO nanorods using low temperature chemical growth were reported [202-206].

1.5 Objective of present study

We have planned our work that involves synthesis characterization and application of semiconductor nanostructures with a special emphasis on elongated systems. The nanostructures are prepared in organic hosts by chemical method. We also focus upon the growing 1 dimensional elongated nanopatterns through physico-chemical routes. IN the present study, we concentrate on II-VI semiconductor systems (ZnS and ZnO based) A comparative study of these doped and undoped materials will be attempted with regard to structural and optoelectronic properties. The various types of characterization tools used are X-ray diffractometer, scanning electron microscopy, Transmission Electron miscopy, UV-VIS spectroscopy, Atomic Force Microscopy, Magnetic Force Microscopy and photoluminescence spectroscopy etc. An emphasis on understanding nanosphere to nanorod changes also has been discussed.

For modification of nanostructures, embedded doped and undoped nanoparticles will be irradiated with swift heavy ions with different kinds of ion species and varied in the range $10^{10} - 10^{13}$ ion/cm^2. Irradiation lead structural and optical properties have been compared and analyzed. Chemically synthesized ion irradiated and photon induced elongated nanostructures have been discussed.

Chapter 2

Materials and Methods

2.1 Development of Nanostructures

The development principles of nanostructures are broadly classified into two categories (1) top down approach (ii) bottom up approach [207]. The synthesis techniques comprise of both (a) Physical methods (b) Chemical methods. Physical methods include Molecular Beam Epitaxy (MBE) [209-211], Electrochemical deposition [212-214], RF sputtering [215, 216], DC magnetron sputtering [217, 218], Low Pressure Chemical Vapour Deposition (LPCVD) [219] , mechanical grinding/alloying [220] , ball milling [221] magnetron co-sputtering [222,223], vapour deposition on cold substrates and on heated substrates [224,225], selective area metal organic chemical vapour deposition (SA-MOCVD) [226,227].

Chemical methods [228,229] have been widely used to produce nanostructured materials due to their simplicity of preparation and provide with large scale production. By allowing competition between nucleation and growth one can realize varying size from nanometers to micrometer. Again, requirement of inexpensive components, relatively shorter synthesis time, less effort, possibility of surface passivation, feasibility of synthesis of metals, alloys, insulators, semiconductors and even compound nanoparticles, possibility of producing single crystalline (monocrystalline) nanoparticles, possibility of proper doping of large number of materials (Mn, Ni, Fe, Cu etc.) even at room temperature, possibility of coating, capping and coupling of synthesized nanoparticles alongwith accurate synthesis of nanoparticles in the form of colloids, powders and thin films made it more popular than physical methods [230].Sometimes combination of both physical and chemical method used to fabricate nanoparticles of a desired system (physicochemical method).

In the chemical synthesis of nanostructure, very often organic ligand environment is used to encapsulate and passivate semiconductor nanoparticles [231-233]. For future developments in the field, as the ligands establish the solution properties of the nanoparticles, aid their luminescence by quenching surface defects,

and maintain their nanoscopic integrity by preventing particle-particle aggregation [234]. Nanostructures have been grown in the hosts such as zeolites [235], porous glass [236,237], miscelles [238,139], membranes [240,141] and anionic polymers [242]. For synthesis of doped and undoped II-VI and III-V compound semiconductors the chemical approach is found to be more efficient then physical one.

Researchers had successfully used both physical and chemical approach to produce spherically symmetric nanostructures to thin film (2D nanostructures). The plethora of physical and chemical processing techniques successfully used to produce 1D elongated nanostructures over last decades are molecular beam epitaxy (MBE) [243], oxygen–plasma assisted MBE [244], ion beam-assisted deposition [245], electron beam evaporation [246], laser-assisted catalytic growth [247], laser photolysis [248], pulsed laser deposition (PLD) [249,250], thermal evaporation [251,252], metalorganic vapor phase epitaxy (MOVPE) [253], spray pyrolysis [254], chemical vapor deposition (CVD) [255], RF magnetron sputtering [256], liquid phase deposition (LPD) [257], electro deposition[258,259], electrostatic self-assembly [260], and Langmuir–Blodgett (LB) [261] techniques are the most utilized by scientists and engineers. Each of them had some specific advantages and disadvantages.

However, It was observed that for development of 1D elongated nanostructure bottom up approach is more suitable in both physical and chemical methods [262, 263]. In this approach of formation of 1D elongated nanostructure, nanoparticles are allowed grow in a particular direction and after certain amount of growth, it was stopped due to lack of reactant in chemical processes and by maintaining some macroscopic parameter in physical process. Amore important challenge in nanowire technology is to develop economical synthesis methods to produce ordered, oriented, and aligned 1D nanostructure onto various substrates.

We have developed spherically symmetric nanoparticles and 1D elongated nanorods using soft chemical approach in organic hosts (PVOH and CTAB). Again, in another approach, we attempt to elongate the spherical nanostructures to elongated using two different physical ways – (1) highly energetic ion bombardment and (2) illuminating with laser

2.2 Modification of Nanostructures:

People have successfully developed nanostructured materials having different size, shape and organization using both chemical and physical approach. But, uniform size and shape distribution and well ordered nanostructures, till out of our achievement. Researchers have tried overcoming this limitation by modifying the previously developed nanostructures (chemically and physically), through some physical ways: annealing [164-266], electron beam irradiation [267,268], ion beam irradiation [269], microwave irradiation [270-272] and laser illumination [272- 277]. However using such modification, it is possible to tune different physical properties of the material to enhance its applicability.

2.2.1 Ion irradiation

The ion irradiation plays a vital role in material science research [278-282]. Now a day, ion beam has become an important aspect for synthesis, modification and characterization of materials. This include ion-implantation [279], ion beam mixing [280], ion beam assisted self organized nanostructure formation [281] and template synthesis [282]. Ion beam irradiation has also been utilized to pattern single component metal [283] and semiconductor [284]. Ripple structures have been reported along preferred crystallographic directions which were and oriented normal and parallel to the direction of the incidence of the ion beam [285,286]. It was believed that either competition between erosion and kinetic restrictions on the diffusion of additional atoms, or to a surface instability arising form a surface curvature dependent sputter yield lead to such ripple formation. [278,284].
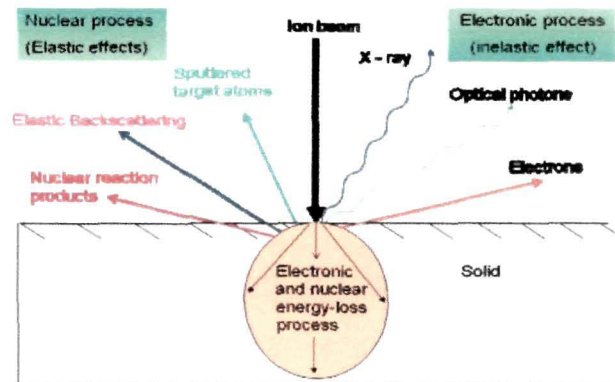
Figure 2.1: A Scheme of ion matter interaction process

The interaction of the ion beam with a solid is a non-equilibrium process. When a stream of energetic charged particles is incident on a crystalline solid the projectile ions interact initially with the near-surface atoms of the solid. The interaction process can lead to ion penetration into the subsurface region of the solid, to the rearrangement of the near-surface atoms, and to the emission of particles and other forums of radiation.

As ion proceeds through the solid, it undergoes successive collisions with the target atoms and surrounding electrons, losing energy at each encounter. The ion matter interaction involves two independent processes, by way of nuclear energy loss and electronic energy loss [287,288]. The former is deals with the collisions between the incident ion and lattice atoms where conservation of energy and momentum applied (elastic collisions), unless nuclear reactions or nuclear resonances occur as a result of subsequent encounter. The later process depicts the interaction of fast ions with surrounding electrons. A proportionate amount of energy is delivered to electronic subsystem through inelastic collision as a result of electronic temperature (10^3 K) rises within a time scale of ~10^{-15} sec. Later, within a time of ~10^{-12} sec energy is transferred to lattice subsystem resulting temp rise (10^3 K).

As the total energy loss is the sum of electronic and nuclear energy loss:

$$S = S_{nuclear} + S_{electronic}$$

$$\left(\frac{dE}{dx}\right)_{total} = \left(\frac{dE}{dx}\right)_{nuclear} + \left(\frac{dE}{dx}\right)_{electronic} \tag{2.1}$$

$$Se = -\left(\frac{dE}{dx}\right)_e = \frac{4\pi n^4 Z_p^2 Z_1 Z_1}{m_e v^2}\left[\ln\left(\frac{2mv^2}{I}\right) - \ln\left(1 - \frac{v^2}{c^2}\right) - \frac{v^2}{c^2}\right] \tag{2.2}$$

Boch - Bethe formula -

$$Sn = -\left(\frac{dE}{dx}\right)_n = N\frac{\partial^2}{2}Z_1 Z_2 e^2 a \frac{M_1}{M_1 + M_2} \tag{2.3}$$

For screened Coulomb potential

The nature of the nuclear and electronic energy losses over all energy ranges complicated and consequently, accurate numerical predictions (from theory) are rather difficult. It is either; the electronic or nuclear stopping power that dominant depends on the energy (the velocity and mass) of the incident ion and density of the medium.

At low energies (~keV scale), if the ion velocity is less than the orbital velocity of electron than the electronic energy loss (S_e) is proportional to the ion velocity (an approximation by Lindhard et al 1963, Firsov 1959). In this regime, the nuclear energy loss dominates where direct transfer of momentum and energy from the projectile ion to the target atoms occur, resulting large energy losses by the projectile, which in turn leads to an irregular path of the ion in the material producing point defects in the material. Also, the target atoms may gain enough kinetic energy to knock-on further atomic and electronic collisions, causing additional defects. In material science, the low energy ions are generally used for surface modification and implantation.
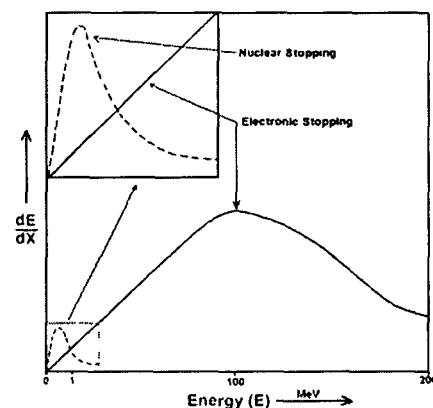
Figure 2.2 : Electronic and nuclear energy loss with respect to ion energy

At relatively higher energy (~MeV scale) where the ion velocity is greater than the orbital velocity of electron, it is the electronic energy loss which comes to forefront. In this case, nuclear energy loss contributes only weakly to the total energy loss. In fact these energetic ions can be classifieds into:

These energetic ions are classified into four categories -

    a) Low energy light ions (LELI)

    b) Low energy heavy ions(LEHI)

    c) High energy heavy ion (HEHI) also know as swift heavy ion

    d) High energy light ion(HELI)

The terms 'high' & 'low' are very much relative and in material science research, they fundamentally mean ~MeV scale & keV scale ion energies.

Low energetic ions (LELI or LEHI) can produce isolated and extended point defects as well meant especially for implantation into a suitable host matrix. In this thesis only HEHI and HELI aspects have been considered.

> **Irradiation with low energy ions**

Ion beam interaction in materials with energy ions having energy such that during slowing down the energy of the ion is dominantly lost through nuclear energy loss (i.e. keV ions) process is well understood. During slowing down, an ion interacts in-elastically with electrons and elastically with other target atoms. If the kinetic energy, E, transferred to the host atom is higher than the displacement threshold energy E_d (~ 8eV for Ga and ~6eV for as) the knock-on atom leaves its lattice site and according to the residual kinetic energy, (E–Ed), it can move for a certain path length. These atoms (primary collisions) recoil and collide with other atoms (secondary collisions) giving rise to higher generation of collisions which produce many low-energy recoils and induce small displacements in nearly random directions. This Sequence of collisions and of displaced atom multiplication is often called collision cascade and it lasts for ~10^{-13}s [289] that is the ion range divided by the average ion velocity. For a 200keV as ion with a speed of ~108 cm/s and a range in Si of 2×10^{-5}cm, the cascade is completed in less than 10-^{12}s. This prompt regime is followed by a redistribution of the energy into surrounding material by both
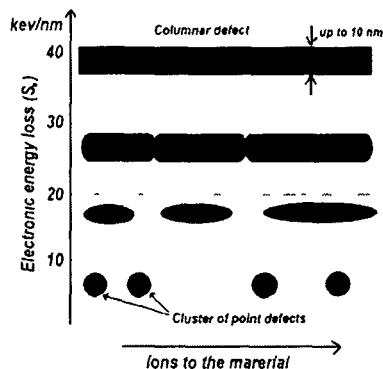
Figure 2.3 : Defect formation at different electronic energy loss in a material
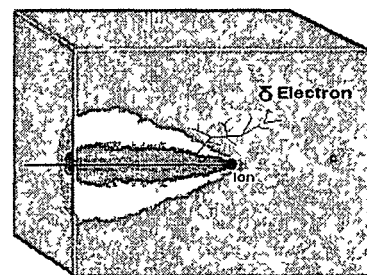
Figure 2.4: Ion passage through a material in high energy ion impact

lattice and electron conduction, this process lasts for an additional time interval of $10^{-11} - 10^{-10}$s. In the following 10^{-9}s the unstable disorder relaxes and some ordering occurs by a local diffusion process. Later on clustering of lattice damage results in the formation of complex defects. This process of clustering and formation of complex defects is governed by the target temperature and by the presence of impurities, if any. The time evolution of the processes taking place during the ion slowing down is shown in Figure 1.1. The process of cooling is very fast in only few picoseconds with rapid thermal quench of the order of 1014^0 K/s – 1015^0 K/s. These results in the formation of different phases and a small volume of 'hot' target atoms may become a small amorphous region surrounded by a crystalline matrix.

> ➤ **Irradiation with high energy ions**

When a material is irradiated with highly energetic ions, it is expected that the lattice atoms are not displaced, but extremely strong electronic excitations occurs around each ion path resulting cylinders containing highly charged ions and electrons which will form a track (called the infra-track) having a radius R_i proportional to velocity of the ion v. Here, in the initial interaction processes of the energy transfer from a high energy ion to electrons bound to inner shells take only 10^{-19}–10^{-17}s and slightly longer (about 10^{-16}s) for collective electronic excitations (formation of plasmons) [290]. Hence, just after the passage of the SHI, the narrow cylindrical target zone coaxial with the ion-path consists of two-component plasma of "cold" lattice atoms and "hot" electrons. Such a narrow region is often called "ionization spike." The initial energy distribution and dynamics of the hot charge carriers within "ionization spikes" have been extensively studied by Schiwietz *et al.* by means of Auger-electron spectroscopy [290].

Roughly, in the initial excitation process one half of electronic energy deposited within a core of radius $r_c = v_p / \omega_p$, where v_p is the projectile velocity and ω_p is the plasma frequency of the target material. The other half of energy deposited by electronic energy loss produces high energy δ rays (electrons) (shown in Figure) that leave the core region and, dissipating their energy far
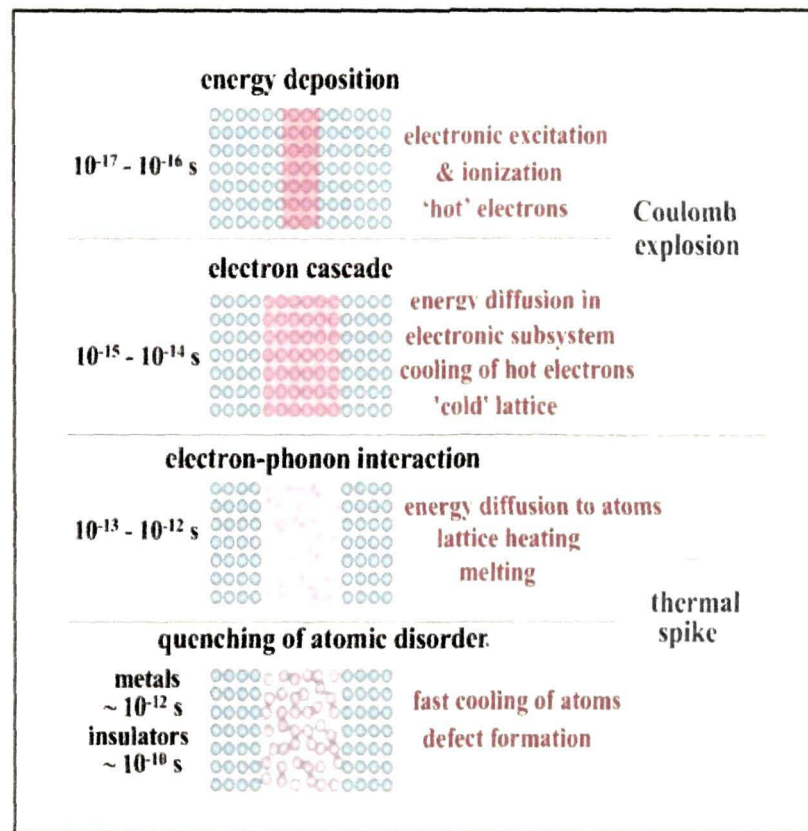
Figure 2.5 : Energetic ions interaction with material at different times scales

away from the core, which are approximately 8 to 10nm in diameter [291]. These liberated δ electrons emanating from the infra track themselves can cause further ionization defects. The radial dimension of the outer cylindrical region (called the ultra track) is determined by the range of the most energetic electron released from the infra track. The region outside the track core, where the defects are caused by delta rays only, is called ultra track (or halo). While the infra track core is only a few nm in a diameter, but the halo can reach a diameter of 100 to 1000 nm. The radial dimension of the outer cylindrical region (ultra track or holo) is determined by the range of the most energetic electron released from the infra track. During the time of delta ray explosion, the core also ions gain kinetic energy due to a violent coulombic repulsion between them, introducing defects and vacancies in the material. This process

is known as *Coulomb explosion* [292] . However, this coulomb explosion depends on how fast the delta electrons return to the core. Delta electrons do not have enough energy which is lost in the inelastic collisions and due to the attractive fore of the positive inner core will move back towards the core unless they get trapped in the bulk.

This Coulomb explosion models based on an electrostatic ions displacement form the ion path is not sufficient to explain the whole mechanism of track formation. The other model used to explain it is thermal spike model where latent tracks are reared as originating from heat transfer and rapid quenching. In this thermal spike models two coupled subsystems are assumed – the electron gas subsystem and the lattice subsystem. The energy form a projectile ion is deposited first in the electron subsystem and subsequently relaxed to the lattice subsystem through electron –phonon coupling, leading to a large temperature increase – thermal spike. This results in cylindrical isotherms with their axes in the projectile trajectory. Within the cylindrical region where the temperature is above the transition temperature (evaporation, melting or pyrolysis temperature for polymers) the material will transform. As the process is very rapid the column of transformed material will be quenched, resulting in the 'freezing' of defects. On the time scale, the Coulomb explosion occurs first and lasts for 10^{-15}s to 10^{-13}s. The thermal spike takes place after the ionic spike in the time period of 10^{-14}s -10^{-12}s. Coulomb explosion always occurs to a certain degree when an ion track is created. However, depending on the material and the projectile ions, the thermal spike may anneal a part or all of the displacement originating from the electrostatic explosion.

Different primary ions having the same velocity produce secondary electrons of the same maximum energy and therefore track of the same diameter is produced which is independent of the ion atomic number. However, the energy density inside the track increased after the passage of the SHI, the solid returns to its equilibrium state leaving behind bulk and surface modifications. In insulating and semi-insulating material damaged tracks along

the trajectory of the ion beam may be formed. Possibility of columnar defects are formed along the ion trajectory is also there. However, it has been these ions form disjointed extended defects or continuous amorphous tracks (latent track) depending on the mass and energy and the semiconductor it is being bombarded upon.

After passing the energetic ions solid return to its equilibrium state leaving behind bulk and surface modifications. The nature of the modification depends on the electrical, thermal and structural properties of the material along with the structure of the projectile ion and irradiation parameters. In insulating and semi-insulating materials, damaged tracks along the trajectory of the ion beam may be formed. In high-temperature superconducting materials columanar defects are formed along the ion trajectory which acts as flux pinning centers. In polymers, gaseous species evolve from the ion tracks because of chain scission and cross linkage. In colossal magneto and noise measurements studies give the basic information of defects due the energetic ion. Large excitons can cause mixing at the interface of metal film on Si.

Thus, when electronic energy loss (Se) is predominant over the nuclear energy loss (Sn), significant material modification can be done. In case of nanostructure, with $S_e > S_n$, there can be significant nanoparticle growth or fragmentation depending upon the ion species and the nature of the medium containing nanoparticle [293]. Many worker were are able to maintain growth of nanoparticle of metallic [294], nonmetallic [295] and semiconducting [296] systems along the beam. It also gives us tunability of the optical [297-299] and magnetic [300-304] properties of nanomaterials by controlling the ion fluence as desired.

Elongation of nonmetals nanostructures were analyzed by A. Merdrum in late nineties [295]. P. Kluth et al studied modification of different metal nanostructures in silica matrix under SHI irradiation and found elongation in many cases [305]. Elongated Au nanoparticles parallel to each other and embedded in a silica matrix film were synthesized by 120 MeV Au ion irradiation ions [306].

2.2.2 Photon illumination

In recent years there has been tremendous research emphasis on finding self-organization strategies to make strongly correlated metal and semiconductor nanostructures. In the area of thin film pattern formation, epitaxial strain driven self-organization in crystallographic systems has been somewhat successful [307 -309]]. When a material is illuminated with a fine spot of with highly intense light beam, it destabilized the long range attractive intermolecular forces and thus destabilized the nanoparticles embedded in the matrix. So, diffusion of the nanoparticles in the matrix was observed. Yang etal found that under UV photon illumination citric acid protected gold nanoparticles, they transformed into two-dimensional (2D) nanonetworks, porous nanoplates and compact nanoplates with hexagonal, triangular or truncated triangular pores through a self-assembly process which was dependent on the citric acid concentration [310]. The photofragmentation of spherical silver nanoparticles could promote the growth of triangular nanoplates was reported by many researches [311-313]. Again, it was observed that the UV as well as visible light could induce the anisotropic growth of nanoparticles to form nanorods and nanowires [314, 315]. However, recent experiments have shown the possibility of modification and organization nanostructures (known as nanostructuring) by illumination of nanosecond and picoseconds laser pulses [316,317]. Controlled laser irradiation can produce nanonetworks [318]. Moreover, organized bimodal size distribution of nanoparticles [319] was also observed by under the pulsed laser irradiation.

LASER Convex lens Film mounted in a scanning system
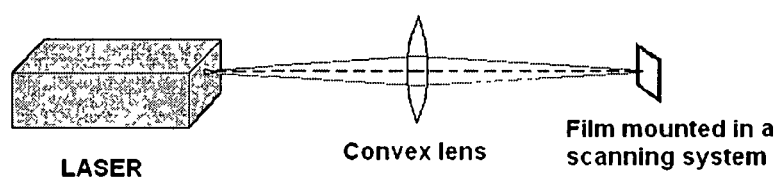
Figure 2.6 : A scheme Laser illumination system

In this thesis we have reported modification and organization of II-VI nanoparticles under low power laser irradiation. In the experiment the focus laser beam is scanned over the 1 cmx 1cm film of nanoparticle for limited time period.

2.3 Characterization of Nanostructures

2.3.1 X-ray Diffraction (XRD)

In crystalline solids, the typical atomic spacing is only a few Å only. So, a material irradiated with X-rays of wavelength ~1Å, will undergo diffraction that can bring in adequate information on the arrangement of the atoms giving raise of definite crystal structure. A simple formula was theorized by W. L. Bragg, considering secular reflection of X-rays on one set of crystal planes. According to Bragg's law two rays will interfere only if the path difference is an integral multiple of λ. [320],
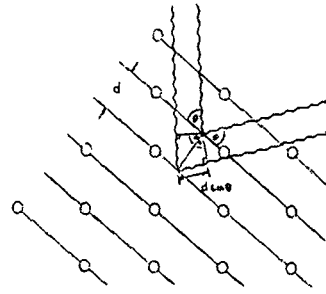
Figure 2.7 : Diffraction in crystal

$$2\lambda = 2d\sin\theta \qquad (2.1)$$

For an unpolarized primary beam incident on a small crystal, the diffraction intensity from a small single crystal is given by [321] -

$$I_p = I_e F^2 \left(\frac{\sin^2[(\pi/\lambda)(\bar{s}-\bar{s}_0).N_1\bar{a}_1]}{\sin^2[(\pi/\lambda)(\bar{s}-\bar{s}_0).\bar{a}_1]}\right)\left(\frac{\sin^2[(\pi/\lambda)(\bar{s}-\bar{s}_0).N_2\bar{a}_2]}{\sin^2[(\pi/\lambda)(\bar{s}-\bar{s}_0).\bar{a}_2]}\right)\left(\frac{\sin^2[(\pi/\lambda)(\bar{s}-\bar{s}_0).N_3\bar{a}_3]}{\sin^2[(\pi/\lambda)(\bar{s}-\bar{s}_0).\bar{a}_3]}\right)$$

$$(2.2)$$

Where $I_e = I_0 \dfrac{e^4}{m^2 c^4 R^2}\left(\dfrac{1+\cos^2 2\theta}{2}\right)$ is being related to the scattering

factor $\dfrac{e^4}{m^2 c^4 R^2}$ and polarization factor $\cos^2 2\theta$ structure factor

$F = \sum f_n \exp(2\pi i/\lambda)(\bar{s}-\bar{s}_0)\bar{r}_n$ and $F^2 = FF^*$, N_1, N_2, N_3 are the respective number of unit cells along the $\bar{a}_1, \bar{a}_2, \bar{a}_1$ directions, and $\bar{s}_0$ and $\bar{s}$ are the unit vectors of the primary and reflected beam respectively. In general, the N_1, N_2, N_3 are such large numbers, that each of the three quotients differ from zero only if the Laue equations (eq. 2.3) are closely satisfied, and hence the diffraction pattern are narrow [320,321].

$$\left(\bar{s}-\bar{s}_0\right).a_1 = h\lambda \qquad \left(\bar{s}-\bar{s}_0\right).a_2 = k\lambda \qquad \left(\bar{s}-\bar{s}_0\right).a_3 = l\lambda \qquad (2.3)$$

For very small crystals where N_1, N_2, N_3 are small numbers the three quotients would naturally get broaden. As the peak width is dependent on the crystalline size, the measurement of the peak width gives a simple method for determining crystal size in the size range up to about 1000 Å. First, the treatment of size dependent broadening was modeled by Scherrer [322,323] .In the simplest approach, for a small cubic crystal, and assuming that they are free form strains and faulting, the peak broading is due only to the small size, the Scherrer equation is given by

$$2R = \frac{0.89\lambda}{\beta \cos\theta} \tag{2.4}$$

Where, $2R$ is the particle diameter, 2θ is the diffraction angle, and β is the half width of the widened diffraction line i.e full width half maxima (FWHM).

Using above equation, one can calculate the average crystallite size in a given sample. The validity of Scherrer equation has been examined by using direct computer simulation of the Bragg diffraction [324]. The presence of size inhomogeneities and point defects does not significantly affect on the accuracy of the size determination. For calculating FWHM, generally Gaussian type profiles for a given particle size distribution is considered. However, the broadening of line width can be affected not only due to particle size but also due to instrumental response, micro-strain [325,326].

The Scherer method is generally valid for crystals of cubic symmetry and if the peak broadening is only due to the crystallite size. Besides this, it applies to Gaussian line widths measured on Debye-Scherrer patterns. If these assumptions are not satisfied, the obtained values have to be considered as approximations. In case of nanocrystals there are many more reasons to be considering this method of determination of size of nanocrystals considered as approximations. The Scherer formula gives only an idea about rough estimation nanocrystals.

However, for the XRD pattern it is possible to identify the crystal structure of the material and to determine the d spacing as well as the crystal parameter (a,b,c) from the JCPDS database [Appendix 5].

2.3.2 UV-Visible Absorption Spectroscopy

In any material, the difference in energy between molecular bonding, non-bonding and anti-bonding orbitals ranges from 125-650 kJ/mole. This energy corresponds to ultraviolet (UV) region, (100-350 nm), and visible (VIS) regions (350-700 nm) of the electro-magnetic spectrum. So, the absorption of visible and ultraviolet (UV) radiation is observed in the corresponding material as a result of which excitation of electrons form the lower energy states to higher energy states. All molecules will undergo electronic excitation following absorption of light.

When a light beam of intensity I_0 passes through a material sample, the intensity of transmitted light decreases exponentially as per Beer-Lambert law [127] and the absorbance of light is proportional to the concentration of the chromophore.

$$I_1 = I_0 e^{-\varepsilon_\lambda c l} \qquad (2.5)$$

Where, I_0 is the incident light intensity, l is the cell path length in cm, c is the solution concentration in moles/liter, and ε_λ is the molar absorptivity, (also referred to as the molar extinction coefficient) which has units of liter/mole/cm.

Again A=$\varepsilon_\lambda c l$ is the absorbance (a defined quantity, also referred to as the optical density, or OD).
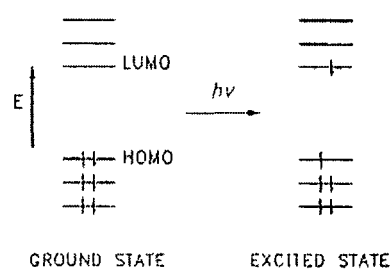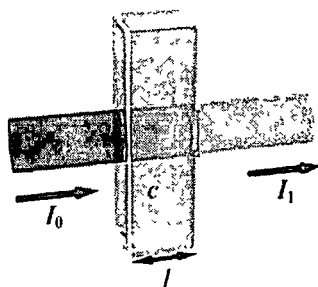
Figure 2.8 : Optical absorption and transmission in a material

Figure 2.9: HOMO to LUMO Transition of electron corresponding to optical absorption

The origin of absorption spectra is due to transition of electrons form bonding molecular orbitals (σ or π) to anti-bonding molecular orbitals (σ* or π*). The lowest energy transition (and most often observed by UV) is typically that of an electron in the Highest Occupied Molecular Orbital (HOMO) to the Lowest Unoccupied Molecular

Orbital (LUMO). In semiconductor material this correspond a transition form the valence band to the conduction band edge. This characteristic absorption peak is used to study the semiconductor material bulk as well as in nano regime. In semiconductor nanostructures, the bandgap enhancement is observed with decreasing cluster size due to the quantum confinement effect [Section 1.21]. As a result, a blue shift in the absorption edge is observed with decreasing cluster size. One can determine the approximate size of the nanostructures using the Bruss equation (eq 1.19).

2.3.3 Fourier Transform Infrared spectroscopy (FTIR)

An infrared spectrum represents a fingerprint of a given specimen with absorption peaks corresponding to the frequencies of inter-atomic vibrations in the molecular system. Because every system is characterized by a unique combination of atoms, no two compounds can ever produce identical infrared spectra. Therefore, infrared spectroscopy can be considered as an important asset in the qualitative analysis of a given material system

In the FTIR spectroscopy, instead of recording the amount of energy absorbed when the frequency of the IR light is varied (monochromator), the transmitted IR light is guided through an interferometer. After passing through the sample, the measured signal is collected in the form of interferograms. Performing a Fourier transform on the signal data results in a spectrum similar to that from conventional (dispersive) infrared spectroscopy. FTIR spectrometers are cheaper than conventional spectrometers because building an interferometer is easy relatively than the fabrication of a monochromator. In addition, measurement of a single spectrum is faster for the FTIR technique because the information at all frequencies is collected simultaneously. This allows multiple samples to be collected and averaged together resulting in an improvement in sensitivity. By and large, all modern infrared spectrometers are FTIR instruments.

Infrared radiation spans a section of the electromagnetic spectrum having wavenumbers ranging roughly from 13,000 to 10 cm^{-1}, or wavelengths from 0.78 to 1000 μm. It is bound by the red end of the visible region at high frequencies and the microwave region at low frequencies. IR absorption positions are generally presented

as either wavenumbers ($\bar{\nu}$) or wavelengths (λ). Wavenumber defines the number of waves per unit length. Thus, wavenumbers are directly proportional to frequency, as well as the energy of the IR absorption. The wavenumber unit (cm^{-1}, reciprocal centimeter) is more commonly used in modern IR instruments that are linear in the cm-1 scale. In the contrast, wavelengths are inversely proportional to frequencies hence, associated energy. At present, the recommended unit of wavelength is μm (micrometers), but μ (micron) is used in some older literature. Wavenumbers and wavelengths can be interconverted using the following equation [127] -

$$\bar{\nu} \ (cm^{-1}) = \frac{1}{\lambda(\mu m)} \times 10^4 \qquad (2.6)$$

By measuring at a specific frequency over time in the FTIR spectrum, changes in the character or quantity of a particular bond can be studied. This is especially useful in measuring the degree of polymerization in polymer manufacture. Modern research instruments can take infrared measurements across the whole range of interest as frequently as 32 times a second. This can be done whilst simultaneous measurements are made using other techniques. This makes the observations of chemical reactions and processes quicker and treats accuracy.

2.3.4 Electron Microscopy

An electron microscope is a type of microscope that uses a beam of electrons to illuminate a specimen and capable of creating a highly-magnified image. An electron microscope has much greater resolving power than optical microscope that uses visible electromagnetic radiation as the source. It provides much higher magnification (up to 1 million times) than the best light microscopes (limited only to magnification of 1000 times). Both electron and light microscopes have resolution limitations, imposed by the wavelength of the radiation they use. The greater resolution and magnification of the electron microscope is because of the de Broglie wavelength of an electron which is much smaller than that of a photon of visible light. The electron microscope uses electrostatic and electromagnetic lenses forming the images by controlling the electron beam to focus it at a specific plane relative to the specimen object. The approach is similar to that of a light microscope which uses glass lenses to focus on or through a specimen to produce an enlarged image.
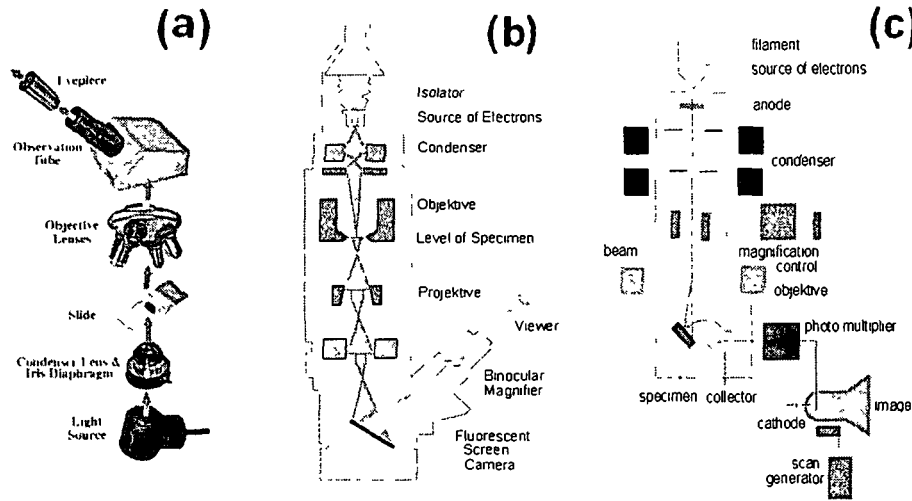
Figure 2.10: Schematic diagram of (a) Optical microscope (b)Transmission Electron Microscope, and (c)Scanning electron microscope

(a) Transmission Electron Microscopy (TEM)

Transmission Electron Microscope (TEM) is a non destructive, noninvasive capable of providing visual information about a specimen of dimension down to several Å. This is the original form of electron microscope. A TEM uses a high voltage electron beam to create a magnified image. The electrons are emitted by an electron gun, commonly fitted with a tungsten filament cathode as the electron source and they are accelerated by an anode typically within 40 to 400 keV with respect to the cathode. After, suitable focusing through a set of electrostatic and electromagnetic lenses, it is allowed to transmit through the specimen. When it emerges from the specimen, the electron beam carries information about the specimen structure that is magnified by the objective lens system of the microscope. The spatial variation of the information (the "image") is viewed by projecting the magnified electron image onto a fluorescent viewing screen coated with a phosphor or scintillator material (zinc sulfide). The image can be photographically recorded by exposing a photographic film/plate directly to the electron beam, or a high-resolution phosphor may be coupled by means of a lens optical system or a fiber optic light-guide to the sensor of a CCD (charge-coupled device) camera. The image detected by the CCD can be interfaced to a pc for display and data actuation [128].

Resolution of the TEM is limited primarily by spherical aberration, but a new generation of aberration correctors has been able to partially overcome spherical aberration to increase resolution. Hardware correction of spherical aberration for the High Resolution TEM (HRTEM) has allowed the production of images with resolution below 0.5 Å (50 pm) at magnifications above 50 million times. The ability to determine the positions of atoms within materials has made the HRTEM an important tool for nano-technologies research and development.

(b) Scanning Electron Microscopy

Unlike TEM, the emergent electron beam of the Scanning Electron Microscope (SEM) does not carry the complete information of the specimen under study. The SEM produces images by a In a SEM, a focused electron beam that is scanned across a rectangular area of the specimen (raster scanning). In the scanning process, at each point on the specimen the incident electron beam loses some energy, and the lost energy is converted into other forms of heat, emission of low-energy secondary electrons, light emission (cathodoluminescence) or x-ray emission etc. The secondary electrons emitted from the specimen are used to produce the image of the sample .

Generally, the image resolution of an SEM is several orders of magnitude smaller than that of a TEM. A rough idea about size, shape and arrangement of crystallites can be assessed at large.

Energy Dispersive x-ray spectroscopy: Energy Dispersive X-ray Spectroscopy (EDS) is an analytical technique that identifies the elemental composition of materials qualitatively and quantitatively. In SEM, when an electron beam scanned over a typical cross-section of the sample specimen, it generates the characteristic x-rays from the atoms (which are the characteristic of the atom) [128]. The EDS system collects the X-rays, sorts them in terms of energy to plotted intensity of X-rays corresponding to the energy. The data can then be further analyzed to produce either
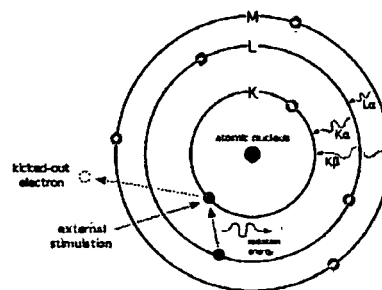
Figure 2.11 : Characteristic X-ray Emission

an area elemental analysis (displayed as a dot map) or a linear elemental analysis (displayed as a line scan) showing the distribution of a particular element within the top two microns of the sample surface. The EDS data can be compared to either known standard materials or computer-generated theoretical standards to help providing either a full "quantitative" or a "semi-quantitative" picture.

2.3.6 Scanning Probe Microscopy

Scanning Probe Microscopy (SPM) is unique in the sense that it forms images of surfaces and interfaces by use of a physical probe that scans the specimen. An image of the top surface is obtained by moving mechanically the probe in a raster scan of the specimen, line by line, and recording the probe-surface interaction as a function of position. Depending upon the nature of interaction , configuration of scanning probe microscopy (SPM) are available:– Atomic force microscopy(AFM), magnetic force microscopy(MFM), scanning tunneling microscopy(STM) etc [129].

(a) Atomic Force Microscopy

The atomic force microscope (AFM) or scanning force microscope (SFM) is an extremely sensitive microscope capable of providing topographical image of the surface. The resolution is over 10,000 times better than the optical diffraction limit.

The AFM consists of a cantilever with a sharp tip (probe) at its end, used to scan the specimen surface. The cantilever is typically made of silicon nitride (Si_3N_4) with a tip of radius of curvature in the order of few nanometers only. When the tip is
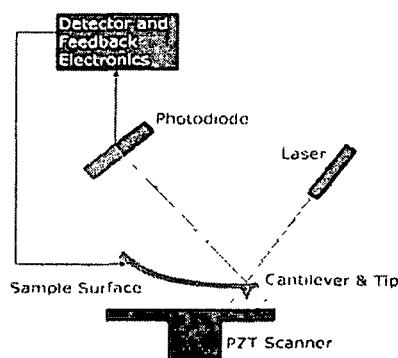
Figure 2.12: Schematic diagram scanning probe microscope (AFM/MFM)
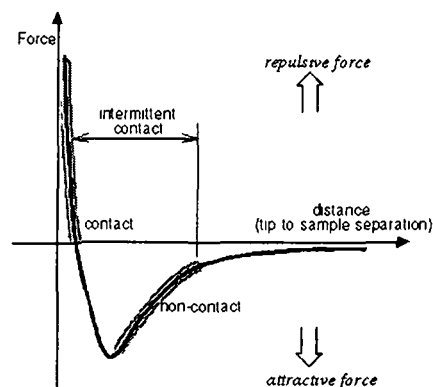
Figure 2.13 : Interatomic force vs. Interatomic distance

brought into the close proximity of the sample surface, forces between atoms of the tip and the surface atom of the sample is governed by a deflection of the cantilever as par popular Hooke's law. Depending on the configuration, forces that are measured in AFM include mechanical contact force, van der Waals force, capillary force, chemical bonding, electrostatic forces, magnetic force etc. Apart from force, additional parameters simultaneously be measured by use of specialized of probes (Scanning thermal microscopy, photothermal micro-spectroscopy, etc.).

Typically, the deflection is measured using a laser spot reflected from the top surface of the cantilever into an array of photodiodes. Other methods in practice optical interferometry, capacitive sensing or piezoresistive AFM cantilevers. These cantilevers are fabricated with piezoresistive elements which act as strain gauge. Using a Wheatstone bridge, strain in the AFM cantilever due to deflection can be measured, however , not as sensitive as laser deflection or interferometry. If the tip is scanned at a constant height, a risk would exist that the tip might collide with the surface, causing damage. Hence, in most cases a feedback mechanism is employed to adjust the tip-to-sample distance in order to maintain a constant force between the tip and the sample. Traditionally, the sample is mounted on a piezoelectric stage that can move the sample along z direction, maintaining a constant force, and the x and y directions for scanning purpose. Alternatively a 'tripod' configuration of three piezo crystals may be employed, of each which is responsible for scanning in the x,y and z directions. This eliminates some of the distortion effects seen with a tube scanner. In newer designs, the tip is mounted on a vertical piezo scanner while the sample is being scanned in X and Y using another piezo block. The resulting map of the area $s = f(x,y)$ represents the topography of the sample. Although, several forces typically contribute to the deflection of an AFM cantilever, the most commonly associated forces are inter- atomic van der walls forces. The dependence of the van-der-Waals force upon the distance between the tip and the sample is shown in figure (2.13). Based on the nature of the force between the tip and the sample, the AFM can be operated in a number of modes.

In general, possible imaging modes are divided into contact modes (static modes - cantilever is static) and a variety of non-contact mode(dynamic modes-cantilever is vibrated). In contact, AFM mode (also known as repulsive mode, an AFM

tip makes soft "physical contact" with the sample) , the tip is attached to the end of a cantilever with a low spring constant. As the scanner gently traces the tip across the sample (or the sample under the tip), the contact force causes the cantilever to bend in order to accommodate changes in topography. In addition to the repulsive van der Waals force described above, two other forces are generally present during contact AFM operation often: a capillary force exerted by a thin water layer is present in an ambient environment, and the force exerted by the cantilever itself. The capillary force arises when the water wicks its way around the tip, applying a strong attractive force ($\sim 10^{-8}$N) that holds the tip in contact with the surface. The magnitude of the capillary force depends on the tip-to-sample separation. In non-contact AFM (NC-AFM), the cantilever is vibrated near the surface of a sample. The spacing between the tip and the sample for NC-AFM is generally on the order of tens to hundreds of angstroms. NC-AFM is desirable because it provides a means for safe measurement of a sample topography with little or no perturbation. Like contact AFM, non-contact AFM can be employed to measure the topography of insulators and semiconductors as well as electrical conductors. The total force between the tip and the sample in the non-contact regime is very low. This low force is advantageous for studying soft or elastic and polymeric samples.

(b) Magnetic Force Microscopy (MFM) : Magnetic force microscopy technique is derived from atomic force microscope (AFM). Unlike typical AFM, a magnetized tip is used to study magnetic materials, and thus, the tip-sample magnetic interactions cab be detected. MFM images the spatial variation of magnetic forces on a sample surface. For MFM, the tip is coated with a ferromagnetic thin film. The system operates in non-contact mode, detecting changes in the resonant frequency of the cantilever induced by the magnetic field's dependence on tip-to-sample separation. The tip-to-sample separation distance is so maintained that the magnetic forces dominates over the van-dar waal forces between them.
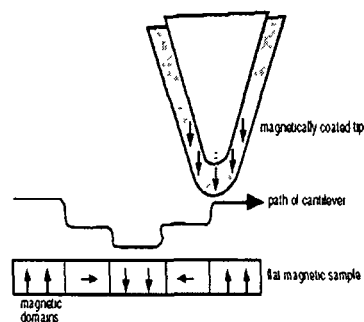
Figure 2.14 : Path of the tip due to magnetic interaction a MFM

2.3.7 Luminescence Spectroscopy

Luminescence spectroscopy deals with the transition of electrons from high energy excited states to allowed low energy states exhibiting emission features. Depending on the mode of excitation there are different kinds of luminescence spectroscopy as listed below [127] -

- Photoluminescence is caused by excitation by light radiation.

- *Electroluminescence results from energy provided by an applied electric field*

- Chemiluminescence occures energy through a chemical reaction.

- Cathodoluminescence is caused by accelerated electrons colliding with atoms

- Sonoluminescence is caused by sound/ultrasound wave

- Thermoluminescence is triggered by heat

Photoluminescence (PL) Spectroscopy

Photoluminescence occurs when a system is excited to a higher energy level by absorbing a photon, and then spontaneously relaxed to a lower energy level, emitting a corresponding photon of lower energy. In order to conserve energy, the emitted photon cannot have more energy than the photon causing excitation, unless two or more excitation photons act in tandem (a case of nonlinear spectroscopy). Again, intermediate nonradiative downward transitions are also possible in the relaxation process. The electrons can also be trapped in intermediate states for a relatively long time, resulting in delayed luminescence.

The photoluminescence is divided into two types, depending on the nature of the ground and the excited states. There are two kinds of excited state – singlet and triplet. In a singlet excited state, the electron in the higher-energy orbital has the opposite spin orientation as the second electron in the lower orbital. These two electrons are said to be paired. In a triplet state these electrons are unpaired, that is, their spins have the same orientation. Return to the ground state from an excited singlet state does not require an electron to change its spin orientation. A change of spin orientation is needed for a triplet state to return to the singlet ground state.

Fluorescence is the emission which results from the return to the lower orbital of the paired electron. In contrast, *phosphorescence* is the emission which results from the transition between states of different multiplicity, generally a triplet excited state
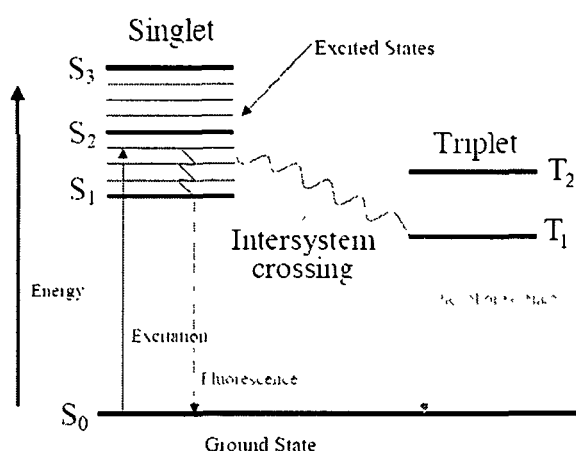
Figure 2.15 : Jablonski diagram describing radiative and non-radiative transitions

returning to a singlet ground state. The Jablonski diagram (Figure 2.14) illustrates the processes involved in the creation of an excited electronic state by optical absorption and subsequent emission. Internal conversion is the radiationless transition between energy states of the same spin state (compare with fluorescence-a radiative process). Intersystem crossing is a radiationless transition between different spin states (compare to phosphorescence). Vibrational relaxation, the most common among the three discussed of the three-for most molecules, occurs very quickly ($<1 \times 10^{-12}$ seconds). Vibrational relaxation is enhanced by physical contact of an excited molecule with other particles in which energy, in the form of vibrations and rotations, can be transferred through collisions [127].

In a semiconductor system, light emission (luminescence) proceeds through electron-hole pair recombination processes (either band to band or mediated by states in the gap region or at the semiconductor surface). After an electron absorbs enough energy, jumps to the conduction band leaving a hole behind, it tends to return to the valence band with a fluorescence emission whose energy is lower than its excitation energy. Corresponding to the band gaps, there is a wide range of absorption from 388 nm to 8857 nm, observed in semiconductors. Only a few of them (CdS and CdSe systems) are in the visible light range (400-700 nm) of the electromagnetic spectrum. The electron must have a minimum E_g band-gap energy to undergo this promotion.
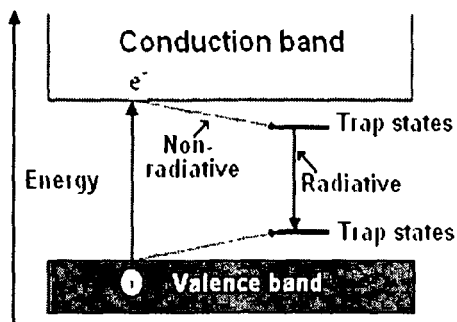
Figure 2.16: Non-radiative and radiative emission and trap states
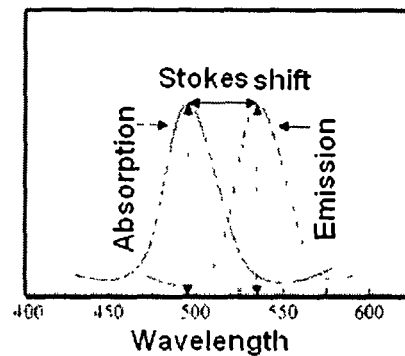
Figure 2.17 : Stokes shift in absorption and emission spectra

The created electron–hole pair (an exciton) may recombine immediately to produce heat or light with energy equal to E_g, but it is more likely that trap states within the material trap either the electron or the hole. (Figure 2.16) These trap states result from numerous factors, including structural defects, atomic vacancies, dangling bonds, and adsorbents at the interface. Radiative recombination of the trapped charge carriers then produces luminescence that is substantially red-shifted from the absorbed light. These trap states are very much related to the size and surface structure of the semiconductor. A very unique property of semiconductor nanostructures is the size dependence of luminescence emission. The surface to volume ratio has a great influence on the nature of the trap states. In the nanoscale regime, as size gets smaller, the band gap becomes larger. So the fluorescence color can be tuned by changing the size of the semiconductor nanostructures.

Fabrication of II-VI semiconductor nanostructures

Both large scale synthesis and preservation of nanoparticles is important from application point of view. In order to improve the rigidity and to protect nanoparticles from environmental attack, embedding them glass, zeolites or polymer is desired [145]. The synthesis of II-VI semiconductor nanostructures in Nafion [242] and Syrlyn membranes were quite satisfactory and are found to show relatively higher stability. In this chapter we will discuss the different fabrication technique used to develop spherically symmetric as well as elongated nanostructure through chemical approach. The as developed nanostructured samples were characterized by X-ray diffraction pattern, UV-Vis spectroscopy and Electron microscopy.

3.1 Materials:

(a) Polyvinyl alcohol (PVOH):

Polymers are believed to be good protecting agents against agglomeration. We consider polyvinyl alcohol (PVOH) as the host matrix. Unlike many polymers, polyvinyl

$$-[CH_2-CH]_n-$$
$$|$$
$$OH$$

Figure 3.1 : Structure of PVOH

alcohol is a water soluble compound. It dissolves slowly in cold water but at higher temperature it goes fairly fast. It is produced by the hydrolysis of polyvinyl acetate which is made by the polymerization of vinyl acetate monomer. It is a good protective colloid for aqueous emulsions and is employed for this purpose in a large variety of emulsion and suspension systems. It also finds use in wet strength adhesives. This water soluble polymer is widely used for textile warp sizing, adhesive, paper sizing agent, ceramic binder and also used in cosmetics, emulsion stabilizer, civil engineering, construction, pharmacy and electronic industries. The details of physical properties of PVOH are explained in Appendix 5.

(b) Cetyl trimethylammonium bromide (CTAB):

Cetyl trimethylammonium bromide or hexadecyltrimethylammoniumIt is a cationic surfactant. Its chemical formula is $((C_{16}H_{33})N(CH_3)_3Br)$.
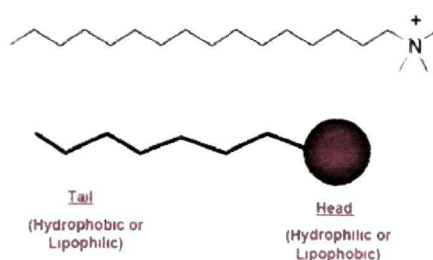
Figure 3.2 : Head and tail in Cetyl-trimethylammonium bromide (CTAB)
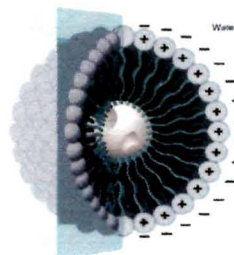
Figure 3.3: Micelle formation in water caused by CTAB

As CTAB is a surfactant, the two end of each CTAB molecule has two specific property one end is high positive polarity and so this end is hydrophilic (head) while the other end is hydrophobic (tail). In water, Ion head (hydrophilic end) repel each other due to long range electrical force and tail (hydrophobic end) chain attract each due to short range vander-wall force promoting micelle formation by the CTAB molecule. At 303K (30 °C) it forms micelles with aggregation number 75-120 (number of molecules present in a micelle once the critical micelle concentration (cmc) has been reached) and degree of ionization α (fractional charge) 0.2 - 0.1 (from low to high concentration). Standard constant of Br^- counterion binding to the micelle at 303 K (30 °C), calculated from Br^- and CTA^+ ion selective electrode measurements and conductometry data by using literature data for micelle size (r = ~3000pm), extrapolated to the critical micelle concentration is $K° \approx$ 400 (it varies with total surfactant concentration so it is extrapolated to the point at which the concentration of micelles is zero). The length of a CTAB molecule is 1800-2300 pm (1.6 to 2.3nm). Details of physical properties are presented in Appendix 5

3.2 Experimental details

3.2.1 Polymer (PVOH) encapsulated nanostructures

- **(a) Fabrication of ZnS nanoparticles in PVOH matrix**

[i] Undoped ZnS nanostructures

For preparation of ZnS nanostructures in polyvinyl alcohol (PVOH), first the matrix was prepared by dissolving 5 %(w/v) PVOH in doubled distilled water. It is done in a magnetic stirrer by stirring the solution (PVOH+D.D.
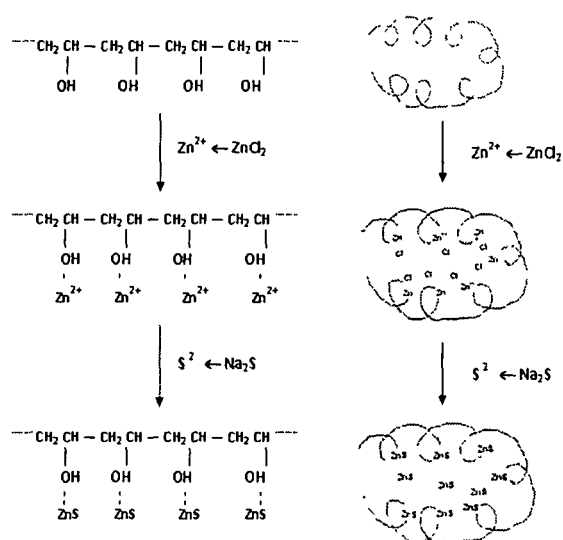
Figure 3.4: Synthesis mechanism of ZnS nanostructures in PVOH matrix

water) a stirring rate ~ 200 rpm at a constant temperature of 70^0C until a transparent solution is found. This transparent solution is the PVOH matrix. Next, 0.15 M $ZnCl_2$ was added to the PVOH matrix under same stirring environment and stirred for another three hours. After that, temperature was reduced to 40°C and 0.01M Na_2S was added drop wise to the solution. Then the solution was kept in cool and dark environment for 24 hours. This final solution obtained, was contained ZnS nanoparticles in embedded in PVOH. It was casted over glass substrate and dried for subsequent characterization.

[ii] Doped ZnS nanostructures

The fabrication technique for doped (transition metal) ZnS embedded in PVOH matrix is very much identical to the method for undoped ZnS nanostructures discuss in 3.2.1 [a] (i). To introduce the doping in ZnS nanostructure, we initially mix up the $ZnCl_2$ with the salt of a metal which we want to be doped. In our synthesis process, a metal chloride/oxide of the transition metal (TM) is used, like for Mn doping $MnCl_2.4H_2O$, for Cr doping Cr_2O_3, for Co doping $CoCl_2$ and for Cu doping $CuCl_2$ were the used compound in the synthesis process.

In the synthesis process of Mn doped ZnS nanostructures (ZnS:Mn), first $ZnCl_2$ was dissolved in water and then $MnCl_2.4H_2O$ is added to the solution under a stirring environment at a temperature of 40^0C . Accordingly, three solutions are prepared by adding three different quantity of $MnCl_2.4H_2O$ (1%, 2% and 3% with respect to $ZnCl_2$). The solution was then added to the PVOH matrix solution and stirred for three hours at a temperature of 70^0 C for another three hours. Next, reducing the temperature to 40^0C, slowly Na_2S was added to the solution drop wise in the stirring environment and again it was stirred for 1 hour. The final The solution was then kept in cool and dark environment for one day, to get the ZnS:Mn nanostructures.

The amount details of the compound used in the synthesis process to develop three different samples with doping concentration 1%, 2% and 3% are given in Appendix (6) clearly.

To introduce other TM impurity to ZnS nanostructures same synthesis process is applied as explained for Mn doped ZnS nanostructures. For fabrication of Cr doped ZnS nanostructures we first make the solution $ZnCl_2$ and Cr_2O_3 while for Co doped it was of $CoCl_2$ and $ZnCl_2$. Similarly, for Cu doped ZnS nanostructures a mixture of $CuCl_2$ and $ZnCl_2$ was used as a starting material.

(b) Fabrication of ZnO nanoparticles in PVOH matrix

The procedure for development of ZnO nanostructure in PVOH matrix, is similar to the procedure for ZnO as previously followed (3.2.1 [a]). We have produced transparent PVOH matrix dissolving 5 %(w/v) PVOH in doubled
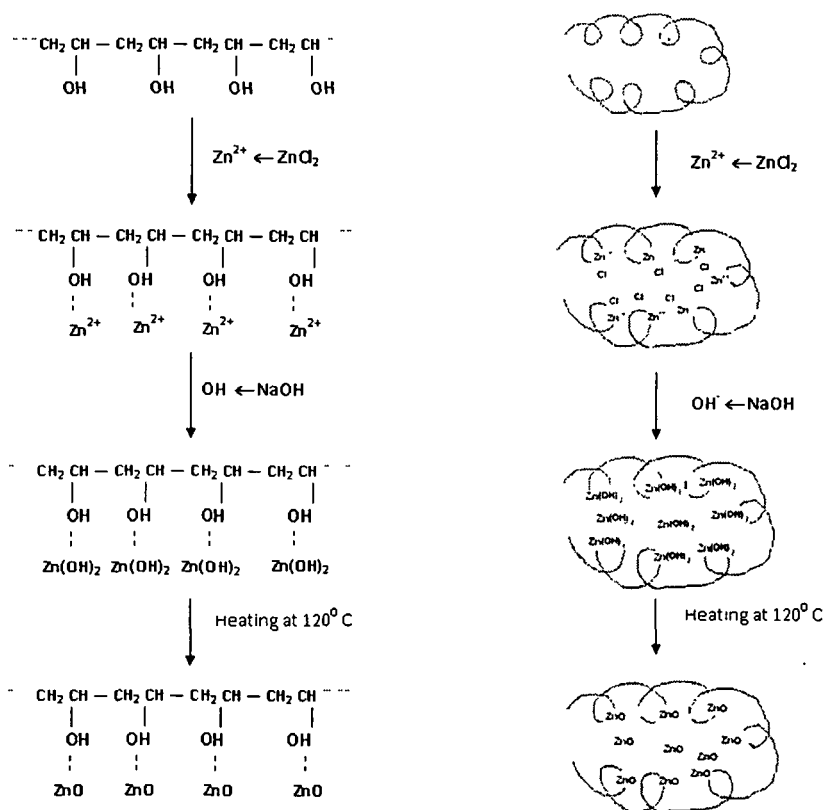
Figure 3.5 : Synthesis mechanism of ZnO nanostructures in PVOH matrix

distilled water under high stirring and at a temperature of 70^{0}C. Then, 0.15M $ZnCl_2$ was added to this PVOH matrix under same stirring environment. After stirring for 1 hour, NaOH was added and temperature was raised to 130^{0}C. Stirring was done at that temperature for 3-4 hours allowing evaporation of water solution. Finally, a highly viscous solution was found containing ZnO nanoparticles. It was casted over glass substrate and heated slowly for obtaining solid films. The samples were kept ready for subsequent characterization.

3.2.2 Surfactant (CTAB) based nanostructures

(a) Fabrication of ZnS nanoparticles in CTAB

In the fabrication process of ZnS nanoparticles in CTAB we have used the mixture of Zinc acetate dihydrate (ZAD) [Zn $(CH_3\ COO)_2.2H_2O$], Cetyl trimethyl ammonium Bromide (CTAB, a micellar cationic surfactant) [C_{19} H_{42} BrN], and sodium hydroxide (mixed at a molar ratio 1 : 0.5: 3) as a starting material. This mixture was ground in a mortar gently for 2 hours. Next, the mixture was transferred to a culture-tube with distilled water and kept in an ultrasonic bath for one hour. At the time of sonication, aq. Na_2S is added drop-wise to the sample. Then the mixture was washed with double distilled water several times through sonication. Finally, the product was dried and preserved for further experimentation and characterization.

(b) Fabrication of ZnO nanoparticles in CTAB

In the process, Zinc acetate dihydrate (ZAD) [Zn $(CH_3\ COO)_2.2H_2O$], Cetyl trimethyl ammonium Bromide (CTAB, a micellar cationic surfactant) [$C_{19}H_{42}BrN$], and sodium hydroxide flakes are mixed at a molar ratio of1 : 0.5: 3. This mixture was ground in a mortar gently for 2 hours. After that, the mixture was transferred to a culture-tube by making a solution with distilled water and was kept in an ultrasonic bath for one hour. The sonicated mixture was then washed with double distilled water several times. To induce oxidation of unreacted species, the as prepared mixture was annealed at a temperature of $60\text{-}80^0$ C for 5 hours. Finally, it was washed using water under sonication for several times. After washing the product was dried and preserved for further experimentation and characterizations.

(c) Fabrication of ZnS nanorods in CTAB

The fabrication process for ZnS nanorods in CTAB comprise of the same materials as used for the case of ZnO nanoparticles: zinc acetate dehydrate (ZAD) [Zn $(CH_3\ COO)_2\ 2H_2O$], cetyl trimethyl ammonium bromide (CTAB, a micellar cationic surfactant) [C_{19} H_{42} BrN], and sodium hydroxide flakes.

This compound was mixed at molar ratio 1 : 0.4: 3 and ground in a mortar for 2 hours. Next, the mixture was transferred to a culture-tube with distilled water and kept in an ultrasonic bath for one hour. In that sonication environment, Na_2S solution is drop-wise added. The sonicated mixture was then washed with double distilled water several times. Again the product is dispersed in water and sonicated. After drying we have found the final product as CTAB based ZnS nanorods. It was preserved for further experimentation and characterizations.

(d) Fabrication of ZnO nanorods in CTAB

(a) Undoped ZnO nanorods: In the process, zinc acetate dihydrate (ZAD) [Zn $(CH_3\ COO)_2.2H_2O$], cetyl trimethyl ammonium bromide (CTAB, a micellar cationic surfactant) [$C_{19}\ H_{42}$ BrN],   and sodium hydroxide flakes are mixed at a molar ratio of 1 : 0.5: 3. This mixture was ground in a mortar gently for 2 hours. Transferring the mixture to a culture-tube with distilled water sonication was made for one hour. The sonicated mixture was then washed with double distilled water several times. To induce oxidation of unreacted species, the as prepared mixture was annealed at a temperature of 60-80^{0}C for 5 hours. Further, washing and sonication was performed. The product was dried finally and preserved for further experimentation and characterization.

(b) Tb doped ZnO nanorods: For preparing Tb doped ZnO nanorods, terbium oxide (Tb_4O_7, 99.9% pure, Otto) compound was used. In the experiment, first terbium oxide was converted to terbium acetate. In this conversion process 0.5 gm of terbium oxide was allowed to react with a 0.4 ml of conc. nitric acid (maintaining pH ~7 by drop-wise addition of sodium hydroxide solution). After the reaction, a white precipitate was found and this precipitate was subjected to repeated washing with distilled water to remove the by products. Finally, the product was treated with 0.4 ml glacial acetic acid to give rise to terbium acetate ($Tb(CH_3COO)_3$). The Tb doped ZnO nanorods were developed by adding as-received terbium acetate in the

reactant-mixture (weight ratio Tb/Zn = 0.02) followed by unidirectional grinding as done in the fabrication process of ZnO nanorods.

The growth mechanism of the Surfactant based ZnS and ZnO nanostructures are quite similar. In all of the above synthesis process first Zinc acetate dihydrate (ZAD) [Zn $(CH_3\ COO)_2.2H_2O$] and Sodium hydroxide(NaOH) results $Zn(OH)_4^{2-}$ a negatively charged tetrahedral that were formed according to the reaction (a), given below. Again CTA^+ was positively charged with a tetrahedral head and a hydrophobic tail. So, CTA^+ $-Zn(OH)_4^{2-}$ pairs are formed initially by electrostatic interaction. The complementarity between CTA^+ and $Zn(OH)_4^{2-}$ endows the surfactant with a capability to act as an ionic carrier. Meanwhile, because CTAB is a kind of strong-acid–weak base salt, it could accelerate the ionization of $Zn(OH)_4^{2-}$. Therefore, part of the $CTA^+-Zn(OH)_4^{2-}$ ion pairs formed a combination of CTAB and $Zn(OH)^2$ according to reaction (b) . The amount of heat produced in the grinding process facilitates the temperature required to complete the reaction. Simultaneously, the other part of the $CTA^+ -Zn(OH)_4^{2-}$ ion pairs still dissociate in the sample.

$$Zn^{+2}+4OH^- \rightarrow Zn(OH)_4^{2-} \qquad (a)$$

$$Zn(OH)_4^{2-} \rightarrow Zn(OH)_2 \qquad (b)$$
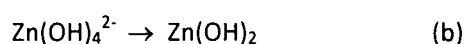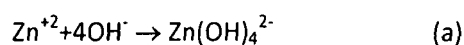
In the synthesis process of ZnS nanoparticle and nanorods the Na_2S react with the $Zn(OH)_2$ and produced ZnS. In case of ZnO nanostructure synthesis upon heating at 120°C, $Zn(OH)_2$ decomposes to ZnO.

$$Zn(OH)_2 \rightarrow ZnO + H_2O \qquad (c)$$

$$Zn(OH)_2 + Na_2S \rightarrow ZnS + Na_2S \qquad (d)$$
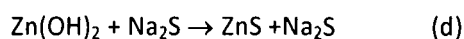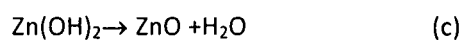
The concentration of CTAB and the molar ratio of Zn^{2+} to OH^- play important role in the fabrication of structurally uniform and pure ZnO samples.

In the development of surfactant based ZnS and ZnO nanostructures, just by varying the surfactant-to-Zinc concentration ratio, we have produced both nanoparticles and nanorods. At certain molar ratio, the slow diffusion of Zinc ion in CTAB helps to produce the nanorods.

3.3 Characterization:

The synthesized products were then characterized and analyzed by X-ray diffraction (XRD), UV-Visible spectroscopy, Fourier Transform Infrared (FTIR) spectroscopy, Electron Microscopy. To study the crystal structure, we have used XRD pattern obtained on a Rikagu Miniflex X-ray diffractomenter with Cu K_α line of wavelength 1.54 Å. The excitonic absorption peak in the UV-Vis spectra obtained from Varian Carry Bio 100 has given us the idea of formation of nanostructures and its size. Finally, Transmission Electron Microscopy (Jeol JSM100CX) was used confirm the formation of nanoparticles and nanorods in different samples.

3.3.1 ZnS nanostructures

(a) X-ray diffraction :

(i) ZnS nanoparticles :
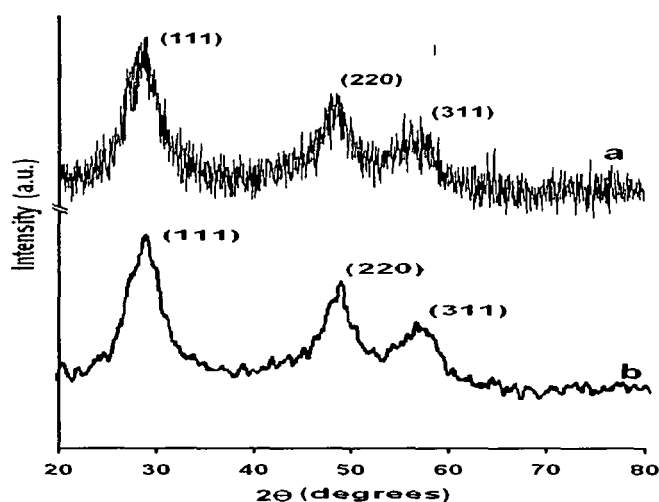
Figure 3.6: XRD pattern of (a) PVOH encapsulated ZnS nanoparticles
(b) CTAB based ZnS nanoparticles

The x-ray diffraction pattern of PVOH encapsulated ZnS nanoparticles and CTAB based ZnS nanoparticles shown in Figure. 3.6, depicts cubic structure corresponding to three diffraction peaks (111), (220) and (311). Using the equation $d_{hkl} = n\lambda/2\sin\theta$ the d-spacing has been calculated and the estimated values are in good agreement with JCPDS file No. 5-0566. For PVOH encapsulated ZnS the crystal lattice parameters estimated

as a = 5.265 Å while for the CTAB based ZnS nanoparticles a = 5.295Å. The broadening of the diffraction peak corresponds to the formation of nanostructures in the sample and it gives a rough estimation of average particle size through the Scherrer formula. Using Scherrer formula we estimated the average crystallite size of the PVOH encapsulated ZnS nanoparticles estimated ~ 6 nm, and for the CTAB bases ZnS nanoparticles it is obtained ~ 10nm. No characteristic peaks due to either impurities or unreacted species like $Zn(OH)_2$ or Na_2S are observed in the XRD spectra, which indicates the formation of pure and hydroxyl-free cubic ZnS nanostructures in PVOH and CTAB.

(ii) ZnS nanorods:

The XRD spectra of the CTAB based ZnS nanorods shown in the Figure 3.7. The diffraction peak positions are quite similar to those of ZnS nanoparticles
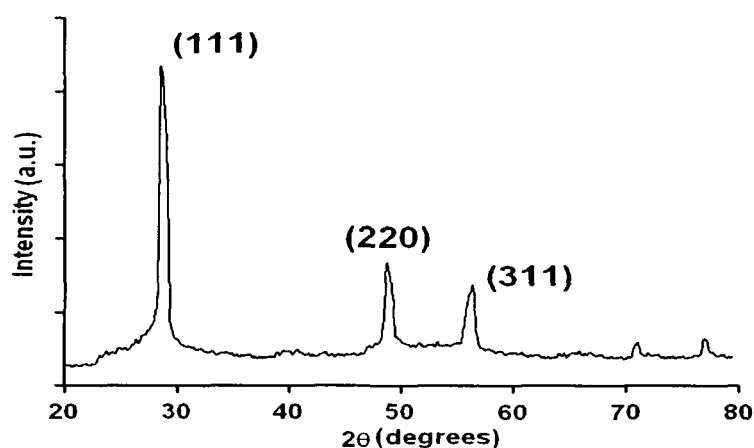
Figure 3.7: XRD pattern of ZnS nanorods in CTAB

as in Figure 3.6 and can also be indexed as that of Cubic structure in agreement withe JCPDS Card 5-0566. The prominent peaks corresponding to (111), (220), (311) reflections to ZnS were observed and found shifted slightly compare to ZnO nanoparticles. The lattice parameter for the ZnO nanorods was found as a = 5.325Å. However, the materials exhibited cubic structure with preferential orientation in the direction of (111), as reveled from the XRD pattern.

(b) Optical absorption spectroscopy

(i) ZnS nanoparticles

The absorption spectrums of the polymer (PVOH) encapsulated ZnS nanoparticles and CTAB based ZnS nanoparticles are shown in Figure 3.8. In curve (a), the single excitonic peak was observable at ~276 nm owing to 1s-1s transition states of ZnS in PVOH. For the CTAB based ZnS nanoparticles,
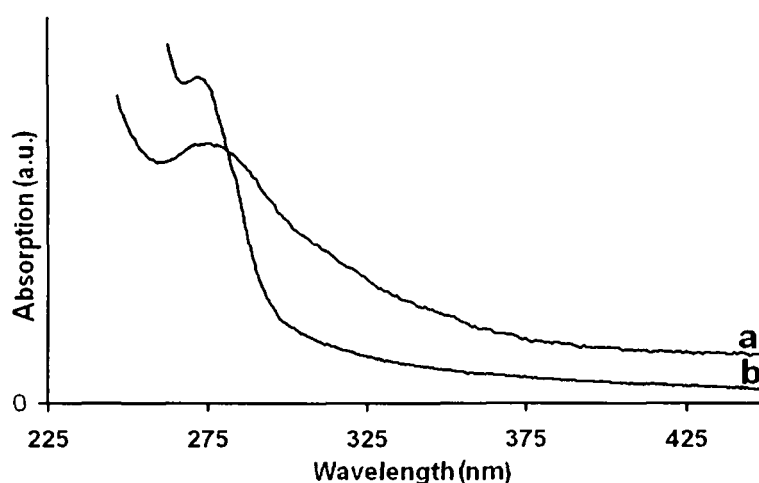
Figure 3.8 : UV-Vis spectra of ZnS nanoparticles in (a) PVOH (b) CTAB

this excitonic peak was found at ~270 nm (Fig. 3.8b). The narrow tailing in the OAS of ZnS in CTAB than in PVOH ensures lower degree of inhomogeneity in (b) than in (a). For CTAB based ZnS, the excitonic peak is sharper which indicates better development of uniform sized nanoparticles compared to PVOH encapsulated ZnS nanoparticles. Both spectra signify the formation of nanostructures as they were found shifted compare to its bulk absorption peak of ZnS (~340nm).

(ii) ZnS nanorods

The UV-Vis absorption spectra of CTAB based ZnS nanorods is shown in Figure 3.9. The spectrum is characterized by an excitonic absorption peak at ~330 nm. However, the long-tailing suggests incomplete growth of nanorod, or/and presence of substantial inhomogeneity in the sample.
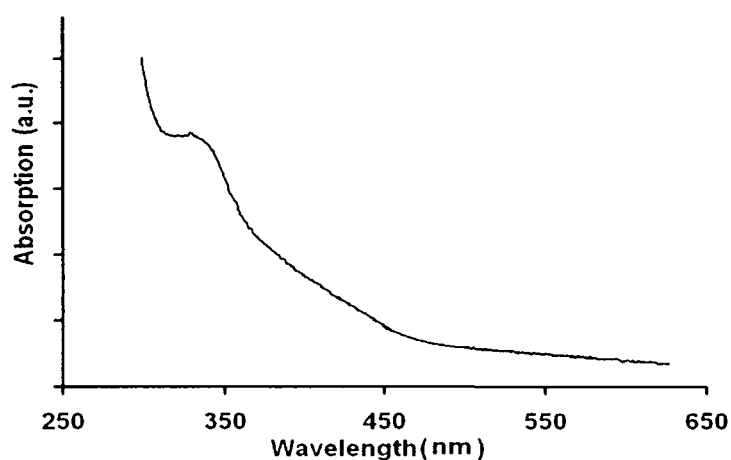
Figure 3.9 : UV-Vis spectra of CTAB based ZnS nanorods

(c) Fourier Transform Infrared Spectroscopy (FTIR)

The existence of polymer and its influence on ZnS nanoparticle system are studied using fourier transform infrared spectroscopy (FTIR). Figure 3.10 shows, the FTIR spectra of PVOH (curve a) and PVOH encapsulated ZnS nanoparticles. Here, in the curve 'a' the absoption peak of –OH group of PVOH located at 3319 cm^{-1} while in cruve 'b' this peak is shifted to 3309 cm^{-1} due to interaction hetween the -OH group and ZnS nanoparticles. Again, the metal sulfide vibrations ~ 500 cm^{-1} is another indication of present of ZnS in the PVOH matrix.
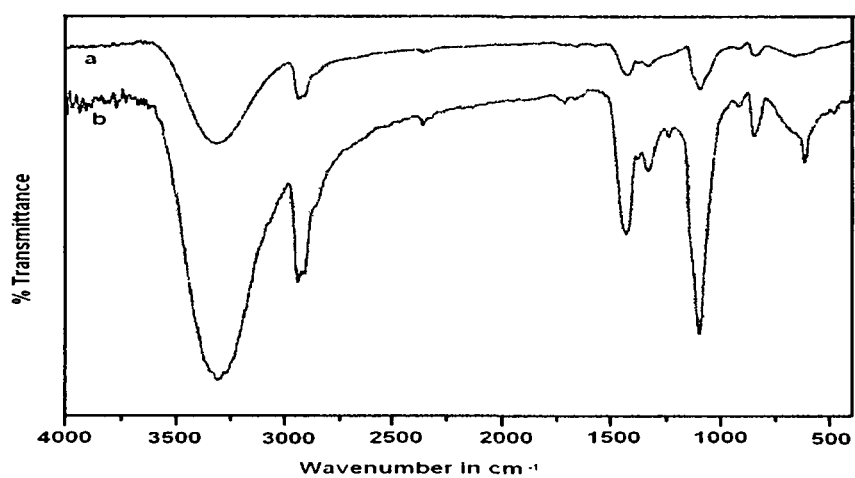
Figure 3.10: FTIR spectra (a) PVOH (b) ZnS in PVOH

(d) Electron Microscopy study

(i) ZnS nanoparticles

The TEM micrograph of the PVOH encapsulated and CTAB based ZnS nanoparticles, gives the visual evidence on the formation of nanoparticles It revals the exact particle size as well as nanoparticle distribution in the samples The ZnS nanoparticles in PVOH were found in the form of several clusters with average size ~10 nm while for CTAB based ZnS nanoparticles, the average size was ~15nm The particles are of uniform size and distributed in isolation for each other
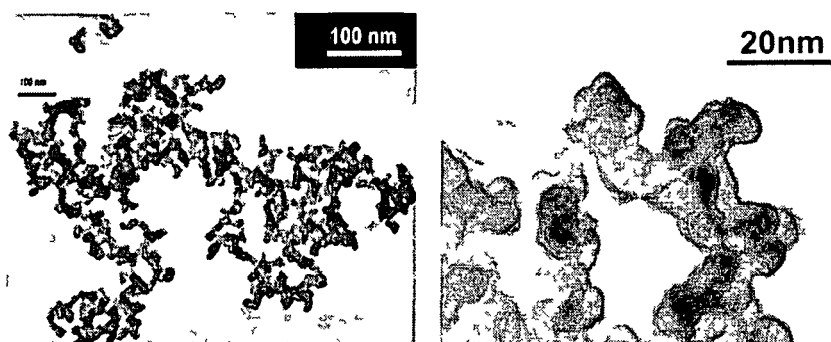
Figure 3.11: TEM images of ZnS nanostructures in PVOH at
(a) lower magnification (b) higher magnification
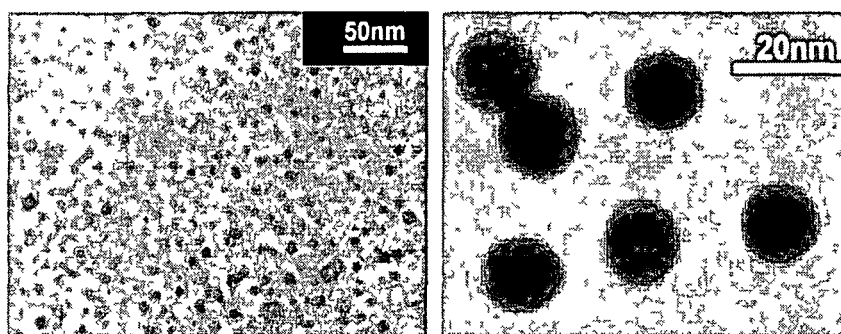
Figure 3.12: TEM images of ZnS nanostructures in CTAB at
(a) lower magnification (b) higher magnification

(ii) ZnS nanorods

The TEM images confirm the formation of ZnS nanorods in CTAB of diameter around 20 nm and of length 60-100 nm (Fig. 3.13). The ZnS nanorods are having uniform diameter of varied length .
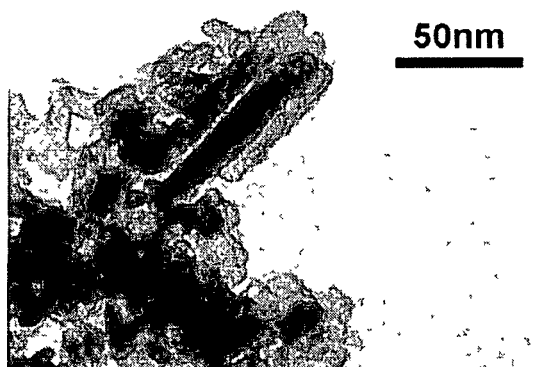
Figure 3.13 : TEM image of ZnS nanorods in CTAB

3.3.2 ZnO nanostructures

(a) X-ray diffraction study

(i) ZnO nanoparticles
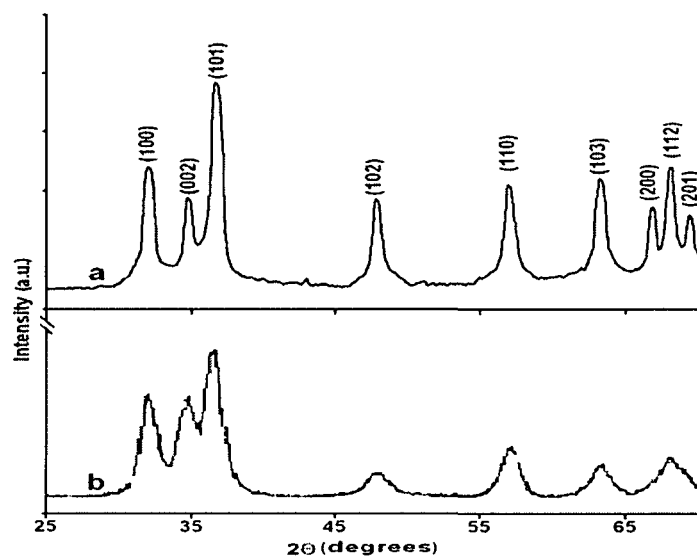
Figure 3.14 : XRD pattern of ZnO nanoparticles (a) PVOH , and (b)CTAB

The phase and purity of the prepared ZnO nanoparticles were determined by X-ray powder diffraction (XRD) patterns which are presented in Figure 3.14. Both ZnO in PVOH and CTAB show prominent diffraction peaks and can be perfectly indexed to the ZnO hexagonal wurzite structure. The ZnO lattice constants obtained by refinement of the XRD data, which are consistent with these of bulk ZnO (JCPDS card No.36-145). The average particle sizes are calculated from Debye-Scherrer formula: for the ZnO nanoparticles in PVOH it is ~35 nm where as for CTAB based nanoparticles, the average particle size it as ~15 nm. Again, the lattice parameter for ZnO nanoparticles in PVOH was a = 3.221Å, c = 5.197Å while in CTAB, a = 3.182Å, c = 5.085Å.

(ii) ZnO nanorods

The XRD pattern of ZnO nanorods in CTAB is similar to that of ZnO nanoparticles and suggesting the formation of hexagonal wurtzite structure in agreement with JCPDS card No.36-145.
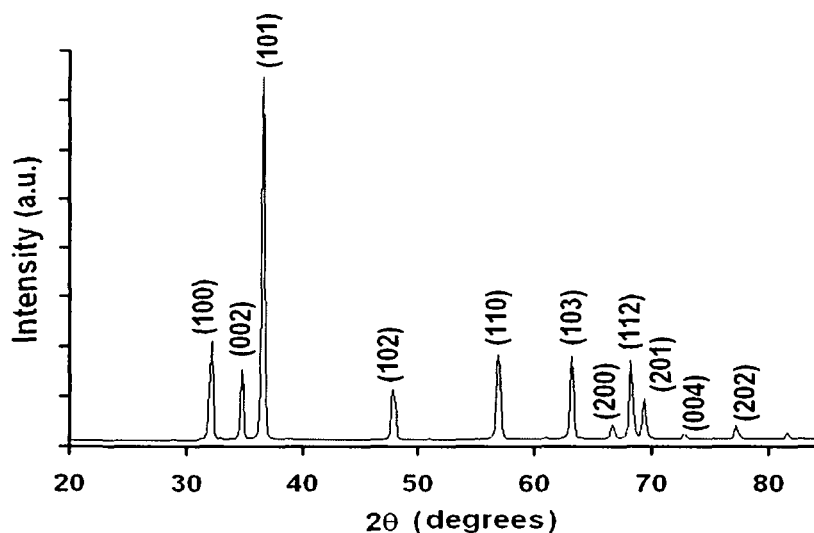
Figure 3.15 : XRD pattern of ZnO nanorods

(b) Optical absorption spectroscopy study

(i) ZnO nanoparticles
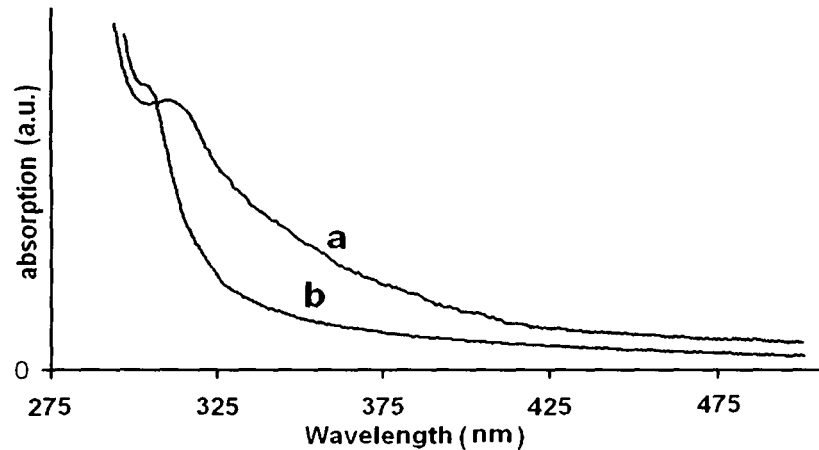
Figure 3.16 : UV-Vis Spectra of ZnO nanoparticles in (a) PVOH, and (b) CTAB

The absorption spectrums of the polymer (PVOH) encapsulated ZnO nanoparticles and CTAB based ZnO nanoparticles are shown in Figure 3.16. In curve a, the single excitonic absorption peak was ~320 nm owing to $1s$-$1s$ transition states in the ZnO in PVOH. Again, for the CTAB based ZnS nanoparticles this excitonic peak was found at 310 nm. The narrow tailing in the OAS of ZnS in PVOH ensures lower degree of inhomogeneity. But for CTAB based ZnO, the excitonic peak is sharper which indicates the development of uniform size distribution of nanoparticles compare to PVOH encapsulated ZnO nanoparticles

(ii) ZnO nanorods

The OAS of ZnO nanorod is shown in the Figure 3.17. The excitonic peak in the spectrum is at ~ 350nm due to HOMO to LUMO transition ($1s$ to $1s$ transition). The prominent and sharp absorption peak found shifted compare to bulk ZnO which is a significance of formation of some low dimensional structures. The low bordering of the absorption peak suggest a kind of uniformity in the nanorods.
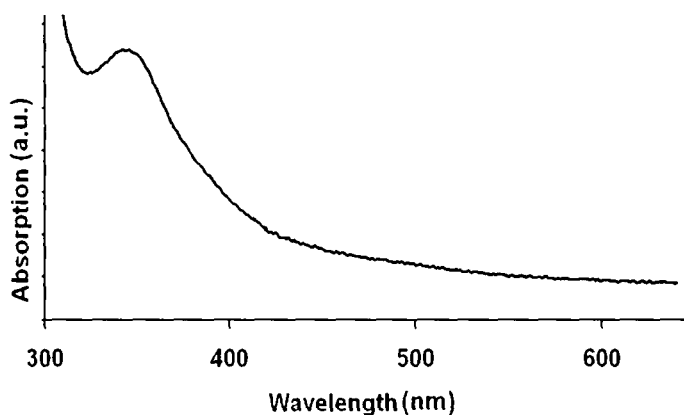
Figure 3.17 : UV-Vis spectra of ZnO nanorods

(c) Fourier Transform Infrared spectroscopy study

In the FTIR spectrum (Figure 3.18) of PVOH (curve a) and ZnO embedded PVOH (curve b), shifting absorption peak due to –OH was observed in the ZnO is embedded in the PVOH matrix compare to the other. This is due to the interaction between –OH group and ZnO nanoparticles. Again, absorption peaks around $\sim 500cm^{-1}$ is due to metal oxide vibrations is indicating the present of ZnO in the PVOH matrix.
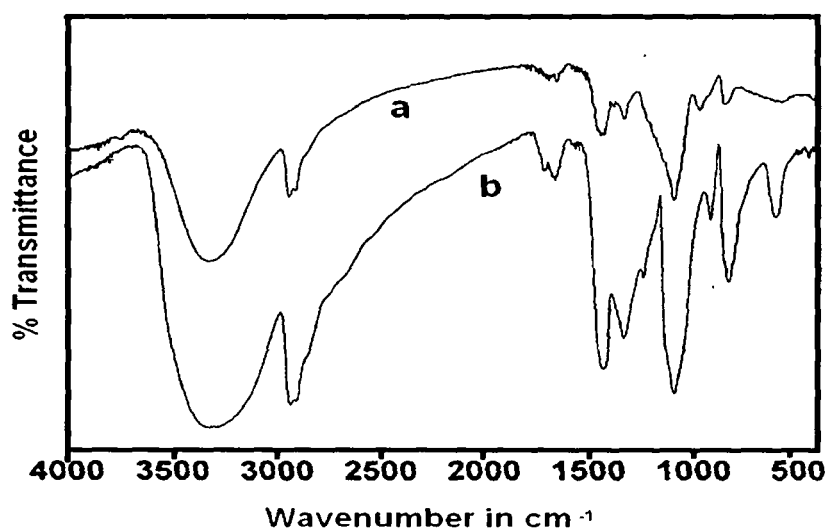
Figure 3.18 : FTIR spectra of (a) PVOH (b) ZnO nanoparticles in PVOH

(d) Electron Microscopy study

(i) ZnO nanoparticles :

The ZnO nanoparticles in PVOH and CTAB are confirmed from the TEM micrograph of the samples The PVOH encapsulated ZnO nanoparticles are found to be irregular shaped and not well separated (Figure 3 19) The average size of the nanoparticles, in this case, varies from 10 nm to 30 nm However, CTAB based ZnO nanoparticles are found to be spherical and well separated (Figure 3 20) An isolated spherical ZnO nanoparticles is shown in the Figure 3 20 B, where a thin CTAB coating around the nanoparticle is witnessed
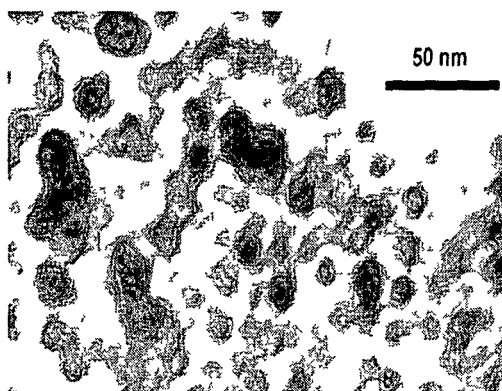
Figure 3.19: TEM image of ZnO nanoparticles in PVOH matrix
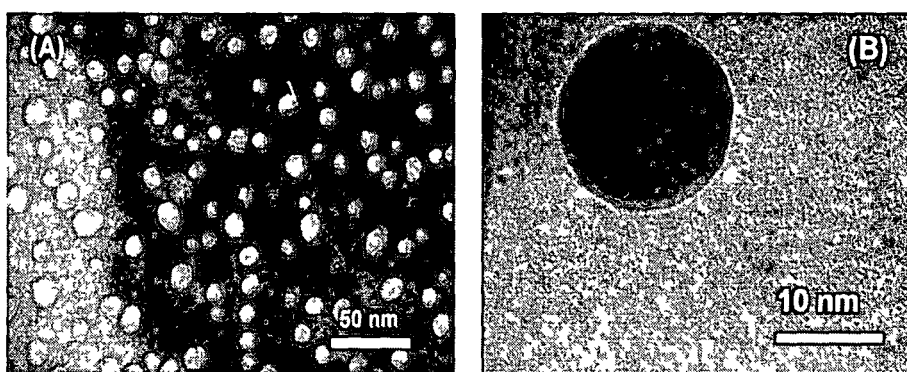
Figure 3.20 : TEM image of ZnO nanoparticles in CTAB
(A) distributed system, and (B) isolated system

(ii) ZnO nanorods

A clear evidence on the formation of elongated ZnO nanostructures is being depicted in Figure 3.21. The nanorods have typical average length 70-120 nm and dia 20-30 nm. Interestingly, we notice that the nanorod have deviated from the ideal solid cylindrical shape. In other words, two extreme ends, resembles commercial ball-pen like structures. Since the hydroxides are decomposed by a strong heat of reaction to produce oxides in the reaction process, organization and assimilation of particles would be slow during initiation and termination
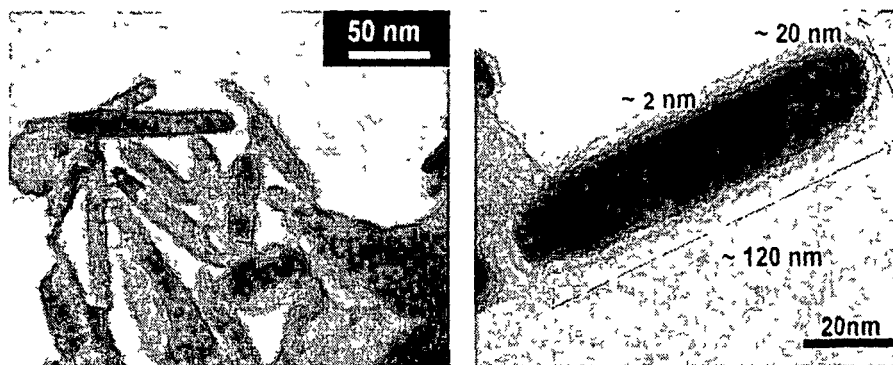
Figure 3.21 : TEM image of ZnO nanorod (A) distributed system,
and (B) isolated system

while forming ZnO nanorods. In reference to the mechanism of growth process first Zn(OH)$_2$ was developed due to compositional mixing facilitated by solid state reaction and finally, ZnO is produced due to gradual decomposition owing to strong heat reaction. A highly magnified image of single nanorod with diameter 20 nm and length 120 nm is shown in figure 3.21(b). The CTAB coating layer of around 2 nm is clearly observed around nanorods which help in protecting nanorods from agglomeration.

Chapter 4

Organization and modification of II-VI semiconductor nanostructures

We have elaborated the development of ZnO and ZnS nanostructures in chapter 3. It is very much necessary to consider the modification in the structural and optoelectronic properties of nanostructures. This can be achieved by selective organization and modification with regard to structural aspects. In this chapter, we stress upon the conditions required for transforming spherical to elongated nanostructures in ZnS and ZnO systems. The spherically symmetric nanoparticles can be changed transformed to asymmetric elongated nanorods by modifying the synthesis process or/and parameters. Also we have employed ion irradiation and photon illumination for such purpose.

4.1 Organization and modification through chemical route

One way of developing elongated nanostructures is the growth mechanism of itself. This has become possible by controlling different macroscopic parameters and concentration of the reactants used in the synthesis process. As a result, materials can be grown along definite direction forming elongated nanostructures. We have already discussed the development of spherically symmetric ZnO nanoparticles of ~20nm and elongated ZnO nanorods having dia ~20 nm and length ~100nm obtained through the physico- chemical synthesis process discussed in the Chapter 3 (section 3.2.2). Using the same physico-chemical (solid state reaction) technique, we can produce nanorods of different lengths by varying the molar ratio of the reactants viz. cetyl-trimethyl ammonium bromide (CTAB) [C_{19} H_{42} BrN], zinc acetate dihydrate (ZAD) [Zn (CH_3 COO)$_2$.2H$_2$O], and sodium hydroxide flakes. For this purpose, we have considered four different molar ratios - 1:0.6:3, 1:0.5: 2.6, 1:0.4:2.2 and 1:0.3:1.8 for preparing four different kinds of samples Z0, Z1, Z2 and Z3 respectively. Each of the mixture was ground independently in a mortar for 1-2 hours. It was expected that the orientational
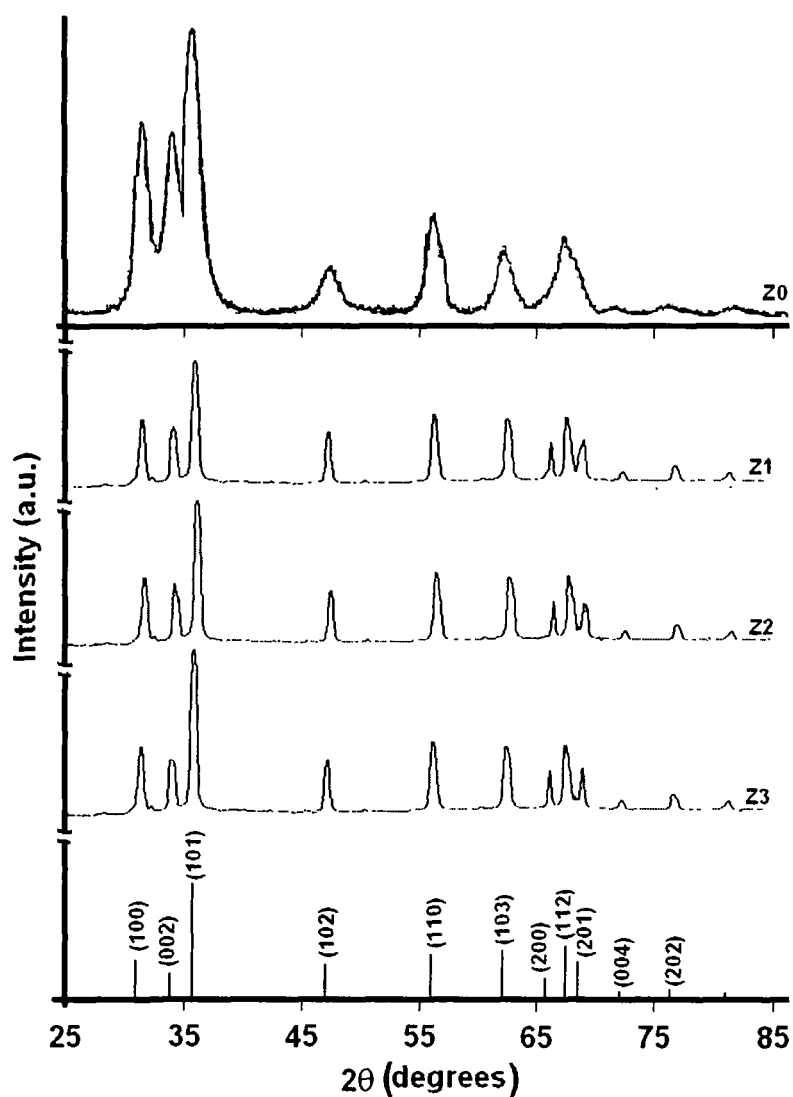
Figure 4.1 : XRD patterns of ZnO nanoparticles (Z0) and nanorods (Z1, Z2, Z3)

grinding would result in the spontaneous decomposition of ZAD to $Zn(OH)_2$ and finally to ZnO [details reaction mechanism is explained in section 3.2.2d). Next, the mixture was transferred to a culture-tube containing double distilled water followed by ultrasonication for 1 h. The sonicated precursor was then subjected to repeated washing. In order to induce effective oxidation of the unreacted species, the mixture

was annealed at a temperature of 60-80°C for 2 h. The annealing process would remove the unwanted carbon products facilitating complete oxidation. The final products were preserved for subsequent experimentation and characterization. The structural phase and crystallographic orientation of the as-grown ZnO samples (Z0, Z1, Z2 and Z3) were identified by XRD measurements recorded by a Rigaku Miniflex diffractometer employing $Cu-K_\alpha$ radiation (1.54 Å) with a scanning rate of 0.02 deg/s. The diffraction patterns of sample Z0, Z1, Z2 and Z3 as shown in figure 4.1, suggest that the as-grown ZnO specimens are polycrystalline in nature with wurtzite phase. The strongest diffraction peak at ~35.5° implied that the nanostructures were grown with a preferred orientation along (101) plane. Note that, the diffractograms are characterized by two important features as one makes a transition from Z0 to Z3. Firstly, there is an increase in intensity of (101) peak relative to other peaks. In addition, the gradual suppression of the line broadening (full width at half maxima (FWHM)) of (101) and (002) peaks are noticed as one moves from Z0 to Z3. Consequently, FWHM of (002) and (101) planes become narrower and sharper for Z1, Z2 and Z3 compared to Z0. The intensity ratio between (101) and (002) peaks for Z0, Z1, Z2 and Z3 samples are found to be 1.42, 1.91, 2.34 and 2.86 respectively. The clear splitting of these peaks (Z1 – Z3) from an overlapped one (Z0) indicates the formation of the elongated nanostructures which is consistent to other reports. Again, no characteristic peak(s) due either to impurities or unreacted species like Zn, CTAB or $Zn(OH)_2$ were observed. The results actually indicate the formation of hydroxyl free, wurtzite ZnO phase. Moreover, the superimposed peaks at ~67° can be extracted back in case of elongated ZnO systems (Figure 4.1). Note that the broadened peak at 2θ ~67° of Z0 specimen splits into three independent peaks namely, (200), (112) and (201) at respective Bragg (2θ angles of 65.8°, 67.2° and 69.1° for Z1, Z2 and Z3. Using Scherrer's formula ($d=0.9\lambda/\beta Cos\theta$, where d is the average crystallite size, 2θ is the diffraction angle, and β is the FWHM), the average crystallite size of ZnO system (Z0) was estimated to be ~12 nm. The crystal lattice parameters for the wurtzite ZnO are a=3.182 Å and c=5.085 Å. For elongated nanostructures (Z1-Z3), the respective parameters are very close having average values a=3.235Å and c=5.189Å. Note that

for bulk ZnO system, a=3.253 Å and c=5.209 Å [330]. Since the c/a ratio (≈ 1.6) is nearly same, the crystal unit cell is expected to be regular hexagon in all of the above
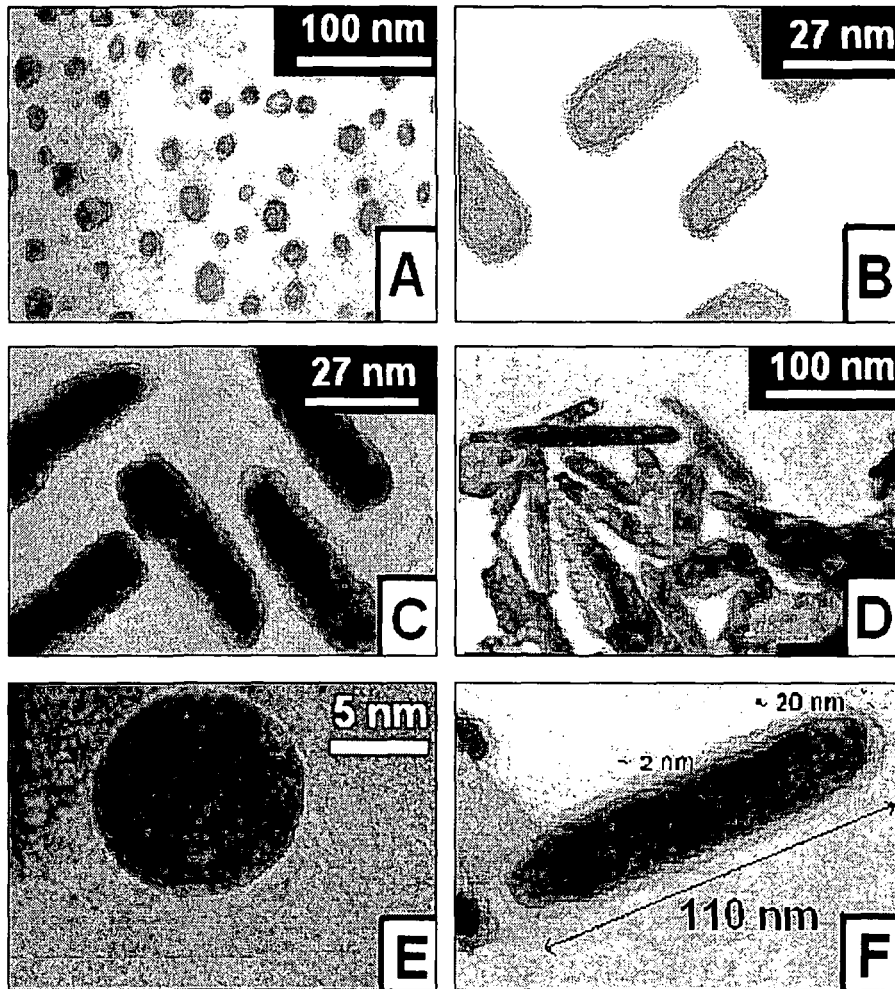
Figure 4.2 : TEM micrographs of the sample (A) *Z0* (1:0.6:3) (B)*Z1* (1:0.5: 2.6) (C)*Z2* (1:0.4:2.2) (D)*Z3* (1:0.3:1.8) (E) isolated nanoparticle from sample Z0, and (F) isolated nanorod from sample Z3

mentioned cases. The visible evidence of the formation of spherically symmetric and elongated ZnO nanostructures (nanoparticles and nanorods) with different aspect ratios are being depicted in figure 4.2. The images are obtained by employing a JEOL JSM-100 CX Microscope working at a beam accelerating voltage of 80 KV. The micrographs reveal homogeneous distribution of the nanostructures. As shown in
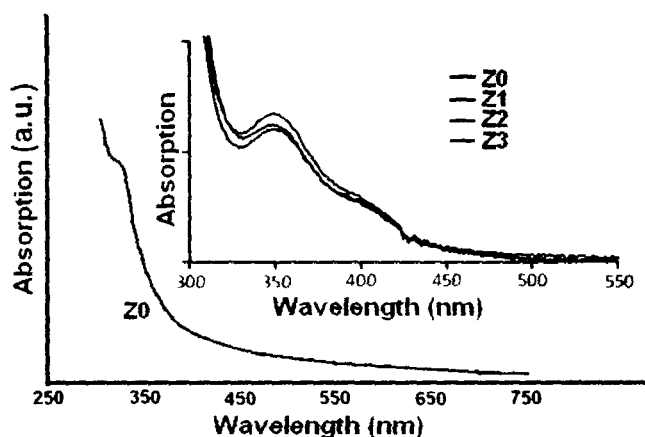
Figure 4.3 : UV-Vis absorption spectra of ZnO nanoparticles and nanorods

It is worth mentioning here that the elongated structures resemble ball point pen like structure instead of regular solid cylinders. As the hydroxides are decomposed by a strong heat of reaction to produce oxides in the reaction process, organization and assimilation of particles would be slow during initiation and termination. As a result, the diameter of the two extreme ends will be relatively smaller as compared to the middle part of the nanorods. The aspect ratio (length-to-dia dimension) is found to be improved as one goes from Z0 system to Z3 one with a maximum value of ~5 for the later case. The typical length and dia of the nanorods for Z3 specimen are ~100 nm and 20 nm; respectively. A close look on the independent nanostructures has revealed that each of the particle or rod is coated with a thin layer of surfactant. Most likely, the agglomeration is prevented by the surfactant capping. A spherically symmetric particle (from sample Z0) and an isolated nanorod (from sample Z3) are shown in figure 4.2(E) and 4.2(F). The approximate thickness of the surfactant layer is about 2nm. We have also realized that larger surfactant-to-ZAD concentration ratio leads to longer nanorods with higher aspect ratio. Nevertheless, one cannot go on increasing indefinitely the stochiometric proportion of the surfactant which could hinder proper solid state mixing. In addition, removable of untreated surfactant becomes a problem even after repeated washing. Therefore, one need to look for a good recipe in order to

thickness of the surfactant layer is about 2nm. We have also realized that larger surfactant-to-ZAD concentration ratio leads to longer nanorods with higher aspect ratio. Nevertheless, one cannot go on increasing indefinitely the stochiometric proportion of the surfactant which could hinder proper solid state mixing. In addition, removable of untreated surfactant becomes a problem even after repeated washing. Therefore, one need to look for a good recipe in order to obtain good quality nanorods. Figure 4.3 represents optical absorption spectra (OAS) of nanoparticle and nanorod samples. The optical absorption spectra (OAS) of the samples show a single sharp excitonic absorption peak owing to 1s-1s transition states, which was observable at ~325nm for Z0 and at ~350 nm for Z1, Z2 and Z3. The shifting of exciton absorption peak towards red indicates that the particles have actually grown into bigger size (in our case, growth is unidirectional). We also notice that the absorption spectrum has a relatively long tailing in case of nanoparticles (Z0). However, the elongated system have relatively better onset of absorption with narrow tailing ensuring better homogeneity and uniform size distribution compared to spherical nanoparticles.

4.2 Organization and modification through ion irradiation

Irradiation experiments were initially intended for studying origin and dynamics of the charged particles/ions. etc. Now-a-days, experiments are mainly performed for material modification and the systems include semiconductors insulators, superconductors etc. Ion irradiation is attractive for modification of structural as well as optical properties of the nanostructures. We have used energetic ion irradiation aspects as an alternative approach for nanostructure modification and elongated nanostructure evolution. The energetic ion irradiation results in the growth of the nanoparticles along the ion path and develops elongated nanostructures such as nanorods [331]. The structural phase transformation along the path (known as latent track) is dependent on the nature of the ion species, its energy as well as other physical properties of the target material [332]. The tunablity of electrical, optical and magnetic properties can be achieved with the help of varying ion fluence and energy

projectile range of the ion (calculated from SRIM) exceeds thickness of the sample films. The samples were mounted on a vacuum shielded vertical sliding ladder having four rectangular faces under ultra high vacuum (~10^{-6} torr) in the Materials Science irradiation chamber available at IUAC, New Delhi, India. Different ion beams (silver, titanium and nitrogen) were used at a constant beam current (~1-5pnA) which were made available from 15UD tandem pelletron. In order to expose the whole specimen target area, the beam was scanned vertically over the sample plane.

In the ion irradiation process, the electronic energy loss due to interaction of the projectile ions with the surrounding electronic clouds is responsible for relevant modification of nanostructure. The electronic energy loss and energy deposition to the material at a particular energy depends on the nature of ion used. So, we must choose the ions in such a way that each kind of ion deposit different amounts of energy resulting in a definite modification. We have used Titanium (Ti^{+11}), Silver (Ag^{+6}) and Nitrogen (N^{+4}) ions. All these species have drastically different energy loss profile shown in the in the Figure 4.4. Among them, silver has highest electronic stopping energy (780.1 eV/Å) compared to other two species, Alternatively, nitrogen
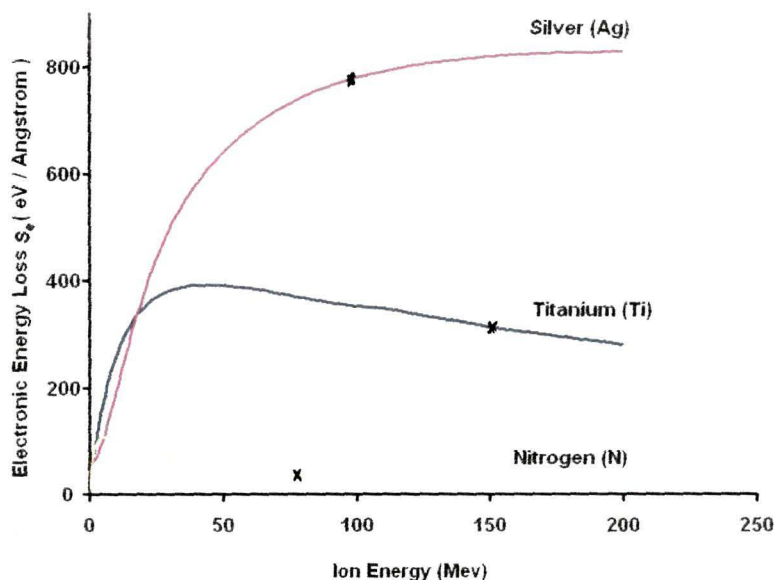
Figure 4.4 : Electronic energy loss vs. energy for Titanium, Silver, and Nitrogen ion

(N) is a light ion, when it passes through the matter, the electronic interaction will be less and the stopping energy is ~35.24 eV/Å. However, titanium (Ti) can deliver moderate amount of energy to the nanostructure materials compare to other two. Expecting elongated nanostructure development, we have irradiated the sample with fluences 1.25×10^{10} ions/cm^2, 5.00×10^{10} ions/cm^2, 2.0×10^{11} ions/cm^2 and 8.0×10^{11} ions/cm^2. The fluence (φ) of irradiation process is maintained through duration of irradiation (t) using the equation -

$$Fluence\ (\phi) = \frac{Time\ (t) \times Beam\ Current \times pnA}{Charge\ State} \tag{3.1}$$

Where,

$$1\ pnA\ (particle\ nano\ ampere)$$
$$= \frac{10^{-9} Coul / \sec}{1.6 x 10^{-19} Coul} \tag{3.2}$$
$$= 6.25 x 10^{9}\ particles / \sec$$

During irradiation, in order to get uniform modification throughout the film the ion beam should not diverge significantly. Therefore, it is necessary that the projectile range of the ion beam must be very high and the electronic energy loss of the ion should be nearly equal along the path of the ion (ion track). We choose the energy of the ion beams at a point where the electronic energy loss curve is flat and the projectile range is high (Figure 4.4). The selected ion energy, energy losses, projectile ranges etc corresponding to each ion are listed in table 4.1. Calculated from the SRIM -

Table 4.1 : Ions used for irradiation experiment and their parameter in material

Energy and ion	Electronic Energy loss eV/ Å (S_n)	Nuclear Energy loss eV/ Å (S_n)	Projectile Range (μm)	longitudinal Straggling (μm)	Lateral Straggling (μm)
150-MeV Ti^{+11}	314.7	0.2932	46.70	1.33	0.5963
100-MeV Ag^{+6}	780.1	3.294	23.06	0.6934	0.7111
80-MeV N^{+4}	35.24	0.01965	144.96	5.67	1.19

4.2.1 Titanium (150-MeV) ion irradiation:

We have taken ZnS, ZnS:Cr nanostructures embedded in PVOH matrix which were developed using the synthesis process already discussed in chapter 3. The sample meant for irradiation experiment was in the form of solid films (1cmx1cm). One sample was reserved as virgin to compare with those of irradiated samples. They were irradiated in a high vacuum (1.6×10^{-6} Torr) chamber by 150-MeV Ti^{+11} beams with approximate beam current 1.0 pnA. The beam was scanned vertically over the sample plane and the fluence was varied in the range 10^{10} -10^{12} ions/cm^2 by varying the time of exposure (Table 4.2) .

Table 4.2 : Fluences and corresponding irradiation time of Ti^{+11} ion

Sample code	Fluence (ion/cm^2)	Beam current (pnA)	Charge state	Time of irradiation
F1	1.25×10^{10}			22 sec
F2	5.00×10^{10}	1.0	+11	88 sec
F3	2.0×10^{11}			352 sec= 5 m 52 sec
F4	8.0×10^{11}			1408 sec=23 m 28 sec

The ion beam induced effects were analyzed with the help of X-ray diffraction patterns, electron micrographs and optical absorption spectra. The, structural morphological and optical features are discussed.

Optical absorption spectra (OAS) of unirradiated (virgin) and irradiated ZnS nanostructures are shown in Figure 4.5. For the unirradiated sample, free exciton absorption around ~275 nm was noticed which has blue-shifted from the corresponding bulk value (~340 nm). Further, it was found that the absorption peak
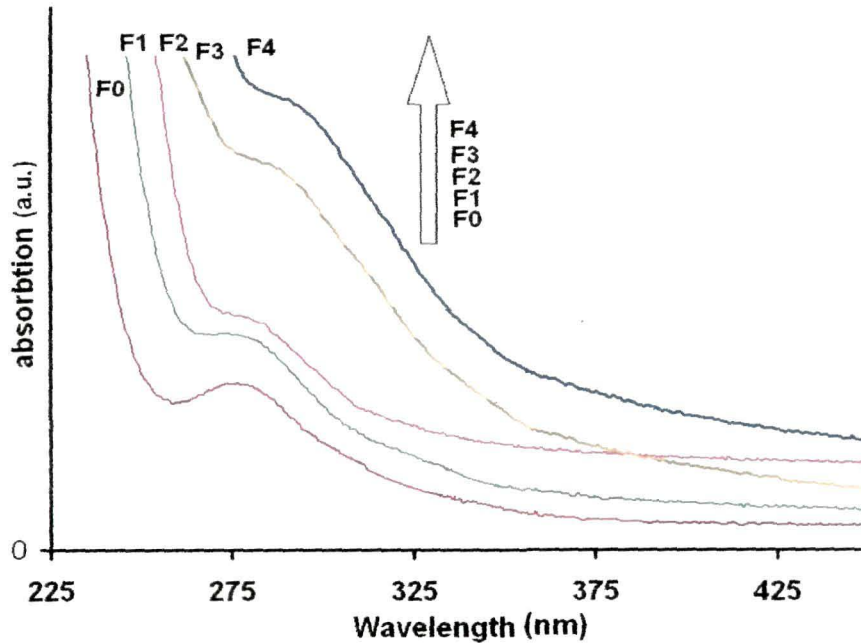
Figure 4.5 : UV-Vis OAS of unirradiated (F0) and irradiated (F1-F4) ZnS nanostructures

has gradually shifted for samples irradiated with higher fluences illustrating the fact that the ion bombardment has lead to substantial nanostructure modification. The excitonic peak becomes broad at the higher fluences. Also, long tailing was observed in case of irradiation with higher fluences. The nanostructures might have grown unevenly at higher fluences. The excessive heat deposition would lead to particle-particle coalesce after destroying the matrix. The rapid solidification of them results in the particle growth. The XRD pattern (Figure 4.6), however, confirms that nanostructures still preserve the crystallinity but they were modified in dimension under irradiation: as line-widths have been varied. But, the cubic structure was preserved after irradiation, for all the cases. In the XRD spectra we note that the FWHM of the peaks increase with the increasing fluences, showing growth of the nanostructures. The transmission electron microscopy (TEM) images provide the best information with regard to visual evidence of the nanostructures and are shown in Figure 4.7. Effectively TEM study suggests the growth of nanoparticles with increasing fluences.
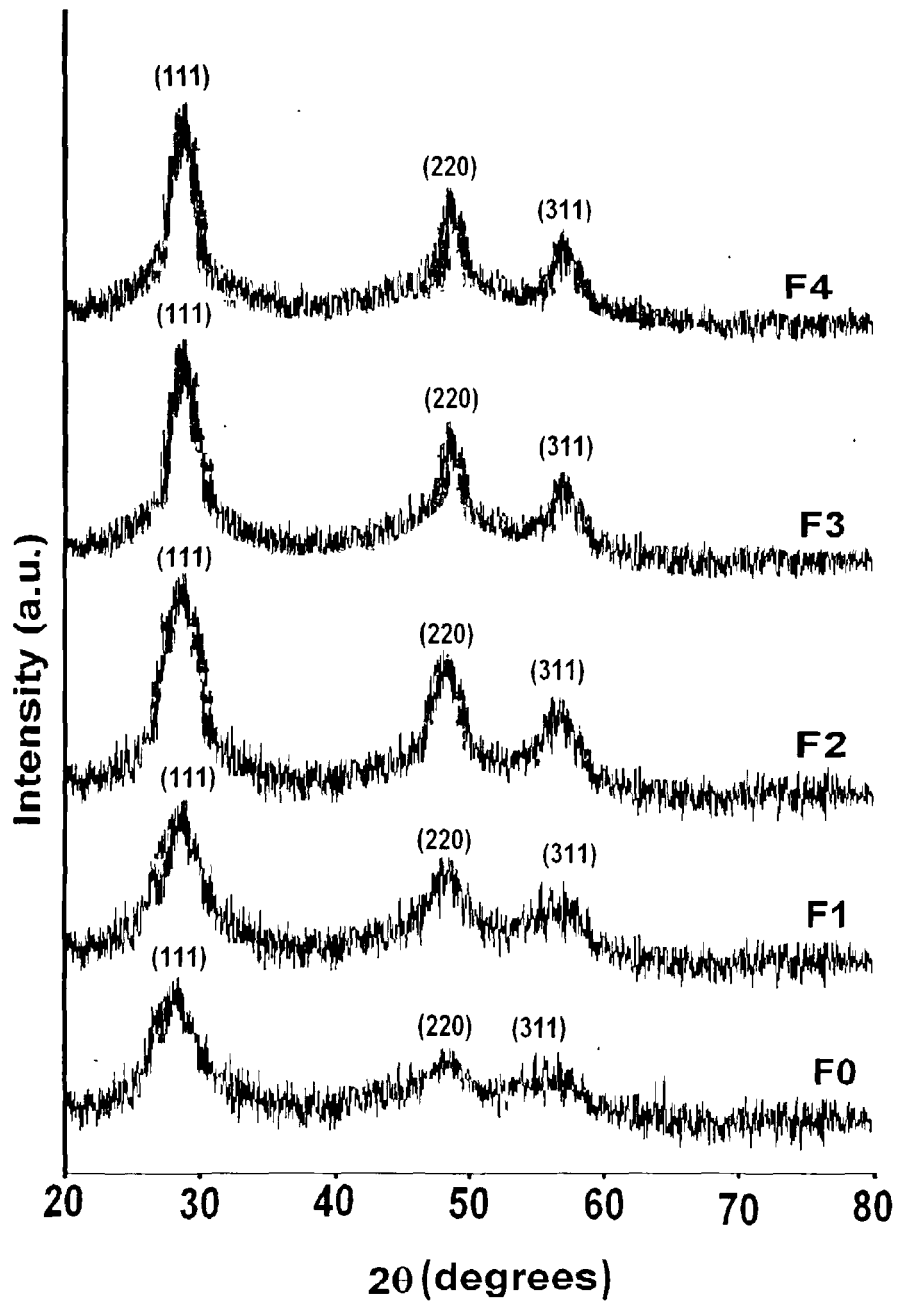
Figure 4.6 : XRD pattern of irradiated and unirradiated ZnS nanostructures
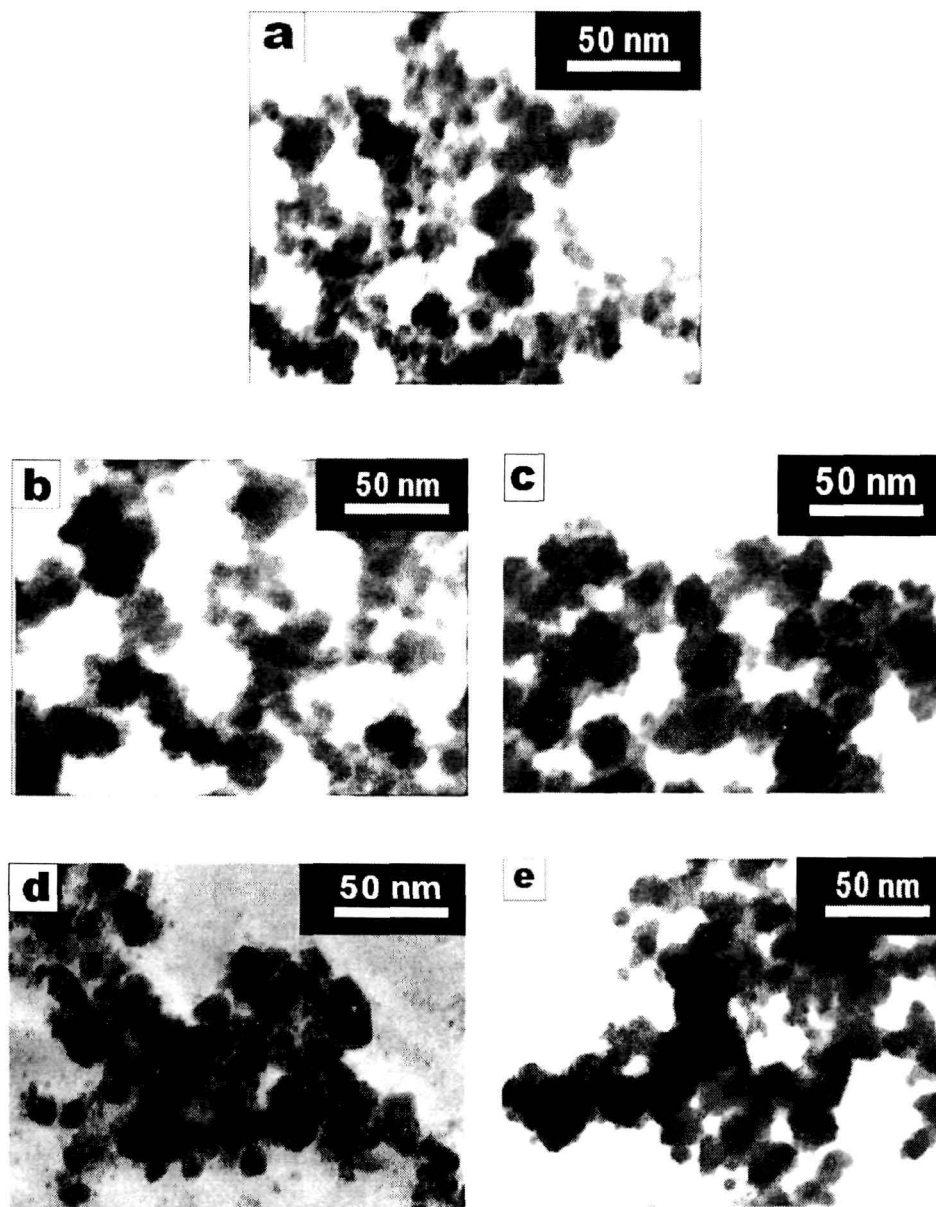
Figure 4.7 : TEM micrographs of (a) unirradiated, and 150-MeV Titantium (Ti^{+11}) ion irradiated ZnS nanostructures at different fluences (b) F 1, (c), F2, (d)F3 and (e) F4
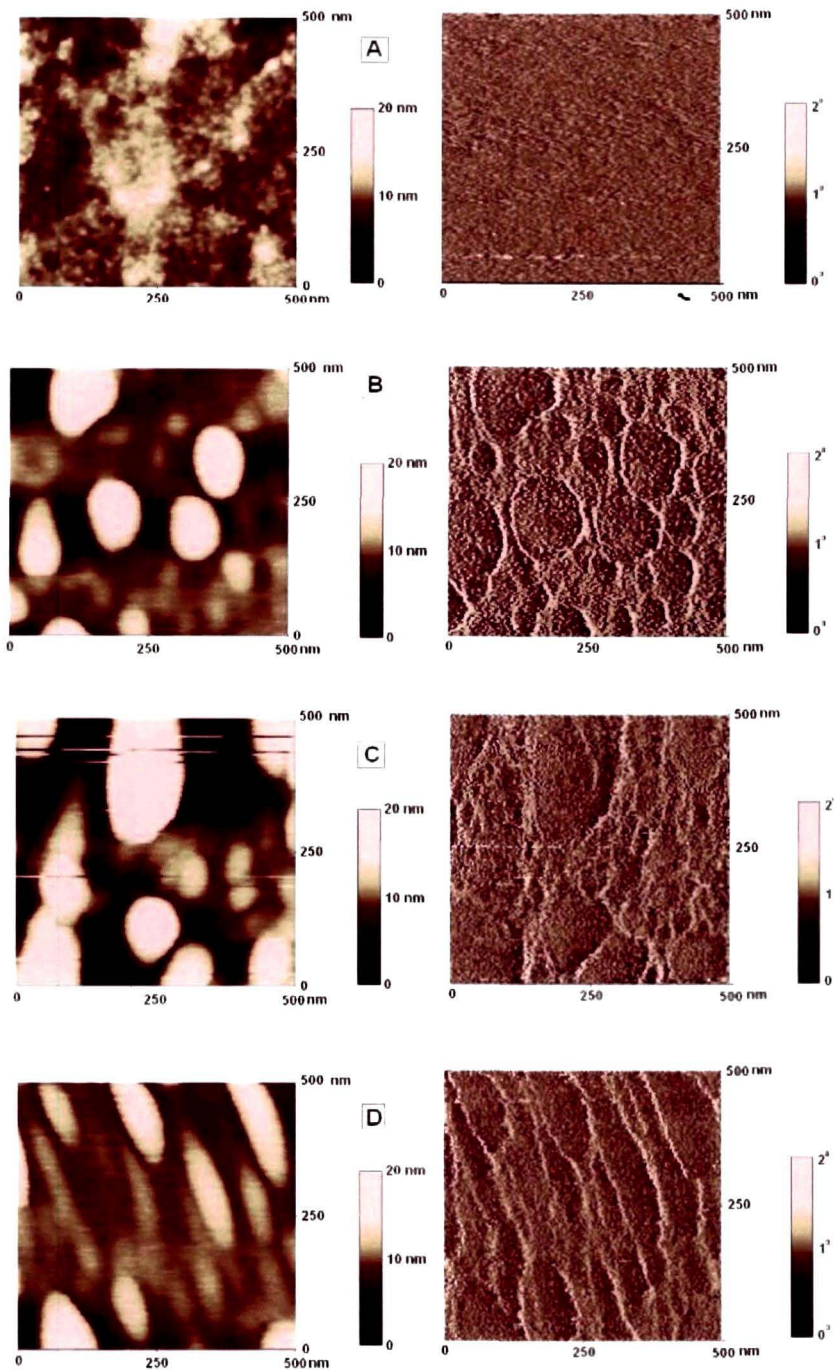
Figure 4.8 : Atomic force microscopy (left) images and Magnetic force Microscopy (right) of a) unirradiated and irradiated b) 5×10^{10}, c) 2×10^{11} d) 8×10^{11}ions/cm^2 ZnS:Cr nanostructures

As the Cr doped ZnS has the ability to show magnetic behavior we perform AFM/MFM along with the XRD, OAS and TEM study. The XRD spectra of irradiated and unirradiated ZnS:Cr (picture not included) show the identical behavior to the undoped ZnS nanostructures. It means, the irradiated Cr doped ZnS nanostructure show the same cubic crystal structure as of undoped ZnS nanostructures and retained its structure upon 150-MeV Ti^{+11} ion irradiations. Under this ion irradiation, the magnetic properties of ZnS:Cr were however, modified as exploited by MFM study, shown in Figure 4.8. The figures are basically phase images of the magnetic impurity (Cr) doped ZnS nanostructures. Figure 4.8 (a) is the phase image of the pristine ZnS:Cr, which does not show appreciable features with regard to magnetic domains owing to matrix encapsulation. The host matrix prevents from detecting magnetic domains by the tip of the MFM. Figure 4.8(b) is the sample irradiated at F2 ($5x10^{11}$ ions/cm^2) where spherical single domains (~30 nm) are visible which correspond to the ZnS:Cr nanoparticles distributed uniformly in the matrix. Irradiation with F3 ($8x10^{11}$ ions/cm^2) leads to distorted domains, as shown in Figure 4.8(c). Surprisingly, sample exposed at F4 ($3.2x10^{12}$ ions/cm^2) results in the aligned magnetic domains normal to ion trajectories. These aligned domains in which elongation upto ~200-250 nm has been observed would find application in magnetic tapes, magnetic recording devices and other spin-based devices.

4.2.2 Silver (100-MeV) ion irradiation

We have also used silver ions to modify the ZnS nanostructures embedded in the matrix. As 100-MeV silver ions have higher value of electronic energy loss (780.1 keV/Å) and they are capable of depositing very high amount of energy into the target materials. Although, Silver is very heavy ion and projectile range is not so large (23.06 μm), it is capable of passing through the films of thickness <1μm in a straight path. For the irradiation experiment, we have used fluences as listed in the table 4.3.

Table 4.3 : Fluences and corresponding irradiation time of Ag^{+6} ion

Sample code	Fluence (ions/cm²)	Beam current (pnA)	Charge state	Time of irradiation
F1	1.25×10^{10}			12 sec
F2	5.00×10^{10}	1.0	+6	48 sec
F3	2.0×10^{11}			192 sec= 3 m 12 sec
F4	8.0×10^{11}			768 sec =12 m 48 sec

Significant red shift of the onset of absorption for ion irradiated ZnS samples was observed in the UV-Vis OAS (Figure 4.9). These results indicated increase of particle size due to nanoparticle growth. Both XRD and TEM also support the growth of the nanoparticles under ion irradiation. The XRD patterns of the unirradiated (pristine) and irradiated ZnS nanostructures embedded in polymer is shown in the Figure 4.10. The diffraction peaks are recorded at $2\theta =$ 28.98°, 48.18° and 56.68° which were corresponding to (1 1 1), (2 2 0) and (3 1 1) crystal planes of ZnS highlighting typical zinc–blend structure. It was

a - unirradiated (F0)
b - 5.0 x 10^{10} ion/cm² (F2)
c - 2.0 x 10^{11} ion/cm² (F3)
d - 8.0 x 10^{11} ion/cm² (F4)
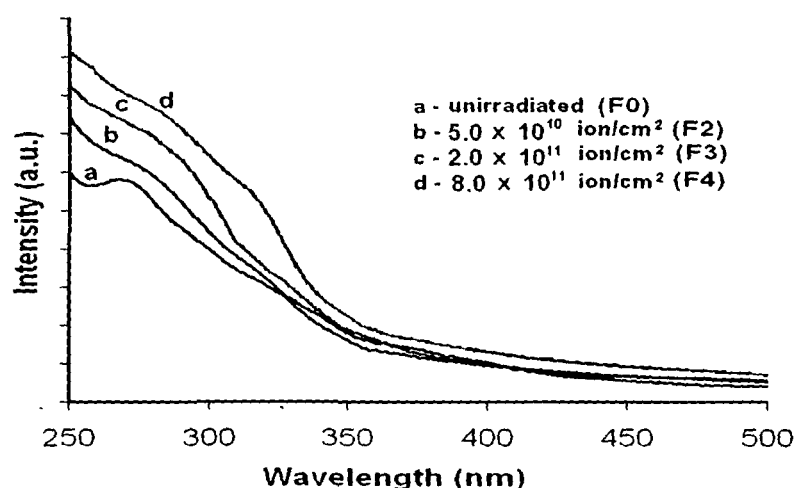
Figure 4.9 : UV-Vis spectra of unirradiated and irradiated ZnS nanostructures

confirmed that crystal structure of the samples remains same irrespective of fluence variation. The peak around $26.4°$ corresponds to the PVOH crystalline phase. With increasing fluence, we have not observed any structural modification except the decrease of the FWHM of the diffraction peaks with increasing fluence. This reduction of FWHM may be attributed to the agglomeration of the nanostructures under ion irradiation. We also observed the sharpness reduction of the XRD peak corresponds to PVOH at $26.4°$ with increasing fluence due to amorphization of the polymer (PVOH). TEM micrograph confirms the growth of nanoparticles with increasing fluence (Figure 4.11).
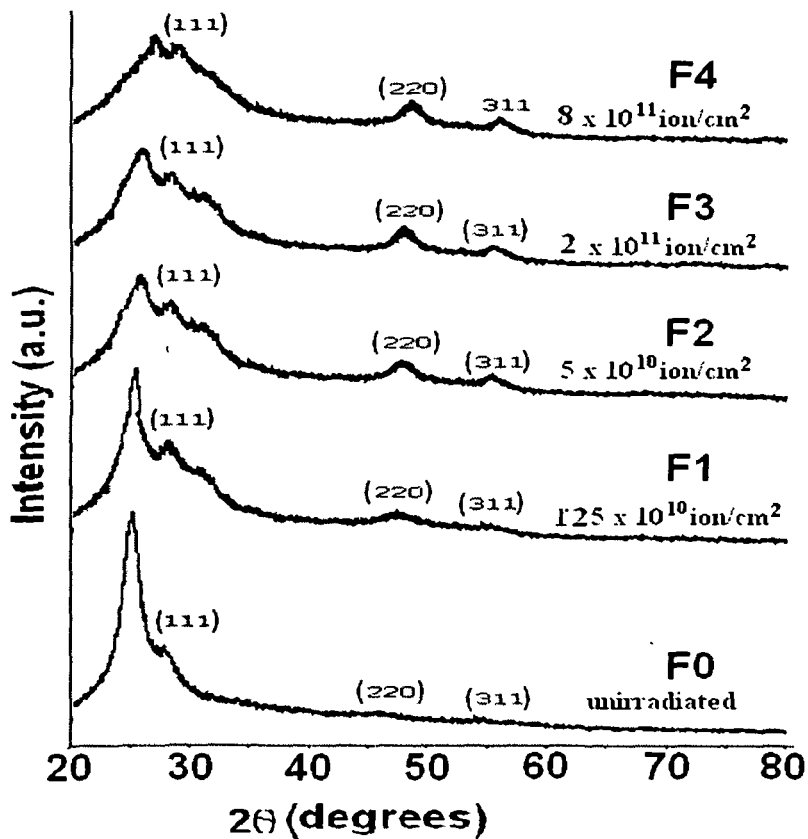
Figure 4.10 : XRD pattern of irradiated and unirradiated ZnS nanoparticles
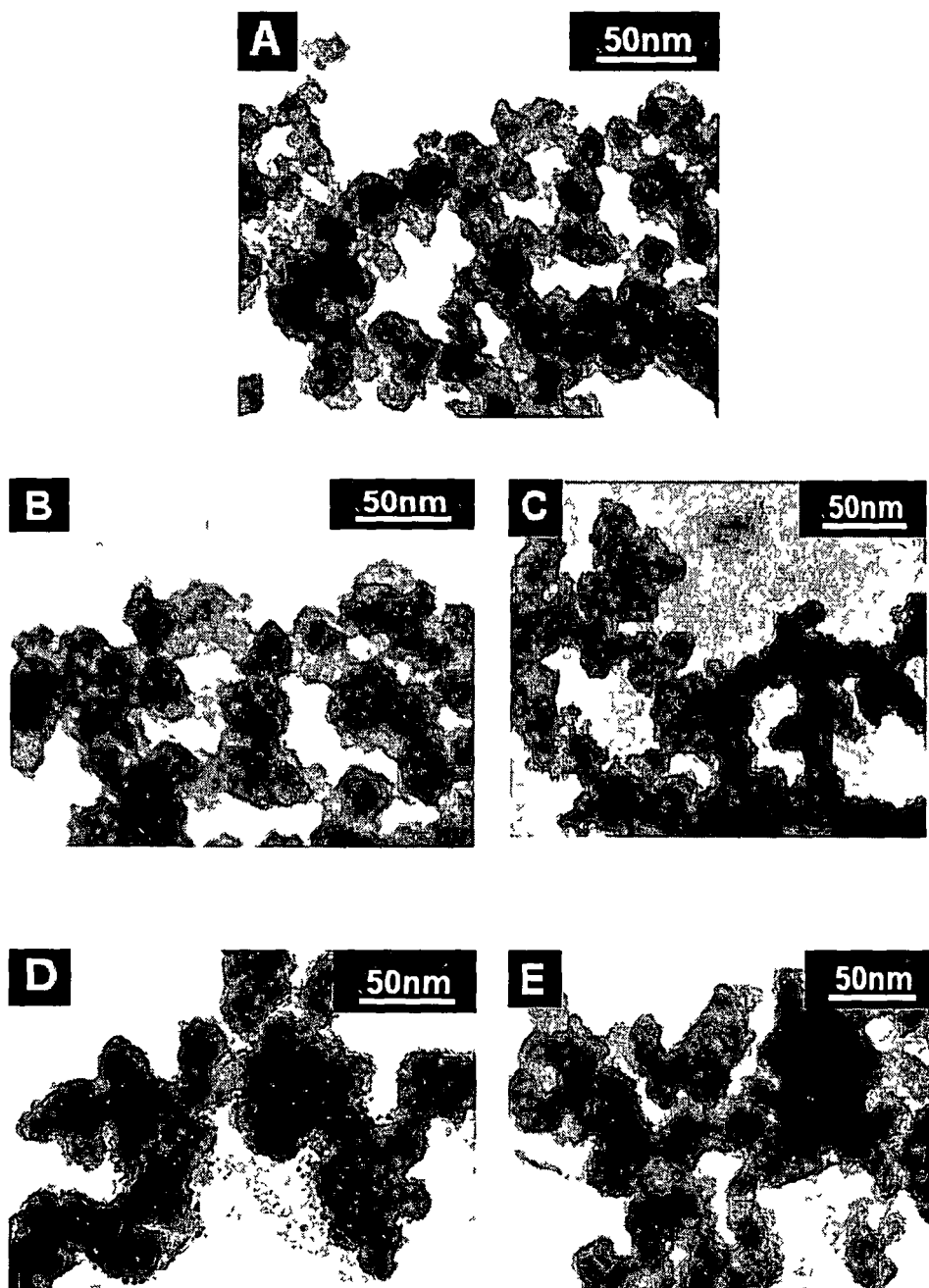
Figure 4. 11 : TEM micrograph of the (A) unirradiated and ion-irradiated ZnS nanoparticle
at fluences (B)F1 (C)F2 (D)F3 (E)F4

4.4.3 Nitrogen (80 MeV) ion irradiation

Finally, we considered 80MeV Nitrogen ion irradiation of PVOH embedded ZnS and CTAB capped ZnO nanostructures. Again, we have also perform irradiation experiment on the Tb doped ZnO nanorod sample. The 1 cm^2 x 1cm^2 films were irradiated with the fluences viz 1.25 x 10^{10} ion/cm^2, 5 x 10^{10} ion/cm^2, 2 x 10^{11} ion/cm^2, 8.0 x 10^{11} ion/cm^2 and 3.2 x 10^{12} ion/cm^2 under ultra high vacuum ($\sim$1.6×10^{-6} torr). During the experiment, the fluences are maintained in the experiment by varying the time of irradiation as derived (Table 4.3). The irradiated ZnS and ZnO samples analyzed separately by UV-Vis OAS, XRD, TEM and atomic force microscope (AFM)

Table 4.3 : Fluences and corresponding irradiation time of N^{+4} ion

Sample code	Fluence (ion/cm^2)	Beam current (pnA)	Charge state	Time of irradiation
F1	1.25 x 10^{10}			8 sec
F2	5.00 x 10^{10}	1.0	+4	32 sec
F3	2.0 x 10^{11}			128 sec= 2 m 8 sec
F4	8.0 x 10^{11}			1408= 8 m 32 sec

Zinc Sulfide (ZnS) nanostructures:

In the UV-Vis absorption spectra (Figure 4.12 of unirradiated and ion irradiated ZnS nanostructure, we have observed appreciable red-shift in absorption edges as one moves from lower to higher values. It suggests therefore, that increase of particle size occurred due to swift ion irradiation. The 1s-1s excitonic peaks for the unirradiated ZnS sample was observed at 278nm gradually shifted to 290 nm for highest fluence (F4).
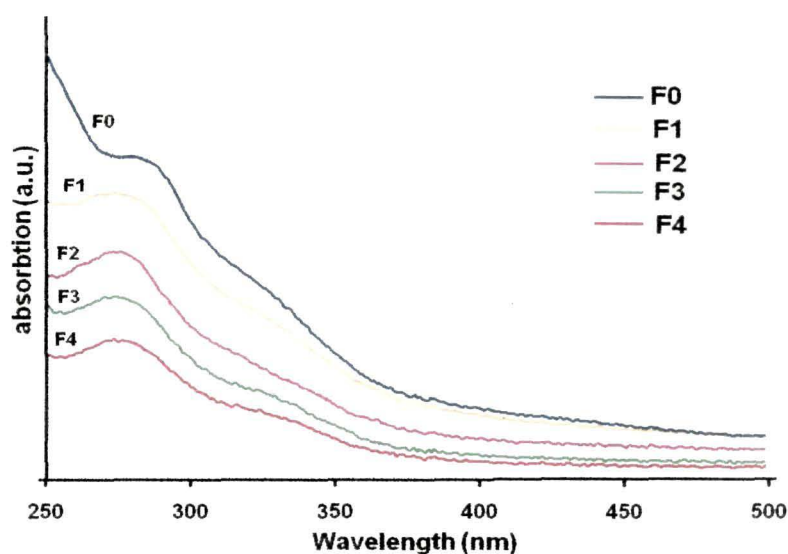
Figure 4.12 : UV-Vis OAS spectra of irradiated and unirradiated ZnS nanoparticles

The XRD patterns (Figure 4.13) depict cubic crystal structure of ZnS systems. The diffraction peaks corresponded to $2\theta = 28.98^0$, 48.18^0 and 56.68^0. The peaks are assigned to (1 1 1), (2 2 0) and (3 1 1) planes of ZnS system and thus exhibiting typical zinc blende structure. The peak around 20.8 corresponds to PVOH crystalline phase [334]. Under irradiation there is no signature of phase transformation of the crystal structure even at the highest fluence. Though the crystal structure remains same, the FWHM of the XRD peaks (upon irradiation) has been gradually reduced with increasing fluence variation. This reduction of FWHM may be attributed to the agglomeration of the nanostructures under ion irradiation. If we compare this agglomeration aspect due to 80-MeV N^{+4} ions with the XRD results (Figure 4.6, Figure 4.10) due to previous two ions (Ag and Ti), it can be suggested that the nature of growth of nanoparticles is substantially low in case of use of N ions. It is due to the low energy deposition to the nanoparticle system. The reduction of sharpness of the XRD peak corresponding PVOH at ~20.8^0 with increase in ion fluence, also supports amorphization of PVOH and recovery of nanostructures from the matrix encapsulation.

The visible evidence that supports ZnS nanostructure modification is shown in a series of TEM micrographs (Figure 4.14). With the increase in fluence (F1-F4), the growth of nanoparticles is observed, like Ti and Ag ion irradiation cases. Qualitatively, for lower electronic energy loss, modification is not significant as compared to that of Ti or Ag ion irradiation. In the previous cases, at highest fluence (F4=8x10^{11} ions/cm^2) the existence of single nanoparticles are rarely found and size has crossed 100 nm, but here, isolated nanoparticles have size less than 100nm. This is due to low energy deposition to the system in the Nitrogen ion irradiation compare to Titanium and silver.
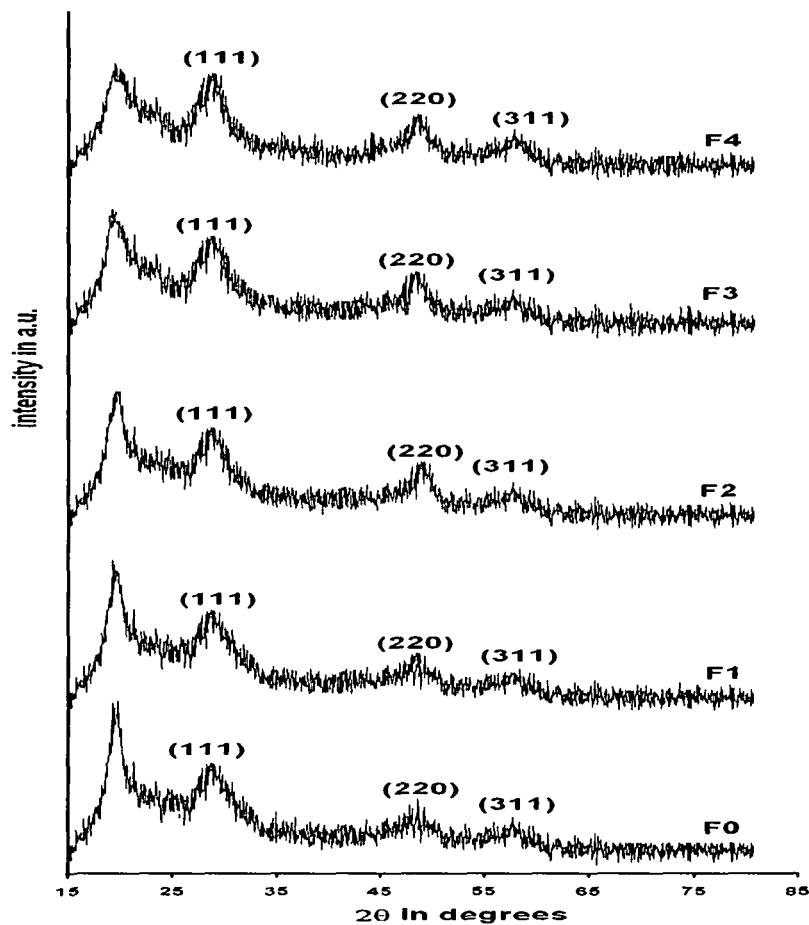
Figure 4.13 : XRD pattern of 80 MeV N^{+4} ion irradiated at fluences (F0-F4) and unirradiated ZnS nanoparticles
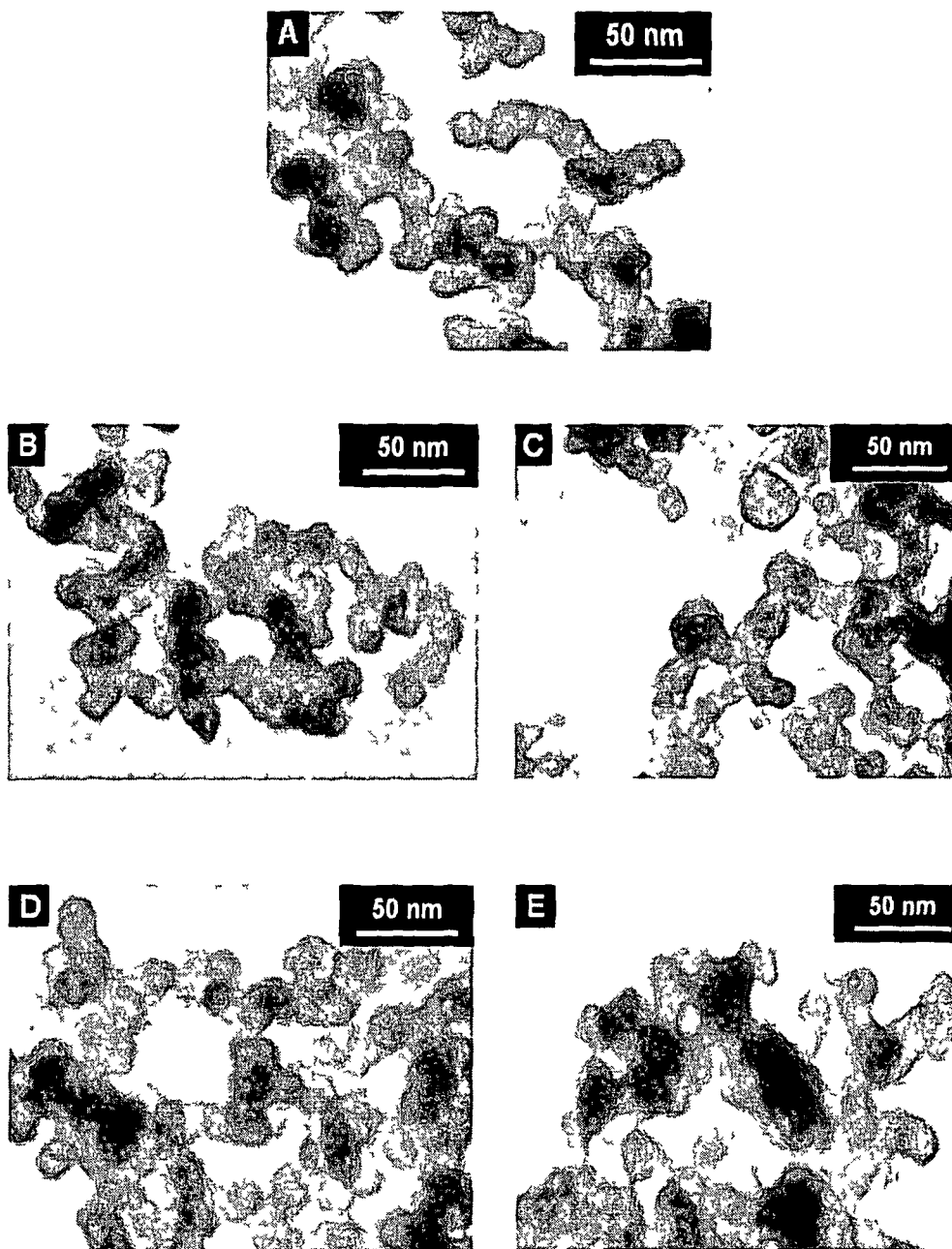
Figure 4. 14   TEM micrograph of 80·MeV N^{+4} ion irradiated ZnS nanoparticles at fluences
(A)F0 (B)F1 (C)F2 (D)F3 (E)F4

Zinc Oxide (ZnO) nanostructures:

In the UV-Vis OAS spectra (Figure 4.15) of the zinc oxide (ZnO) nanoparticles we have observed the excitonic absorption peak at ~320nm and it is found to be shifted with increasing fluence. The red shift of this absorption peak was observed as in the previous cases and suggests the fluence dependent particle size enhancement. However, the excitonic peak was also found to get broadened as we increase the ion fluence which is the signature of increased inhomogeneity with ion fluence variation.
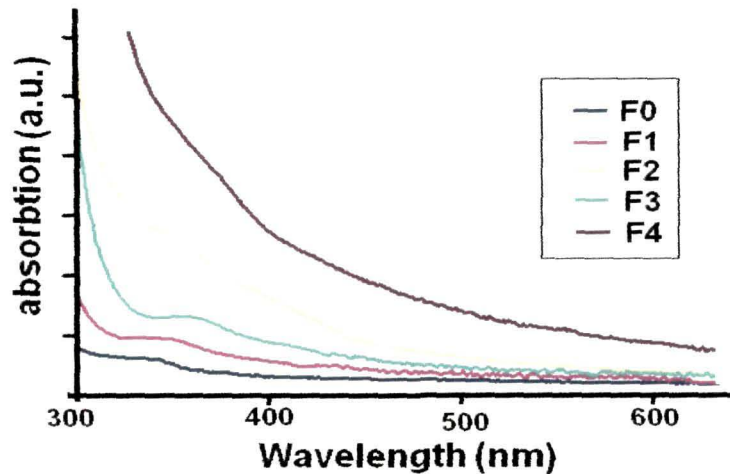
Figure 4.15 : UV-Vis spectra of unirradiated (F0) and 80 MeV N^{+4} ion irradiated (F1-F4) ZnO nanoparticles

The structural phase and crystallographic orientation of the unirradiated and irradiated samples were identified in the XRD pattern shown in the figure 4.16. The XRD pattern clearly represents the polycrystalline nature and wurtzite phase of the samples. No transformation of this wurtzite phase was observed under 80 MeV Nitrogen ion irradiation. The strongest diffraction peak at ~35 implied that the nanostructures were grown with a preferred orientation along (101) plane. In the irradiated ZnO samples when we moved upto higher fluence, we found adequate improvement in the intensity of the (101) peak

relative to other peaks. To be more specific, one clear observation was the FWHM of (002) and (101) planes, which become smaller as move from F1 to F4 and finally, splitting of these peaks was observed. The splitting aspect is one indication of the formation of elongated nanostructures. No characteristic peak(s) due either to impurities or unreacted species like Zn, CTAB or $Zn(OH)_2$ were observed.
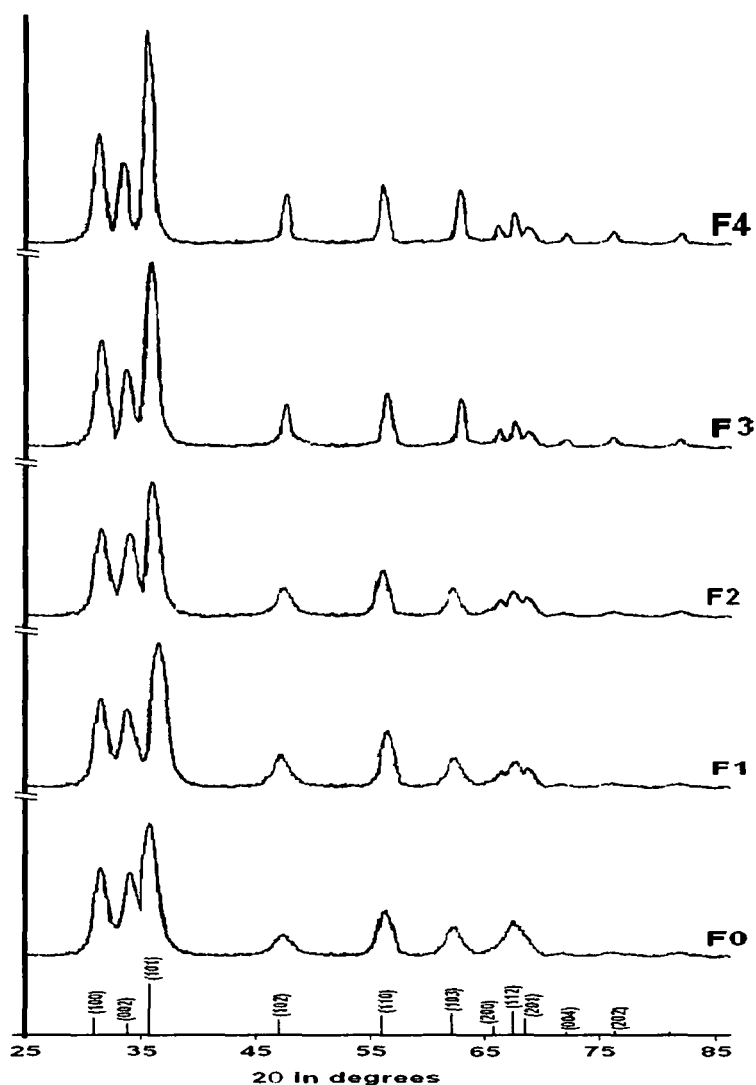
Figure 4.16 : XRD pattern of unirradiated (F0) and irradiated (F1,F2,F3,F4) ZnO nanoparticles at different fluences
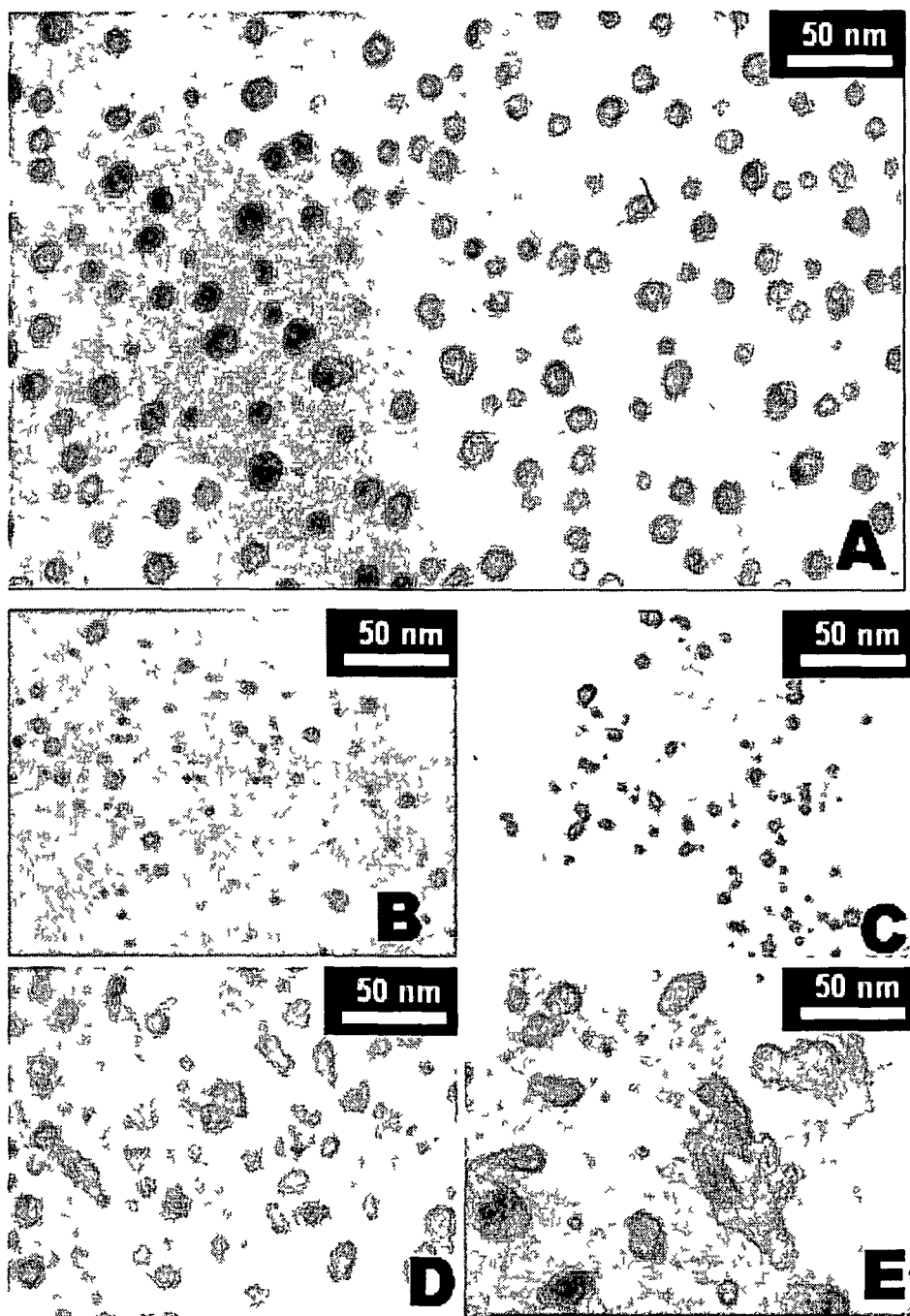
Figure 4.17 : TEM micrograph of 80 MeV N^{+4} ion irradiated ZnO nanoparticles at fluences (A)F0 (B)F1 (C)F2 (D)F3 (E)F4
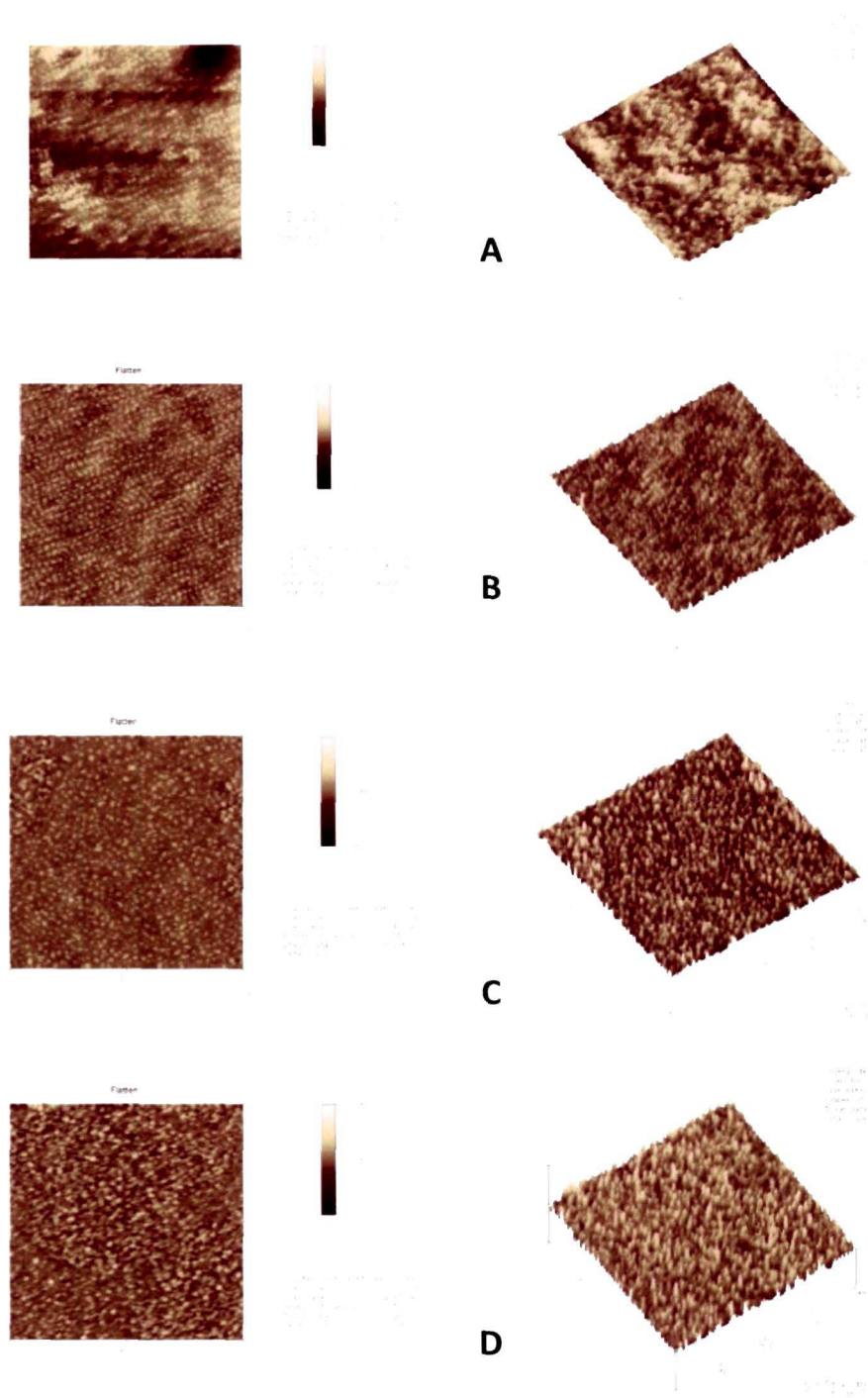
Figure 4.18: AFM images of 80 MeV N^{+4} ion irradiated ZnO nanoparticle films at fluences (B)F1 (C) F2 (D) F3 (E) F4
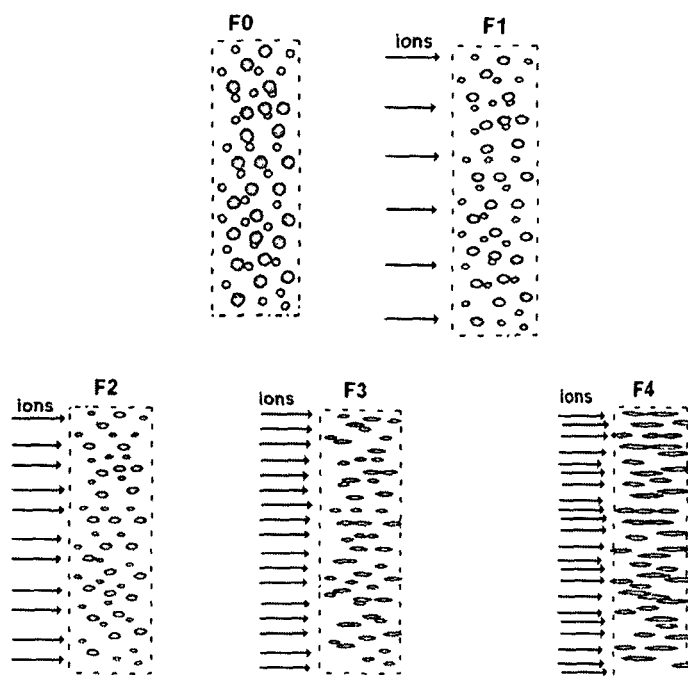
Figure 4.19 : Schematic of ZnO nanostructures modification under 80 MeV N^{+4} ion irradiation at fluences F0, F1, F2 , F3 and F4 and its modification

TEM studies provide the visual impression on the structural evolution and modification of nanostructures which are depicted in Figure 4.17. The uniformly distributed ZnO nanoparticles of average size ~15nm are found to be gradually elongated with increasing fluence. At lowest fluence (1.25 X 10^{10} ion/cm^2), no substantial structural modification was observed. Some evidence of elongation in the form of oblate structures are observable at higher fluences (i.e. $5x10^{10}$ ion/cm^2 and $2x10^{10}$ ion/cm^2). At the highest fluence ($8x10^{10}$ ion/cm^2), the ZnO nanoparticles are turned into almost nanorods by unidirection growth. Atomic force microscopy (AFM) images (Figure 4.18) also revels the formation of such elongated nanostructures in the beam direction i.e vertical to the sample surface. In Figure 4.18 the left column represents a set of 2d topology where as 3d morphological impressions are shown in the right column. It is quite clear that with increase in ion fluence, matrix gradually

gets amorphized allowing particles to grow independently along the beam direction. Ion beams, therefore, can be employed for obtaining vertically aligned ZnO nanostructures. The growth process of elongated ZnO nanostructures is shown schematically in the Figure 4.19.

The advantage of using Nitrogen beam is surface activation- a phenomena of removing undesired reactants, defects from surface of the nanostructures. The fast ions produce amorphized regions along the ion tracks known as *"columnar defects"* . Ideally, the density of creation is governed by the ion fluence, while ion species and sample material type determine the extent of amorphization. In fact, in nanomaterials surface atoms are more active and respond to swift heavy ions. Ions traversing through the sample lose energy by exciting the electronic subsystem (i.e. 10^{-15} s) and each ion has direct impact into the nano-specimen and there is least overlapping effect. So, at these fluences, the spherically symmetric nanoparticles can be transformed into oblate liked. Above this critical fluence, overlapping effect starts and *growth of nanoparticles is accompanied by the interparticle mass- transport* leading to organized nanoparticle growth. The competition among nanoparticles to coalesce and grow independently in confined space has led to vertically aligned rods.

ZnO:Tb nanorods:

We have also irradiated Tb-doped ZnO nanorods with 80MeV nitrogen ions with fluence varying in the range 10^{10} - 10^{13} ion/cm^2. The UV-Vis OAS spectra of both irradiated and unirradiated samples are depicted in Figure 4.20. The un-irradiated nanorods (Figure 4.20 (a)) show long tailing and two prominent peaks at ~365 nm (~3.4 eV) and ~270 nm (~4.59 eV). The 365 nm peak maxima is attributed to the excitonic ground state ($n=0$), whereas the 270 nm corresponds to the first ($n=1$) excited excitonic state. The ground state excitonic energy (~3.4 eV) is enhanced compared to the free exciton energy in the bulk (~3.30 eV) owing to 1D confinement of carriers [105].
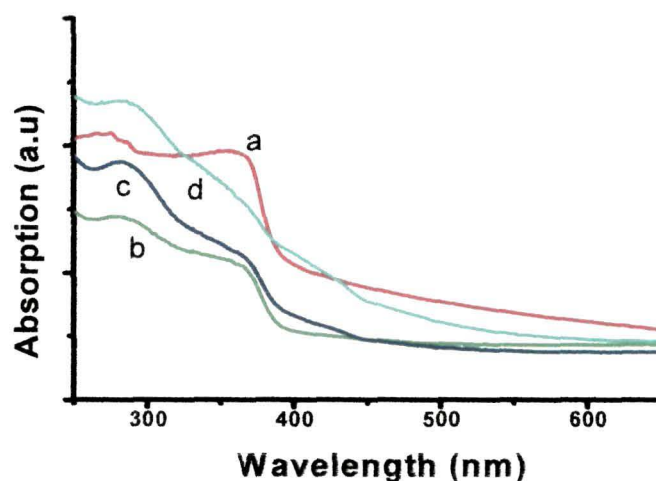
Figure 4.20 UV-Vis OAS spectra of a) unirradiated ZnO:Tb nanorods, and irradiated ZnO nanorods irradiated with a fluence of b) 5×10^{11}, c) 2×10^{12}, d) 8×10^{12} ions/cm^2

The presence of long tailing due to significant inhomogeneity in the sample is found to be suppressed for ion irradiated samples (Fig. 4.20 (b,c)), though ground state excitonic absorption position is found to be undisplaced. This clearly indicates that controlled nitrogen irradiation could bleach out the undesired species at best alongwith improved surface passivation and without affecting the ground state excitonic feature. Conversely, the excited state absorption peak of irradiated nanorods was shifted to 285 nm (Fig. 4.20 (b,c,d)). So, there is an appreciable red-shift of ~235 meV in the first excitonic excited state absorption of irradiated specimens, compared to the pristine one. It is now clear that a metastable state is created between the ground state and the first excited state as a result of nitrogen ion irradiation. This newly generated state could be due to the improved symmetric distribution of the nanorods owing to recovery from matrix encapsulation which is otherwise suppressed in a given matrix. The excited state excitonic absorption feature is found to be more prominent with increase in ion fluence. In contrast, the
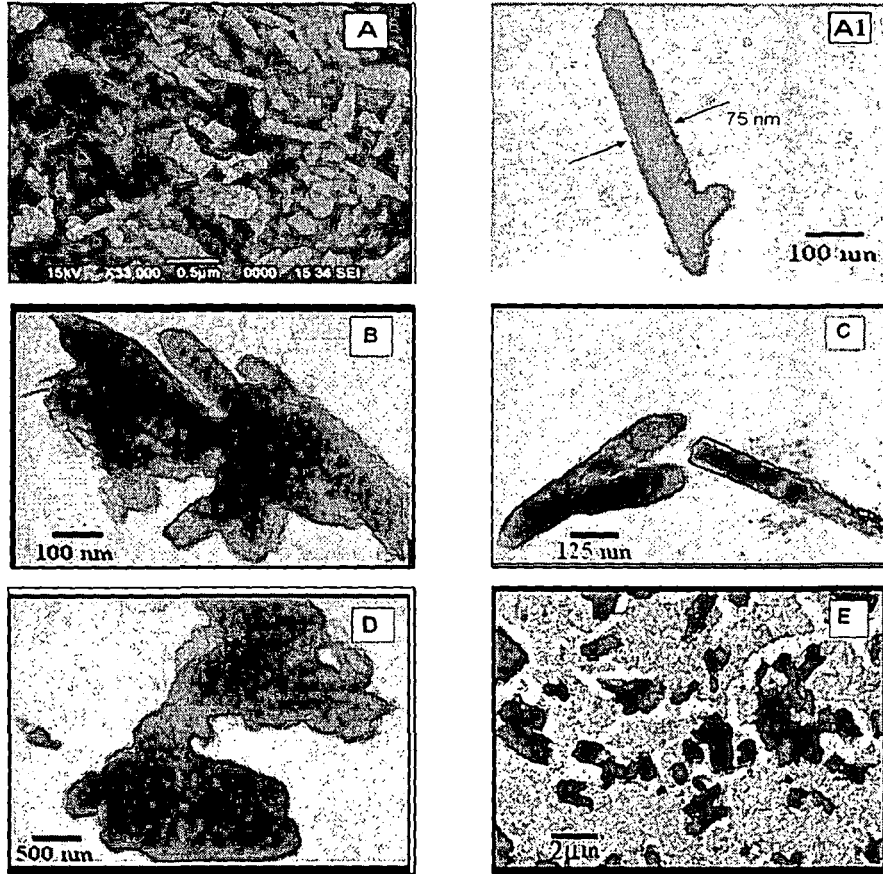
Figure 4.21: (A) SEM image of ZnO:Tb nanostructures without irradiation, (A1) TEM image of a fully grown isolated nanorod of diameter 75 nm without irradiation, and TEM image after irradiation with a fluence of (B) 5×10^{11}, (C) 2×10^{12}, and (D) 8×10^{12} ions/cm^2; respectively. An overview of the agglomerated nanorods (case 'D') at lower magnification is shown in (E).

fluence (8×10^{12} ions/cm^2) the ground state absorption becomes featureless followed by a long tailing. We have thus realized that with the proper selection of fluences, energetic nitrogen beam can improve not only the quality but also help in preserving ground state and excited state carrier population of elongated nanosystems (nanorods) under investigation. The actual modification was observed in the TEM images [Figure 4.21]. The nanorods of dia 70-80 nm [Figure 4.21 (A1)] have showed growth due to ion irradiation with increasing fluences.

4.2 Organization and modification through photon illumination

The third method that we have employed was through intense light illumination process. In this process, we have illuminated PVOH dispersed ZnS nanosystems with a 2mW red He-Ne laser of wavelength λ=632.8 nm. For this purpose we considered the films of ~500nm thickness casted by spin coating technique. The samples are illuminated for 30 minutes and 60 minutes and then characterized by transmission electron microscopy.
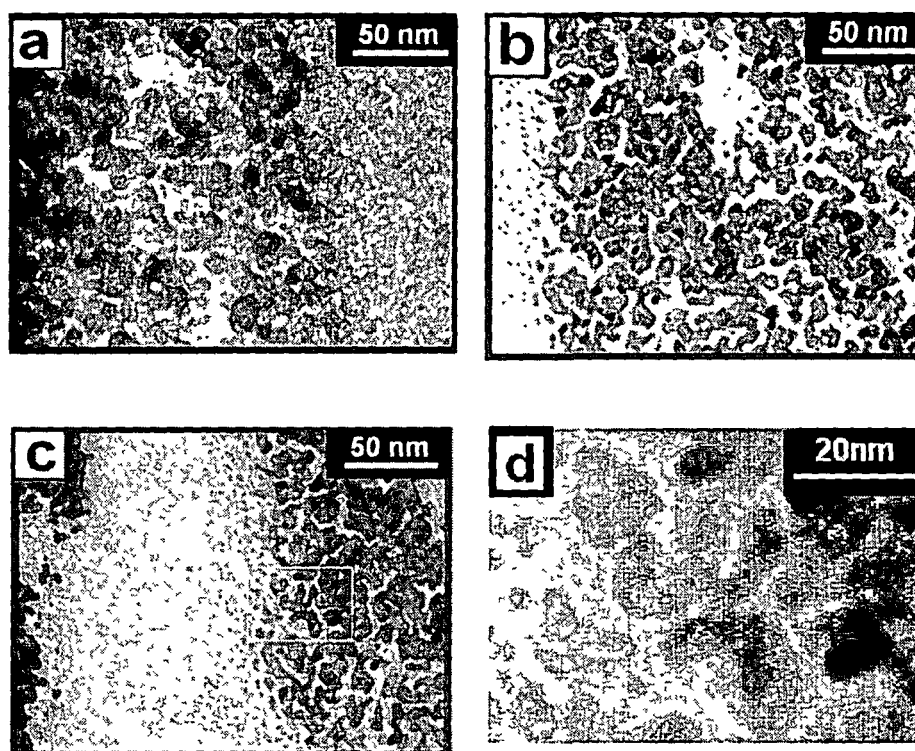
Figure 4.22: TEM image of ZnS nanostructures (a) without illumination, illuminated for (b) 30 min, and (c) 60 min (d) magnified view of a section of figure (c)

Fig. 4.22(a) depicts an electron micrograph of dispersed ZnS nanostructures. Interparticle coalesce leading to channel and island like structures are apparently visible upon photon illumination (Figrue 4.22 b,c). At higher magnification (selected region of TEM micrograph c, shown in d) the structures are found to be

oblate/elongated ones. The modified nonstructural evolution can be treated as a consequence of light matter interaction in the nanoscale regime.

Due to strong particle-particle interaction, the particle agglomeration occurs during self-assembly of nanostructures. Note that the interaction forces between the organic molecules and the inorganic nanoparticles play crucial role in controlling the structures and consequently, the properties of the nanoscale material. When ZnS nanoparticles are embedded in the insulating PVOH matrix, it show long term stability but diffusion of atoms in the polymer is present. The mass transport is driven by the free surface energy of the nanoparticles and associated with lattice defects and grain boundaries. These diffusion processes, at times, result in the variation of size and shape distribution. The diffusion process is accelerated through laser illumination. Control laser irradiation helps atoms deffuse and assembles in order to minimize surface energy. As a result, nanopatterns of varying dimensions one formed as evident in Figure 4.22 (a,b,c). The elongation, through small, was observable for longer exposure time.

5.1 Luminescence Characteristics for optoelectronics /photonics applications

As far as application in luminescent and optoelectronic devices is concerned the optical properties of the investigated nanostructures play a key role in determining efficiency and figure of merit. We discuss the size and system dependent optoelectronic properties. The radiative emission mechanism in nanoscale particles have never always been easy to interpret and understand. The luminescence response of impurity doped systems is much more complicated. This is because of the presence of various kinds of defects (which exist as nonradiative centers) of different origins and material system dependent carrier life time dynamics. The light emission properties of undoped and doped nanostructured systems have been investigated.

The band-edge, defect related (Zinc vacancy, Sulfur vacancy, Oxygen vacancy etc.) and impurity related emission characteristics are discussed qualitatively as well as quantitatively. Further, a meaningful analysis on the ion irradiation (fluence) dependent tunability in the PL response is being presented.

The optical properties were explored by optical absorption and photoluminescence (PL) spectroscopy. The UV-Vis spectra of corresponding samples are explained in the Chapter 3 and Chapter 4. In this chapter, the luminescence characteristics are discussed based on PL studies. The room-temperature PL spectra of the nanostructures were studied by a Perkin Elmer LS-55 spectrophotometer using λ_{ex}=325nm line (of Xe- source) as the excitation wavelength and the data were collected by a computer controlled standard monochromator based photo-detection system. The λ_{ex}=325nm line is used to excite the electrons form the valence-band to conduction-band. Sometimes, we have varied the λ_{ex} to distinguish the luminescence peak from that of the Raman peaks (appears near the λ_{ex} in the spectrum).

5.1 Luminescence response of ZnS nanostructures

Following figures (Figure 5.1, Figure 5.2, Figure 5.3) demonstrate the PL spectra (λ_{ex} =325 nm) of undoped ZnS nanoparticles and nanorods.
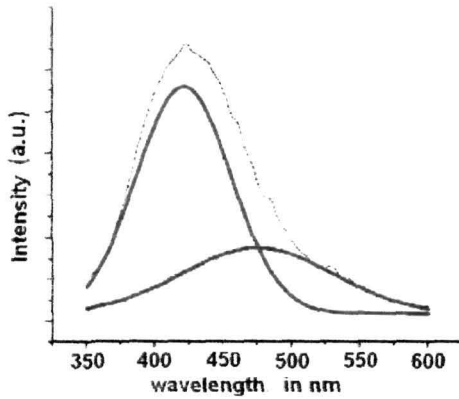
Figure 5.1 : PL spectra of ZnS nanoparticles in PVOH matrix (λ_{ex} =325 nm)
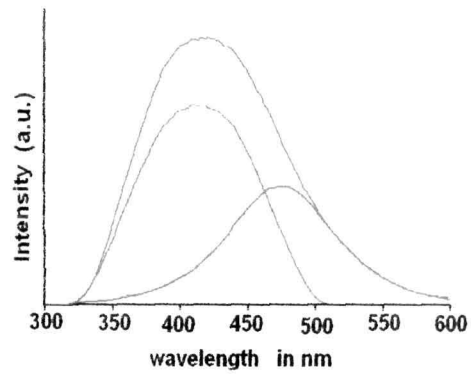
Figure 5.2 : PL spectrum of ZnS nanoparticles in CTAB (λ_{ex} =325 nm)
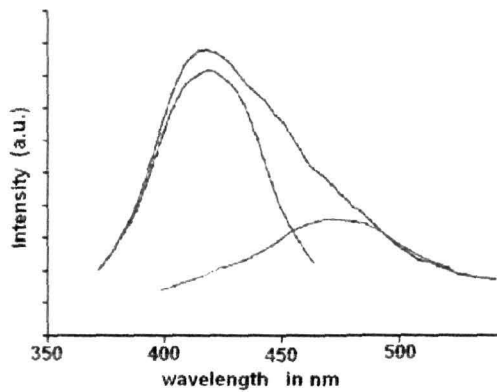
Figure 5.3 : PL spectrum of ZnS nanorod in CTAB (λ_{ex} =325 nm)

Basically, the PL spectra of ZnS nanoparticles and nanorods, show a strong blue-luminescence, peaking at ~420 nm ˙ and having an extended tail. As observed, the highly asymmetric and broadened emission spectra indicate the involvement of number of luminescence centers that correspond to different kinds of defects. The defects can be lattice vacancy, interstial and impurity related types. The radiative

transitions via all these states can be superimposed which result in a broad peak centered at ~ 420 nm
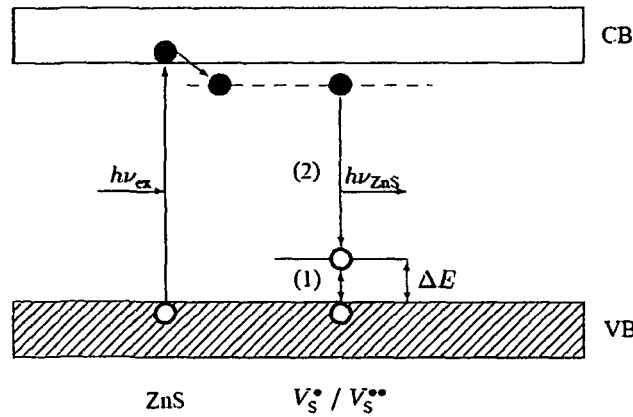
Figure 5.4 : Luminescence mechanism in ZnS nanostructures

In general, both Schottky and Frenkel defects exist in all crystalline solids, but at any time only one type of defects is dominant as they are associated with different energy of formation. It was known that Schottky defects are more dominant in cubic ZnS. Schottky defects of ZnS primarily involve the S^{2+} vacancies ($V^{\bullet}_s$) and the Zn^{2+} vacancies (V^{-}_{Zn}). In ZnS nanoparticles, surface S^{2+} vacancies ($V^{\bullet}_s$) are dominant over the other defects. In ZnS, 'Zinc interstitial (Zn_i) ' and 'S vacancy ($V^{\bullet}_s$) ' act as 'shallow donors' (electron traps) where as ' S interstitial (S_i)' and ' Zn vacancy(V^{-}_{Zn})' act as 'deep acceptor' (hole traps) levels . So, sulfur vacancies ($V^{\bullet}_s$) generate localized donor sites just below the conduction band [Figure 5.4]. Excitation of these produce a positive charge and conduction band electrons. This localized charge exerts a potential, which can further trap electrons. So upon excitation, Sulfur vacancies ($V^{\bullet}_s$) are pumping the electrons into conduction band. Emission occurs when a captured electron recombines with a hole [151].

Figure(5.4) depicts schematically the energy transfer processes that occur in nanocrystalline ZnS upon UV excitation. The excitation of the ZnS nanocrystals starts with the creation of a Mott-Wannier exciton by the incident photon ($h\nu_{ex}{>}E_g$). The excited electron is than transferred to a shallow trap (denoted by the dashed line) as in the bulk ZnS. As the electron effective mass ($m^{*}_e= 0.27\ m_e$) is quite small, this

shallow trap-state is delocalized over the entire nanocrystal. The hole (with a significantly larger effective mass m^*_h = 0.54 m_h) remained which initially in the valence band of the ZnS nanocrystal will be trapped for a longer period of time. The recombination of the electron-hole pairs can occur via non-radiative relaxation and radiative emission or defect related emission. Nonradiative relaxation will occur through certain defect states or surface states (Figure 5.4). In the process, first the hole is trapped at a sulfur vacancy, denoted by V_s^* , resulting in a V_s^{**} state. Subsequent recombination with an electron in a shallow trap gives rise to the violet emission:

$$(1) \qquad V_s^* + hv^+_{VB} \leftrightarrow V_s^{**}$$

$$(2) \qquad V_s^{**} + e^- \rightarrow V_s^* + hv^+_{ZnS}$$
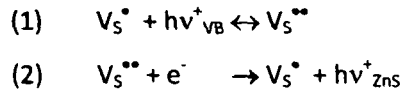
The steps denoted by (1) and (2) are schematically shown in Fig. 5.4. Thus, the intense blue emissions at ~422 nm are attributed to sulfur vacancy (V^*_s) and interstitial sulfur (S_i) lattice defects. It was found that the peak intensity ~422 nm gets decreased with the use of excess sulfur based reactants (PL spectra not incuded). Thus this PL peak (peak 1 λ ~ 420 nm) is due to sulfur vacancy related surface states and their extent of passivation [335]. The intensity of the emission peak at ~420 nm is so high that it quenched the other defect related peak 420 nm, suggesting that the number of surface defects was much greater than that of internal defects due to the high surface to volume ratio of ZnS nanoparticles. The other peak (λ~480 nm) observed is due to the Zn vacancy (V_{Zn}) present in the material system. The asymmetry in PL response comes from the variation in defect concentration present in the material. In case of ZnS nanorods, concentration of defect due to Znic vacancy is more and the PL curve [Figure 5.2] is found to be more asymmetric.

The intense blue luminescence response of nanoscale ZnS has a lot of applicability owing to significantly high quantum efficiency much higher than its bulk form. It can be used as a promising phosphor material for light emitting devices and for electroluminescence devices. In Contrast, the impurity activated ZnS gives us doped nanostructured systems that could display remarkable color tunability along with high luminescence efficiency. Note that, almost all transition metals (Mn, Cr, Co, Cu etc) exhibit variable oxidation states. The flexibility in the oxidation states is due to

their typical electronic structures with outermost shells partly filled. When such elements are incorporated into a semiconductor host material, then upon excitation
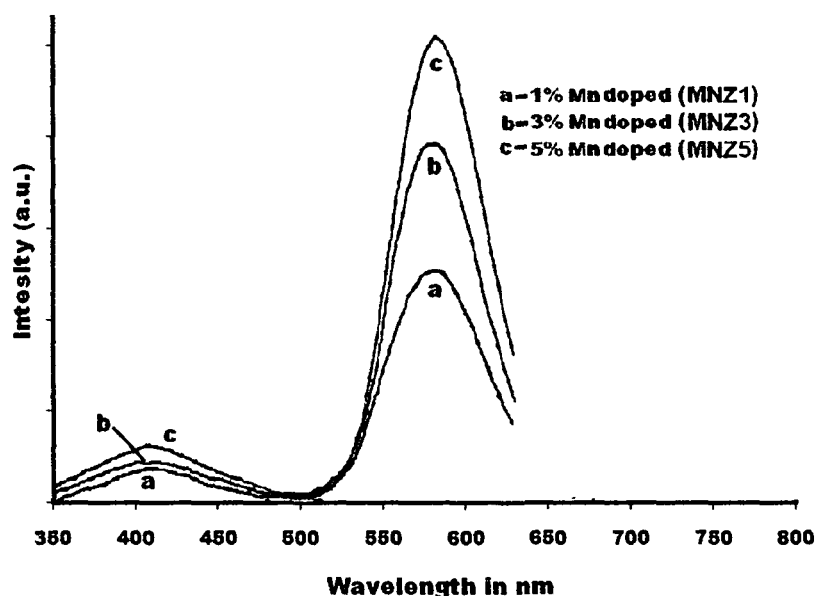
Figure 5.5 : PL spectra of ZnS:Mn nanostructures at different doping levels (1%, 2%, 3%)

they exhibit characteristic emissions via impurity levels. The PL response of various transition metal(TM) doped system have been investigated. The PL response of Mn doped ZnS nanoparticles are shown in the Figure (5.5). Here, alongwith the blue emission peak (~420nm) due to the sulfur vacancy, an intense luminescence peak was observed ~580nm and is ascribed to the impurity (Mn^{+2}) activated peak. Earlier, yellow orange emission, due to delocalization of d-electrons of form Mn was to ZnS by Bhargava et al and many other groups [111,118-120]. This yellow orange emission was so intense that it could suppress the sulfur vacancy related peak. With increase of Mn-dopant concentration, the ratio of Mn^{+2}-to-S^{-2} vacancy related emission intensity increases. Therefore it shows the tunablity aspects of the ZnS:Mn sample.

In the emission process of ZnS:Mn recombination of electron –hole pairs can occur via different routes. The first blue peak (~422nm) is due to the electron hole recombination through the sulphur vacancy ($V_S^•$) where as the impurity activated peak is found at ~580 nm. The emission from Mn^{2+} can be excited either directly by recombination of a bound exciton at Mn^{2+} or via trapping of a hole by Mn^{2+}.

Subsequent recombination with an electron in a shallow trap results in Mn^{2+} in an excited state, $(Mn^{2+})^*$, which gives rise to the well-known orange Mn^{2+} emission:

(1) $Mn^{2+} + hv^+_{VB} \rightarrow Mn^{3+}$

(2) $Mn^{3+} + e^- \rightarrow (Mn^{2+})^*$

(3) $(Mn^{2+})^* \rightarrow Mn^{2+} + hv^+_{Mn}$
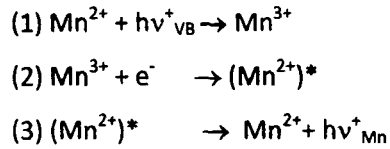
These processes, denoted by (1), (2) and (3) are also schematically shown in Figure 5.6.The transfer of the delocalized electron to the manganese will probably not immediately result in Mn^{2+} in the $^4T_1$ excited state. Most likely, the Mn^{2+} will be in a higher excited state, from which it will relax nonradiatively to the metastable $^4T_1$ state.
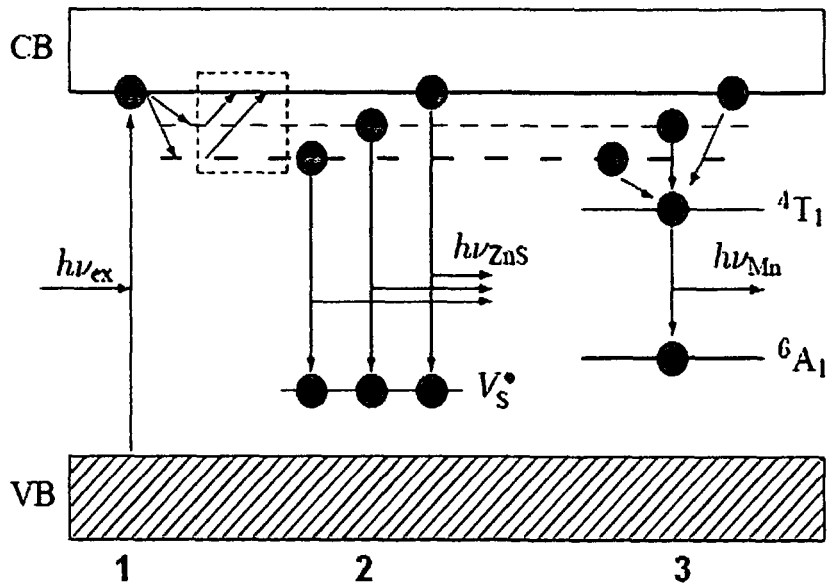
Figure 5.6 : A scheme of luminescence mechanism in ZnS:Mn nanostructures

The thermally-activated quenching of the defect emission and the accompanying increase in the Mn^{2+} emission can now be understood: at elevated temperatures the holes are detrapped from the $V_S^{\bullet\bullet}$ levels and some of the holes that are released may now be retrapped by Mn^{2+}. After a subsequent recombination with an electron, Mn^{2+} in excited state is formed resulting in Mn^{2+} emission. This can explain the increase of the Mn^{2+} related emission intensity in the temperature regime where the violet defect-related emission gets quenched [128].
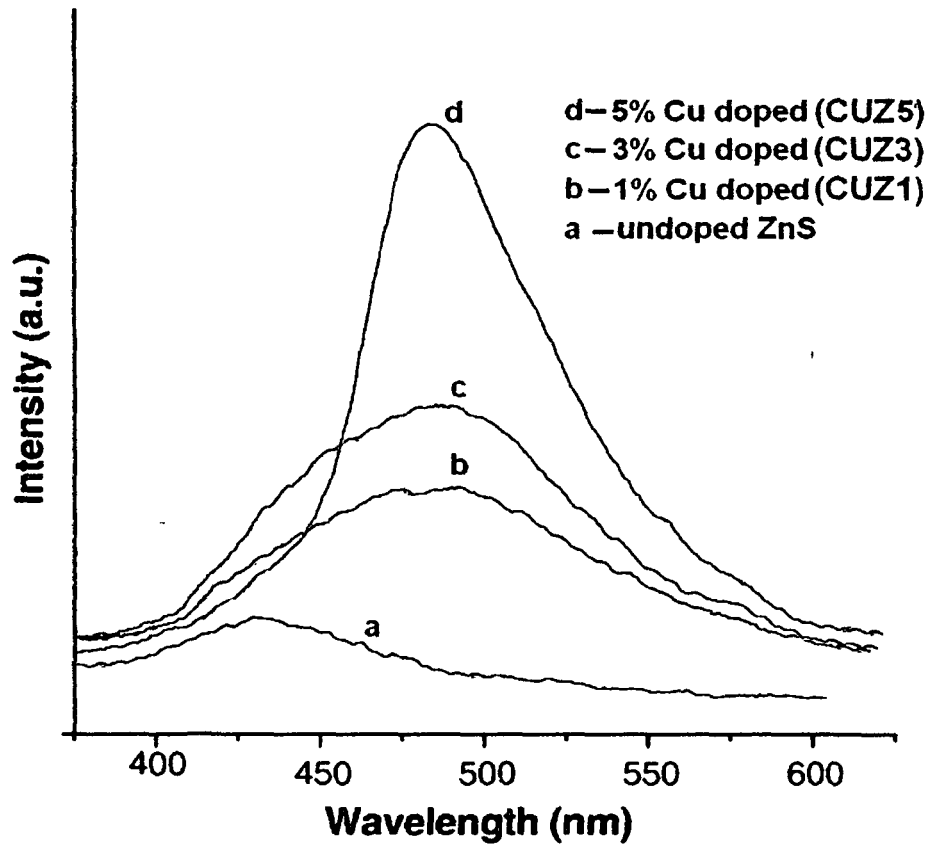
Figure 5.7 : PL spectra of ZnS:Cu nanostructures with different doping concentration

In the luminescence spectra of Cu doped ZnS system [Figure 5.7] the impurity activated peak was observed at ~500nm in the blue-green region of the electromagnetic spectrum. This green emission arises from the recombination between the shallow donor level due to sulfur vacancy (V_s^*) and the t_2 level (emerge according to crystal field theory) of Cu^{2+}. It should be mentioned here that as CuS nanoparticles do not show any luminescence under UV radiation, the observed green emission originates from Cu^{2+} ions that are embedded in the ZnS matrix and substitute Zn^{2+} ions in ZnS nanoparticles. With the increase of the Cu^{2+} concentration, the green emission peak position is gradually shifted to longer wavelength (from 480 to 500 nm). As mentioned, the energy level of sulfur vacancy (V_s^*) relative to the valence band nearly keeps constant in these samples despite the variation of the Cu^{2+} concentration. So it can be concluded that the t_2 energy level of Cu^{2+} ions is farther from the valence band with increasing Cu^{2+} concentration. Based on the PL results

observed, the schematic energy level diagram of ZnS:Cu nanoparticles can be schematically shown (Figure 5.8). This figure explains the emission mechanism of ZnS:Cu nanoparticles and illustrates the above assignment [121].
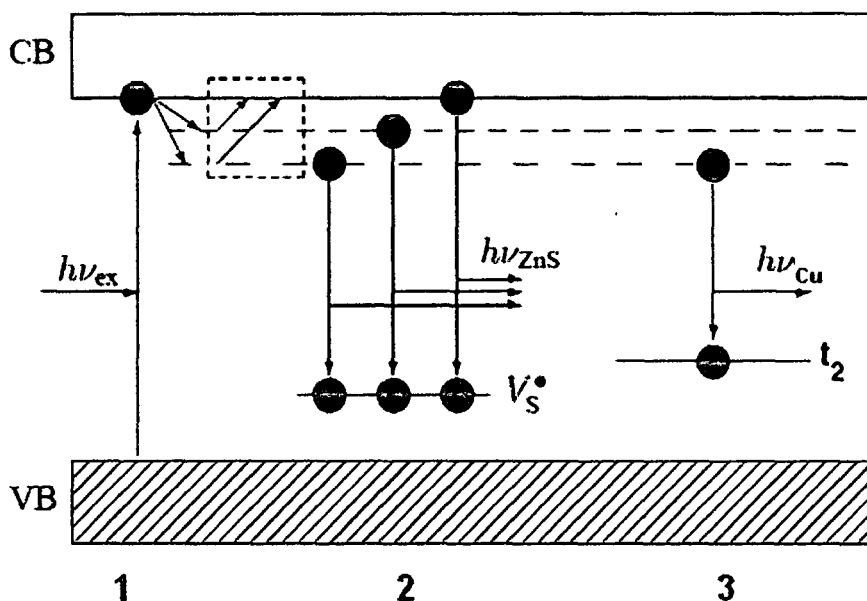
Figure 5.8 : A scheme of luminescence mechanism in ZnS:Cu nanostructures

These blue-green emissions dominate and can mask the band-edge emission and the trap related emissions. However, the luminescence of ZnS:Cu^{2+} nanocrystals is obviously stronger than that of ZnS:Mn^{2+} nanocrystals due to the fact that a number of radiative centers participate in the former case whereas in ZnS:Mn^{2+}, only one type of radiative center is at work resulting visible luminescence. The luminescent intensity is more dependent on the concentration of impurity ions.

Similar kind of results have been observed in the emission spectra of Cobalt doped ZnS (ZnS:Co) system. In the spectra, as one can see the impurity (Co^{2+}) peak has dominated the other defect-related and band-edge emissions along with sulfur vacancy peak (~420nm). As we increase the doping concentration enhancement, in the impurity activated luminescence peak was observed.
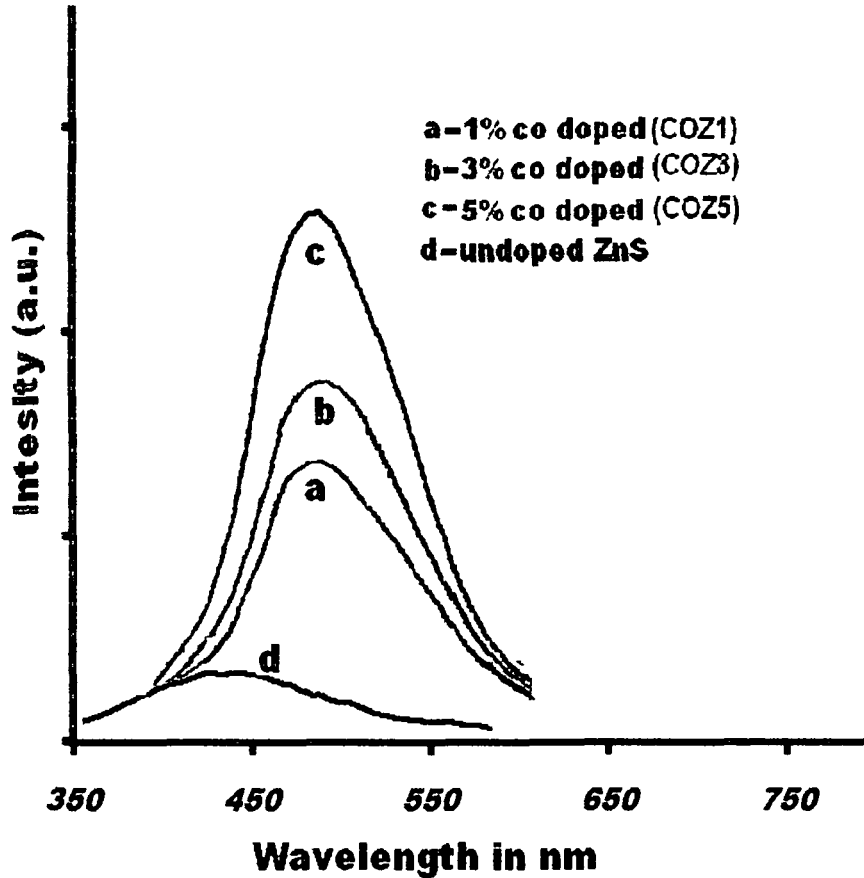
Figure 5.9 : PL spectra of ZnS:Co nanostructures in different doping concentration

It was observed that transition metal-doping enhances the luminescence response of the ZnS nanostructures and it is possible to tune the luminescence as well as quantum-yield just by varying the concentration of dopant in ZnS host. Such a material is highly applicable in multicolor light emitting devices as a phosphor material. In such devices we will have to excite the material by a low intensity UV/blue to get high intensity light of different color. However, it is possible to produce different colors of light by making a composite of these doping systems with different proportions. It is also expected that it will provide very stable fluorescence owing to its intense luminescence response.

5.2 Luminescence response of ZnO nanostructures

The luminescence specta of ZnO nanoparticles [Figure 5.10, Figure 5.11] and nanorods [Figure 5.12] were studied and the results are presented below. As can be observed, the PL spectra consists of a sharp peak at ~375nm along with a broad peak that corresponds to different defect states inherent in the system. The sharp peak corrsesponds to near band edge emission or popularly called donor(D)- acceptor(A) pair transition.
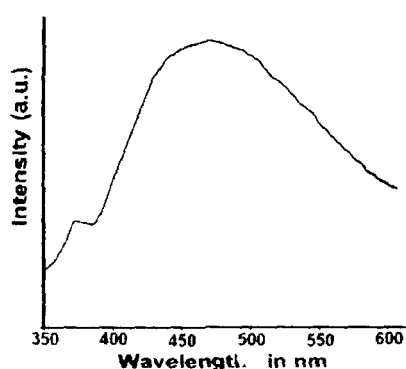
Figure 5.10 : PL spectra ZnO nanoparticles dispersed in PVOH matrix
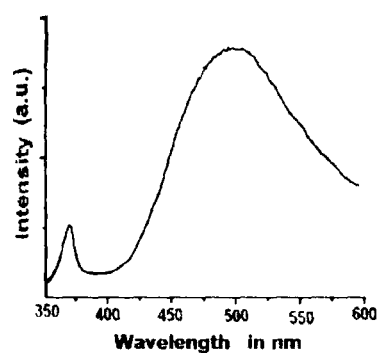
Figure 5.11 : PL spectra of CTAB capped ZnO nanoparticles
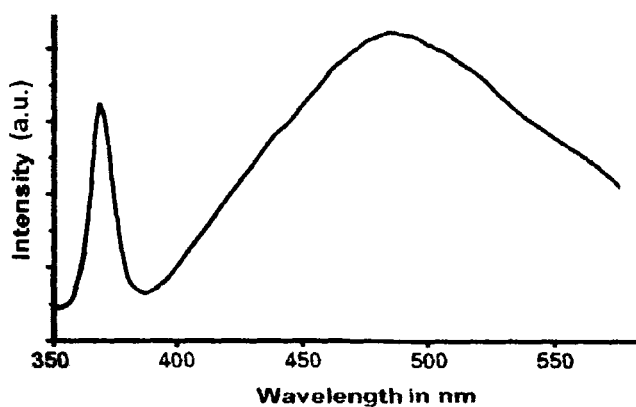
Figure 5.12 : PL spectra of CTAB capped ZnO nanorods

Despite the use of various passivation methods, adequate defect states are expected at the surface of nanocrystallites. The concentration of surface states, very often depend on the synthesis protocols and passivation processes. These surface states acts as surface traps for charge carriers and excitons, which generally degrade the optical and electrical properties of the nanosystems.
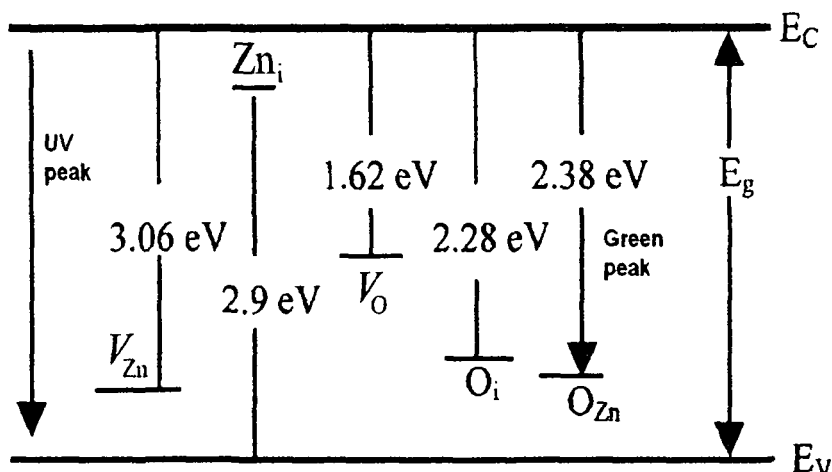
Figure 5.13 : Defect states in ZnO system

The surface states can be suitably used for radiative transitions. ZnO has a characteristic has a green emission from the defect states along with the typical band edge (near ultra violet) emission (E_g 3.37 eV, λ =386 nm). It was also reported that the green emission would suppress the band-edge emission due to several reasons.

Theoretical and experimental studies [336,337] showed that the defect states in a ZnO nanostructure can be of several types, including:

- neutral, singly or doubly charged Zn vacancies (V_{Zn});
- neutral or singly charged oxygen vacancies (V_O);
- singly charged or neutral interstitial Zn (Zn_i);
- interstitial O (O_i);
- a complex of V_O and Zn_i ($V_O Zn_i$);
- a complex of V_{Zn} and Zn_i ($V_{Zn} Zn_i$); and
- substitution O at Zn position (O_{Zn}).
- Substitution of Zn at O position

According to Aleksandra et al. [337], the singly charged oxygen vacancy (V_0^+) is located at 1.62 eV, below the conduction band in the ZnO band gap and results in an emission at ~500 nm. The most widely, but not universally accepted mechanism for green luminescence from ZnO is the electron-hole recombination on singly ionized oxygen vacancies. In solution-based synthesis, the oxygen vacancies appear to be intrinsic and may result from the abrupt heterogeneous nucleation and growth, mediated by the uneven surface energies. If the radiative center is associated in part with the surface, their concentration would be expected to decrease with the aggregation of nanostructures [338]. In our ZnO nanoparticle and nanorod systems, amongst all the defects quoted above oxygen vacany (V_0^+) is believed to be the most prominent one which could suppress the other defects. However, from PL spectra analysis it was found that the green-to-UV peak ratio is higher for PVOH embedded ZnO system than CTAB based ZnO nanoparticles.

Aspect ratio dependent luminescence response of ZnO nanorods:

The gradual structural transformation from particles to rods have already been discussed in chapter 4. The PL studies of ZnO nanoparticles (Z0) and nanorods of different aspect ratio (Z1, Z2, Z3) are presented in Figure 5.14. The luminescence response of these nanorods is basically dependent on the length, diameter as well as shape. We have studied the luminescence behavior of all these samples under the UV excitation (325 nm). In the PL spectra (Fig.5.12), the prominent peak observable at ~362-375 nm is ascribed to the near-band edge (NBE) emission of nanoscale ZnO products. Note that, the NBE peak has shifted slightly towards red for Z1-Z3 samples (nanorods) compared to that of Z0 (nanoparticles) one. Previously, the NBE was observed in the range of 378-385nm for elongated ZnO systems [203]. Secondly, a relatively broad peak observable at ~480 nm is assigned to the defect related emission. This broad peak observed in the visible-green region is attributed to the recombination of photo-generated holes with singly ionized oxygen vacancies [337].
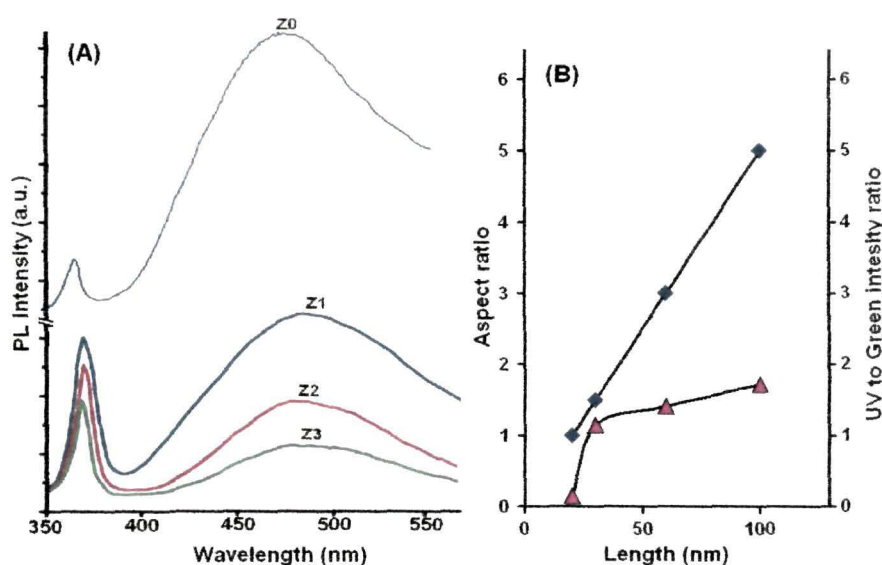
Figure 5.14 : Luminescence response of ZnO nanoparticles and nanorods (Z0, Z1.Z2 and Z3)

In order to make a clear picture on the correlation between the nature of nanostructures and the PL responses, we have estimated the physical parameters which are presented in table 5.1. In our case, since the ZnO nanoscale products are formed as a result of spontaneous decomposition of hydroxyl products into oxide ones, it is likely that during crystal growth phenomena, there can be adequate amount of oxygen related defects. The defects may vary from singly ionized oxygen vacancy to oxygen antisites. Also, the presence of interstitial defects cannot be fully ignored. It is important to quote here that the surface to volume ratio is extremely high in case of nanoscale materials and most of the atoms are therefore displayed on the surface of the material than its core. In this context, a clear evidence of strong surface-defect related emission was observable for spherically symmetric nanoparticles (Z0) as shown in Figure 5.14A. The defect related emission (Green) is approximately six orders of magnitude stronger than its NBE (UV) counterpart. Conversely, for one dimensional structure (Z1-Z3), the NBE (UV) emission gradually shoots up as compared to the defect emission (Green). When the aspect ratio increases from 1.5 to 5, the UV-to-Green intensity ratio gets improved from 1.15 to 1.72 (Figure 5.14(A), Table 5.1). The strong, symmetric and tunable responses of both the emission features suggest that our ZnO products are of high quality with minimum inhomogeneity.

129

Table 5.1: Aspect ratio dependent luminescence response

Sample	Avg. diameter (nm)	Average length (nm)	UV emission peak (nm)	Green emissio n peak (nm)	Aspect ratio (length/ dia)	UV to Green Intensity ratio
Z0	20	20	~362	~475	1:1	0.15
Z1	20	30	~370	~480	1.5:1	1.15
Z2	20	60	~370	~480	3:1	1.41
Z3	20	100	~370	~480	5:1	1.72

In Figure 5.14 (B), we correlate the aspect ratio vs. length (labeled by ■) and UV-to-Green intensity ratio vs. length (labeled by ▲) of the nanostructures (Z0-Z3). Two important inferences can be drawn. Firstly, with linear increase in aspect ratio one need not obtain a linear trend in the UV-to-Green emission. The trend would saturate at a definite aspect ratio. Secondly, between aspect ratio 1 and 1.5 (when the particles start growing into oblates) the response is sharp. Further, when the dimension (length) of the nanorods is several orders of magnitude larger than the diameter, there is only slow improvement in the UV-to-Green emission features. Thus, between the transition from a spherical symmetric nanosphere system to an oblate one, a drastic enhancement in the UV emission could be assured. The UV emission response gets quenched appreciably at the cost of defect related green emission for nanorods with higher aspect ratio.

This aspect ratio dependent luminescence study reveals possibility of tunable band-edge and defect related emissions. We found that the nanorods with higher aspect ratio show more intense UV peak, thus ensuring possibility of deployment of these nanorods in developing UV laser and other light emitting devices. On the other hand, nanostructures with dominant green emission can be useful for oxygen based sensing devices. Elaborate mechanism correlating nanorod dimension and extent of tunable emission is currently under investigation.

5.2 Modification of luminescence response by ion irradiation and photon illumination

We have developed ZnS and ZnO nanostructures using different chemical approaches which are discussed in chapter 3. Further, these nanostructures were modified through ion irradiation and photon illumination. Different kinds of modification were observed under these processes (discussed in Chapter 4). Along with the structural modification, these nanostructures endure modification of the luminescence properties along with the other physical properties.

(a) Modification of luminescence response by Titanium ion irradiation:

The PL spectra of irradiated and unirradiated PVOH embedded ZnS at fluences 1.25×10^{10} ions/cm^2, 5×10^{10} ions/cm^2, 2×10^{11} ions/cm^2 and 8×10^{11} ions/cm^2 are shown in Figure 5.15.
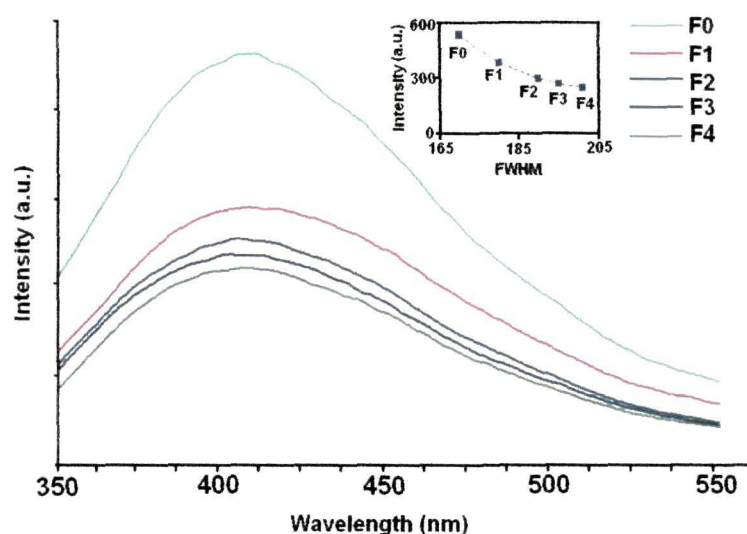
Figure 5.15 : PL spectra of unirradiated (F0) and 150MeV Titanium ion irradiated (F1-F4) ZnS nanostructures

In the luminescence spectra of undoped ZnS the relatively intense sulfur vacancy peak ~ 420nm dominates the band-edge and defect related emission. When we have irradiated the material with low fluence (F1), adequate suppression of the emission peak was observed. At higher fluences also we have observed gradual suppression of the peak intensity owing to the

reduction in the concentration of surface traps as a result of nanoparticle growth. The FWHM of the PL peak is found to increase with increase in ion fluence.

(b) Modification of luminescence response by Silver ion irradiation

The PL spectra of irradiated and unirradiated PVOH embedded ZnS at fluences of 1.25×10^{10} ions/cm^2 , 5×10^{10} ions/cm^2 , 2×10^{11} ions/cm^2 and 8×10^{11} ions/cm^2 are shown in Fig. 5.16.
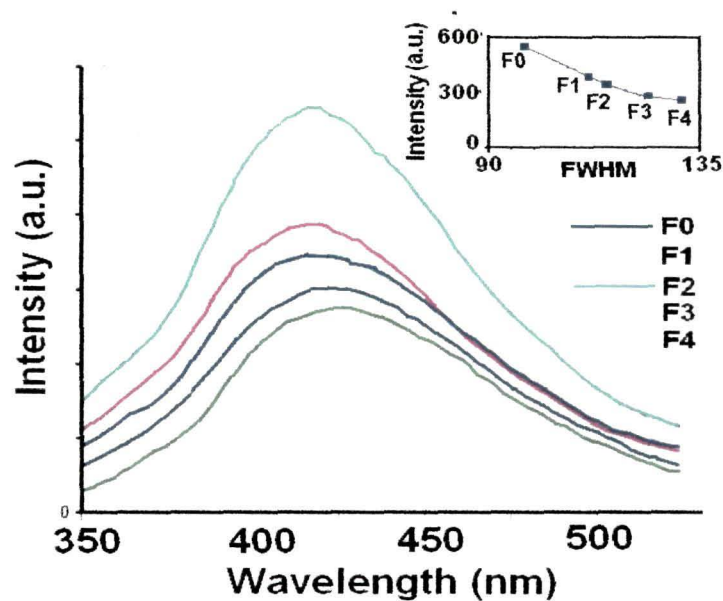
Figure 5.16 : PL spectra of unirradiated (F0) and 100MeV Silver ion irradiated (F1-F4) ZnS nanostructures

In the luminescence spectra of undoped ZnS the highly intense sulfur vacancy peak ~ 420 nm dominates band-edge and defect related emission. As the ion fluence (0 to 8×10^{11} ions/cm^2) increases, there is an adequate suppression of this emission owing to reduction in the concentration of surface traps as a result of nanoparticle growth. However, blue shift of the emission peak also observed with increasing fluence. The FWHM of the PL peak is found to be increased with increase in ion fluence. ;

(c) Modification of luminescence response by Nitrogen ion irradiation

Zinc Sulfide (ZnS) nanostructures:

The PL spectra of irradiated and unirradiated PVOH dispersed ZnS nanostructures (fluences 1.25 x 10^{10} ions/cm^2 , 5 x 10^{10} ions/cm^2 , 2 x 10^{11} ions/cm^2 & 8x 10^{11} ions/cm^2) are shown in the Figure 5.17.
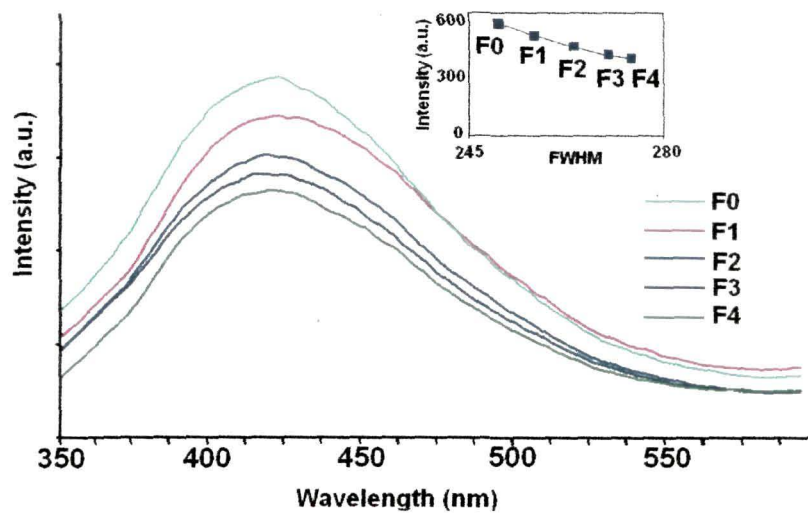
Figure 5.17 : PL spectra of unirradiated (F0) and 80MeV Nitrogen ion irradiated (F1-F4) ZnS nanostructures

In the spectra we observed the similar kind of suppression of luminescence as we observed in Titanium and Silver ion irradiation. But here the suppression of luminescence is less compared to them. The FWHM of the PL peak is found to increase with the increase in ion fluence but having quite small magnitudes as compared to Ag and Ti cases.

Zinc Oxide (ZnO) nanoparticles:

Again, in the PL spectra (Figure 5.18) of irradiated and unirradiated ZnO we found some different kinds of responses at different fluences. Here, we have observed two major peaks: a UV near band-edge emission peak, ~380 nm, and a green emission peak ~500 nm. The band-edge emission is sharp while the other peak is broad.
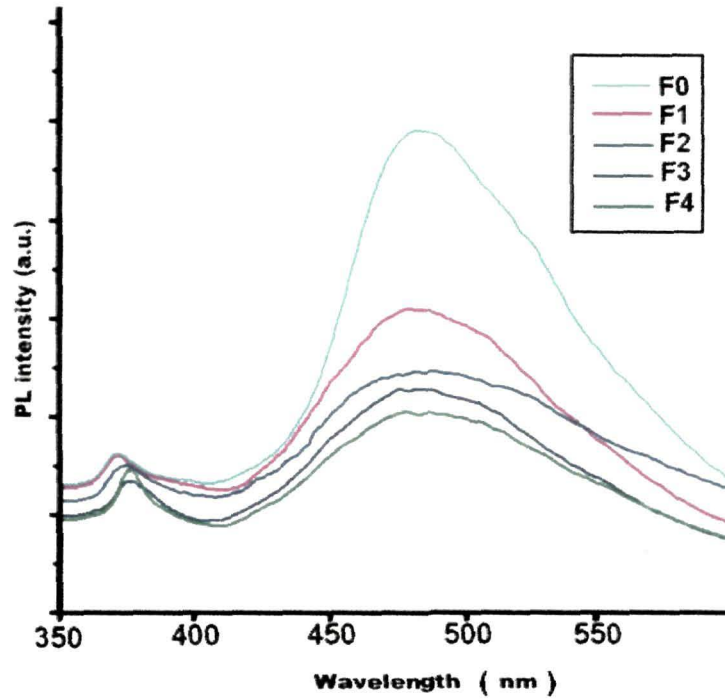
Figure 5.18 : PL spectra of unirradiated (F0) and 80MeV Nitrogen ion irradiated (F1-F4) ZnO nanostructures

After irradiation, with increasing fluence, we observed drastic suppression of this green emission (~500 nm) but gradual reduction in the UV emission (~380 nm). In the unirradiated ZnO, we noticed that the related emission (Green) is approximately six orders of magnitude stronger than its NBE (UV) emission. At a fluence of 1.25×10^{10} ions/cm^2 we observed suppression of the green emission and the UV-to-green peak ratio becomes ~3. At the next three fluences along with the suppression of the green peak we observed blue shift of the UV peak owing to adequate growth of the nanoparticles, as observed form the TEM studies. At a fluence of 2×10^{11} ions/cm^2, a clear elongation of the nanoparticles are observed (chapter 4, Figure 4.17d) and then UV-to-Green intensity ratio gets improved significantly. At the final fluence, due to further growth toward elongation more suppression of the green peak was observed along with the red shift of the UV peak. However, under ion irradiation as the nanoparticles are

grown in a particular direction with increasing fluence, the excitonic binding energy of the ZnO nanostructure reduces with the increasing fluence [Appendix 10, Figure 5.17]. As the nanoparticles are elongated to nanorods inside the film, without destroying stability of the system, it offers plentiful prospective applications [60,62,63].
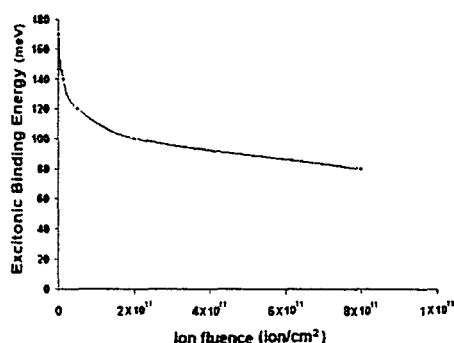
Figure 5.19 : Variation of exciton binding energy due to 80 MeV N^{+6} ion irradiation with increasing fluence

Upon 80 MeV nitrogen ion irradiation, the nanoparticles are elongated inside the matrix and it is possible to keep them perpendicular to the substructure. However as these elongated nanorods are encapsulated in a matrix it will have better stability compared to different kinds of elongated nanostructures developed vertically on a substrate.

Tb doped ZnO (ZnO:Tb) nanorods :

The luminescence response relatively complex for ZnO:Tb nanorods and it becomes more complicated after irradiation. The PL photoluminescence (PL) spectra (λ_{ex}=325 nm) of the nanorods before and after irradiation, are shown in Figure 5.20. In the asymmetrically broadened PL spectra, the defect related emissions dominate the band edge emission of ZnO and hence the band edge emission (~370 nm) is only poorly resolved. The central maxima at ~ 405 nm are ascribed as the emission from the zinc vacancies present in the ZnO lattice. The asymmetric nature of the luminescence patterns is ascribed to the presence of other inherent emission peaks (due to the distributed defect states on the surface and in the interior of a given nanostructured system) at higher wavelengths. In particular, the impression at ~ 430 nm is the emission due to the presence of zinc interstitials. The zinc interstitial related emission becomes more prominent for Tb doped ZnO nanorod system (Figure5.20 (b,b')). Further, for irradiated Tb:ZnO samples, this emission gets suppressed owing to the improvement in zinc vacancy related emission (~405 nm).
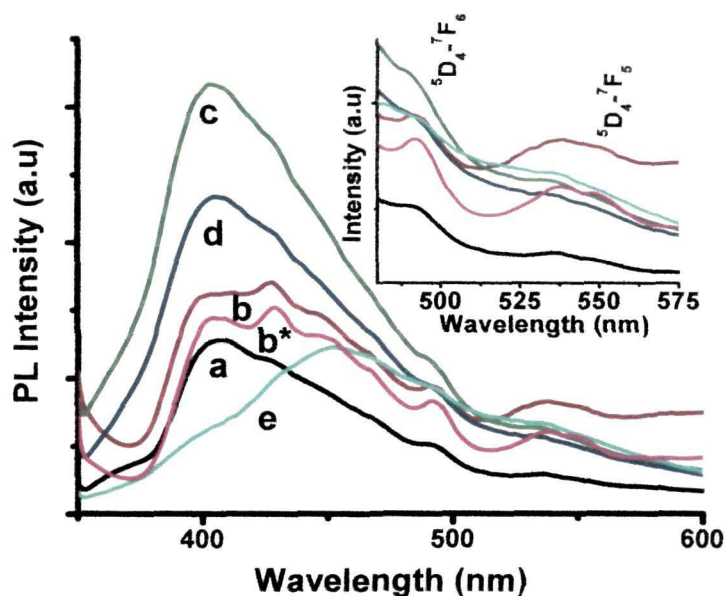
Figure 5.20 : Scheme of various transitions involved in Tb-doped ZnO nanosystem. a) un-irradiated undoped ZnO; b) un-irradiated Tb-doped ZnO nanorods, and Tb-doped ZnO nanorods irradiated with a fluence of c) $5x10^{11}$, d) $2x10^{12}$, and e) $8x10^{12}$ ions/cm^2; respectively. The label 'b*' corresponds to as synthesized Tb doped ZnO where as 'b' represents nanorods after repeated washing and dispersed in PVOH

A feebly resolved peak at ~ 490 nm of the undoped nanorods (Fig. 5.20 (a)) is attributed to the blue emission of ZnO. The same peak corresponding to the Tb doped ZnO nanorods gets enhanced (Fig. 5.20 (b, b*)) because of the superimposition of the Tb^{3+} related $^5D_4$-$^7F_6$ transition which occurs almost in the same wavelength range. Another weakly resolved band with a central maxima ~535 nm is seen for undoped nanorods, that corresponds to the oxygen vacancy related green emission. This peak becomes distinct and broad in the spectrum of Tb doped ZnO nanorods as a result of the overlapping emission pattern arising due to the transition ($^5D_4$-$^7F_5$) of Tb^{3+} at ~548 nm with the aforesaid green emission. The probable transition events are also shown in schematic Figure 5.21. The PL spectra of the N ion irradiated nanorod samples exhibit significant alteration. The PL response of the nanorods, irradiated with a fluence of $5x10^{11}$ ions/cm^2 is more intense than the unirradiated nanorods,

but irradiation with fluence of 2×10^{12} ions/cm^2 exhibits highest PL intensity (Figure 5.21 (b)-(d)). Note that the central *peak-to-blue* and central *peak-to-green* emissions are found to be enhanced for irradiated Tb-doped ZnO nanorods, upto a fluence of 2×10^{12} ions/cm^2. It is expected that upon ion
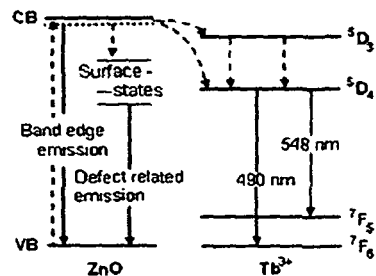
Figure 5.21: Various transitions involved in ZnO:Tb nanosystems.

irradiation the nanorods overcome the PVOH matrix encapsulation allowing recovery of free excitons and resulting in the enhancement of defect related emission. The Tb^{3+} related emission peaks are still in view after irradiation (Figure. 5.20 (c)-(e)). This indicates that Tb^{3+} related peak appears due to the energy transfer from the deep level states to the $^5D_4$ energy level of Tb^{3+} cations (Figure 5.21). While returning from the conduction band, most of the photo-excited electrons relax in the defect states and transfer their energy to the $^5D_4$ energy level of Tb^{3+} resulting in the $^5D_4$-$^7F_6$ and $^5D_4$-$^7F_5$ transitions. The visual evidence of recovery from matrix encapsulation can also be seen in the electron micrographs (Figure. 4.21c in chapter 4). In contrast, the same sample which was irradiated with a fluence of 8×10^{12} ions/cm^2, the PL intensity decreases drastically alongwith a red shift in the PL spectra (Figure 5.20(e)). This indicates that at this fluence, the nanorods get completely dislodged from the supporting matrix, leading to agglomeration events (Fig. 5.20 (e); and 4.21 c,d). The agglomeration leads to the suppression of the zinc vacancy, zinc interstitial related emissions. The agglomerated system is characterized by a disordered phase where quantum confinement effect would no longer valid. However, the Tb-related emission peak remained intact even if the structural ordering was lost. The agglomerated nanosystems' (corresponding to a fluence of 8×10^{12} ions/cm^2) is found to have a symmetric peak at ~455 nm. The quantitative aspects correlating structural modification and luminescence patterns, for rare-earth doped irradiated ZnO nanorods, might form the basis of nanoscale luminescent/display devices.

(d) Modification of luminescence response due to photon illumination

The modification of the luminescence properties of ZnS due to He-Ne laser illumination is studied. In case of non-illuminated ZnS specimen, the peak due to sulfur vacancy (~420 nm) is the most intense peak which dominates all the other defect related peaks (especially zinc vacancy).
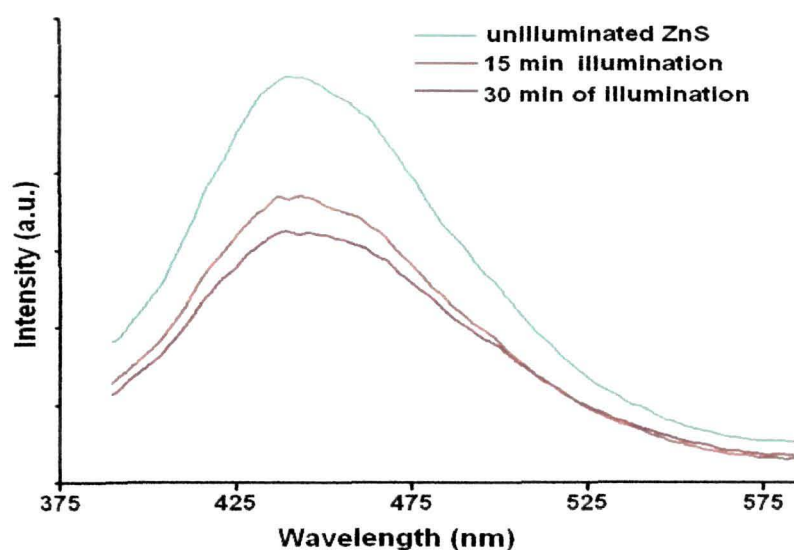
Figure 5.22 : PL spectra of ZnS under laser illumination

After 15 min and 30 min of laser illumination, the peak position remains though remains same, intensity gets reduced by substantial amounts. The TEM micrograph (Figure 4.22) we observe that, upon 15 min of laser illumination the spherical symmetric nanostructures have grown in to larger size as a result of which particle organization is modified. We thus observe a suppression of PL intensity peak indicating drastic reduction of sulfur vacancies. Compared to no illumination for 15 min cases, upon illumination for 15 and 30 min, suppressed defect emission was observed with reduced peak intensity. The asymmetric broadening aspect was intact in all the three cases.

Chapter 6

Conclusion and future directions

With the progressive development of the powerful imaging techniques like SEM, SPM and TEM it has become possible to obtain visual information about nanoscale structures without deteriorating the sample specimen. The development of spherically symmetric as well as elongated ZnS and ZnO nanostructures have been studied extensively following physico-chemical and ion beam approaches. An attempt was made to correlate structure and optoelectronic properties while considering irradiation aspects. Doping with TM elements and a representative rare-earth metal (Tb) has lead to the introduction of definite luminescence centers and hence tunable emission patterns. Development of different nanostructured systems and understanding their light emission properties were the major objectives in the present work.

To be specific, we have fabricated II-VI semiconductor nanostructures namely, ZnS and ZnO, both in spherical as well as in elongated forms. To enhance the stability of the nanoparticles, they are encapsulated in two organic hosts, PVOH and CTAB. Along with the undoped ZnS, TM doped (Mn, Cr, Cu and Co) ZnS nanostructures were also synthesized and characterized. Our investigation on PVOH and CTAB hosts has revealed that the PVOH encapsulated ZnS nanostructures exist in the form of clusters with unavoidable size inhomogeneity. But, CTAB assisted ZnS nanoparticles were well separated and exhibited comparatively uniform size distribution. Similarly, in case of ZnO system, the nanoparticles are found to be well separated and of uniform size in CTAB environment than PVOH. Further, we could efficiently produce elongated ZnS and ZnO nanopatterns (nanorods) in CTAB environment. It has also been possible to vary the length of the ZnO nanorods by varying the physical conditions of the involved reactions. For ion irradiation experiment, we choose three different kinds of ion species (light: 80 MeV N^{+4}, medium: 150 MeV Ti^{+11}, heavy: 100 Ag^{+6}) so as to receive varying energy deposition. In general, after ion irradiation of the ZnS and ZnO nanoscale systems, significant particle growth was observed. But, the nature of

growth varied with the ion and ion fluence used. In case of undoped ZnS nanosystems, the growth was not uniform and possibility of obtaining elongated patterns was found to be unlikely. However, under 150 MeV Ti^{+11} ion irradiation, Cr doped ZnS nanostructures got modified resulting in oblate and elongated structures. As the patterns are found along the direction perpendicular to the beam direction, we expect hammering effect on the nanostructures. Both topography and evolution of magnetic domain boundaries of the irradiated ZnS:Cr structures have supported this unusual behavior. We have found that the ion irradiation has the ability to modify the structure and magnetic domains at definite ion fluences. It was finally observed that a light ion with very low energy deposition has the ability to develop very good elongated nanostructures. By using 80 MeV N^{+4} ion irradiation on spherically symmetric ZnO nanoparticles, elongated nanorods were obtained at a fluence of $2x10^{11}$ ions/cm^2. The best elongated patterns were observed at $8x10^{11}$ ions/cm^2. Also, an attempt was made to elongate ZnS nanostructures through photon illumination using a 2mW He-Ne Laser. Under laser illumination, diffusion of the nanoparticles was observed with instances of small elongation. A detailed investigation is necessary with regard to laser power variation, particle size and host media containing nanoparticles.

Note that, ZnS and ZnO are among the most studied wide band-gap semiconductors and they have potential in luminescent device applications. The properties that attract scientific community include high quantum yield, sharp fluorescence emission, size/shape dependent tunable emission, broad excitation range, high photostability etc. The undoped ZnS nanostructures show intense blue emission even though it was coated with organic host. Basically, the luminescence response of ZnS is due to the sulfur vacancy which can quench out the band-edge and other defect related emissions. By controlling the sulfur vacancy in the synthesis process, the luminescence intensity can be controlled as per requirements. In the same way, TM doped ZnS display typical luminescence patterns. The ZnS:Mn nanostructures show orange yellow emission (~585nm) whose intensity can be precisely tuned by varying the doping concentrations. Similarly, ZnS:Co and ZnS:Cu systems are characterized by their respective responses in the green region of the electromagnetic spectrum. Thus doping of ZnS nanoparticles gives us the color

tunability opportunity along with the intensity. Again, through ion irradiation process with increasing fluence (which results in particle growth), we observed the reduction in sulfur vacancy and luminescence intensity. Photon illumination of ZnS nanostructures embedded in PVOH also shows luminescence suppression with increase of illumination time. On the other hand, nanoscale ZnO shows both band-edge emission (UV emission) and defect related emission (Green emission). In case of ZnO system, the nanoparticles, irrespective of the nature of the host material (PVOH or CTAB) the defect related green emission seems to dominate over the other. Interestingly, in case of nanorods, both the emissions are prominent. The aspect ratio dependent luminescence study (particle-to-rod of different dimension) has revealed that the emission pattern of the ZnO nanostructures can be precisely tuned by controlling the aspect ratio of the nanorods. It was predicted that for chemical sensors (oxygen), the nanoparticles or nanorods with smaller length is useful while for UV optical sensors nanorods of larger dimension are preferable. Further, low ion irradiation of ZnO gave the opportunity to control both kinds of emission characteristics. From the technological application point of view, the vertically aligned elongated ZnO nanostructures formed as a result of ion irradiation is more significant compared to randomly oriented ones obtained through chemical routes. Lastly, Tb doped ZnO nanorods under ion irradiation gives an idea that ($^5D_4 \leftrightarrow ^7F_6$ and $^5D_4 \leftrightarrow ^7F_5$) transitions can be improved as a result of enhancement in the oxygen related defects. The detailed mechanism is presented in one of our recent report [339]

The study of ZnO and ZnS nanostructures is also limited by a different characterization tools as there is always a time-gap between synthesis and analysis. Improvement of the characterization methods is required to understand the mechanism of growth and coalescence. The future study may be planned to use the developed nanostructures for deploying in photovoltaic and optoelectronic prototype devices. The most prospective studies can be as below:

(a) Development of some other binary semiconductor nanostructures

In the present work we have limited our attention to ZnS and ZnO nanoparticles and nanorods. This may be extended to other binary systems (ZnTe, ZnSe etc.) which are also promising candidate in bulk as well as in nanoscale form.

Similarly, doping of ZnS, in this study is restricted to TM and it show luminescence response in certain region of the visible spectrum. Possibility of introduction of rare earth metal doping into ZnS, can uncover the emission response in some other region of the visible spectrum. Integration of such various systems is attractive for the development of white light emitting devices (WLEDS).

(b) Development of luminescent devices

The prototype device making depends on environmental stability and nature of interfacing optics and electronics. Investigation with doped and undoped ZnS nanostructures can be planned to achieve electroluminescence, multicolor luminescence patterns etc. The size and structure dependency can also be considered which need to be encountered by theoretical modeling.

(c) Development of UV sensors:

The size dependent UV color sensing can be considered for biological sensing and imaging. The fluorescent materials have already been proven to be best candidates to replace organic dyes etc.

(d) Ion irradiation/photon illumination:

A comparative study on keV and MeV ion scale of ion irradiation will help not only to understand the role of nanoscale defects but also to correlate size and radiative processes. The fast radiative and slow nonradiative processes can account for the stability of a luminescence pattern.

Finally, 'Nanoscience and Nanotechnology' is still in its infancy and requires involvement of material scientists, physicists, chemists and biologists who can work together in a common platform. The transfer of products from research laboratory to industry has to undergo several tests before making them commercially available. In this regard, waste arrangement and environmental issues need to be addressed.

[1]　R. Birringer and H. Gleiter, *"Encyclopedia of Material Science and Engineering Suppl. "*, Ed. by R. W. Cahn (Pergamon, New York, 1988), Vol. I, p.339

[2]　*Quantum Crystallites and Nonlinear Optics*, L. E. Brus, Appl. Phys. A **53**, 465 (1991)

[3]　*Nanometer-sized semiconductor clusters : materials synthesis, quantum size effects, and photophysical properties*, Y. Wang , N. Herron, J. Phys. Chem. **95**, 525 (1991)

[4]　*Semiconductor clusters, nanocrystals and quantum dots* , A. P. Alivisatos, Science **271**, 933 (1996)

[5]　*Quantized Semiconductor Particles: A novel state of matter for materials science*, H. Weller, Adv. Mater. **5**, 88 (1993)

[6]　*Faraday's diary, Vol. VII, The Royal Institution of Great Brittain*, Ed. by T. Martin, Bell and Sons: London, page 63 (1936)

[7]　*Some modern absorption glasses*, G. Jaeckel, Z. Tech. Physik, **7** (1926) 301

[8]　*Effects of Crystal Surface on the Optical Absorption Edge of AgBr*, C. R. Berry, Phys. Rev. **153**, 989 (1967)

[9]　*Structure and optical absorption of silver iodide microcrystals* , C. R. Berry, Phys. Rev. **161**, 848 (1967)

[10]　*A Physics of Low-Dimensional Systems*, A. Ya Shik, L. G. Bakueva, S. F. Musikhin, S. Rykov, (Under the general editorship of I Il'in, A Ya Shik) (a) V.B. Sandomirskii, Sov. Phys. JETP **16**, 1630 (1963) (b) A.G. Stasenko, Sov. Phys. Sol. State **10**, 186 (1968)

[11]　*Size-dependent surface plasmon resonance in silver silica nanocomposites*, S. Thomas, S. K. Nair, E. M. A. Jamal, S H Al-Harthi, M. R. Varma, M. R. Anantharaman, Nanotechnology **19**, 075710, (2008)

[12]　*Cap-shaped gold nanoparticles for an optical biosensor*, M. Himmelhaus, H. Takei, Sensors and Actuators B, **63** (2000) 24.

[13]　*Self-Assembled Nanoparticle Probes for Recognition and Detection of Biomolecules*, D. J. Maxwell, J. R. Taylor, S. Nie, J. Am. Chem. Soc. **124**, 9606 (2002)

[14]　*A DNA-based method for rationally assembling nanoparticles into macroscopic materials*, C. A. Mirkin, R. L. Letsinger, R. C. Mucic, J. J. Storhoff, Nature **382**, 607 (1996)

[15]　*Bio-Barcodes Based on Oligonucleotide-Modified Nanoparticle*, J.-M. Nam, S. J. Park, C. A. Mirkin, J. Am. Chem. Soc. **124**, 3820 (2002)

[16]　*Nanoparticles for bioanalysis*, S. G. Penn, L. He, M. J. Natan, Current Opinion Chem. Biol. **7**, 609 (2003)

[17] *One-Pot Colorimetric Differentiation of Polynucleotides with Single Base Imperfections Using Gold Nanoparticle Probes*, J. J. Storhoff, R. Elghanian, R. C. Mucic, C. A. Mirkin, R. L. Letsinger, J. Am. Chem. Soc. **120**, (1998) 1959.

[18] *Scanometric DNA Array Detection with Nanoparticle Probes*, T. A. Taton, C. A. Mirkin, R. L. Letsinger, Science **289**, 1757 (2000)

[19] *Solar cells to dye for*, M. Grätzel, Nature **421**, 586 (2003)

[20] *Dye-sensitized solar cells*, M. Gratzel, J. of Photochemistry and Photobiology C: Photochemistry Reviews **4**, 145, (2003)

[21] *Perspectives on the Physical Chemistry of Semiconductor Nanocrystals*, A. P. Alivisatos, J. Phys. Chem. **100**, 13226 (1996)

[22] *The Quantum Mechanics of Larger Semiconductor Clusters ("Quantum Dots")* M. G. Bawendi, M. L. Steigerwald, L. E. Brus, Annu. Rev. Phys. Chem. **41**, 477 (1990)

[23] *Surface electron transfer processes*, VCH:New-York (1995) by R. J. D. Miller, G. L. McLendon, A. J. Nozik, W. Schmickler, F. William, p31

[24] *Clusters &Colloids*, ed. G. Schmid, VCH:New-York (1994)

[25] *Quantum size effect in the optical-spectra of semiconductor micro-crystals*, A. I. Ekimov, A. A. Onushchenko, Sov. Phys. Semicond. **16**, 775 (1982)

[26] *Interband absorption of light in a semiconductor sphere*, A. L. Efros, A. L. Efros, Sov. Phys. Semicond. **16**, 772 (1982)

[27] *Luminescence spectra and Raman excitation profiles in small CdS particles*, G. C. Papavassiliou, J. Solid State Chem. **40**, 330 (1981)

[28] *A simple model for the ionization potential, electron affinity, and aqueous redox potentials of small semiconductor crystallites*. Brus, L. E. J. Chem. Phys. 1983, 79, 5566–5571.

[29] *Electron-electron and electron-hole interactions in small semiconductor crystallites - the size dependence of the lowest excited electronic state*, L. E. Brus, J. Chem. Phys. **80**, 4403 (1984)

[30] *Optical Properties of Semiconductor Nanocrystals*, by S.V. Gaponenko, Cambridge University Press, USA (1998)

[31] *Wannier exciton in microcrystal,s* Y. Kayanuma, Solid state comm. **59**, 406 (1986)

[32] *Quantum-size effects of interacting electrons and holes in semiconductor microcrystals with spherical shape*, Y. Kayanuma, Phys. Rev. B **38**, 9797 (1998)

[33] *Incomplete confinement of electrons and holes in microcrystals*, Y. Kayanuma and H. Momiji, Phys. Rev.B **41**, 10261 (1990).

|34| *Measurement of the size dependent hole spectrum in CdSe quantum dots* D J Norris, A Sacra, C B Murray, and M G Bawendi, Phys Rev Lett 72, 2612 (1994)

|35| *Measurement and assignment of the size-dependent optical spectrum in CdSe quantum dots*, D J Norris and M G Bawendi, Phys Rev B 53, 16338 (1996)

|36| *Size-dependent electronic level structure of InAs nanocrystal quantum dots Test of multiband effective mass theory*, U Banin, C J Lee, A A Guzelian, A V Kadavanich, A P Alivisatos, W Jaskolski, G W Bryant, Al L Efros, M Rosen, J Chem Phys 109, 2306 (1998)

|37| *Simplified LCAO Method for the Periodic Potential Problem*, J C Slater and G F Koster, Phys Rev B 94, 1498 (1954)

|38| *Calculation of the band gap for small CdS and ZnS crystallites*, P E Lippens and M Lannoo, Phys Rev B 39, 10935 (1989)

|39| *A Semi-empirical tight-binding theory of the electronic structure of semiconductors* P Vogl, H P Hjalmarson, J D Dow, J Phys Chem Solids 44, 365 (1983)

|40| *Electronic structure of and quantum size effect in III-V and II-VI semiconducting nanocrystals using a realistic tight binding approach*, R Viswanatha, S Sapra, T Saha- Dasgupta, D D Sarma Phys Rev B 72, 045333 (2005)

|41| *Evolution of the electronic structure with size in II-VI semiconductor nanocrystals*, S Sapra, D D Sarma Phys Rev B 69, 125304 (2004)

|42| *Study of the Growth of Capped ZnO Nanocrystals A Route to Rational Synthesis*, R Viswanatha, D D Sarma Chem Eur J 12, 180 (2006)

|43| *Exciton spectra of semiconductor clusters* M V Rama Krishna and R A Friesner, Phys Rev Lett 67, 629 (1991)

|44| *Solving Schrodinger's equation around a desired energy Application to silicon quantum dots* L W Wang and A Zunger, J Chem Phys 94, (1994) 2158

|45| *Local-density-derived semiempirical pseudopotentials*, L W Wang and A Zunger, Phys Rev B 51, 17398 (1995)

|46| *Pseudopotential calculations of nanoscale CdSe quantum dots*, L W Wang and A Zunger, Phys Rev B 53, 9579 (1996)

|47| (a) *InP quantum dots Electronic structure surface effects, and the red shifted emission* H Fu and A Zunger, Phys Rev B 56, 1496 (1997) (b) *Local-density-derived semiempirical nonlocal pseudopotentials for InP with applications to large quantum dots* H Fu, A Zunger, Phys Rev B 55, (1997) 1642

|48| *Direct Pseudopotential Calculation of Exciton Coulomb and Exchange Energies in Semiconductor Quantum Dots* A Franceschetti and A Zunger, Phys Rev Lett 78, 915 (1997)

[49] *High-Energy Excitonic Transitions in CdSe Quantum Dots,* L. W. Wang and A. Zunger, J. Phys. Chem. B **102**, 6450 (1998)

[50] *Rapid radiative decay and enhanced optical nonlinearity of excitons in a quantum well,* E. Hanamura, Phys. Rev. B **38**, 1228 (1988)

[51] *Very large optical nonlinearity of semiconductor microcrystallites,* E. Hanamura, Phys. Rev. B **37**, 1273 (1988)

[52] *Biexciton states in semiconductor quantum dots and their nonlinear optical properties,* T. Takagahara, Phys. Rev. B **39**, 10206 (1989)

[53] *Excitonic optical nonlinearity and exciton dynamics in semiconductor quantum dots,* T. Takagahara Phys Rev. B **36**, 9293 (1987)

[54] *Polymer-Stabilized Gold Nanoparticles and Their Incorporation into Polymer Matrices,* M. K. Corbierre, N. S. Cameron, M. Sutton, S. G. J. Mochrie, L. B. Lurio, A. Ruhm, and R. B. Lennox, J. Am. Chem. Soc. **123**, 10411 (2001)

[55] *Spherical Assemblies of Semiconductor Nanoparticles in Water-Soluble Block Copolymer Aggregate,* M. Moffitt, H. Vali, A. Eisenberg , Chem. Mater. **10**, 1021 **(1998)**

[56] *From ZnS en0 5 Nanosheets to Wurtzite ZnS Nanorods under Solvothermal Conditions* G Xi, C. Wang, X Wang, Q. Zhang, H. Xiao, J Phys Chem C **112**, 1946 (2008)

[57] *Preparation of ZnS nanotubes via surfactant micelle-template inducing reaction,* R. Lv, C. Cao, Y. Guo, H. Zhu, Journal Of Materials Science **39**, 1575 (2004)

[58] *Spontaneous Polarization-Induced Nanohelixes, Nanosprings, and Nanorings of Piezoelectric Nanobelts,* X. Y. Kong, Z. L. Wang , Nano Lett. **3**, 1625 (2003)

[59] *Three-dimensional crystalline SiC nanowire flowers,* G. W. Ho, A. S. W. Wong, D. J. Kang, M. E. Welland, Nanotechnology **15**, 996 (2004)

[60] *Improved dye-sensitized solar cells with a ZnO-nanoflower photoanode,* C. Y. Jiang,_ X. W. Sun, G. Q. Lo, D. L. Kwong, J. X. Wang , App. Phys Lett. **90**, 263501 (2007)

[62] *Controlled Synthesis of ZnO Nanoflowers and Nanorods by Sonochemical Method,* P. K. Singh, A. Mittal, V. Agarwala, Adv. Mat. Resh. **67**, 277 (2009)

[63] *ZnO Nanobridges and Nanonails,* J. Y. Lao, J Y. Huang, D. Z. Wang, and Z. F. Ren, Nano Letters **3**, 235 (2003)

[64] *Dendritic Nanowire Ultraviolet Laser Array,* Yan H, He R, Johnson J, Law M, Saykally R J and Yang P. J. Am. Chem. Soc. **125**, 4728 (2003)

[65] *Synthesis and characterization of silica nanosprings by a low temperature chemical vapor deposition,* D. Zhang, J. Jasinski, M. Dunlap, M. Badal, V. J. Leppert, V. Katkanant, Appl Phys A **92** , 595 (2008)

|66| *Silver Nanorings. Nanofabrication and Optical Properties*, J. Stern, NNIN REU 2006 Research Accompl. Optics, 106

|67| *Optical Properties of Gold Nanorings*, J. Aizpurua, P. Hanarp, D. S. Sutherland, M. Ka, G. W. Bryant, F. J. G. de Abajo, Phys. Rev. Lett. **90**, 057401 (2003).

|68| *Magnetic Bistability and Controllable Reversal of Asymmetric Ferromagnetic Nanorings*, F. Q. Zhu, G. W. Chern, O. Tchernyshyov, X. C. Zhu, J. G. Zhu, C. L. Chien, Phys. Rev. Lett. **96**, 27205 (2006)

|69| *Helical Microtubules of Graphitic Carbon*, S. Ijima, Nature **354**, 56 (1991)

|70| *Ultralong single-wall carbon nanotubes*, L. X. Zheng, M. J. O'Connell l, S. K. Doorn, X. Z. Liao, Y. H. Zhao, E. A. Akhadov, M. A. Hoffbauer, B. J. Roop, Q. X. Jia, R. C. Dye, D. E. Peterson, S. M. Huang, J. Liu, Y. T. Zhu Nature Materials **3**, 673 (2004)

|71| *Electronic, thermal and mechanical properties of carbon nanotubes*, M. S. Dresselhaus l, G. Dresselhaus, J. C. Charlierand E. Hern'andez, Phil. Trans. R. Soc. Lond. A **362**, 2065 (2004)

|72| *A Carbon Nanotube Field-Emission Electron Source*, W. A. De Heer, A. Chtelain, D. A. Ugarte, Science **270**, 1179 (1995),

|73| *Electronic structure of atomically resolved carbon nanotubes*, J. W. G. Wilder, L. C. Venema, A. G. Rinzler, R. E. Smalley, C. Dekker, Nature **391**, 59 (1998)

|74| *Magnetoconductance of carbon nanotubes*, Lin, M.F. and K.W.K. Shung,. Physical Review B **51**, 7592 (1995)

|75| *Fabrication and growth mechanism of metal (Zn, Sn) nanotube arrays andmetal (Cu, Ag) nanotube/nanowire junction arrays*, C. L. Cheng , J. S. Lin, Y. F. Chen, Materials Letters **62**, 1666 (2008)

|76| *TiO₂ nanotube layers with metallic nanoparticles*, H. Tsuchiya, N. Tokuoka, S. Honda, Y. Shinkai, Y. Shimizu, S. Fujimoto, Journal of Physics: Conference Series **165**, 012037 (2009)

|77| *A simple solution route to ZnS nanotubes and hollow nanospheres and their optical properties*, H. Zhang, S. Zhang, S. Pan, G. Li, J. Hou , Nanotechnology **15**, 945 (2004)

|78| *Fabrication and microstructure analysis on zinc oxide nanotubes*, R M Wang l, Y J Xing, J Xu and D P Yu, New J. of Phy. **5**, 115 (2003)

|79| *Growth of silicon nanowires via gold/silane vapor-liquid-solid reaction*, J. Westwater, D. P. Gosain, S. Tomiya, S. Usui, H. Ruda J. Vac. Sci. Technol. B **15**, 554 (1997)

|80| *Bulk-quantity Si nanowires synthesized by SiO sublimation.* Y. F. Zhang, Y. H. Tang, C. Lam, N. Wang, C. S. Lee, I. Bello, S. T. Lee, J. Crystal Growth **212**, 115 (2000)

|81| *Preparation and photoluminescence of highly ordered TiO_2 nanowire arrays.* Y. Lei, I. D. Zhang, G. W. Meng, G. H. Li, X. Y. Zhang, C. H. Liang, W. Chen, S. X. Wang, App. Phys. Lett. **78**, (2001) 1127.

|82| *Catalytic growth of semiconducting In_2O_3 nanofibers,* C. H. Liang, G. W. Meng, Y. Lei, F. Phillipp, L. D. Zhang, Adv. Materials **13**, 1330 (2001)

|83| *Epitaxial directional growth of indium-doped tin oxide nanowire arrays,* Pho Nguyen, Hou T. Ng, J. Kong, A. M. Cassell, R. Quinn, J. Li, J. Han, M. McNeil, M. Meyyappan P. Nguyen, Nano Letters **3**, 925 (2003)

|84| *Magnetic orderings in Al nanowires suspended between electrodes.* T. Ono, S. Tsukamoto, K. Hirose, Appl. Phys. Lett. **82**, 4570 (2003)

|85| *A simple method for the synthesis of highly oriented potassium-doped tungsten oxide nanowires,* H. Qi, C.Y. Wang, J. Liu, Adv. Mater. **15**, 411 (2003)

|86| *Nanoscale silicon wires synthesized using simple physical evaporation,* D. P. Yu, D. P. Yu, Z. G. Bai, Y. Ding, Q. L. Hang, H. Z. Zhang, J. J. Wang, Y. H. Zou, W. Qian, G. C. Xiong, H. T. Zhou, and S. Q. Feng, Appl. Phys. Lett. **85**, 5104 (2004)

|87| *Amorphous silica nanowires: Intensive blue light emitters,* D. P. Yu, Q. L. Hang, Y. Ding, H. Z. Zhang, Z. G. Bai, J. J. Wang, Y. H. Zou, W. Qian, G. C. Xiong, and S. Q. Feng, Appl. Phys. Lett. **73**, 3076 (1998)

|88| *Functional Nanoscale Electronic Devices Assembled Using Silicon Nanowire Building Blocks,* Y. Cui, C. Lieber, Science **291**, 851 (2001)

|89| *Nanobelts of semiconducting oxides.* Z. W. Pan, ., Z. R. Dai, Z. L. Wang, Science **291**, 1947, (2001)

|90| *Hydrogen-assisted Thermal Evaporation Synthesis of ZnS Nanoribbons on a Large Scale,* Y. Jiang, X. M. Meng, J. Liu, Z. Y. Xie, C. S. Lee, S. T. Lee, Adv. Materials **15**, 323 (2003)

|91| *Fabrication of wurtzite ZnS nanobelts via simple thermal evaporation,* Q. Li, C. Wang, Appl. Phys. Lett. **83**, 359 (2003)

|92| *The selective synthesis of single-crystalline CdS nanobelts and nanowires by thermal evaporation at lower temperature,* C. Li, Z. Liu, Y. Yang1, Nanotechnology **17**, 1851 (2006)

|93| *Single-Crystal CdSe Nanosaws.* C. Ma, Y. Ding, D. Moore, X. Wang, Z.L. Wang, J. Ameri. Chem. Society **126**, 708 (2004)

|94| *Map for the Controlled Synthesis of CdSe Nanowires Nanobelts, and Nanosaws—A Step Towards Nanomanufacturing* Ma, C and Z L Wang, Road Advanced Materials, 2005 2005(17) p 1-6

|95| *Zinc selenide nanoribbons and nanowires,* Y Jiang, X M Meng, W C Yiu, J Liu, J X Ding, C S Lee, S T Lee, J Phys Chem B **108**, 2784 (2004)

|96| *Nanobelt and nanosaw structures of II-VI Semiconductors* Ma, C , et al , International Journal of Nanotechnology **1**, 431 (2004)

|97| *Mathematical Methods for Physicist,* G B Arfken, H J Weber, Academic Press San Diego, (1995)

|98| *Size-Dependent Photoluminescence from Single Indium Phosphide Nanowires,* M S Gudiksen, J Wang, C M Lieber J Phys Chem B **106**, 4036 (2002)

|99| Energy Levels in Embedded Semiconductor Nanoparticles and Nanowires, K K Nanda, F E Kruis, H Fissan, Nano Lett **1**, 605 (2001)

|100| R Dingle, in Festkorperprobleme in *Advances in Solid State Physics,* edited by H J Queisser

|101| *Focus on advanced semiconductor heterostructures for optoelectronics,* M C Amann, F Capasso, A Larsson, M Pessa, New J Phys **11**, 125012 (2009)

|102| *Excitons in semiconductor confined systems* A D'Andrea, R Del Sole, Solid State Commun **74**, 1121 (1990)

|103| *Unified formulation of excitonic absorption spectra of semiconductor quantum wells, superlattices, and quantum wires,* P Lefebvre, P Christol, H Mathieu, Phys Rev B **48** 17308 (1993)

|104| *Band-structure-corrected local density approximation study of semiconductor quantum dots and wires,* J Li, L W Wang, Phys Rev B **72**, 125325 (2005)

|105| *Quantum confinement in ZnO nanorods* Y Gu, I L Kuskovsky, M Yin, S O'Brien, G F Neumark, Appl Phys Lett **85**, 3833 (2004)

|106| *Preparation of Monodisperse CdS Nanocrystals by Size Selective Photocorrosion* H Matsumoto, T Sakata, H Mori, H Yoneyama, J Phys Chem **100** 13781 (1996)

|107| *Synthesis and characterization of nearly monodisperse CdE (E = sulfur selenium tellurium) semiconductor nanocrystallites* C B Murray, D J Norris and M F Bawendi, J Am Chem Soc **115**, 8706 (1993)

|108| *Focus on Dilute Magnetic Semiconductors,* S A Chambers, B Gallagher, New J Phys **10**, 055004 (2008)

|109| *Doping semiconductor nanocrystals,* S C Erwin, L Zu, M I Haftel, A L Efros, T A Kennedy, D J Norris, Nature **436**, 91, (2005)

[110] *Recent developments in rare-earth doped materials for optoelectronics* A J Kenyon, Progress in Quantum Electronics **26**, 225 (2002)

[111] *Red light photoluminescence emission from Mn and Cd co-doped ZnS one-dimensional nanostructures* J Z Liu, P X Yan, G H Yue, J B Chang, D M Qu, R F Zhuo, J Phys D Appl Phys **39**, 2352 (2006)

[112] *Single-nanowire electrically driven lasers*, X Duan, Y Huang, R Agarwal, C M Lieber, Nature **421**, 241 (2003)

[113] *Linearly polarized emission from colloidal semiconductor quantum rod* J T Hu, L S Li, W Yang, L Manna, L W Wang, A P Alivisatos, Science **292**, 2060 (2001)

[114] *Optical properties of manganese-doped nanocrystals of ZnS*, R N Bhargava, D Gallagher, Phys Rev Lett **72** (1994) 416

[115] *Doped nanocrystalline materials — Physics and applications* R N Bhargava, J Lumin **70** (1996) 85

[116] *Quantum Dot Bioconjugates for Ultrasensitive Nonisotopic Detection* W C W Chen, S Nie, Science **281**, 2016 (1998)

[117] *Electron transfer dynamics in MoS2 nanoclusters Normal and inverted behavior*, F Parsapour, D F Kelley, S Craft, J P Wilcoxon, J Chem Phys **104**, 4978 (1996)

[118] *Improved brightness efficiency, and stability of sputter deposited alternating current thin film electroluminescent ZnS Mn by codoping with potassium chloride* K E Waldrip, J S Lewis, Q Zhai, M R Davidson, P H Holloway, S S Sun, Appl Phys Lett **76** (2000) 1276

[119] *Structural and luminescence properties of nanostructured ZnS Mn*, D Adachi, S Hasai, T Toynma, G Okamoto, Appl Phys Lett **77**, 1301 (2000)

[220] *Structure and luminescence of annealed nanoparticles of ZnS Mn*, A D Dinsmore, D S Hsu, S B Qadri, J O Cross, T A Kenndey, H F Gray, B R Datna, J Appl Phys **88**, 4985 (2000)

[121] *Luminescence of nanocrystalline ZnS Cu^{2+}* A A Bol, J Ferwerda, J A Bergwerff, A Meijerink, J Lumin **99**, 325 (2002)

[122] *Photoluminescence and electroluminescence of ZnS Cu nanocrystals in polymeric networks*, J M Huang, Y Yang, S H Xue, B Yang, S Y Liu, J C Shen, Appl Phys Lett **70** (1997) 2335

[123] *Luminescence of Cu^2 and In^3 co-activated ZnS nanoparticles* P Yang, M K Lu, C F Song, D Xu, D R Yuan, X F Cheng, G J Zhou, Opt Mater **20**, 141 (2002)

[124] *Optical properties of Sm-doped ZnS nanocrystals*, T Kushida, A Kurita, M Watanabe, Y Kanematsu, K Hirata, N Okubo, Y Kanemitsu, J Lumin **87**, 466 (2000)

|125| *Wavelength- and angle-selective properties of optical memory effect by interference of multiple-scattered light in Sm-doped ZnS nanocrystals,* A. Kurita, Y. Kanematsu, M. Watanabe, K. Hirata, T. Kushida, J. Lumin. 87, 986 (2000)

|126| *Upconversion luminescence of* Eu^{3+} *and* Mn^{2+} *in* $ZnS:Mn^{2+}$, Eu^{3+} *codoped nanoparticles,* W. Chen, A. G. Joly, J. O. Malm, J. O. Bovin, J. Appl. Phys. 95, 667 (2004)

|127| *Irradiation-induced luminescence enhancement effect of* $ZnS:Mn^{2+}$ *nanoparticles in polymer films,* I. Yu, H. Liu, Y. wang, F. E. Fernandez, W. Jia, L. Sun, C. Jin, D. Li, J. Liu, S. Huang, Opt. Lett. 22, 913 (1997)

|128| *Photoluminescence lifetime of nanocrystalline* $ZnS \cdot Mn^{2+}$, K. Yan, C. K. Duan, Y. Ma, S. D. Xia, J. C. Krupa, Phys. Rev. B 58, 13585 (1998)

|129| *High quality ZnSe, and ZnS nanocrystals formed by activating zinc carboxylate precursors,* .S. L. Lin, N. Pradhan, Y. J. Wang, X. G. Peng Nano Letters 4, 2261 (2004).

·|130| *One-dimensional nanostructures for electronic and optoelectronic devices,* G. Shen, D. Chen, Front. Optoelectron. China 3, 125 (2010)

|131| *Crystal Orientation-Ordered ZnS Nanowire Bundles,* D. Moore, Y. Ding, Z.L. Wang, J. Am. Chem. Soc. 126, 14372 (2004)

|132| *Conversion of ZnO Nanowires into Nanotubes with Tailored Dimensions,* J. Elias, R. T. Zaera, G. Y. Wang, C. L. Clment, Chem. Mater. 20, 6633 (2008)

|133| *Dvices and chemical sensing applications of metal oxide nanowires,* G. Shen, P. C. Chen, K. Ryu, C. Zhou, J. Mater. Chem. 19 828 (2009)

|134| *Vertical nanowire light-emitting diode,* R. Konenkamp, R.C. Word, C. Schlegel, Appl. Phys. Lett. 85 (2004) 6004

|135| *Preparation of ZnS nanorods by a liquid crystal template,* D. Zang, L. Qi, H. Cheng, Ma. J. Colloid Interface Sci. 246, 413 (2002).

|136| *Synthesis and properties of CdSe/ZnS core/shell nanorods,* T. Mokari, U. Banin. 15, 2955 (2003)

|137| *Formation of ZnS nanorods by simple evaporation technique,* S. Velumani, J. A. Ascencio, App. Phys. A 79, 153 (2004).

|138| *Synthesis of ZnS nanorods by annealing precursor ZnS nanoparticles in NaCl flux,* C. Lan, K. Hong, W. Wang, G. Wang. Solid State Commun. 125, 455 (2003).

|139| (a) *Rectangular porous ZnO-ZnS nanocables and ZnS nanotubes,* X. Wang, P. Gao, J. Li, C. J. Summers, J. L. Wang. Adv. Mater. 14, 1732 (2002)

(b) *Preparation of ZnS nanotubes via surfactant micelle-template inducing reaction,* R. Lv, C. Cao, Y. Guo, H. Zhu, J. Mat. Sci. 39, 1575 (2004)

|140| *Wurtzite ZnS nanosaws produced by polar surfaces,* D Moore, C Ronning, C Ma, Z L Wang Chem Phys Lett **385**, 8 (2004)

|141| *Wurtzite ZnS Nanosaws produced by polar surfaces,* D Moorea, C Ronninga, C Maa, Z L Wang, Chem Phys Lett **385**, 8 (2004)

|142| *Nanobelts Nanocombs and Nano-windmills of Wurtzite ZnS,* C Ma, D Moore, J Li, Z L Wang, Advanced Materials **15**, 228 (2003)

|143| *Hierarchical Structured Nanohelices of ZnS* D Moore, Y Ding, Z L Wang, Angewandte Chem Inter Ed **45**, 5150 (2006)

|144| *On the Incorporation of Trivalent Rare Earth Ions in II–VI Semiconductor Nanocrystals,* A A Bol, R V Beek, A Meijerink, Chem Mater **14**, 1121 (2002)

|145| *Handbook of Nanophase and Nanostuctured Materials—Synthesis,* ed by Wang (Eds), Z L Wang, Z Zhang, Y Liu, Tsinghua University Press and Kluwer Academic/Plenum Publishers, (2003)

|146| *Luminescence characteristics of impurities-activated ZnS nanocrystals prepared in microemulsion with hydrothermal treatment* S J Xu, S J Chua, B Liu, L M Gan, C H Chew, G Q Xu, Appl Phys Lett **73**, 478 (1998)

|147| *Luminescence enhancement of core-shell ZnS Mn/ZnS nanoparticle,* L X Cao, J H Zhang, S L Ren, S H Huang, Appl Phys Lett **80**, 4300 (2002)

|148| *Photophysical Properties of ZnS Nanoclusters with Spatially Localized Mn^{2+},* K Sooklal, B S Cullum, S M Angel, C J Murphy, J Phys Chem **100**, 4551 (1996)

|149| *Luminescence of Mn^2 doped ZnS nanocrystallites* C M Jin, J Q Yu, L D Sun, K Dou, S G Hou, J L Zhao, Y M Chen, S H Huang, J Lumin **315**, 66 (1996)

|150| *Synthesis of ZnS nanorods by annealing precursor ZnS nanoparticles in NaCl flux,* C Lan, K Hong, W Wang, G Wang, Solid State Comm **125**, 455 (2003)

|151| *Formation and Photoluminescence of Zinc Sulfide Nanorods,* S Senthilkumaar, R T Selvi, J Appl Sci **8**, 2306 (2008)

|152| *From ZnS eno_s Nanosheets to Wurtzite ZnS Nanorods under Solvothermal Conditions* G Xi, C Wang, X Wang, Q Zhang, H Xiao, J Phys Chem C **112**, 1946 (2008)

|153| *Wurtzite ZnS nanosaws produced by polar surfaces,* D Moore, C Ronning, C Ma, Z L Wang, Chem Phys Lett **385**, 8 (2004)

|154| *Formation of ZnS nanorods by simple evaporation technique,* S velumani, J A Ascencio Appl Phys A **79**, 153 (2004)

|155| *Temperature-Controlled Catalytic Growth of ZnS Nanostructures by the Evaporation of ZnS Nanopowders* X S Fang, C H Ye, L D Zhang, Y H Wang, Y C Wu, Adv Func Mater **15**, 63 (2005)

[156] *Template-free ZnS nanorod synthesis by microwave irradiation,* M V Limaye, S Gokhale, S A Acharya, S K Kulkarni, Nanotechnology **19,** 415602 (2008)

[157] *Biocompatible ZnO/Au Nanocomposites for Ultrasensitive DNA Detection Using Resonance Raman Scattering,* L Yichun, Z Mingya, S Guiye, L Yajun, H Baiqu and Y Guoliang J Phys Chem B **112,** 6484 (2008)

[158] *Zinc oxide nanorod for intracellular pH sensing,* S M Al-Hilli, R T Al-Mofarji, M Willander, Appl Phys Lett **89,** 173119 (2006)

[159] *Functionalizing Zn- and O-terminated ZnO with thiols* P W Sadik, S J Pearton, D P Norton, E Lambers, F Ren, J Appl Phys **101,** 104514 (2007)

[160] *ZnO Spintronics and Nanowire Devices,* S J Pearton, D P Norton, Y W Heo, L C Tien, M P Ivill, Y Li, B S Kang, F Ren, J Kelly, A F Heard, J Electro Materials **35,** 862 (2006)

[161] *Manganese-doped ZnO nanobelts for spintronics* C Ronning, P X Gao, Y Ding , Z L Wang, D Schwen, Appl Phys Lett **84,** 783 (2004)

[162] *Spin Manipulation in Co-Doped ZnO* X Qingyu, L Hartmann, Z Shengqiang, A Mcklich, M Helm, G Biehne, H Hochmuth, M Lorenz, M Grundmann, H Schmidt Phys Rev Lett **101,** 076601 (2008)

[163] *Zinc oxide nanowires controlled low temperature growth and some electrochemical and optical nano-devices,* M Willander, L L Yang, A Wadeasa, S U Ali, M H Asif, Q X Zhao, O Nur, J Mater Chem **19,** 1006 (2009)

[164] *A comparative analysis of deep level emission in ZnO layers deposited by various methods,* H A Ahn, Y Y Kim, D C Kim, S K Mohanta, H K Cho, J Appl Phys **105,** 013502 (2009)

[165] *Blue-yellow ZnO homostructural light-emitting diode realized by metalorganic chemical vapor deposition technique,* W Liu, S L Gui, J D Yel, S M Zhu, S M Liu, X Zhou, R Zhang, Y Shi, Y D Zheng, Y Hang, C L Zhang, Appl Phys Lett **88,** 092101 (2006)

[166] *A comparative analysis of deep level emission in ZnO layers deposited by various methods* H A Ahn, Y Y Kim, D C Kim, S K Mohanta, H K Cho, J Appl Phys **105,** 013502 (2009)

[167] *Linearly Polarized Emission from Colloidal Semiconductor Quantum Rods* J Hu, L Li, W Yang, L Manna, L Wang, A P Alivisatos, Science **292,** 2060 (2001) repeat

[168] *Origin of defect emission identified by polarized luminescence from aligned ZnO nanorods,* N E Hsu, W K Hung, and Y F Chen, J Appl Phys **96,** 4671 (2004)

[169] *Hybrid Nanorod-Polymer Solar Cells,* V Huynth, J J Dittmer, A P Alivisatos, Science **295,** 2425 (2002)

[170] *Lasing from Semiconductor Quantum Rods in a Cylindrical Microcavity*, M. Kazes, D.Y. Lewis, Y. Ebenstein, T. Mokari, U. Banin, Adv. Mater. **14**, 317 (2002)

[171] *Light amplification in semiconductor nanocrystals Quantum rods versus quantum dots*, H. Htoon, J.A. Hollingworth, A.V. Malko, R. Dickerson, V.I. Klimov, Appl. Phys. Lett. **82**, 4776, (2003)

[172] *The effect of the interlayer design on the electroluminescence and electrical properties of n-ZnO nanorod/p-type blended polymer hybrid light emitting diodes*, A. Wadeasa, O. Nur, M. Willander, Nanotechnology **20**, 065710 (2009)

[173] *Organic/inorganic heterostructures for enhanced electroluminescence*, Z. Huang, Z. Xu, S. Zhao, Y. Li, F. Zhang, L. Song, Y. Wang, X. Xu, Solid State Commun. **142**, 417 (2007)

[174] *A Laser Ablation Method for the Synthesis of Crystalline Semiconductor Nanowires*, A. M. Morales, C. M. Lieber, Science **279**, 208 (1998).

[175] *Realization of Gated Field Emitters for Electrophotonic Applications Using Carbon Nanotube Line Emitters Directly Grown into Submicrometer Holes*, Y. H. Lee, Y. T. Jang, D. H. Kim, J. H. Ahn, B. K. Ju. Adv. Mater. **13**, 479 (2001)

[176] *Nanowires: Small is beautiful*, G. Fasol, Science **280**, 545 (1998)

[177] *Chemistry and Physics in One Dimension: Synthesis and Properties of Nanowires and Nanotubes*, J. Hu., T. W. Odom and C. M. Leiber, Acc. Chem Res. **32**, 435 (1999)

[178] *Nanophotonic switch using ZnO nanorod double-quantum-well structures*, T. Yatsui, S. Sangu, T. Kawazoe, M. Ohtsu, S. J. An, J. Yoo, G. C. Yi, Appl. Phys. Lett. **90**, 223110 (2007)

[179] *Ferromagnetic Cr-doped ZnO for spin electronics via magnetron sputtering*, B. K. Roberts, A. B. Pakhomov, V. S. Shutthanandan, K. M. Krishnan, J. Appl. Phys. **97**, 10D310 (2005)

[180] *Magnetic and electric properties of transition-metal-doped ZnO films*, K. Ueda, H. Tabata, T. Kawai, Appl. Phys. Lett. **79**, 988 (2001)

[181] Bunn C W 1935 Proc. Phys. Soc. Lond. 47 835

[182] *A hybrid green light-emitting diode comprised of n-ZnO/(InGaN/GaN) multi-quantum-wells/p-GaN*, C. Bayram, F. Hosseini, F. H. Tehrani, D. Rogers, M. Razeghi, Appl. Phys. Lett. **93**, 081111 (2008)

[183] *Laser emission of low-threshold excitation from ZnO nanowires*, L. Cao, B. Zou, C. Li, Z. Zhang, S. Xie, G. Y. Beijing, Euro. phys. Lett., **68**, 740 (2004)

[184] *Vapor- liquid-solid mechanism of single crystal growth*, R S Wagner and W C Ellis, Appl. Phys. Lett. **4**, 89 (1964)

|185| *Zinc oxide nanowires and nanorods fabricated by vapour-phase transport at low temperature* C X Xu, X W Sun, Z L Dong, M B Yu, T D My, X H Zhang, S J Chua, T J White, Nanotechnology 15, 839 (2004)

|186| *Formation and properties of ZnO nano-particles from gas phase synthesis processes*, H Kleinwechter, C Janzen, J Knipping, H Wiggers, P Roth J Mater Sci 37, 4349 (2002)

|187| *Spontaneous Polarization-Induced Nanohelixes, Nanosprings, and Nanorings of Piezoelectric Nanobelts*, X Y Kong, Z L Wang, Nano Lett 3, 1625 (2003)

|188| *Formation of ZnO nanostructures by a simple way of thermal evaporation*, B D Yao, Y F Chan, N Wang, Appl Phys Lett 81, (2002) 757

|189| *Catalytic growth of ZnO nanotubes*, X Kong, X Sun, X Li, and Y Li, Mater Chem Phys 82, 997 (2003)

|190| *Photoelectrochemical Properties of Highly Oriented ZnO Nanotube Array Films on ITO Substrates* M Guo, P Diao, S M Cai, Chinese Chem Lett 15, (2004) 1113

|191| *Optical properties of the ZnO nanotubes synthesized via vapor phase growth*, Y J Xing, Z H Xi, Z Q Xue, X D Zhang, J H Song, R M Wang, J Xu, Y Song, S L Zhang, D P Yu, Appl Phys Lett 83, 1689 (2003)

|192| *Self-catalytic synthesis and photoluminescence of ZnO nanostructures on ZnO nanocrystal substrates*, W D Yu, X M Li, and X D Gao, Appl Phys Lett 84, 2658 (2004)

|193| *Effect of zinc sources on the morphology of ZnO nanostructures and their photoluminescence properties*, W D Yu, X M Li, X D Gao, P S Qiu, W X Cheng, and A L Ding, Appl Phys A 79, 453 (2004)

|194| *Low-field electron emission from tetrapod-like ZnO nanostructures synthesized by rapid evaporation*, Q Wan, K Yu, T H Wang, and C L Lin, Appl Phys Lett 83, 2253 (2003)

|195| *Stable field emission from tetrapod-like ZnO nanostructures* Q H Li, Q Wan, Y J Chen, T H Wang, H B Jia, D P Yu, Appl Phys Lett 85, 636 (2004)

|196| *Zinc oxide nanowires controlled low temperature growth and some electrochemical and optical nano-devices* M Willander, L L Yang, A Wadeasa, S U Ali, M H Asif, Q X Zhao, O Nur, J Mater Chem 19, 1006 (2009)

|197| *Solid Au nanoparticles as a catalyst for growing aligned ZnO nanowires a new understanding of the vapour–liquid–solid process*, M Kirkham, X Wang, Z L Wang, R L Snyder, Nanotechnology 18, 365304 (2007)

|198| *MOCVD growth of ZnO nanostructures using Au droplets as catalysts* V E Sandan, D J Rogers, F H Tehrani, R McClintock, M Razeghi, H J Drouhin, M C Clochard, V Sallet, G Garry, F Fayoud Proc SPIE. **6895**, 68950Z (2008)

|199| *Au-assisted growth approach for vertically aligned ZnO nanowires on Si substrate* G Zhang, A Nakamura, T Aoki, J Temmyo, Y Matsui Appl Phys Lett **89** 113112 (2006)

|200| *Electrodeposition of ZnO nanorods for device application*, B Postels, A Bakin, H Wehmann, M Suleiman, T Weimann, P Hinze, A Waag, Appl Phys A **91**, 595 (2008)

|201| *ZnO nano-rods synthesized by nano-particle-assisted pulsed-laser deposition* T Okada, B H Agung, Y Nakata, Appl Phys A **79**, 1417 (2004)

|202| *Self-assembly of densely packed and aligned bilayer ZnO nanorod arrays* L Chow, Lupan, H Heinrich, G Chai, Appl Phys Lett **94**, 163105 (2009)

|203| *Growth of ZnO nanorods by aqueous solution method with electrodeposited ZnO seed layers* Z Liu, E Lei, J Ya, Y Xin, Appl Surf Sci **255**, 6415 (2009)

|204| *Seeded growth of ZnO nanorods from NaOH solutions* M Breedon, C Rix, K Kalantar-zadeh, Mater Lett **63**, 249 (2009)

|205| Synthesis and size control of ZnO nanorods by conventional pulsed-laser deposition without catalyst, Z W Liu, C K Ong, Mater Lett **61**, 3329 (2007)

|206| *Nucleation control for ZnO nanorods grown by catalyst-driven molecular beam epitaxy* L C Tien, S J Pearton, D P Norton, W T Hung, F Ren, Appl Surf Sci **253**, 4620 (2007)

|207| *Nanostructures & nanomaterials synthesis properties & applications* By Guozhong Cao, Imperial college press, UK

|208| *Molecular Beam Epitaxy - Applications to Key Materials* by Farrow, R F C (1995) William Andrew Publishing/Noyes, New York

|209| *Molecular beam epitaxy growth mechanism and wire width control for formation of dense networks of narrow InGaAs quantum wires* C Jiang, T Muranaka, H Hasegawa **63**, 293 (2002)

|210| *Origin of non-uniformity in MBE grown nanometer-sized InGaAs ridge quantum wires and its removal by atomic hydrogen-assisted cleaning* Thin Solid Films **380**, 189 (2000)

|211| Application of selective epitaxy to fabrication of nanometer scale wire and dot structures, A Lebens, C S Tsai, K J Vahala, T F Kuech, Appl Phys Lett **56**, 2642 (1990)

[212]   *Surface and interface properties of nanocrystalline semiconductors,* S N Sahu, B K Patel, S N Behera, K K Nanda, Ind J Phys A **74**, 93 (2000)

[213]   *Electrodeposition of nanostructured coatings and their characterization—a review,* I Gurrappa, L Binder, Sci Technol Adv Mater **9**, 043001 (2008)

[214]   *Spectroscopic and structural characterization of electrochemically grown ZnO quantum dots* S Mahamuni, K   Borgoham, B S Bendre, V J Leppert, S Risbud, J Appl Phys **85**, 2861 (1999)

[215]   *The size control of silver nano-particles in SiO2 matrix film*   K Kurihara, C Rockstuhl, T Nakano, T Arai, J Tominaga, Nanotechnology **16**, 1565 (2005)

[216]   *Characterization of nano-structured TiN thin films prepared by R F magnetron sputtering* T S Kima, S S Parkb, B T Leec, Materials Letters, **59**, 3929 (2005)

[217]   *Structure, mechanical and tribological properties of d c magnetron sputtered TiB₂ and TiB₂(N) thin films,* H Denga, J Chena, R B Inturia and J A Barnarda, Surface and Coatings Technology **76**, 609 (1995)

[218]   *Ion-assisted nanorod growth by dc magnetron sputtering* A V Rogov, S S Fanchenko, A E Varfolomeev, physica status solidi **202**, 2737 (2005)

[219]   *Quantum size effect in silicon nanocrystals prepared by dc magnetron sputtering* S K Bera, S Chaudhuri, A K Bandyopadhyay , B R Chakraborty, A K Pal, J Phys D Appl Phys **34**, 273 (2001)

[220]   *High spatial density nanocrystal formation using thin layer of amorphous Si₀₇Ge₀₃ deposited on SiO₂* Yoon T S, Kwon J Y, lee D H, Kim K B, Min S H, Chae D H, Kim D H, Lee J D, Park B G, Lee H L, J Appl Phys **87**, 2449 (2000)

[221]   *Iron nanoparticles produced by high-energy ball milling* J E Muñoz1, J   Cervantes, R Esparza, G Rosas, J Nanopart Res **9**, 945 (2007)

[222]   *Visible photoluminescence of Ge microcrystals embedded in SiO₂ glassy matrices* L T Canham,, Appl Phys Lett **59**, 3168 (1991)

[223]   *Visible photoluminescence of Ge microcrystals embedded in SiO₂ glassy matrices* Y Maeda, M A Tsumkamato, Y Yazawa, Y Kanemitsu, Y Matsumoto, Appl Phys Lett **59**, 3168 (1999)

[224]   *Nucleation control of silicon on silicon oxide for low-temperature CVD and silicon selective epitaxy* M Kato, T Sato, J Murota, N Mikoshiba, J Cryst Growth **99** 240 (1990)

[225]   Preparation and properties of nanocrystalline semiconductor selenium films, A Umehera, S Nitta, H Furukawa, S Nonomura, Appl Surface Sci **119**, 176 (1997)

|226| *GaAs tetrahedral quantum dot structures fabricated using selective area metalorganic chemical vapor deposition,* T. Fukui, S. Ando, Y. Tokura, T. Toriyama, Appl. Phys. Lett. **58**, 2018 (1991)

|227| *Formation and characterization of coupled quantum dots (CQDs) by selective area metalorganic vapor phase epitaxy,* K Kumakura, J. Motohisa, T. Fukui T, J. Cryst. Growth **170**, 700 (1997)

|228| *Nanomaterials Chemistry- Recent Developments and New directions,* ed by C. N. R. Rao, A. Muller, A. K. Cheetham, Wiley-VCH Verlag GmbH & Co. KGaA (2007)

|229| *Nanochemistry a chemical approach to nanomaterials,* by Geoffrey Ozin and Andre Arsenault, Cambridge: Royal Society of Chemistry (2005)

|230| Handbook of Nanostructured Materials and Nanotechnology- Vol 1: synthesis and processing, ed by H. S Nalwa, Academic Press, USA

|231| On the Ligand's Role in the Fluorescence of Gold Nanoclusters, Z. Wu, R. Jin, Nano Lett. **10**, 2568 (2010)

|232| *Enzymatic synthesis of a drug delivery system based on polyhydroxyalkanoate-protein block copolymers,* H. N. Kim , J. Lee , H. Y. Kim, Y. R. Kim, Chem. Commun. **46**, 7104, (2009)

|233| *Chiral II-VI Semiconductor Nanostructure Superlattices Based on an Amino Acid Ligand,* J. N. Rebilly, P. W. Gardner, G. R. Darling, J. Bacsa, M. J. Rosseinsky, Inorg. Chem. **47**, 9390 (2008)

|234| *Structure of capped cadmium selenide clusters by EXAFS,* M. A. Marecus, W. Flood, M. Stiegerwald, L. E. Brus, M. J. Bawendi, Phys. Chem **95**, 1572 (1991)

|235| Stability of silver cluster in zeolite A and Y catalysts, T. Yamamoto, S. Takenaka, T. Tanaka, T. Baba, J. Phys.. Conf. Ser. **190**, 012171 (2009)

|236| *Amorphous Polysilsesquioxanes as a Confinement Matrix for Quantum-Sized Particle Growth Size Analysis and Quantum Size Effect of CdS Particles Grown in Porous Polysilsesquioxanes,* K. M. Choi, K. J. Shea, J. Phys Chem. **98**, 3207 (1994)

|237| *Quantum confinement effects of CdS nanocrystals in a sodium borosilicate glass prepared by the sol□gel process,* H. Mathieu, T. Richard, J. Allegre, P Lefebvre, G. Arnaud, W. Granier, L. Boudes, J. L. Marc, A. Pradel, M. Ribes, J. Appl. Phys. **77**, 287 (1995)

|238| *Semiconductor crystallites a class of large molecules,* M. L. Steigerwald, L. E. Brus, Acc Chem Res **23**, 183 (1990)

|239| *Synthesis of cadmium sulfide in situ in reverse micelles influence of the preparation modes on size, polydispersity, and photochemical reactions* M. P. Pileni, L. Motte, C. Petit, Chem. Mater. **4**, 338 (1992)

[240] Semiconductor particles in bilayer lipid membranes. Formation, characterization, and photoelectrochemistry, X. K. Zhao, S. Baral, R. Rolandi, J. H. Fendler, J. Am. Chem. Soc. **110**, 1012 (1988)

[241] Polymer-trapped semiconductor particles, Walter Mahler, Inorg. Chem. **27**, 435 (1988)

[242] *Ultrasmall particles of cadmium selenide and cadmium sulfide formed in Nafion by an ion-dilution technique*, E. S. Smotkin, R. M. Brown, L. K. Rabenberg, K. Salomon, A. J. Bard, Al. Campion, M. A. Fox, T. E. Mallouk, S. E. Webber, J. M. White, J. Phys. Chem. **94**, 7543 (1990)

[243] *Site-specific growth of Zno nanorods using catalysis-driven molecular-beam epitaxy*, Y. W. Heo, V. Varadarajan, M. Kaufman, K. Kim, D. P. Norton, F. Ren, P. H. Fleming, Appl. Phys. Lett. **81**, 3046 (2002).

[244] *A two-step obtainment of quantum confinement in ZnO nanorods*, A C Mofor, A. El-Shaer, M. Suleiman, A. Bakin, A. Waag Nanotechnology **17**, 4859 (2006)

[245] *Focused-ion-beam fabrication of ZnO nanorod-based UV photodetector using the in-situ lift-out technique*, O. Lupan, L. Chow, G. Chai, L. Chernyak, O. Lopatiuk-Tirpak, H. Heinrich, Physica Status Solidi A, 2673 (2008)

[246] *Nanoscale silicon prepared on different substrates using electron-beam evaporation and their field-emission property*, X. Xie, Q. Wan, W. Liu, C. Men, Q. Lin, C. Lin , Applied Surface Science **217**, 39 (2003)

[247] *Laser-Assisted Catalytic Growth of Single Crystal GaN Nanowires*, X. Duan, C. M. Lieber, J. Am. Chem. Soc. **122**, 188 (2000)

[248] *Boundary angle dependence of magnetoresistance induced by tilted nanocolumn boundaries in $La_{0.7}Sr_{0.3}MnO_3$ grown on step-edged (100) GaAs substrates*, I. Satoh, T. Kobayashi, J. Appl. Phys. **91**, 6529 (2002).

[249] *Ordered Arrays of Ferroelectric Nanoparticles by Pulsed Laser Deposition on PS-b-4VP(PDP) Supramolecule-Based Templates*, Z. V. Wendy, A. H. G. Vlooswijk, A. Ferri, A. M. Andringa, B. Noheda, G. T. Brinke, Chem. Mater. **21**, *4719 (2009)*,

[250] *Spontaneous Ordering of Oxide Nanostructures*, S. Aggarwal, A. P. Monga, S. R. Perusse, R. Ramesh, V. Ballarotto, E. D. Williams, B. R. Chalamala, Y. Wei, R. H. Reuss, Science **287**, 2235 (2000)

[251] *A simple large-scale synthesis of very long aligned silica nanowires*, J. Q. Hu, Y. Jiang, X. M. Meng, C. S. Lee, and S. T. Lee, Chem.Phys. Lett. **367**, 339 (2003)

[252] Self-organized, ordered array of coherent orthogonal column nanostructures in epitaxial $La_{0.8}Sr_{0.2}MnO_3$ thin films , J. C. Juang, E. I. Meletis, and K. I. Gnanasekar, Appl. Phys. Lett. **80**, 4831 (2002).

|253| *Fabrication of vertically aligned ultrafine ZnO nanorods using metal–organic vapor phase epitaxy with a two-temperature growth method,* K Kitamura, T. Yatsui, M. Ohtsu, G C Yi, Nanotechnology **19**, 175305 (2008)

|254| *Synthesis of optical quality ZnO nanowires utilizing ultrasonic spray pyrolysis* M. T. Htay, Y. Tani, Y. Hashimoto, K. Ito, J Mater Sci: Mater Electron **20**, S34 (2009)

|255| *Highly Oriented ZnO Nanorod Arrays by a Novel Plasma Chemical Vapor Deposition Process,* D. Bekermann, A. Gasparotto, D Barreca, L. Bovo, A. Devi, R. A. Fischer, O. I. Lebedev, C. Maccato, E. Tondello, G. V. Tendeloo, Cryst. Growth Des. **10**, 2011 (2010)

|256| *Growth of GaN nanowires by ammoniating Ga$_2$O$_3$ thin films deposited on quartz with radio frequency magnetron sputtering ,* L Yang, C. Xue, C. Wang, H. Li, Nanotechnology **14**, (2003) 50–52 PII: S0957-4484(03)53122-1

|257| *Preferential Growth of Long ZnO Nanowire Array and Its Application in Dye-Sensitized Solar Cells,* C Xu, P Shin, L. Cao, D. Gao, J. Phys. Chem C **114**, 125 (2010)

|258| *Cuprite Nanowires by Electrodeposition from Lyotropic Reverse Hexagonal Liquid Crystalline Phase,* L. Huang, H. Wang, Z. Wang, A. Mitra, D. Zhao, and Y. Yan, Chem. Mater. **14**, 876 (2002).

|259| *Fabrication and optical properties of large-scale uniform zinc oxide nanowire arrays by one-step electrochemical deposition technique,* M. J. Zheng, L. D. Zhang, G. H. Li, and W. Z. Shen, Chem. Phys. Lett **363**, 123 (2002).

|260| *Nanowire manipulation on surfaces through electrostatic self-assembly and magnetic interactions* M. G Bellino, E J. Calvo, G J Gordillo, Physica Status Solidi (RRL) **3**, 1 (2008)

|261| *Langmuir–Blodgett Silver Nanowire Monolayers for Molecular Sensing Using Surface-Enhanced Raman Spectroscopy,* A Tao, F. Kim, C. Hess, J. Goldberger, R. He, Y. Sun, Y. Xia, P. Yang , Nano Letters **3**, 1229 (2003)

|262| *Growth of elongated nanostructures,* D. G. Vlachos, Materials Science and Engineering A **204**, 90 (1995)

|263| *One-Dimensional Nanostructures (Lecture Notes in Nanoscale Science and Technology)* ed by Z. M. Wan , Springer (2008)

|264| *Modification of yttrium-iron-oxide nanoparticle films using inductively-coupled plasma annealing,* K. Takenaka, H. Nakayama, Y. Setsuhara, H. Abe, K. Nogia, Surface and Coatings Technology **202**, 5336 (2008)

|265| *Modification of metal nanoparticle in SiO₂ by thermal oxidation,* H. Amekura, Y. Takeda, K. Kono, H. Kitazawa, N. Kishimoto, Rev Adv Mater. Sci. 3, 178 (2003)

|266| *The effect of seed layer on morphology of ZnO nanorod arrays grown by hydrothermal method,* Y. Taoa, M. Fu, A. Zhaoa, D. Hea, Y. Wanga

aKey Laboratory of Luminescence and O

|267| *Nanostructuring of silicon (100) using electron beam rapid thermal annealing,* S. Johnson, A. Markwitz, M. Rudolphi, H Baumann, J. Appl Phys. 96, 605 (2004)

|268| *Evaluation of Organic Monolayers Formed on Si (111) Exploring the Possibilities for Application in Electron Beam Nanoscale Patterning,* T. Yamada, N. Takano, K. Yamada, S. Yoshitomi, Tetsuya Osaka, Jpn. J. Appl. Phys 40 4845 (2001)

|268| *Laser-induced modification of polymericbeads coated with gold nanoparticles,* I. Alessandri, L. E. Depero, Nanotechnology 19 (2008) 305301 ,

|269| *Ion beam for synthesis and modification of nanostructures,* D. K. Avasthi, J. C. Pivin, Current Science 98, 780 (2010)

|270| *Single mode microwave irradiation to improve the efficiency of polymer solar cell based on poly (3-hexylthiophene) and fullerene derivative,* O. Yoshikawa, T. Sonobe, T. Sagawa, S. Yoshikawa, Appl. Phys. Lett. 94, 083301 (2009)

|271| *Microwave Effects in Silicon Low Dimensional Nanostructures,* P., Enrico, L. Rossella, F. Marco, Journal of Nanoscience and Nanotechnology 10, 2650, (2010)

|272| *Control of the synthesis of nanostructured materials under laser and microwave irradiation,* M. D. Bal'makov, G. M. Muradova, Glass Physics and Chemistry 36, 116 (2010)

|273| *Nano-structure formed by nanosecond laser annealing on amorphous Si surface,* D. Klinger, E. Łusakowska, D. Zymierska, Materials Science in Semiconductor Processing 9, 323 (2006)

|274| *Effects of Temperature on Laser-Induced Shape Modification of Silver Nanoparticles Embedded in Glass,* A.Stalmashonak, A. A.Unal, H.Graener, G. Seifert, J. Phys. Chem. C 113, 12028, (2009),

|275| *Direct ArF laser photopatterning of metal oxide nanostructures prepared by the sol–gel route,* H. Ridaoui, F. Wieder, A. Ponche, O. Soppera, Nanotechnology 21 065303 (2010)

|276| *Laser-induced modification of metal nanoparticles formed by laser ablation technique in liquids,* N.V. Tarasenko·, A.V. Butsen and E.A. Nevar, Applied Surface Science

247, 118 (2005)

|277| *Gold Nanoparticle-Assisted Laser Surface Modification of Borosilicate Glass, Substrates,* S. Hashimoto, T. Uwada, M. Hagiri, H. Takai, T. Ueki, J. Phys. Chem. C 113, 20640 (2009)

|278| *Proceedings of 11th International Conference on Ion Beam Modification of Materials ed. by* Vredenberg, A. M. Polman, A., Stolk, P. A., Snolesand, E. Brongersma, L. M.), North Holland, Amsterdam, (1998)

|279| *Exciton–erbium interactions in Si nanocrystal-doped SiO₂,* P. G. Kirk, A. PolmanA, J. Appl. Phys. 88, 1992 (2000)

|280| *Raman scattering studies on silver nanoclusters in a silica matrix formed by ion-beam mixing,* P. Gangopadhyaya, R. Kesavamoorthy, K. G. M. Nair, R. Dhandapani, J. Appl. Phys. 88, 4975 (2000)

|281| *Spontaneous nanostructural island formation and layer-to-island mass transport in Ge layers on Si (111) surfaces,* A. K. Das, S. K. Ghose, B. N. Dev, G. Kuri, T. R. Yang, Appl. Surf. Sci. 165, 260 (2000)

|282| *Optical waveguide fabrication by ion beams in the PADC-polymer,* S. K. Chakravarti, J. Vetter, Nucl. Instru. and Meth. B 62, 109 (1991)

|283| *Scaling Laws of the Ripple Morphology on Cu(110),* S. Rusponi, G. Costantini, C. Boragno, and U. Valbusa, Phys. Rev. Lett. 81, 4184 (1998)

|284| *Roughening instability and evolution of the Ge(001) surface during ion sputtering,* E. Chason, T. M. Mayer, B. K. Kellerman, D. T. McIlroy, and A. J. Howard, Phys. Rev. Lett. 72, 3040 1994

|285| *The mechanisms of etch pit and ripple structure formation on ion bombarded Si and other amorphous solids,* G.W. Lewis, M.J. Nobes, G. Carter, J.L. Whitton , Nuclear Instruments and Methods B 170, 363 (1980)

|286| *Ion induced nanoscale surface ripples on ferromagnetic films with correlated magnetic texture,* K Zhang, F Rotter, M Uhrmacher, C Ronning, J Krauser and H Hofsäss, New J. Phys. 9, 29 (2007)

|287| *Energy Dissipation by Ions in the keV Region,* J. Lindhard, M. Scharff, Phys. Rev. 124, 128 (1961)

|288| *Electronic energy loss of ions in solids in the energy range 10-104 keV/nucleon,* I. Gertner, M. Meron, B. Rosner, Phys. Rev. A 18, 2022 (1978)

|289| W. L. Brown. Mat. Res. Soc. Symp. Proc. 51, 53 (1985).

|290| *Search for short-time phase effects in the electronic damage evolution – A case study with silicon,* G. Schiwietz, K. Czerski, M. Roth, F. Staufenbiel, and P. L. Grande. Nucl. Instr. Meth. B 226, 1287 (2004)

|291| *Microstructure of sulfide nanocrystals formed by ion-implantation,* A. Meldrum, C.W. White, L.A. Boatner, I.M. Anderson. R. A. Zuhr, E. Sonder, J.D. Buadai, D.O. Henderson, Nucl. Instrum. Methods, B Beam Interact Mater Atoms **148**, 957 (1999)

|292| *Coulomb Explosion and Thermal Spikes ,* E. M. Bringa* and R. E. Johnson, Phys. Rev. Lett. **88**, 165501 (2002)

|293| *Nanometric size effects on irradiation of tin oxide powder,* A. Berthelot, S. Hemon, F. Gourbilleau, C. Dufour, E. Dooryhee, E. Paumier, E. Dooryhe, S Begin, Collin, Nucl. Instreum methos, B Beam Interact. Mater Atoms **146**, 437 (1998)

|294| P. Kluth, B. Johannessen, R. Giulian, C.S. Schnohr, G. J. Foran, D. J. Cookson, A.P. Byrne, M.C. Ridgway, *Radiation Effects & Defects in Solids.* **162**, 501 (2007)

|295| A. Meldrum, L. A. Boatner, C.W. White, R.C. Ewing, Mat. Resnnovatr **3** , (2000), 190

|296| D. Mohanta, G.A. Ahmed, A. Choudhury, F. Singh , D.K. Avasthi, G. Boyer, G.A. Stanciu, EPJ: Appl. Phys. **35** (2006) 29-36

|297| *Swift heavy ion induced structural modification and photo-luminescence in CaS:Bi nanophosphors,* V. Kumar, R. Kumar, S. P. Lochab, N. Singh, Journal of Nanoparticle Research 9, 661 (2007)

|298| *Effect of high energy ion irradiation on electrical and optical properties of organic nonlinear optical crystals,* P. S. Aithala, H.S. Nagarajaa, P. M. Raoa, D.K. Avasthib A. Sarmab, Vacuum 48,991 (1997)

|299| *Influence of ion bombardment on the photoluminescence response of embedded CdS nanoparticles,* D. Mohanta, F. Singh, D.K. Avasthi, A. Choudhury, Central European Journal of Physics 4,187 (2006)

|300| *Swift heavy ions for controlled modification of soft magnetic properties of $Fe_{0.85} N_{0.15}$ thin film,* R. Gupta, A. Gupta, R. Bhatt, R. Ruffer, D.K. Avasthi, J. Phys.: Condens. Matter **22**, 226001(2010)

|301| *Modification of magnetic properties of epitaxial Co/Cu multilayers by 1 MeV C^+ irradiation,* M. C. Sung , D. G. You, H. S. Park, J. C. Lee, S. Y. Ie, I. S. Kim, J. Lee1, C. N. Whang, S. Im1, K. Jeong, T. G. Kim, J. S. Yang, and J. H. Song, J. Appl. Phys. **90**, 2036 (2001)

|302| *Modification of magnetic properties of FeRh intermetallic compounds by energetic ion beam bombardment,* S. Kosugi, N. Fujita, Y Zushi, T Matsui, N Ishikawan, Y Saito, A Iwase, Nuclear instruments & methods in physics research. Section B, Beam interactions with materials and atoms **267**, 1612 (2009)

|303| *Enhancement of ferromagnetism in Pd nanoparticle by swift heavy ion irradiation*
P. K. Kulriya, B. R. Mehta, D. K. Avasthi, D. C. Agarwal, P. Thakur, N. B. Brookes, A. K. Chawla,R. Chandra, Appl. Phys. Lett. **96**, 053103 (2010),

|304| *Ion-beam modification of the magnetic properties of $Ga_{1-x} Mn_xAs$ epilayers*, E. H. C. P. Sinnecker, G. M. Penello, T. G. Rappoport, M. M. Sant'Anna, D. E. R. Souza, M. P. Pires, J. K. Furdyna and X. Liu, Phys. Rev. B **81**, 245203 (2010)

|305| P. Kluth, B. Johannessen, R. Giulian, C.S. Schnohr, G. J. Foran, D. J. Cookson, A.P. Byrne, M.C. Ridgway *Radiation Effects & Defects in Solids*. **162**, 501 (2007)

|306| *Synthesis of elongated Au nanoparticles in silica matrix by ion irradiation*, Y. K. Mishra, F. Singh, D. K. Avasthi, J. C. Pivin, D. Malinovska, E. Pippel, Appl. Phys. Lett. **91**, 063103 (2007);

|307| *Self-organized growth of nanostructure arrays on strain-relief patterns*, H. Brune, M. Giovannini, K. Bromann, and K. Kern, Nature **394**, 451 (1998).

|308| *Domain formation and strain relaxation in epitaxial ferroelectric heterostructures*, B. S. Kwak, A. Erbil, J. Budai, M. F. Chisholm, L. A. Boatner, and B. J. Wilkens, Phys. Rev. B **49**,14865 (1994).

|309| *Stress-induced self-organization of nanoscale structures in SiGe/Si multilayer films*, C. Teichert, M. G. Lagally, L. J. Peticolas, J. C. Bean, and J. Tersoff, Phys. Rev. B **53**, 6334 (1996).

|310| *Morphological transition of gold nanostructures induced by continuous ultraviolet irradiation*, S. Yang, T. Zhang, L. Zhang, Q. Wang, R. Zhang, B. Ding, Nanotechnology **17** 5639 (2006)

|311| *Photoinduced Conversion of Silver Nanospheres to Nanoprisms*, R. C. Jin, Y. W. Cao, C. A. Mirkin, K. L. Kelly, G. C. Schatz, J. G. Zheng, Science **294**, 1901 (2001)

|312| *Photochemically Grown Silver Nanoparticles with Wavelength-Controlled Size and Shape*, A. Callegari, D. Tonti, M. Chergui, Nano Lett. **3**, 1565 (2003)

|313| *Synthesis and Properties of Tadpole-Shaped Gold Nanoparticle*, J. Hu, Y. Zhang, B. Liu, J. Liu, H. Zhou, Y. Xu, Y. Jiang, Z. Yang, Z. Q. Tian, J. Am. Chem. Soc. **126** 9470 (2004)

|314| Effects of Intensity and Energy of CW UV Light on the Growth of Gold Nanorods, Oscar R. Miranda and Temer S. Ahmadi, J. Phys. Chem. B **109**, 15724 (2005)

|315| *Preparation of Rodlike Gold Particles by UV Irradiation Using Cationic Micelles as a Template*, K. Esumi, K. Matsuhisa, K. Torigoe, Langmuir **11**, 3285 (1995)

|316| Thin Film Nanoprocessing by Laser/STM Combination, A.A. Gorbunov, W. Pompe: Phys. Status Solidi A **145**, 333 (1994)

[317] *Nanostructure fabrication using laser field enhancement in the near field of a scanning tunneling microscope tip,* J Jersch, K Dickmann, Appl Phys Lett **68**, 868 (1996)

[318] *Formation of Gold Nanonetworks and Small Gold Nanoparticles by Irradiation of Intense Pulsed Laser onto Gold Nanoparticles,* F Mafun, J Kohno, Y Takeda, T Kondow, J Phys Chem* B **107** 12589 (2003)

[319] *Bimodal Size Distribution of Gold Nanoparticles under Picosecond Laser Pulses* S Inasawa, M Sugiyama, Y Yamaguchi, J Phys Chem B, **109**, 9404 (2005)

[320] *Introduction to Solid State Physics,* by Charles Kittel, Willey (2004)

[321] *The crystal structure of solids* (ch3) , Edward Arnold, London,1975, by C J brown, J B Forsyth

[322] P Scherrer, "Bestimmung der Grosse und der inneren Struktur von Kolloidteilchen mittels Rontgenstrahlen," *Nachr Ges Wiss Gottingen* **26** (1918) pp 98-100

[323] J I Langford and A J C Wilson, "Scherrer after Sixty Years A Survey and Some New Results in the Determination of Crystallite Size," *J Appl Cryst* **11** (1978) pp 102-113

[324] A new formula for the breadth of Debye Scherrer lines, J Bouman and P M De Wolff , Physica **9**, 833 (1942)

[325] *Determination of the Particle Sizes, Microstrains, and Degree of Inhomogeneity in Nanostructured Materials from X-ray Diffraction Data* A S Kurlov and A I Gusev, Glass Physics and Chemistry **33**, 276–282 (2007)

[326] *Microstrain and Crystallite Size of Natural Microcrystalline Quartz by X-ray Line Broadening Analysis* H Nagao, N Aikawa, Journal of the American Ceramic Society **71**, C421 (2005)

[327] *Modern Spectroscopy* J Michael Hollas, Wiley, 4 edition (2004)

[328] *Characterization of Materials* John Wiley & Sons (2002)

[329] *Scanning Probe Microscopy The Lab on a Tip,* by Ernst Meyer , Hans Josef Hug, Roland Bennewitz , Springer (2004)

[330] *CRC Handbook of Chemistry and Physics (85th)* Ed David R Lide, CRC press (2003)

[331] *Scanning probe microscopy luminescence and third harmonic generation studies of elongated CdS Mn nanostructures developed by energetic oxygen ion impact,* D Mohanta, G A Ahmed, A Choudhury, F Singh , D K Avasthi, G Boyer , G A Stanciu, EPJ Appl Phys **35**, 29 (2006)

[332] *Ion Explosion Spike Mechanism for Formation of Charged - Particle Tracks in Solids,* R I Fleischer, P B Price, R M Walker, J Appl Phys **36**, 3645

|333| *Energy-dependent anisotropic deformation of colloidal silica particles under MeV Au irradiation* T V Dillen, A Polman, W Fukarek, A V Blaaderen, Appl Phys Lett **78**, 910 (2002)

|334| M A Xiao-Dong, Q Xue-Feng, J Yin, Z Zi-Kang, J Mater Chem 12 (2002)

|335| S Lee, D Song, D Kim, J Lee, S Kim, I Y Park, Y D Choi, Mater Lett 58 (2004) 342

|336| *The electronic structure and spectral properties of ZnO and its defects* P S Xu et al Nuclear Instruments and Methods' In Physics Research Section B Beam Interactions with Materials and Atoms **199**, 286(2003)

|337| *Optical Properties of ZnO Nanostructures* B D Aleksandra, Y H Leung, Small **2**, 944 (2006)

|338| *Semiconductor Clusters in the Sol-Gel Process –Quantized Aggregation Gelation, and Crystal-Growth in Concentrated ZnO Colloids*, J Am Chem Soc **113**

|339| *Development of Tb-doped ZnO nanorods Effect of nitrogen ion irradiation on luminescence and structural evolution* S Bayan, U Das, and D Mohanta, Physica Status Solidi A 1,1 2010

Appendix 1

Table : Value of χ_{nl} for different value of n and l

n \ l	1	2	3	4
0	3.142	6.283	9.425	12.556
1	4.4493	7.725	10.904	14.066
2	5.764	9.095	12.323	
3	6.988	10.417	13.698	
4	8.183	11.705		
5	9.356	12.967		
6	10.513	14.207		
7	11.657			
8	12.791			
9	13.916			

Appendix 2

Table : Parameters a, b, c used for estimating the band gap according to eq. (1.21)

Semiconductor	a $nm^{-2}eV^{1}$	b $nm^{-2}eV^{1}$	c $nm^{-2}eV^{1}$
ZnS	0.2349	0.0418	0.2562
ZnO	0.2174	0.0392	0.2134
ZnSe	0.0845	0.1534	0.2128
CdS	0.1278	0.1018	0.1821
CdSe	0.0397	0.1723	0.1111
GaAs	0.1969	0.2631	0.0728
GaP	0.0359	0.1569	0.1564
InAs	0.0374	0.2569	0.1009
InP	0.0461	0.3153	0.0623

Appendix 3

Table : Properties of Zinc Oxide and Zinc Sulfide

		Zinc Sulfide		Zinc Oxide	
Molar Mass		97.474 g/mol		81.408 g/mol	
Solubility in water		negligible		0.16 mg/100 mL (30 °C)	
Crystal Structrue		Cubic (Zinc Blende)	Hexagonal (Wurzite)	Cubic (Zinc Blende)	Hexagonal (Wurzite)
Band gap		3.68eV	3.91 eV	-	3.37 eV
Lattice Parameter at 300K	a	0.541 nm	0.3811 nm	-	0.32495
	c	-	0.6234 nm	-	0.52069
	c/a	-	1.636	-	1.602
Neighbour Dist.		0.234 nm	0.234 nm	-	0.195 nm
Density at 300K		4.11 g.cm-3	3.98 g.cm-3	-	5.606 g.cm-3
Refractive index (n_D)		2.368	2.356	2.008	2.029
Melting point		1185^0C	1850^0	-	1975 °C
Bohr Excitonic Radius		2.5nm		2.34nm	
m_e^*		$0.34m_e$		$0.27m_e^*$	
m_h^*		$1.76m_e^*$		$1.78m_e$	
dielectric constant		9.2		8.5	

Appendix 4

Joint Committee on Powder Diffraction Standards (JCPDS)

The International Centre for Diffraction Data (ICDD) or Joint Committee on Powder Diffraction Standards (JCPDS) maintains a database of powder diffraction patterns, the Powder Diffraction File (PDF), including the d-spacings (related to angle of diffraction) and *relative intensities of observable diffraction peaks. Patterns may be experimentally* determined or computed based on crystal structure and Bragg's law. It is most often used to identify substances based on x-ray diffraction data, and is designed for use with a diffractometer. Comparing the X-ray diffraction pattern for any material with JCPDS database we can get the crystal structure of the material and the crystals plans form which diffraction occurs.The database is exhaustive, over 500,000 entries as of 2009; computer algorithms allow rapid peak matching. The organization was founded in 1941 as the **Joint Committee on Powder Diffraction Standards (JCPDS)**. In 1978, the name of the organization was changed to the current name to highlight the global commitment of this scientific endeavor. Thus, using JCPDS we can identify unknown materials. With every entry, the database also contains bibliographic references, chemistry descriptions, structural classifications, crystallographic and physical properties.

Appendix 5

Table : Physical properties of the host materials

Physical properties of PVOH

Glass transition temperature	$343^{\circ}K$
Melting temperature	$413\ ^{\circ}K$
Refractive index	1.55
Specific gravity	1.55
p^{H}	5-7
Viscosity	25-32cp
Specific heat (J/gm-K)	1.66
Thermal conductivity (W m-1K-1)	2.0
Molar mass a single structure unit (g)	58.2
Dielectric constant	2.0
Physical properties CTAB	
Molar mass	364.45 g/mol
Melting temperature (K)	$237\text{-}243^{0}K$
p^{H}	5.0-7.0

Appendix 6

Table : Reactance concentration for obtaining ZnS:TM nanostructures

(a) Mn doped ZnS nanostructures (ZnS:Mn)

Sample	Sample Code	$ZnCl_2$ (Mole)	$MnCl_2$ (Mole)	Na_2S (Mole)
ZnS:Mn	MNZ1	0.15	0.0015	0.01
	MNZ3	0.15	0.0030	0.01
	MNZ5	0.15	0.0075	0.01

(b) Cr doped ZnS nanostructures (ZnS:Cr)

	Sample Code	$ZnCl_2$(Mole)	Cr_2O_3 (Mole)	Na_2S (Mole)
ZnS:Cr	CRZ1	0.15	0.0015	0.01
	CRZ3	0.15	0.0030	0.01
	CRZ5	0.15	0.0075	0.01

(c) Co doped ZnS nanostructures (ZnS:Co)

	Sample Code	$ZnCl_2$ (Mole)	$CoCl_2$ Mole	Na_2S (Mole)
ZnS:Co	COZ1	0.15	0.0015	0.01
	COZ3	0.15	0.0030	0.01
	COZ5	0.15	0.0075	0.01

(d) Cu doped ZnS nanostructues (Zns:Cu)

	Sample Code	$ZnCl_2$ (Mole)	$CuCl_2$ (Mole)	Na_2S (Mole)
ZnS:Cu	CUZ1	0.15	0.0015	0.01
	CUZ3	0.15	0.0030	0.01
	CUZ5	0.15	0.0075	0.01

Appendix 7

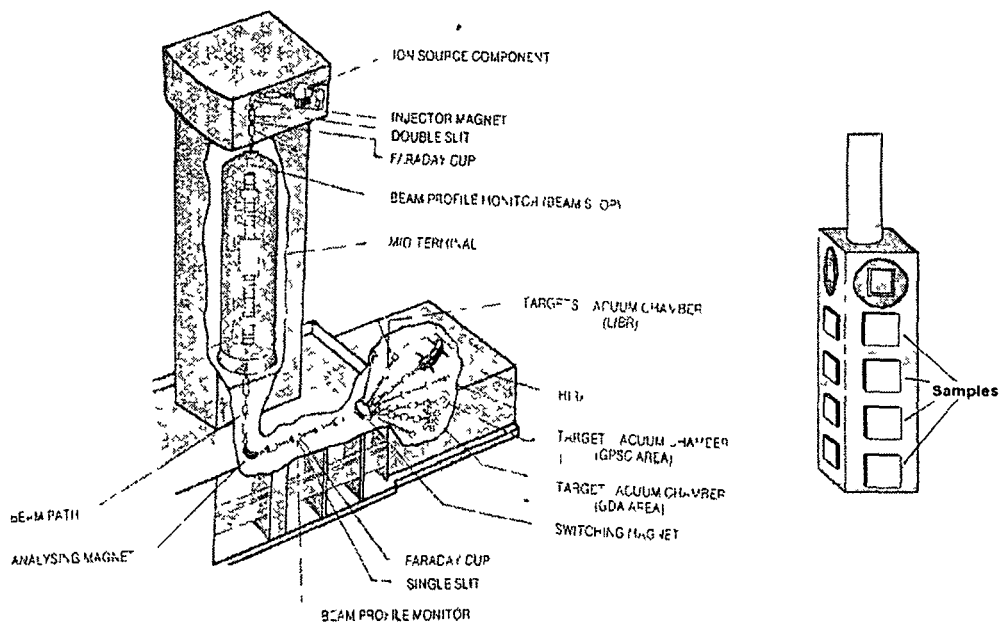## Ion irradiation Chamber and ion trajectory

Figure Schematic of ion irradiation chamber and ion trajectory and the ladder used in the vacuum chamber where the samples are mounted to irradiate

The ion irradiation experiments were done at 15UD Palletron available at Inter University Accelerator center at New Delhi Schematic of the 15UD pattetron is shown in the figure Irradiation is performed by mounting the samples in ladder (Figure B) in the material science chamber The ladder can move up/down as well can be rotate and so we can irradiate 16- 20 samples without releasing the vacuum at a time

173

Appendix 8

Fluence in ion irradiation experiment:

It is defined as the total number of irradiating ions incident per square centimeter (ions/ cm^2) of the sample.

Fluences are calculated using the following formula
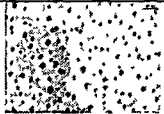
$$Fluence\ (\phi) = \frac{Time\ (t) \times Beam\ Current \times pnA}{Charge\ State}$$

Beam currents for ion irradiation experiments are usually taken in the range of 1-5 nA.

$$1\ pnA\ (particle\ nano\ ampere) = \frac{10^{-9}\ Coul\ /\ \sec}{1.6x10^{-19}\ Coul} = 6.25x10^9\ particles\ /\ \sec$$

Appendix 9

Table 5.2 : Excitonic binding energy of nanorod with different aspect ratio

Sample	F0	F1	F2	F3	F4
peak position in OAS	345 nm	351 nm	364 nm	372 nm	376 nm
PL peak position (UV peak)	362nm	365nm	376 nm	382nm	382nm
PL peak position (Green peak)	~ 580nm	~ 580nm	~ 580nm	~ 580nm	~ 580nm
Excitonic Binding Energy	170mev	140mev	120mev	100mev	80mev
TEM micrograph					

ADDENDA

Structural and optical properties of 150 MeV Ti^{+11} irradiated doped nanostructures

U Das*[1], D Mohanta[1], A K Bordoloi[2], F Singh[3], A Tripathi[3], D K Avasthi[3] and A Choudhury[1]

[1]Department of Physics, Tezpur University, P.O. Napaam, Assam-784 028, India
[2]North Lakhimpur College, North Lakhimpur, Assam-787 001, India
[3] Inter University Accelerator Centre, Aruna Asaf Ali Road, New Delhi-110 067, India

E-mail . upam@tezu ernet in

Abstract We report transition metal (Mn, Cu) impurity doped ZnS nanoparticles fabricated by a simple solution growth technique and their response to 150-MeV Ti^{+11} ion irradiation. The size of the nanostructures increases with ion fluence due to melting led grain growth. The increased size as a results of grain growth has been observed in the optical absorption spectra in terms of red shift The dopant related and fluence dependent luminescence properties are studied by Photoluminescene spectroscopy and the results are discussed.

Keywords · Nanostructures, ion irradiation

PACS Nos. 31.20.Ka; 81 05 Dz; 82.35.Np

1. Introduction

A semiconductor nanostructure, which uses the principle of three dimensional carrier confinement, have emerged as important technological assets for their dimensional dependent optoelectronic properties. The nanoscaled systems exhibit properties *e.g.* quantum size effect or three dimensional carrier confinement, quantization of the bulk electronic states. In addition, energy gap enhancement occurs with decreasing crystallite size. In recent years, size dependent electronic and optical properties of nanoparticles [1-4] have been studied by different workers. In fact that the band gap of these materials varies with crystallite size makes them and interesting category of materials for potential optoelectronics and photonics application. Among binary semiconducting systems, ZnS are the most widely investigated system having a direct band gap of 3.7eV at 300°K.

---

* Corresponding Author

Again, doped nanomaterials provide improved functionality for prospective applications in nanotechnology [5-9]. The properties of intrinsic nanomaterials or host nanomaterials can be tuned by doping with some impurity. It is an important phosphorescent material both in doped and undoped form. It has been established that when doped with some magnetic impurities, the nanostructures develop a unique class of material called diluted magnetic semiconductors (DMS) which are promising candidates for magnetic memories, sensors and other spin-based devices [10, 11]. Such semi-magnetic and semiconducting structure, where carrier and spin confinement is possible provides a matchless system for spin manipulation and spin transportation [12].

Here we have used the solution growth technique because it provides a homogeneous distribution of impurity atoms in the host nanoparticles. With this technique it is easy to control the size and shapes of the nanoparticles and the technique provides higher production yields at low costs.

Swift heavy ion irradiation is a useful tool for the development of nanostructures through ion implantation, ion beams mixing and template synthesis *etc* [13-17]. In this particular report, we highlight impact of 150 MeV Ti^{11+} ions on the photoluminescence and morphological changes in polymer encapsulated ZnS:Mn and ZnS:Cu nanostructures.

2. Experimental

First, 5% (w/v) transparent polyvinyl alcohol (PVOH) matrix was prepared under moderate stirring (~200 rpm) and heating (65°C) for 3 hours. Next 0.15 M $ZnCl_2$ was added to the PVOH matrix under stirring environment. The solution was immediately brought back to ice cold temperature and left undisturbed overnight. H_2S gas was allowed to diffuse through the solution for maximum absorption. The solution is than kept in cool and dark environment for 24 hours and then casted on 1 × 1 cm^2 laboratory slides for the irradiation experiments.

For doped ZnS nanoparticle we use solution casting technique. For Mn^{+2} doping instead of only $ZnCl_2$ a mixture of $ZnCl_2$ and $MnCl_2$ is added to the PVOH matrix. For Cu^{+2} doping instead of only $ZnCl_2$ a mixture of $ZnCl_2$ and $CuCl_2$ is added to the PVOH matrix.

The irradiation was carried out on four identical samples. The nanoparticle samples were mounted on a vacuum shielded vertical sliding ladder having four rectangular faces. One sample was reserved as virgin one to compare with the irradiated samples. They were irradiated at high vaccum (1.6 × 10^{-6} torr) by 150-MeV Ti^{+11} beam with approximated beam current 1.0 pnA (particle nano ampere). The fluence was varied in the range 10^{10} to 10^{12} ion/cm^2. In order to expose the whole target area, the beam was scanned vertically over the sample plane. The energy of the ion beam was chosen in such a way that the projectile range of the incident ion (21.3 μm, as computed by SRIM program) exceeds thickness of the sample films (~ 0.5 μm). Again the ion beam energy and thickness of the target was selected so that modification due to electronic energy loss (S_e) affects the sample. Energy dependent electronic energy loss (S_e) and nuclear energy loss (S_n) for Ti^{+11} ions has been shown in table 1.

Table 1. Stopping energies and projectile range of energetic T_i^{+11} beam through ZnS nanostructures in PVOH.

Energy MeV	Electronic energy loss $S_e = (dE/dx)$ eV/Å	Nuclear energy loss $S_n = (dE/dx)$ eV/Å	Projectile range R (μm)
100	512.37	0 23	15 26
150	587.29	0 17	21 32

3. Results and discussion

The X-ray diffraction pattern of Bulk ZnS and ZnS nanoparticles shown in Figure 1 and Figure 2, depicts cubic structure corresponding to three diffraction peaks (111), (220) and (311) at 27.5°, 46.2° and 56°; respectively. The broadening of XRD diffraction peak compared to bulk confirms the formation of nanoparticle. The XRD gives an idea of rough estimation of average particle size ~ 10 nm, obtained by measuring full-width-at half maxima (FWHM) and Scherrer formula $d \approx 0.9\lambda/w \cos\theta$. The 2D-topological view of nano-ZnS, taken by atomic force microscopy (AFM) and shown in Figure 3 agrees well with the prediction made by.
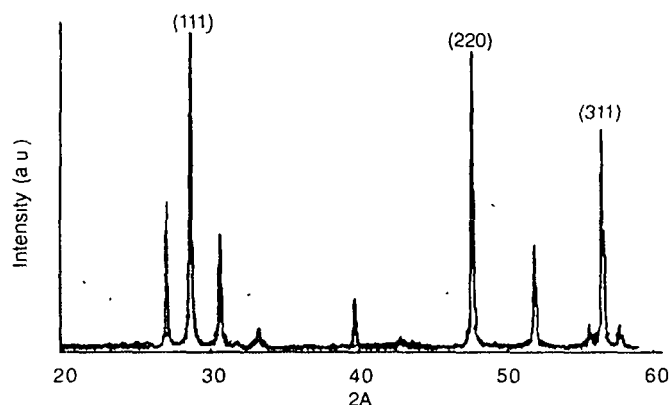
Figure 1. XRD pattern of Bulk ZnS
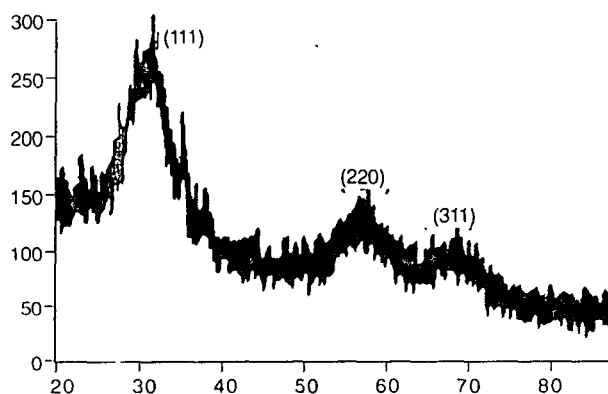
Figure 2. XRD pattern of undoped ZnS nanoparticle

In the XRD diffraction pattern of doped ZnS nanoparticle there is no new diffraction peak, but instead leads to gradual shifts in the lattice parameters of the host material with dopant concentration is observed in accordance with Vegard's Law [18]. Several groups successfully used this tool for study of doping for bulk semiconductor [19] and inorganic nanocrystals. [21,22].

In the UV-vis spectra [Figure 4] of ZnS nanoparticles films which are irradiated with different fluences show red sift of absorption threshold. With increasing fluence of ion irradiation. This is a signature of significant grain growth.
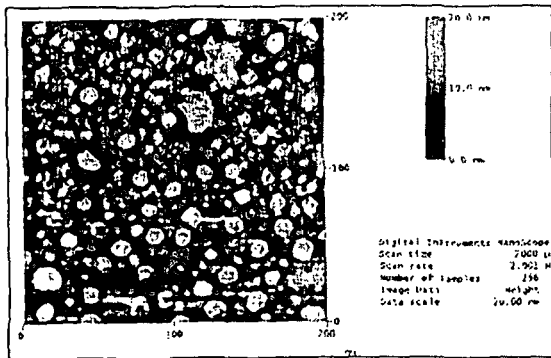

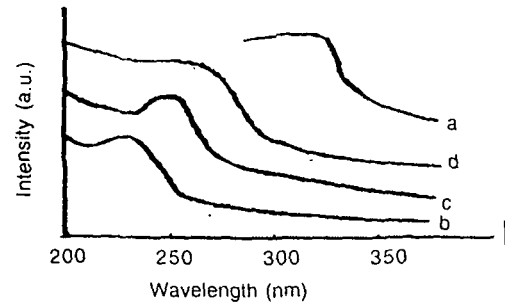**Figure 3.** AFM topography of undoped unirradiated ZnS.

Figure 4. UV-Vis absopbtion spectra of a) Bulk ZnS b) unirradiated ZnS nano c) irradiated ZnS nano at 2 × 10^{11} ion/cm^2 d) irradiated ZnS nano 8 × 10^{11} ions/cm^2.

Normally, the photoluminescence study provides information relating to different energy states available between valence band and conduction band responsible for radiative recombination. It is well known that when emission peak energies are less than the band gap energy of the material, these emission peaks ascribe to transition involving donors, acceptors, free electrons and holes.
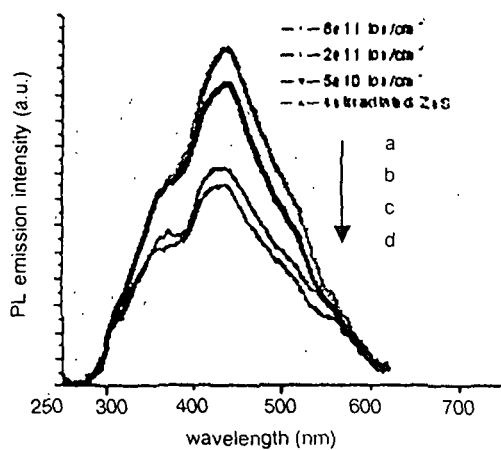

Figure 5. PL emission spectra of a) unirradiated and irradiated b) 5 × 10^{10}, c) 2 × 10^{11} ions/cm^2 undoped ZnS nanoparticles.
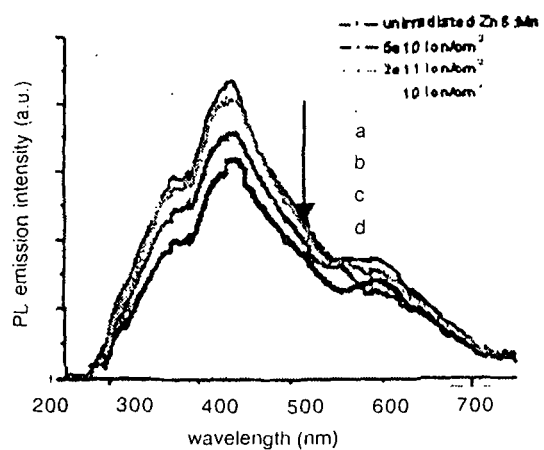

Figure 6. PL emission spectra of a) unirradiated and irradiated b) 5 × 10^{10}, c) 2 × 10^{11} d) 8 × 10^{11} ions/cm^2 ZnS:Mn nanoparticles.

The luminescence spectra of undpoed ZnS nanoparticle [fig 5] consists of two peaks. First one around 375nm is due to band edge emission and second one around 420 is due to surface states led trap related emission. Here emission due to surface states dominants the band edge emission. As the ion fluence (0 to 8×10^{11} ion/cm²), increases in there is adequate suppression in trap related emission owing to reduction in surface traps as a result of nanoparticle growth.

In the luminescence spectra of Mn doped ZnS nanoparticle [figure 6] three types of peaks are observed First one is due to band edge emission, second is due to surface states of the nanostructures as observed in pure ZnS nanoparticle. The third peak is at 580 nm is ascribed as orange yellow Mn^{++} emission. The impurity related emission is due to transition between its localized electronic levels in the band gap of the host material. The T1-A1 transition corresponds to the peak around 580 nm with the increase in ion fluence (0 to 8×10^{11} ion/cm³), there is adequate suppression in trap related emission owing to reduction in surface traps as a result of nanoparticle growth.

In the luminescence spectra of Cu doped ZnS nanoparticle [Figure 7] luminescence peak is around 500 nm. This blue-green emission is due to a transition from the conduction band to the t2 level of excited Cu^{++} in the ZnS band gap Band-edge emission and trap related emissions are dominated and masked by the Cu^{++} emission in the ZnS band gap. The PL peaks decrease in intensity with the increase in ion dose, possibly due to suppression in recombination emission owing to grain growth phenomena under ion irradiation.
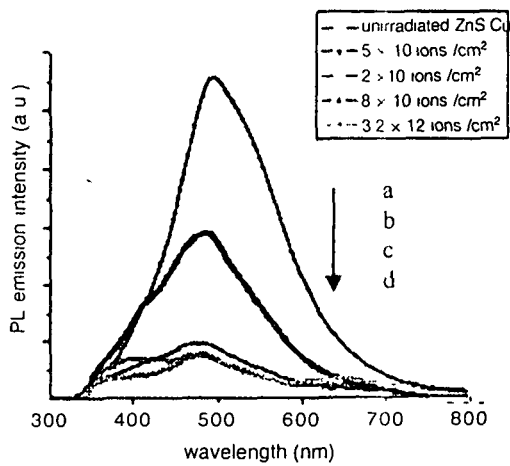
Figure 7. PL emission spectra of a) unirradiated and irradiated b) 5×10^{10}, c) 2×10^{11} d) 8×10^{11} ions /cm² ZnS.Cu nanoparticles.
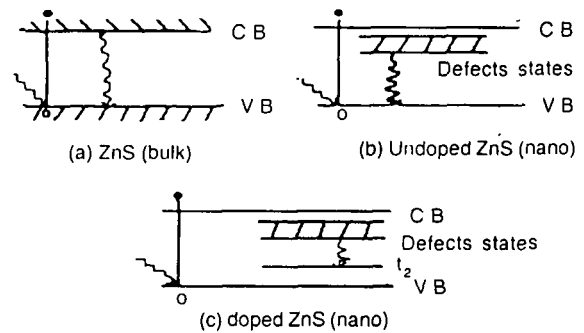
Figure 8. Band structure of (a) bulk ZnS (b) nano Zns and (c) nano ZnS doped with some impurity.

In doped ZnS nanoparticle the any impurity can lead to impurity levels in the band gap they caused luminescence. The luminescence around 400 nm is due to photo excited electrons, which are excited to electronic excitonic electronic level of LUMO. Again, due to rapid transition to HOMO level, a strong luminescence occurs in case of undoped nanoparticles. Without doping, radiative transition occurs from conduction levels to the

valence levels only. While in doped nanostructures another type of luminescence is there due to inter-band transitions in accordance with the crystal field theory

4. Conclusion

In conclusion, we have produced doped and undoped ZnS nanostructures by simple and inexpensive chemical route Photoluminescence shows a new emission peak due to doping Nanostructures embedded in polymer show regular grain growth process under ion irradiation The size of the grain can be tuned by selecting the proper ion fluence in the irradiated doped nanostructures the emission peak due to surface states show blue shift while the doped related emission peaks do not shift appreciably

Acknowledgment

References

[1]   A P Alivisatos *J Phys Chem* **100** 13226 (1996)

[2]   A D Yoffe *Adv Phys* **42** 173 (1993)

[3]   Y Kayanuma *Phys Rev* **B38** 9797 (1998)

[4]   J Nanda, K S Narayan, B A Kuruvilla, G L Murthy and D D Sarma *Appl Phys Lett* **72** 1335 (1998)

[5]   J Zhao and R H Xie *J Nanosci Nanotech* **3** 459 (2003)

[6]   M Terrones, A Jorio, M Endo, A M Rao, Y A Kim, T Hayashi H Terrones, J C Charlier, G Charlier, G Dresselhaus and M S Dresselhaus *Materialstory* **10** 30 (2004)

[7]   R N Bhargava *J Luminescence* **70** 85 (1996)

[8]   M Shim, C Wang, D J Norris and P Guyot-Sionnest *MRS Bull* **26** 1005 (2001) , P G Kirk and A Polman *J Appl Phys* **88** 1992 (2000)

[9]   W Chen, J S Zhang and A G Joly *J Nanosci, Nanotech* **4** 919 (2004)

[10] G A Prinz *Science* **282** 1660 (1998)

[11] D P Divincenzo *J Appl Phys* **85** 4785 (1999)

[12] T Dietl *Braz J Phys* **34** 2B (2004)

[13] A Meldrum, C W White, L A Boatmer, L M Anderson, T A Zuhr, E Sonder, J D Budai and D O Henderson *Nucl Instrum Meth* **B148** 957 (1999)

[14] Y Takeda, V T Gritsyna N Umeda, C G Lee N Kishimot *Nucl Insrum Meth* **B148** 1029 (1999)

[15] J D Budai, C W White, S P Withrows, R A Suhr and J G Zhu *Mater Res Sov Symp Proc* **452** 89 (1997)

[16] P Gangopadhyay, R Kesavamoorthy, K G M Nair and R Dhandapani *J Appl Phys* **88** 4975 (2000)

[17] A K Pal *Bull Mater Sci* **22** 341 (1999)

[18] L Vegard and H Schjelderup *Physik Z* **18** 93 (1917)

[19] J K Furdyna *J Appl Phys* **64** R29 (1988)

[20] O E Raola and G F Strouse *Nano Letters* **2** 1443 (2002)

[21] K M Hanif, R W Meulenberg and G F Strouse *J Am Chem Soc* **124** 11495 (2002)

Fabrication of ZnO nanorods for optoelectronic device applications

R Chakraborty[1], U Das[1*], D Mohanta[1,2] and A Choudhury[1,3]

[1]Nanoscience Laboratory, Department of Physics, Tezpur University, PO Napaam, Tezpur-784 028, Assam, India
[2]Laboratory for Molecular Scale Engineering, Electrical and Computer Engineering,
University of Wisconsin-Madison, WI-53706, USA
[3]Gauhati University, Gopinath Bordoloi Nagar, Guwahati-781 014, Assam, India

E-mail : upam2005@gmail com

Abstract : Hydroxyl free zinc oxide nanorods have been synthesized by a catalyst free surfactant based one-step solid state reaction process. The powder X-ray diffraction studies reveal well defined wurtzite peaks due to crystalline ZnO, while optical absorption spectra represent prominent exciton absorption and remarkable blueshift in the onset of absorption. As predicted by transmission electron microscopy, the ZnO nanorods are ~100 nm long and of ~20 nm dia Further, luminescence aspects of such nanorods are studied for possible deployment in optoelectronics devices.

Keywords : Nanorods, optoelectronics, luminescence.

PACS Nos. : 61.46.Km, 81.07.Wx, 78.67 -n, 81.07.-b

1. Introduction

Recently, one-dimensional semiconductor systems such as nanorods, nanotubes, nanoneedles, nanowires *etc.* have gained enormous research interests as they are considered to be potential candidates for microelectronics, photonics, and sensing applications [1–8]. Till date, extensive literature is available highlighting fabrication details/methods *e.g.*, chemical vapor deposition [9–12], arc discharge [13], laser ablation [14], template based method [15,16] *etc.*

Zinc oxide (ZnO), a II-VI binary-compound semiconductor, has a wurtzite structure with a direct band gap of 3.37 eV at room temperature. The wide band gap along with large exciton binding energy (~60 meV) makes ZnO as an attractive candidate for UV sensors/detectors [17]. Compared to the bulk-ZnO, nano-ZnO exhibits extremely large excition binding energy and therefore, excitions in the later case are much more stable

---

*Corresponding Author

at room temperature $(k_\beta T \sim 25$ meV). As an alternative candidate of nanoelectronics, it was reported that p-type conductivity can be induced in natural hexagonal crystal structure of ZnO nanowire and was ascribed to the presence of oxygen vacancies. Also, the combined magnetic and transport properties as well as high Curie temperature *etc.* have made doped-ZnO a potential candidate for spintronic applications [18,19]. Further, polarized light emission from ZnO nanorods has been demonstrated recently [20].

In this letter, we report one-step synthesis of ZnO nanorods adopting a cost effective, catalyst free solid state reaction route. The as prepared samples were characterized by X-ray diffraction (XRD), transmission electron microscopy (TEM) and absorption spectroscopy. In addition, photoluminescence studies are performed to reveal optoelectronic properties.

2. Experimental details

ZnO nanorods were synthesized at room temperature by a simple and convenient physico-chemical reaction. The source material was a mixture of zinc acetate dihydrate (ZAD) [$Zn(CH_3COO)_2.2H_2O$], cetyl trimethyl ammonium bromide (CTAB, a cationic surfactant) [$C_{19}H_{42}BrN$], and sodium hydroxide flakes in molar ratio 1 : 0.5 : 3. Without applying direct pressure, the mixture was ground in a mortar for 1–2 hours. Next, the mixture was transferred to a culture-tube and kept in an ultrasonic bath for one hour. The sonicated mixture was then washed with double distilled water several times. In order to induce oxidation of unreacted species, the as prepared mixture was annealed at temperature 60–80°C for 2 hours. Finally, the product was preserved for further experimentation and characterization.

In order to reveal structural morphology, with regard to size, shape distribution and crystallinity the sample was studied by powder diffraction and electron microscopy. The XRD pattern was recorded on a powder sample with a Rigaku D/max-2000 diffractometer employing Cu-$K\alpha$ radiation ($\lambda = 1.54$ Å) with a scanning rate of 0.02 degree/s. The TEM images were taken by employing a JEOL JSM-100 CX microscope working at a beam accelerating voltage of 80 KV. Optical properties were investigated by absorption and photoluminescence (PL) spectroscopy. The room-temperature PL spectra were recorded by a Perkin-Elmer LS-55 spectrophotometer using $\lambda = 325$ nm as the excitation wavelength.

3. Results and discussion

The structural phase and crystallographic orientation of the as-grown nano-ZnO samples (Figure 1) were identified by XRD measurements. The diffraction pattern suggests that as-grown nanostructures are polycrystalline in nature with wurtzite crystal phase in consistency with earlier reports [21].

The strongest diffraction (101) peak at 34.51° implied that the structures were
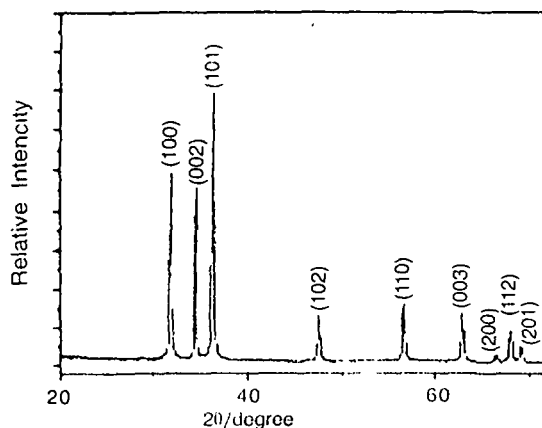
Figure 1. XRD spectra of ZnO nanorods.

grown with preferred orientation of (101) plane. From the presented data, the crystal lattice parameters are estimated as : a = 3.235 Å and c = 5.189 Å, which are close to a = 3.253 Å and c = 5.209 Å of ZnO (JCPDS Card No. 80-00075). In the XRD pattern, no characteristic peak due either to impurities or unreacted species like Zn, CTAB or $Zn(OH)_2$ is observed. This results actually indicates the formation of hydroxyl free, wurtzite ZnO phase.

The absorption spectrum is represented in Figure 2. Single sharp exciton absorption peak was noticed at ~350 nm owing to 1s-1s transition states. Also, narrow tailing in the OAS ensures us that there is adequate suppression in the degree of
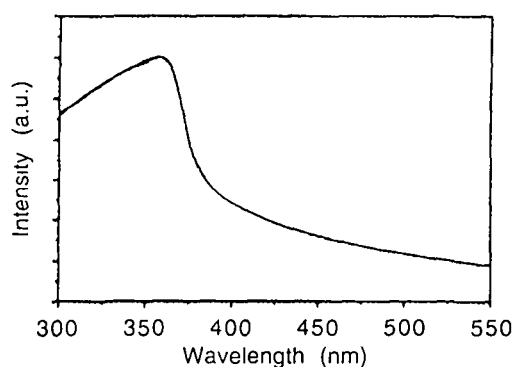
Figure 2. UV-VIS optical absorption spectra of ZnO nanorods

inhomogeneity due to improved and organizational growth of particles while synthesis was in progress.

A clear evidence of the formation of elongated ZnO nanostructures is being depicted in Figure 3. The Figure shows an isolated ZnO nanorod, which has a typical length of ~100 nm and of dia ~20 nm. Interestingly, we notice that the nanorods have deviated from the ideal solid-cylindrical shape. In other words, two extreme ends of the nanorods have smaller dia compared the middle parts and therefore, resembling commercial ball-pen like structures.

Figure 3. TEM image of ZnO nanorods.

Since the hydroxides are decomposed by a strong heat of the reaction to produce oxides in the reaction process, organization and assimilation o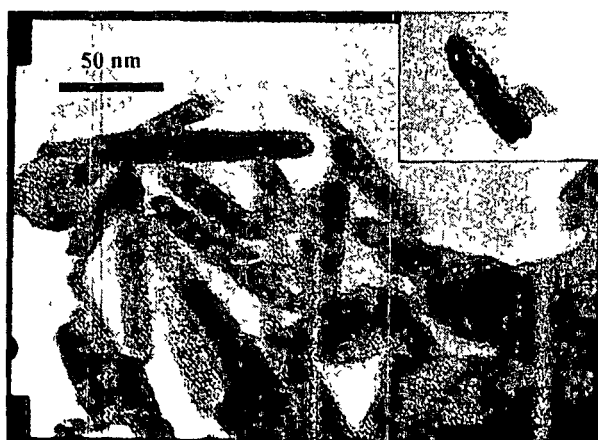f particles would be slow during initiation and termination in the formation of ZnO nanorods. In reference to the mechanism of growth process first, $Zn(OH)_2$ was formed due to compositional formed mixing facilitated by solid state reaction and finally, ZnO is produced due to gradual decomposition owing to strong heat of reaction.

The photoluminescence studies are presented in Figure 4. The 325 nm line of
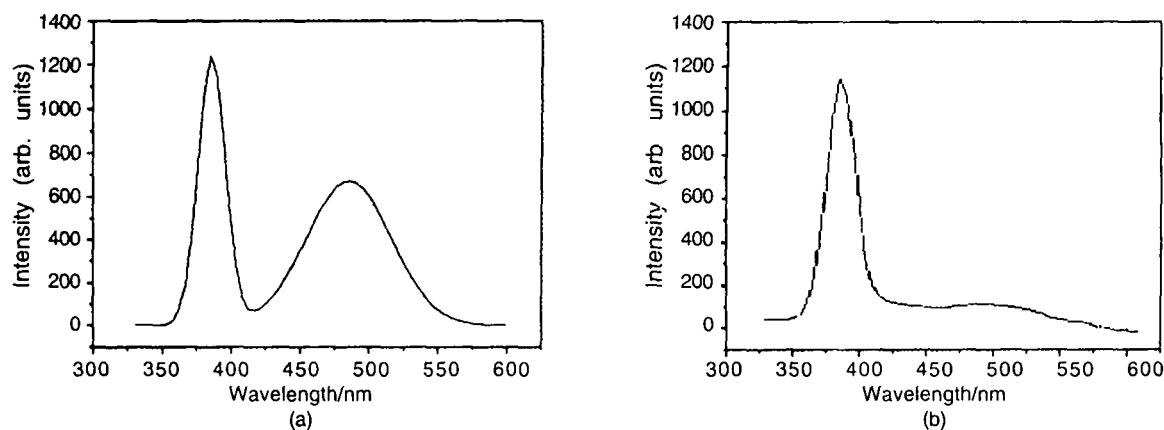
Figure 4. Room temperature PL spectra of (a) nano and (b) bulk ZnO

Xe-lamp was used as the excitation source and the data were collected by a computer controlled standard monochromator based photodetection system. The sharp peak at ~375 nm shows the near-band-edge (NBE) emission. This is generally associated with the excitonic transitions [22], which has been observed between 378–385 nm by earlier workers [23–26]. A second broad band peak ~485 is noticeable only in nano-ZnS sample and is ascribed to the trap related emission. The trap emission is associated with the nonradiative centers, generally inherent in nanostructures owing to extremely large surface-to-volume ratio.

Previously, the presence of broader PL band in the visible green region was attributed to the recombination of photogenerated holes with the singly ionized oxygen vacancies [22] Also, it was reported that the defect induced emission can be suppressed by choosing a suitable substrate that avoids lattice mismatch to a large extent [27] In our powder sample system, there is no such reason that can control trap emission The symmetric nature of the green emission with FWHM ~105 nm reflects uniform roughness all throughout the nanorods Highlighting polarized light emission characteristics, tunability of near band edge and defect emission was demonstrated by earlier workers [20] In our case, strong and symmetric response of both the emission features of PL also support organized growth of quality nanorods Considering absorption and emission spectra we have estimated binding energy of excitons E_b ~120 meV The calculated value is close to the value estimated by other workers [28]

4. Conclusion

In summary, we have described a one step solid state synthesis of ZnO nanorods The method described here is simple, robust and cost effective for large scale production One dimensional nanorods of length at least five times more than the base dimension were produced The powder diffraction study provides signature of hexagonal wurtzite structure with (101) as preferred orientation Symmetric nature of trap-luminescence, centered at ~485 nm suggests uniform smoothness over the nanorod surfaces The binding energy of our ZnO nanorod sample was predicted to be ~120 meV Temperature dependent and time resolved study of such nanostructures, will help further, to explore and understand nature of light emission in terms of radiative and nonradiative transitions

Acknowledgments

References

[1]   W Lu and C M Lieber *J Phys* **D39** R387 (2006)

[2]   M Saito, M Kirihara T Taniguchi and M Miyagi *Appl Phys Lett* **55** 607 (1989)

[3]   S Iijima *Nature* **354** 56 (1991)

[4]   R J Tonucci, B L Justus, A J Campillo and C E Ford *Science* **258** 783 (1992)

[5]   H E Dai, W Wong Y Z Lu S Fan and C M Lieber *Nature* **375** 769 (1995)

[6]   A M Morales and C M Lieber *Science* **279** 208 (1998)

[7]   S J Tans, R M Verschueren and C Dekker *Nature* **393** 49 (1998)

[8]   X F Duan, Y Huang Y Cui, J F Wang and C M Lieber *Nature* **409** 6 (2001)

[9]   M Yazawa, M Koguchi, A Muto, M Ozawa and K Hiruma *Appl Phys Lett* **61** 2051 (1992)

[10] Y Wu and P Yang *Chem Mater* **12** 605 (2000)

[11] C C Chen and C C Yeh *Adv Mater* **12** 738 (2000)

[12] Z G Bai, D P Yu, H Z Zhang, Y Ding, X Z Gai, Q L Hang, G C Xiong and S Q Feng *Chem Phys Lett* **303** 311 (1999)

[13] Y C Choi, W S Kim Y S Park, S M Lee, D J Bae Y H Lee G-S Park W B Choi, N S Lee and J M Kim *Adv Mater* **12** 746 (2000)

[14] (a) X F Duan and C M Lieber *Adv Mater* **12** 298 (2000), (b) A M Morals and C M Lieber *Science* **279** 208 (1998)

[15] (a) M H Huang, A Choudrey and P Yang *Chem Commun* **12** 1063 (2000), (b) J Zhu and S Fan *J Mater Res* **14** 1175 (1999)

[16] Y Li, G W Meng, L D Zhang and F Philipp *Appl Phys Lett* **76** 2011 (2000)

[17] S P Chang, S J Chang, Y Z Chiou, C Y Lu, T K Lin, Y C Lin, C F Kuo and H M Chang *J Elec Chem Soc* **154** J209 (2007)

[18] B K Roberts, A B Pakhomov, V S Shutthanandan and K M Krishnan *J Appl Phys* **97** 10D310 (2005)

[19] T S Herng, S P Lau, a_S F Yu, H Y Yang and X H Ji *J S Chen, N Yasui and H* Inaba **99** 086101 (2006)

[20] N E Hsu, W K Hung and Y F Chen *J Appl Phys* **96** 4671 (2004)

[21] S J Kwon, J-H Park and J-G Park *Appl Phys Lett* **87** 133112 (2005)

[22] L Spanhel and M A Anderson *J Am Chem Soc* **113** 2826 (1991)

[23] L E Greene, M Law, J Goldberger, F Kim, J C Johnson, Y Zhang, R J Saykally, P Yang and Angew *Chem Int Ed* **42** 3031 (2003)

[24] J W P Hsu, D R Tallant, R L Simpson, N A Missert and R G Copeland *Appl Phys Lett* **88** 252103 (2006)

[25] W M Kwok, A B Djurisic, Y H Leung W K Chan and D L Phillips *Appl Phys Lett* **87** 223111 (2005)

[26] K Vanheusden, W L Warren, C H Seager, D R Tallant, J A Voigt and B E Gnade *J Appl Phys* **79** 7983 (1996)

[27] H Chik, J Liang, S G Cloutier, N Kouklin and J M Xu *Appl Phys Lett* **84** 3376 (2004)

[28] H P He, Z Z Ye, S S Lin, H P Tang, Y Z Zhang, L P Zhu, J Y Huang and B H Zhao *J Appl Phys* **102** 013511 (2007)

Development of Tb-doped ZnO nanorods: Effect of nitrogen ion irradiation on luminescence and structural evolution

S. Bayan, U. Das, and D. Mohanta*

Nanoscience Laboratory, Department of Physics, Tezpur University, P. O. Napaam, Assam-784028, India

*Corresponding author: e-mail best@tezu.ernet in, Phone. 91 3712 267007 5558, Fax. 91 3712 267007

In this work, we present surfactant-(cetyl-trimethyl ammonium bromide, CTAB) assisted solid-state fabrication and characterization of hydroxyl-free ZnO and Tb-doped ZnO nanorods. 80-MeV nitrogen ion irradiation (fluence: upto 8×10^{12} ions/cm^2) was performed to explore irradiation-induced modification in the structural and optical properties of the nanorods. In the asymmetrically broadened photoluminescence (PL) spectra of the irradiated samples, the band-edge emission ($\sim$370 nm) is found to be suppressed due to the dominance of the defect related emissions. Apart from ZnO-defect-related emissions (within 405–535 nm) due to zinc/oxygen vacancies, interstitial etc., we have adequately identified the Tb-related $^5D_4-^7F_6$ and $^5D_4-^7F_5$ transitions at $\sim$490 and 548 nm, respectively. At the highest fluence (8×10^{12} ions/cm^2), the nanorod structural ordering is lost, which is characterized by a luminescence quenching. The nitrogen irradiation at the chosen energy/ fluence, and selective Tb-related transitions are promising for precise control over tunability in the specific luminescence patterns of interest.

1 Introduction

Owing to increasing demands of display and optoelectronic devices, intensive research efforts are being pursued worldwide on various aspects of semiconductor nanostructured systems [1–3]. High-quality semiconductor nanocrystals can be processed by a wide variety of physical and chemical routes. Doping with suitable optically active impurities has its own importance when a specific emission is desired. In recent years, the fabrication of binary semiconductor nanocrystals doped with either transition-metal ions [4, 5], or rare-earth ions [6, 7] has gained a great deal of interest within the research community. Zinc oxide (ZnO), a wide direct band gap (3.37 eV at 300 K) semiconductor, exhibits intense light emission characteristics from the UV to the visible range in the electromagnetic spectrum [8–10]. With the advent of processing routes, it has been possible to produce not only good-quality spherical ZnO nanoparticles (quantum dots) of narrow size distribution but also nanostructures of a large variety e.g. rods, needles, strips, shells, urchin and flower-like structures [11, 12].

On the other hand, bombardment of the nanocrystal systems with energetic ions is an interesting concept to reveal in-depth information with regard to structural and morphological evolution during ion–nanomatter interaction. Attempts have been made so far that highlight ion-induced nanoparticle growth [13], nanostructure elongation [14, 15], ripple formation [16] and other such effects. While nanoparticle growth, splitting and directed growth are reported for ion energy in the MeV scale, ion implantation [17] and ripple formation are observed for ions carrying energy in the keV scale. The effect of controlled ion irradiation on asymmetrically shaped nanostructures could reveal many exciting properties that include surface polishing, polarized light emission, tunability in the trapped related emission, etc In particular, irradiation-related study on rare-earth-doped elongated systems is rarely discussed in the existing literature. In this report, we present cost-effective, one-step solid-state fabrication of quality Tb-doped ZnO nanorods and explore their structural and luminescence responses after 80-MeV nitrogen ion irradiation.

2 Experimental details

2.1 Synthesis of ZnO and Tb/ZnO nanorods

ZnO nanorods were synthesized using a simple solid-state reaction approach. A mixture of zinc acetate dihydrate (ZAD), a cationic surfactant cetyl-trimethyl ammonium

bromide (CTAB, 99.9% pure, Loba-Chemie), and sodium hydroxide (NaOH) with a molar ratio of 1:0.4:3 were ground together in an agate mortar for ~1 h at room temperature. The unidirectional soft grinding was accompanied by the abrupt decomposition and excess heat release while the reaction was in progress. After ultrasonication, the product was washed repeatedly with deionized water and ethanol and finally dried in air (~70 °C) for 2 h.

For preparing Tb-doped ZnO nanorods, at first, terbium oxide (Tb_4O_7, 99.9% pure, Otto) was converted to terbium acetate. 0.5 gm of terbium oxide was reacted with a 0.4 mL of conc. nitric acid (maintaining pH ~ 7 by dropwise addition of sodium hydroxide solution) resulting in a white precipitate. In order to remove unwanted byproducts, the product was subjected to repeated washing with distilled water. Finally, the product was treated with 0.4 mL glacial acetic acid to give rise to terbium acetate [$Tb(CH_3COO)_3$]. The Tb-doped ZnO nanorods were developed by adding as-received terbium acetate in the reactant-mixture (weight ratio Tb/Zn = 0.02) followed by unidirectional grinding.

2.2 Irradiation of the nanorods Nontoxic and transparent polyvinyl alcohol (PVA) matrix medium was selected to disperse ZnO nanorods. ZnO nanorod-dispersed PVA films were casted on laboratory glass slides ($1 \times 1 \, cm^2$) for the irradiation experiment. The samples were irradiated in the Material Science chamber under a high vacuum (pressure of $\sim 10^{-6}$ mbar) condition and using 80 MeV-N^{4+} ion beams (with a beam current of ~1 pnA, particle-nanoampere), available at the 15UD tandem pelletron accelerator of Inter University Accelerator Centre, New Delhi. The ion-beam fluence was measured by integrating the ion charge on the sample ladder, which was insulated from the chamber. The ion fluence was varied in the range of 5×10^{11}–8×10^{12} ions/cm^2.

The structural and optical properties of undoped and Tb-doped ZnO nanorods were characterized by X-ray diffraction (XRD), scanning electron microscopy (SEM), transmission electron microscopy (TEM), absorption and emission spectroscopy tools. The results are discussed with a specific objective to understand irradiation-induced effects on Tb-doped ZnO nanorod systems.

3 Results and discussion Figure 1 illustrates the XRD patterns of the pure and Tb-doped ZnO nanorods. In consistency with the other reports [7, 8], the diffraction peaks corresponded to the hexagonal wurtzite structure of ZnO with preferred orientation along the (101) plane (Fig. 1A). The XRD pattern of the Tb-doped system is similar to the undoped one and no extra peak was detected that might correspond to other byproducts or reactant species (e.g. TbO_2, Tb_2O_3, Tb_4O_7, etc.). Since terbium crystallizes into hexagonal closed packed structure, it can easily be accommodated into the hexagonal ZnO host lattice ($a = 3.257$ Å, $c = 5.233$ Å). As shown in the magnified version of Fig. 1A (i.e. Fig. 1B), the characteristic XRD patterns reveal a uniform shift in the diffraction peaks
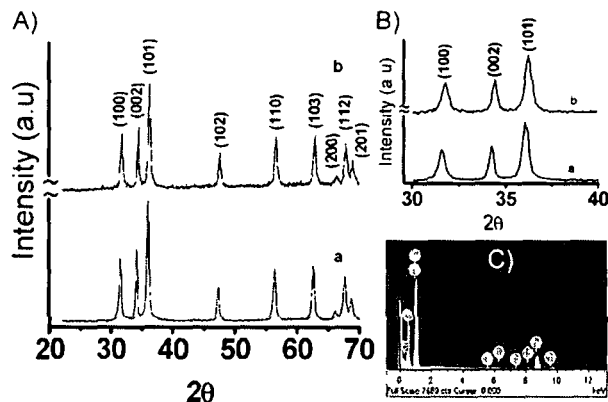

Figure 1 (online colour at: www.pss-a.com) (A) is the XRD pattern of (a) undoped ZnO nanorods, and (b) Tb-doped ZnO nanorods. (B) represents the magnified view of (A) that is shown in the selected diffraction angle range. (C) corresponds to the EDS spectra of Tb-doped ZnO nanorods.

towards larger angle in the case of Tb-doped ZnO nanorods ($a = 3.250$ Å, $c = 5.197$ Å) with respect to its ZnO counterpart. This may be attributed to the lattice mismatch aroused due to the incorporation of the larger-sized Tb^{3+} cations (1.18 Å) into the Zn^{2+} site (0.74 Å) of the host lattice. A similar kind of shift of the diffraction peaks towards larger diffraction angle on doping with rare-earth elements was reported by Zhang et al. [18]. It is necessary to make an in-depth analysis on the structural modification due to Tb doping. Applying the Williamson–Hall model [19], given by: $\beta \cos\theta = 0.9\lambda/D + 4\varepsilon \sin\theta$, one can obtain the average crystallite size (D) and microstrain (ε) for a system of interest. Here, β is the full width at half maxima (FWHM) at Bragg's angle (2θ), with λ being the X-ray wavelength (CuK$_\alpha$ = 1.54 Å). Since the expression represents the equation of a straight line, the lattice strain can be calculated from its slope, whereas the intercept on the y-axis gives the crystallite size. Accordingly, the values of lattice parameter, microstrain and average crystallite size for undoped and Tb-doped ZnO nanorods can be estimated (using Figs. 2a and b) and are presented in Table 1. The microstrain experienced by the Tb-doped ZnO system is about eight times more than its undoped counterpart. The substantial increment in strain
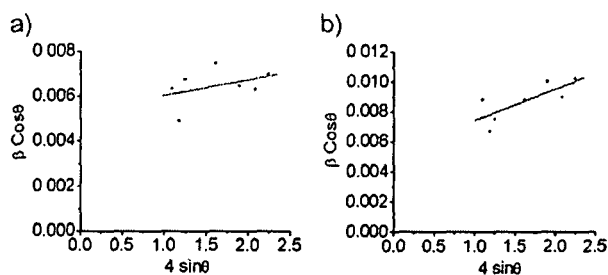

Figure 2 (online colour at: www.pss-a.com) Williamson–Hall plot of (a) undoped and (b) Tb-doped ZnO nanorods.

Table 1 Lattice parameter, microstrain and crystallite size of undoped and Tb-doped ZnO nanorods.

sample	microstrain	crystallite size (nm)	lattice parameter (Å)
ZnO	6.87×10^{-4}	28.84 ± 0.11	$a = 3.257, c = 5.233$
Tb/ZnO	2.11×10^{-3}	29.16 ± 0.03	$a = 3.250, c = 5.197$

value is assigned to the inevitable chemical incompatibility arising due to Tb incorporation into the ZnO host. The presence of Tb in doped ZnO nanorod system was also verified from the energy-dispersive spectra (EDS). Zinc and terbium atoms corresponding to the lowest ground-state energy were found to be located at the same position (Fig. 1C).

The visible evidence of nanorods was obtained from SEM (JEOL-JSM6390LV) and TEM (JEOL JSM-100 CX) studies which are presented in Figs. 3a and b. The average length and diameter of the nanorods are found to be ~600 and ~75 nm, respectively. The diameter of the nanorods at the extreme ends is found to be considerably smaller than the central parts. Since the decomposition of hydroxides into oxides is accompanied by a strong heat of reaction, the nanoparticle growth is expected to be slow during the initiation and termination of the final product (nanorods). The nanorods are found to be surface polished and resemble with the structure of solid-cylindrical ballpoint pens.

Figure 4 depicts the UV-visible absorption spectra of both the irradiated and unirradiated samples of Tb-doped ZnO nanorods. The un-irradiated nanorods (Figs. 4a and b) show long tailing and two prominent peaks at ~365 nm (~3.4 eV) and ~270 nm (~4.59 eV). The 365-nm peak is attributed to the excitonic ground-state ($n = 0$), whereas the 270 nm corresponds to the first ($n = 1$) excited excitonic state. The ground-state excitonic energy (~3.4 eV) is enhanced compared to the free exciton energy in the bulk (~3.30 eV) owing to 1D confinement of carriers [20]. The ground-state excitonic energy (3.4 eV), in our case, is comparatively smaller than the reported value (3.53 eV) where the nanorods are considered in the strong quantum confined regime. However, the first excited-state (4.59 eV) is consistent with the reported one [20]. The presence of long tailing due to significant inhomogeneity in the sample is found to be suppressed for ion-irradiated samples (Figs. 4c
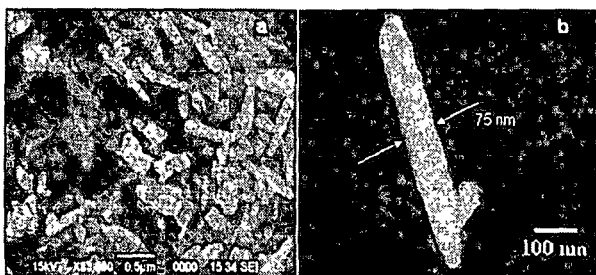
Figure 3 (a) SEM image of Tb-doped ZnO nanorods, and (b) TEM image of a fully grown isolated nanorod of diameter ~75 nm.
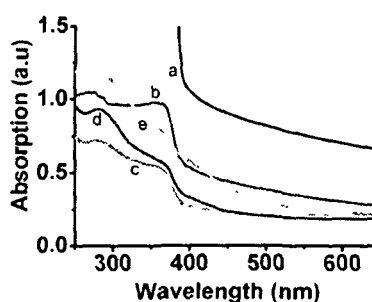
Figure 4 (online colour at: www.pss-a.com) UV-visible spectra of (a) unirradiated undoped ZnO, (b) unirradiated Tb-doped ZnO nanorods, and Tb-doped ZnO nanorods irradiated with a fluence of (c) 5×10^{11}, (d) 2×10^{12} and (e) 8×10^{12} ions/cm^2; respectively.

and d), though the ground-state excitonic absorption position is found to be undisplaced. This clearly indicates that controlled nitrogen irradiation could bleach out the undesired species at best along with improved surface passivation and without affecting the ground-state excitonic feature. Conversely, the excited-state absorption peak of irradiated nanorods was shifted to 285 nm (Figs. 4c–e). So, there is an appreciable redshift of ~235 meV in the first excitonic excited-state absorption of irradiated specimens, compared to the pristine one. It is now clear that a metastable-state is created between the ground-state and the first excited-state as a result of nitrogen ion irradiation. This newly generated state could be due to the improved symmetric distribution of the nanorods owing to recovery from matrix encapsulation which is otherwise suppressed in a given matrix. The excited-state excitonic absorption feature is found to be more prominent with increased ion fluence. In contrast, the ground-state absorption that was sharp in the case of the unirradiated nanorod specimen becomes broad owing to relaxed ground-state absorption. At the highest fluence (8×10^{12} ions/cm^2) the ground-state absorption becomes featureless followed by a long tailing. We have thus shown that with the proper selection of fluences, energetic nitrogen beam can improve not only the quality but also help in preserving ground-state and excited-state carrier population of elongated nanosystems (nanorods) under investigation.

The PL spectra of the nanorods ($\lambda_{ex} = 325$ nm) before and after irradiation are shown in Fig. 5A. In the asymmetrically broadened PL spectra, the defect-related emissions dominate the band-edge emission of ZnO and hence the band-edge emission (~370 nm, dashed line) is only poorly resolved. The central maxima at ~405 nm are ascribed as the emission from zinc vacancies present in the ZnO lattice [21]. The asymmetric nature of the luminescence patterns is ascribed to the presence of other inherent emission peaks (due to distributed defect states on the surface and in the interior of a given nanostructured system) at higher wavelengths owing to the asymmetric geometry of the nanosystems. In particular, the impression at ~430 nm is the emission due to the presence of zinc interstitials [21]. The zinc-interstitial-related emission becomes more prominent
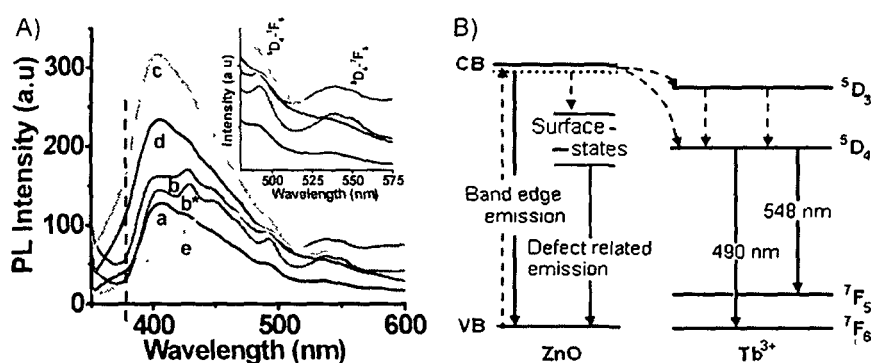
A)

B)

Figure 5 (online colour at: www.pss-a. com) A: Room-temperature PL spectra of (a) unirradiated undoped ZnO, (b) unirradiated Tb-doped ZnO nanorods, and Tb-doped ZnO nanorods irradiated with a fluence of (c) 5×10^{11}, (d) 2×10^{12} and (e) 8×10^{12} ions/cm^2, respectively. The label 'b*' corresponds to as synthesized Tb-doped ZnO, whereas 'b' represents nanorods after repeated washing and dispersing in PVA. B: Scheme of various transitions involved in Tb-doped ZnO nanosystem.

for Tb-doped ZnO nanorod system (Figs. 5Ab,b*). Further, for irradiated Tb/ZnO samples, this emission gets suppressed owing to the improvement in zinc-vacancy-related emission (~405 nm). A feebly resolved peak at ~490 nm of the undoped nanorods (Fig. 5Aa) is attributed to the blue emission of ZnO [21]. The same peak corresponding to the Tb-doped ZnO nanorods gets enhanced (Figs. 5Ab,b*) because of the superimposition of the Tb^{3+}-related $^5D_4$–$^7F_6$ transition that occurs almost in the same wavelength range [22]. Another weakly resolved band centered at ~535 nm was seen for undoped nanorods, which corresponds to the oxygen-vacancy-related green emission [23, 24]. This peak becomes distinct and broad in the spectrum of Tb-doped ZnO nanorods as a result of the overlapping emission pattern arising due to the transition ($^5D_4$–$^7F_5$) of Tb^{3+} at ~548 nm with the aforesaid green emission [25]. The probable transition events are also shown in schematic Fig. 5B.

The PL spectra of the irradiated nanorod samples exhibit significant alteration. The PL response of the nanorods, irradiated with a fluence of 2×10^{12} ions/cm^2 is more intense than the unirradiated nanorods, but irradiation with a fluence of 5×10^{11} ions/cm^2 exhibits the highest PL intensity (Figs. 5Ab–d). Note that the central peak-to-blue, and central peak-to-green emissions are found to be enhanced for irradiated Tb-doped ZnO nanorods, upto a fluence of 2×10^{12} ions/cm^2 (Table 2). It is expected that upon ion irradiation the nanorods overcome the PVA matrix encapsulation allowing recovery of free excitons and resulting in the enhancement of defect-related emission. The Tb^{3+}-related emission peaks are still in view after irradiation (Figs. 5Ac–e). This indicates

that the Tb^{3+}-related peak appears due to the energy transfer from the deep level states to the $^5D_4$ energy level of Tb^{3+} cations (Fig. 5B). While returning from the conduction band, most of the photoexcited electrons relax in the defect states and transfer their energy to the $^5D_4$ energy level of Tb^{3+} resulting in the $^5D_4$–$^7F_6$ and $^5D_4$–$^7F_5$ transitions. The visual evidence of recovery from matrix encapsulation can also be seen in the electron micrographs (Figs. 6a and b). In contrast, the same sample that was irradiated with a fluence of 8×10^{12} ions/cm^2, the PL intensity decreases drastically along with a redshift in the PL spectra (Fig. 5Ae). This indicates that at this fluence, the nanorods get completely dislodged from the supporting matrix, leading to agglomeration events (Figs. 5Ae and 6c,d). The agglomeration leads to the suppression of the zinc vacancy and zinc interstitial related emissions. The agglomerated system is characterized by a disordered phase where the quantum confinement effect would no longer be valid. However, the Tb-related emission peak remained intact even if the structural ordering was lost. The agglomerated nanosystem (corresponding to a fluence of 8×10^{12} ions/cm^2) is found to have a symmetric peak at ~455 nm.

Taking PL maxima into consideration, the variation in the symmetry factor vs. ion fluence can be plotted (Fig. 7). The improvement in the symmetry factor (δ/Δ, δ is the magnitude of the lower-end asymmetry and Δ is the FWHM) from 0.28 to 0.48 was observed while fluence was varied from 5×10^{11} to 8×10^{12} ions/cm^2. Thus, one can adequately improve the symmetry factor without retaining structural ordering for overexposed samples. It is believed

Table 2 Characteristic PL response vs. ion fluence variation for Tb/ZnO nanorods.

fluence (ions/cm^2)	energy absorbed (J/cm^2)	central peak position (nm)	relative PL intensity	
			central-to-blue	central-to-green
0 (undoped)	0	405	2.3	4.2
0 (Tb-doped)	0	405	1.7	1.9
5×10^{11}	6.4	405	2.5	4.0
2×10^{12}	25.6	405	2.8	4.9
8×10^{12}	102.4	405 (455^a)	0.7	1.0

^{a}Though the central position is shifted to 455 nm, the original central peak at 405 nm (corresponding to zinc vacancy) remains intact.
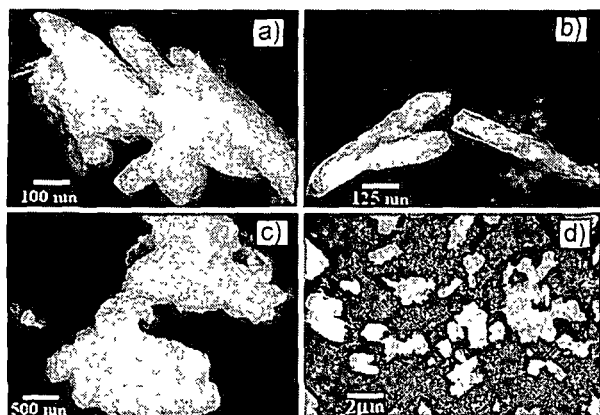
Phys. Status Solidi A **207**, No. 8 (2010)

1863

Figure 6 TEM image of the Tb/ZnO nanorods after irradiation with a fluence of (a) 5×10^{11}, (b) 2×10^{12} and (c) 8×10^{12} ions/cm^2; respectively. An overview of the agglomerated nanorods (case 'c') at lower magnification is shown in (d).
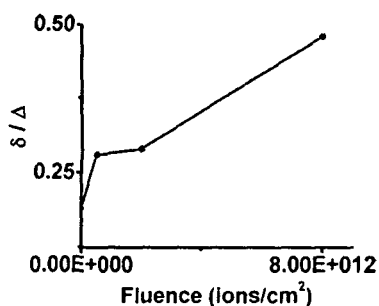

Figure 7 (online colour at: www.pss-a.com) Symmetry factor vs. ion fluence variation.

that with controlled nitrogen ion irradiation, one can recover not only band-edge emission but also improve the defect-related tunable and selective emissions.

4 Conclusions By adopting a user-friendly surfactant-assisted growth process, one can produce high-quality Tb-doped ZnO nanorods. The excitonic ground-state and excited-state absorption features are evident in the optical absorption spectra. Nitrogen ion irradiation, at selected fluences, has a direct impact on defect-related emission owing to significant surface modification. Recovery of the nanorods from the polymer matrix due to ion irradiation enables the suppression of the non-radiative emission and improvement of the radiative emission via surface traps. The Tb-related $^5D_4$–$^7F_5$ and $^5D_4$–$^7F_6$ transitions are found to be overlapped with the respective blue and green bands of the luminescence patterns. The quantitative aspects correlating structural modification and luminescence patterns, applicable for rare-earth-doped irradiated ZnO nanorods might form the basis of nanoscale luminescent/display devices and are currently being investigated by our group.

References

[1] X. Peng, L. Manna, W. Yang, J. Wickham, E. Scher, A. Kadavanich, and A. P. Alivisatos, Nature **404**, 59 (2000).

[2] J. Hu, L.-S. Li, W. Yang, L. Manna, L.-W. Wang, and A. P. Alivisatos, Science **292**, 2060 (2001).

[3] C. B. Murray, D. J. Norris, and M. G. Bawendi, J. Am. Chem. Soc. **115**, 8706 (1993).

[4] R. N. Bhargava, D. Gallagher, X. Hong, and A. Nurmikko, Phys Rev. Lett. **72**, 416 (1994).

[5] M. Tanaka, J. Lumin. **100**, 163 (2002).

[6] S. Okamoto, M. Kobayashi, Y. Kanemitsu, and T. Kushida, Phys. Status Solidi B **229**, 481 (2002).

[7] A. Ishizumi and Y. Kanemitsu, Appl. Phys. Lett. **86**, 253106 (2005).

[8] M. Haupt, A. Ladenburger, R. Sauer, K. Thonke, R. Glass, W. Roos, J. P. Spatz, H. Rauscher, S. Riethmuller, and M. Moller, J. Appl. Phys. **93**, 6252 (2003).

[9] Y.-K. Tseng, C.-J. Huang, H.-M. Cheng, I.-N. Lin, K.-S. Liu, and I.-C. Cheng, Adv. Funct. Mater. **13**, 811 (2003).

[10] X. Liu, X. Wu, H. Cao, and R. P. H. Chang, J. Appl. Phys. **95**, 3141 (2004).

[11] A. B. Djurišiæ, Y. H. Leung, K. H. Tam, L. Ding, W. K. Ge, H. Y. Chen, and S. Gwo, Appl. Phys. Lett. **88**, 103107 (2006).

[12] S. Gao, H. Zhang, R. Deng, X. Wang, D. Sun, and G. Zheng, Appl. Phys. Lett. **89**, 123125 (2006).

[13] Y. K. Mishra, D. K. Avasthi, P. K. Kulriya, F. Singh, D. Kabiraj, A. Tripathi, J. C. Pivin, I. S. Bayer, and A. Biswas, Appl. Phys. Lett. **90**, 073110 (2007).

[14] S. M Kluth, J. D. Fitzgerald, and M. C. Ridgway, Appl. Phys. Lett. **86**, 131920 (2005).

[15] D. Mohanta, G. A. Ahmed, A. Choudhury, F. Singh, D. K. Avasthi, G. Boyer, and G. A. Stanciu, Eur. Phys. J. Appl. Phys. **35**, 29 (2006).

[16] J. Lian, W. Zhou, Q. M. Wei, L. M. Wang, L. A. Boatner, and R. C. Ewing, Appl. Phys. Lett. **88**, 093112 (2006).

[17] P. G. Kik and A. Polman, J. Appl. Phys. **88**, 1992 (2000).

[18] L.-L. Zhang, C.-X. Guo, J.-J. Zhao, and J.-T. Hu, Chin. Phys. Lett. **22**, 11225 (2005).

[19] G. K. Williamson and W. H. Hall, Acta Metall. **1**, 22 (1953).

[20] Y. Gu, Igor, L. Kuskovsky, M. Yin, S. O'Brien, and G. F. Neumark, Appl. Phys. Lett. **85**, 3833 (2004).

[21] B. Lin, Z. Fu, and Y. Jia, Appl. Phys. Lett. **79**, 943 (2001).

[22] Z.-B. Fang, Y.-S. Tan, X.-Q. Liu, Y.-H. Yang, and Y.-Y. Wang, Chin. Phys. **13**, 1330 (2004).

[23] F. A. Kroger and H. J. Vink, J. Chem. Phys. **22**, 250 (1954).

[24] K. Vanheusden, W. L. Warren, C. H. Seager, D. R. Tallant, J. A. Voight, and B. E. Gnade, J. Appl. Phys. **79**, 7983 (1996).

[25] K. E. McBean, M. R. Phillips, and E. M. Goldys, Microsc. Microanal. **12**, 327 (2006).

Chromium Doped ZnS Nanostructures: Structural and Optical Characteristics

D P Gogoi[a], U Das[a], G A Ahmed[a], D Mohanta[a], A Choudhury[a],
G A Stanciu[b]

[a]Nanoscience Research Laboratory Department of Physics Tezpur University Naapam, Tezpur,
Assam [b]Centre for Microscopy Microanalysis & Image Processing University "Politehnica" of
Bucharest Romania

Abstract. Chromium doped ZnS nanoparticles arranged in the form of fractals were fabricated by using inexpensive physico-chemical route The Cr ZnS samples were characterized by diffraction and spectroscopic techniques Unexpected growth of fractals with several micrometer dimensions and of core size $1\mu m$ (tip to tip) was confirmed through TEM micrographs At higher magnification, we found that individual fractals consist of spherical nanoparticles of average size < 30 nm The mechanism leading to such organized structures describing fractal pattern is encountered in this work

INTRODUCTION

Among II-VI semiconductor systems, ZnS is the most popular wide band gap system having a direct band gap of ~3 7eV at 300^0K ZnS is a promising host material due to its thermal and environmental stability Transition metal doped semiconductor nanostructures e g Mn ZnS, Mn ZnO, Cu ZnS are believed to be potential candidates owing to strong emission due to impurity states [1-3] Incorporation of both transition-metal ions and rare-earth ions ZnS nanostructures by adopting chemical and physical techniques have been reported in recent years [4-6] It has been used as base material for cathode ray tube luminescent materials [7,8] On the other hand, Cr doped ZnS has not received much attention owing to significant chemical incompatibility arising due to lattice mismatch at the host lattice Over the years, chemically synthesized doped semiconductor nanostructures have attracted scientific community owing to inexpensive procedures for large scale production Fabrication of micro structured fractals requires self assembly since direct manipulation of such self similar structures at the lower end of the scale is extremely difficult to achieve [9] There is a growing interest and continuous demand in the fabrication of self similar materials, parts, features etc for application in nanotechnology One of the difficult tasks was to produce materials that incorporate multiple length scales simultaneously, from nano and micro, to micro scale In fact, fractals could achieve this goal because of their self similarity and sustainability in the real world as well as in theory [10,11] In this paper, we report physico-chemical synthesis of Cr ZnS nanostructures and their

spectroscopic and structural characterizations. A theoritical approach on the formation of resulting fractals is also attempted

EXPERIMENTAL

Cr-doped ZnS encapsulated in polyvinyl alcohol matrix (PVOH) was fabricated using a low cost colloidal solution casting route. For this 2% (w/v) PVOH in double distilled water was magnetically stirred at ~200 rpm at a constant temperature for six hours until a transparent solution was formed. Next, aqueous solution of $ZnCl_2$ was added to the PVOH matrix under stirring condition and then aqueous solution of CrO_3 solution was mixed at room temperature. To this precursor Na_2S solution was drop wise injected, which led to the growth of 'Cr.ZnS' nanoparticles Optical properties of the samples were studied through PL-spectra. The structural aspects were revealed by XRD, TEM, AFM, MFM studies. The freshly prepared samples of Cr·ZnS, deposited on glass substrates are used for AFM, MFM, PL and XRD measurements, where as liquid samples were kept for TEM studies.
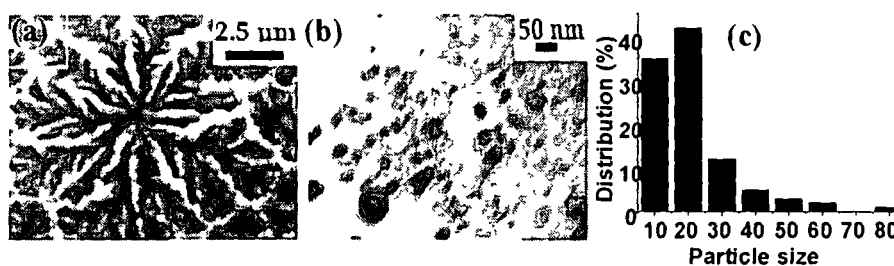

FIGURE 1. TEM micrographs (a) Fractal patterns at higher magnification,
(b) spherical nanoparticles of Cr ZnS in PVA matrix at closer inspection (c) Distribution of particles with average grain size

RESULTS AND DISCUSSION

At lower magnification unexpected growth of fractal-like patterns [10,11] were confirmed though TEM micrographs (Figure 1a), while at higher magnification these fractals were found to consist of individual nanoparticles of average size less than 30 nm (Figure 1b). In figure 1c, distribution (%) of nanoparticles with particle size in a 0.585 sq. µm area is shown. It is observed that the maximum number of particles lie within the range of 10 nm to 20 nm. The fractal like feature was further confirmed by systematically measuring its fractal dimension, typically defined by the divider formula [12]

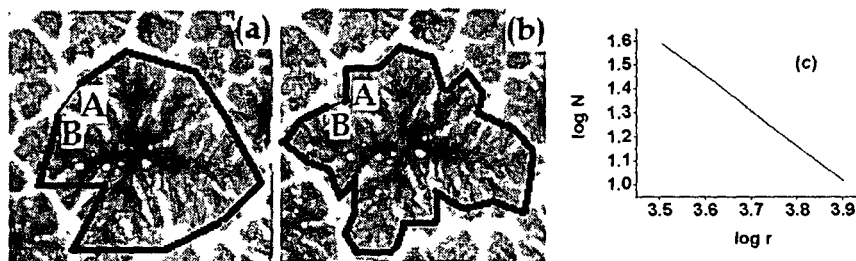$$D_f = \lim_{r \to 0} \frac{\log N(r)}{\log(r)}$$

503

FIGURE 2. Analysis of the fractal patterns, (a) A straight rular of length r (thick line), walks along the nanomaterial surface contour, starting from point A, and ends at point B, Left : r= 125 μm, and in figure (b) r = 50 μm, The distance between A and B (thin line) is measured to be d. The path length N is then defined as the sum of the number of steps and d/r . (c) A log-log graph of N versus (μm) The fractal dimension , D_f is the absolute value of the slope, in this case, D_f = 1.48.

where r is the length unit, $N(r)$ is the size of the geomatric object measured with unit r. To measure D_f, We used a methode illustrated by Andrea Lomannder et. al. [9]. For a given value of r , the ruler usually cannot walk along the contour exactly with an integer number of steps, giving rise to the mismatch between the start and the endpoints (points A and B in figure 3). In such cases, N was calculated as the sum of the number of full steps and the fractional length between the start and the end points with respect to r. In the example shown in figure 3(a), r=125 μm, it looks 10 steps (thick line) starting from A to proceed to the point B along the contour. The remaining distance between A and B (thin line) is 50 mμ, whose fractional length with respect to r is 50/125 = 0.4, thus the total contour length is 10.4. In figure 3(b) r = 50μm, the contour length yeilded an average value of N=38.75. The measured value of N depended on the location of the starting point of the contour. Inspired by the Nyquist sampling theorem [13], several values of N starting at different points on the contour were measured and averaged. The graph of log[r] vs. Log[N] gave the fractal dimension D_f = 1.48. This value corresponds to the fractal dimension D_f of a viscous fingering system [14], whose formation mechanism is known as diffusion-limited aggregation (DLA) [15,16]. In the plane, D_f = 1.71; however, in real systems, depletion effects may decrease D_f from this ideal value to 1.4 [13.14]. Thus, it can be interpreted that the fractal like feature was formed through DLA-like process. Change of pH and the presence of disulphide bond are important for the formation of fractals through DLA-like process [9]. Molecular self- assembly takes place via a subtle balance between non covalent bond interactions that result in the formation of well-defined structures [17-22]. The cysteine disulphide bond should remain stable at lower pH [23,24]. In a recent work [2], The authours have shown production of Cr:ZnS nanoparticles without formation of fractals. We have though followed the similar method replaced treatment of H_2S by acidic Na_2S treatment. We expect that, in our case the presence of excess disulfide bond could be responsible for the formation of fractals.

504

X-RAY DIFFRACTION STUDIES

The X-ray diffraction pattern of the Cr:ZnS nanoparticles embedded in PVOH matrix is shown in figure 3. It depicts cubic crystalline structure corresponding to three diffraction peaks (111), (220) and (311). The average particle size estimated is 12 nm as obtained by measuring full-width-at half maxima (FWHM) according to Scerrer's formula [25]

$$d = \frac{0.9\lambda}{\omega \cos\theta}$$

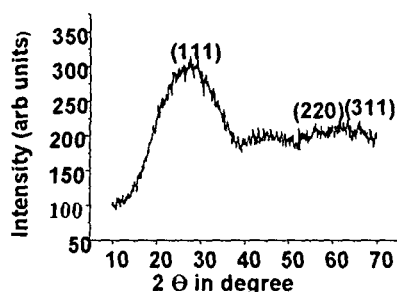It has also been observed that maximum numbers of particles are oriented with crystalline state (111).

FIGURE 3. XRD pattern of Cr doped ZnS
nanostructures in PVA

Photoluminescence Study

Figure 4 represents photoluminescence response of Cr doped ZnS nanostructures in PVOH matrix at excitation wavelength 300 nm. The appearance of the PL peak with energy close to the band gap energy is recognized as band gap emission [26]. On the other hand emission peak corresponding to low energy values ascribed to the transition involving donors, acceptors, free electrons and holes. We ascribe the emission peak at ~380 nm as the band edge emission of ZnS and the peak at around 550 nm is expected due to d-electron transfer of Cr^{2+} into the ZnS host.
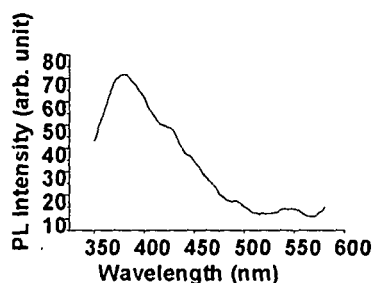

505

AFM AND MFM STUDIES

The surface morphology of the samples casted on glass substrates were studied by using scanning probe microscopy (SPM). A typical AFM and MFM micrographs for the sample is shown in Figure 5. AFM image of the sample exhibits uniform surface morphology as shown in figure 5(a). Magnetic force microscopy is a well established method to probe the micro-magnetic properties of samples with lateral resolution down to ~50 nm. The advantage of SPM is that less sample is needed, thinning or polishing of the sample is not necessary. Moreover, the technique yields information on both the structural (AFM mode) as well as the magnetic (MFM mode) aspects with regard to sample's surface. Therefore, the topology and magnetic domain structure of a sample can efficiently be correlated at the nanometer scale. Transition metals like Mn, Fe, Co, Ni doped ZnS, ZnTe systems are found to display spin glass state, where as V or Cr doped ZnS, ZnSe, ZnTe are ferromagnetic in nature [2].
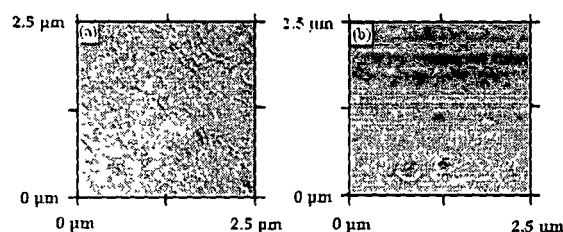

FIGURE 5. (a) AFM and (b) MFM micrographs of Cr doped ZnS embedded in PVA

To exploit magnetic properties, we have carried out MFM studies on the Cr doped ZnS samples. The figure 5(b) is basically a phase image of the sample; it shows clear response to the magnetic field. The average size of the magnetic cores (black spot) is measured as ~ 165 nm and white regions spreading over the cores are ascribed to region of influence by the respective particles. Thus, it is evident that ZnS:Cr nanoparticles can respond appreciably to magnetic force and fields and MFM in this regard, can be a very good tool to exploit magnetic domains and particle-particle interactions.

CONCLUSIONS

We have fabricated Cr-doped ZnS nanostructures by a simple and inexpensive chemical route. Photoluminescence shows a new emission peak ~ 550 nm due to incorporation of Cr^{+2} ions into ZnS host. Spherically isolated magnetic domains are found in MFM micrographs. A new direction for generation of fractals with II-VI based transition metal doped diluted magnetic semiconductor is reported. Here, the synthesized fractals are of dimension 1.48. This is evident that the growth of fractals were due to diffusion limited aggregation. The mechanism of fractal formation at nanoscale level is in progress.

ACKNOWLEDGMENTS

REFERENCES

1   W Lu and C M Lieber, *J Phys D* 39, R387 (2006)
2   U Das, D Mohanta and A Choudhury, *Ind J Phys* 81, 155-159 (2007)
3   D Mohanta S S Nath and A Choudhury, *Bull Mater Sci* 26, 289 (2003)
4   Y Wu, K Arai, N Kuroda, T Yao, A Yamammoto, M Y Shan and T Goto, *Jpn J Appl Phys* 36, Ll 648 (1997)
5   K Shibata, K Takabayashi, I Souma, J Shen, K Yanata and Y Oka, *Physica E* 10, 358 (2001)
6   C S Kim, S Lee, J Kossut, J K Furdyna and M Dobrowolska, *J Cryst Growth* 395, 214-215 (2000)
7   R Vacassy, S M Scholz, J Dutta, H Hoffmann, C J C Plummer, G Carrot, J Hilborn and M Alkine, *Matter Res Soc Symp Proc* 501, 369 (1998)
8   P Calandra, M Goffred and V T Livery, *Colloid Surf A* 160, 9-13 (1999)
9   Andrea Lomander, Wonmuk Hwang, and Shuguang Zhang, *Nano Lett* 5, 1255-1260 (2005)
10   10 B Mandelbrot, *The Fractal Geometry of Nature*, 3rd ed , W H Freeman and Company, New York, (1983)
11   B Mandelbrot, *Fractal and Chaos*, The Mandelbrot Set and Beyond, Springer-Verlag, New York, (2004)
12   12 C Beck and F Scho gl, *Thermodynamics of Chaotic Systems* Cambridge University Press Cambridge, (1993)
13   D Skoog and J Leary *Principles of Instrumental Analysis*, 4th Ed , Saunders College Publishing, Philadelphia, (1992)
14   P Meakin, *Phys Rev A* 27, 1495-1507 (1983)
15   T Witten and L Sander, *Phys Rev Lett* 47, 1400-1402 (1981)
16   T Witten and L Sander, *Phys Rev B* 27, 5686-5697 (1983)
17   G M Whitesides, *Nat Biotechnol* 21, 1161-1165 (2003)
18   S Zhang, *Nat Biotechnol* 21, 1171-1178 (2003)
19   M Reches and E Gazit, *Science* 300, 625-627 (2003)
20   N Kroger, R Deutzmann and M Sumper, *J Biol Chem* 276, 26066-26070 (2001)
21   L L Bratt and M O Stone, *Nature* 413, 291-293 (2001)
22   S Mann and H Co Ifen, *Angew Chem Int Ed* 42, 2350-2365 (2003)
23   P Gupta, H Rizwan, H Khan and M Saleemuddin, *Int J Biol*
24   J Horng, S Demarest, and D Rsleigh, *Proteins Struct Funct Genet* 52, 193-202 (2003)
25   P Scherre, *Gott Nachr* 2 98 (1990)
26   A K Pal, *Bull Mater Sci* 22341 (1999)